DISSERTATION

SYNTHETIC APERTURE SOURCE LOCALIZATION

Submitted by

Chad Waddington

Department of Mathematics

In partial fulfillment of the requirements

For the Degree of Doctor of Philosophy

Colorado State University

Fort Collins, Colorado

Summer 2018

Doctoral Committee:

Advisor: Margaret Cheney

James Given
Jennifer Mueller
Oliver Pinaud
Liuqing Yang

ABSTRACT

SYNTHETIC APERTURE SOURCE LOCALIZATION

The detection and localization of sources of electromagnetic (EM) radiation has many applications in both civilian and defense communities. The goal of source localization is to identify the geographic position of an emitter of some radiation from measurements of the fields that the source produces. Although the problem has been studied intensively for many decades much work remains to be done.

Many state-of-the-art methods require large numbers of sensors and perform poorly or require additional sensors when target emitters transmit highly correlated waveforms. Some methods also require a preprocessing step which attempts to identify regions of the data which come from emitters in the scene before processing the localization algorithm. Additionally, it has been proven that pure Angle of Arrival (AOA) techniques based on current methods are always suboptimal when multiple emitters are present. [25]

We present a new source localization technique which employs a cross correlation measure of the Time Difference of Arrival (TDOA) for signals recorded at two separate platforms, at least one of which is in motion. This data is then backprojected through a Synthetic Aperture Radar (SAR)-like process to form an image of the locations of the emitters in a target scene. This method has the advantage of not requiring any *a priori* knowledge of the number of emitters in the scene. Nor does it rest on an ability to identify regions of the data which come from individual emitters, though if this capability is present it may improve image quality.

Additionally we demonstrate that this method is capable of localizing emitters which transmit highly correlated waveforms, though complications arise when several such emitters are present in the scene. We discuss these complications and strategies to mitigate them.

Finally we conclude with an overview of our method's performance for various levels of additive noise and lay out a path for advancing study of this new method through future work.

ACKNOWLEDGEMENTS

I would like to acknowledge the long support of my advisor Dr. Margaret Cheney without whose guidance this dissertation would not have been possible. Her perseverance with me through two universities and the jump to the Air Force Research Lab has been invaluable. Likewise I am indebted to Dr. Jim Given for many fruitful conversations via phone and e-mail. Credit for the first seeds of what has grown into this dissertation go to him.

For many conversations and guidance on radar, writing a dissertation, and research in the ‘real world’ I thank the members of RYMD who have supported my transition beyond this dissertation even as I finish it.

For encouragement to stick with it even when the progress was slow or negligible I thank numerous members of my family and friends.

I am also indebted to all of the other personnel at AFRL for offering me the tremendous opportunity to transition into the professional lab environment while continuing to spend significant amounts of my time completing the work in this document. Without the financial and managerial support I received here, my time completing this work could never has been as supportive and enriching as it has been.

To many wonderful teachers throughout my academic career, thank you. In particular I would like to thank my high school chemistry teacher whose encouragement to read voraciously in both science and science fiction led me down a path I may otherwise have never considered.

To my longest friend, our continual competition to outdistance each other and ourselves has helped to make me the man I am today. As iron sharpens iron, so one man sharpens another. Thank you for being the iron upon which I have sharpened myself for so many years.

To my parents, your constant support in all things from moving me across the country again and again to covering my car insurance and cell phone bills when the money was too tight has been appreciated more than I can express. Knowing that you are always there and always willing

to pitch in has allowed me to leap over obstacles that may otherwise have given me pause. I will probably never know just how vital your support has been in making my dreams a reality.

Finally to my wife, you have been my biggest fan and a constant support. Your faith in my ability to finish this undertaking never wavered and you never let me doubt myself. Your constant push to keep moving forward has been invaluable. Beyond this, your incredible cooking skills and decorating flare have ensured that wherever we landed along this journey each new house or apartment quickly became home. You never fail to find new adventures and excitement wherever we go. Without you I may have finished this work, but my life in the processes of doing so could never have been as rich, rewarding, and full as it has been with you. Thank you.

DEDICATION

This dissertation is dedicated to my wife Emily and to all of the teachers and professors who inspired and encouraged my love of learning.

TABLE OF CONTENTS

LIST OF FIGURES

Chapter 1

INTRODUCTION

The detection and localization of sources of electromagnetic (EM) radiation has many applications in both the civilian and defense communities. An example of such an application is the geolocation of hikers lost on a mountain or in a forest by the detection and localization of the EM radiation from the signals emitted by their radios. Another practical application of source localization is the search for modern personal and commercial ships and airplanes in the event of a crash or other catastrophic failure; such craft contain emergency radio sources for exactly such purposes. [3]

Current state-of-the-art methods require a large number of receiving antennas and/or significant preprocessing of the data to identify regions of data which are hypothesized to come from an emitter. Some methods in wide use also require the user to either know the number of emitters in a scene of interest a priori or to make a guess at the number. Additionally these methods are often not well equipped to identify and localize sources in a scene containing several emitters which are transmitting highly similar waveforms.

We present a method of source localization which is based on the principles of Synthetic Aperture Radar (SAR) imaging. Our method uses the cross correlation of the electromagnetic signals recorded at two passive (non-transmitting) moving antennas to form a filtered backprojection image of the radio frequency (RF) emitters in a scene of interest. This method aims to fulfill the goals of traditional source localization schemes, namely to detect and geolocate emitters in a scene of interest, by applying the mathematical framework of SAR to create an image of the intensity of the RF radiation in the scene.

This method overcomes the requirement that localization systems measure a scene with more receivers than there are transmitters present by using the data collected from the scene from many locations to form an image, the resolution of which will depend on certain flight path parameters.

Due to its close relationship with traditional SAR imaging methods we have called this new method Synthetic Aperture Source Localization (SASL).

This method is capable localizing several RF emitters in a scene of interest using only two antennas as long as at least one antenna is in motion. This method requires no a priori knowledge of the signals being transmitted beyond the necessity that the receiving hardware be capable of recording whatever frequency bands of signals are of interest in the scene under observation. Since the antennas are passive, the platforms on which they are housed can be built much smaller and cheaper than those required for traditional SAR systems. Such platforms also require less power since the bulk of the energy cost of a SAR system goes into the transmitting platform. Thus, despite the similarities in the data collection process, the potential exists for executing this method of localization at lower cost, both in terms of dollars and energy than that required for traditional SAR data collection systems.

We begin this thesis by examining the history of source localization and overviewing existing methods in the literature. In Chapter 3 we provide an introduction to the mathematics of SAR including both Monostatic and Bistatic SAR systems. We show how the data recorded at SAR receiving platforms is filtered and backprojected to create an image of the target scene and how artifacts arise in the image.

In Chapter 4 we introduce the method of Synthetic Aperture Source Localization including an analysis of the backprojection operator and construction of an appropriate filter to minimize image artifacts. This introduction to the method is done under ideal conditions in which the operator is able to separate the signals from different sources prior to data processing. In Chapter 5 we construct and analyze numerical simulations of the the SASL model built up in Chapter 4 and identify limitations to the model.

In Chapter 6 we return to the idealized assumptions regarding the data made in Chapter 4 and derive a model for the recorded data under the more realistic case in which the recorded signal is the superposition of all signals transmitted from the scene. Here we assume that the contributions from different emitters cannot be separated a priori. This leads us to an examination of the so called *cross terms* which arise when the received signal contribution from one emitter is cross correlated with that received from another emitter in the scene.

In Chapter 7 we derive an expression for the contribution to the data of such terms and determine the family of curves which defines the backprojections of such terms in our image. We then prove that, in a noiseless data collection, the family of the backprojection curves for terms arising from diagonal term emitter data intersect in a unique point regardless of receiver flight path and that this point is the emitter location. In contrast, we prove that the family of backprojection curves for the cross terms do not have a unique point of intersection except in a few special cases, and that in these cases the point of intersection is the location of an emitter in the scene of interest.

We are thus able to conclude that the only persistent peaks in the SASL image will be at the location of the emitters. Therefore, although cross term effects may play a roll in cluttering the image with undesirable phantom artifacts these artifacts should become less pronounced as the flight path of the data-collecting antennas is lengthened.

Chapter 8 further extends the model toward a more realistic data collection scenario by examining the effects of flying three dimensional flight paths and of having more than one receiver in motion during the data collection process. Chapter 9 then analyzes the effect on the image in the presence of noise in the recorded signal. We also discuss the difficulty in rigorously quantifying the noise present in the post processing data for our method because of the presence of noise in both the received signal and in the signal used for the cross correlation filtering process. Finally in Chapter 10 we summarize our conclusions and present the problems and extensions to the method to be addressed in future work.

Throughout this paper we will use the Fourier transform convention

$$H(f) = \mathcal{F}\left\{h(t)\right\} = \int h(t)e^{i2\pi ft}dt \tag{1.1}$$

$$h(t) = \mathcal{F}^{-1}\left\{H(f)\right\} = \int H(f)e^{-i2\pi ft}df \tag{1.2}$$

where f is the variable for the frequency domain and t is the variable of the time domain. Unless otherwise specified we will use lowercase letters to denote functions in the time domain and their uppercase counterparts to denote the corresponding Fourier transform pairs in the frequency domain.

Chapter 2

SOURCE LOCALIZATION

2.1 Historical Development of Direction Finding Techniques

The goal of all source localization techniques is to determine the location of an emitter of some radiation from measurements of the field at a point or points separated from the emitter in both time and space. In our work we will be concerned with emitters of electromagnetic (EM) radiation.

The basic concepts and principles behind the theory of direction finding and source localization have existed almost as long as the theory of electromagnetic waves themselves. Only 15 years after Maxwell published the four differential equations governing the behavior of electromagnetic waves which bear his name, Heinrich Hertz discovered the directivity of antennas. In 1888 while conducting experiments to verify Maxwell's theories Hertz found that various polarizing filters could be used to influence the reception of electromagnetic waves and that various physical changes to the apparatus affected the resulting transmitted wave. [4,5]

The principle of a direction finding antenna based on Hertz's work was first patented in 1907 by Otto Scheller. Scheller's design became widely used in the navigation of airplanes and was used to create an audible homing tone which allowed pilots to locate a runway and land safely in conditions of reduced visibility. Various improvements to the state of the art, including miniaturization of antennas and direction finding based on the Doppler phenomenon continued to appear throughout the next 70 years. [5]

Since the 1980s digital signal processing techniques requiring implementation on digital computer systems have become ever more prevalent. It is convenient to consider the birth of what may be termed “modern source localization techniques" from this point. We can break down the modern approaches to source localization into two broad categories which can be further subdivided into relatively broad subcategories. [4]

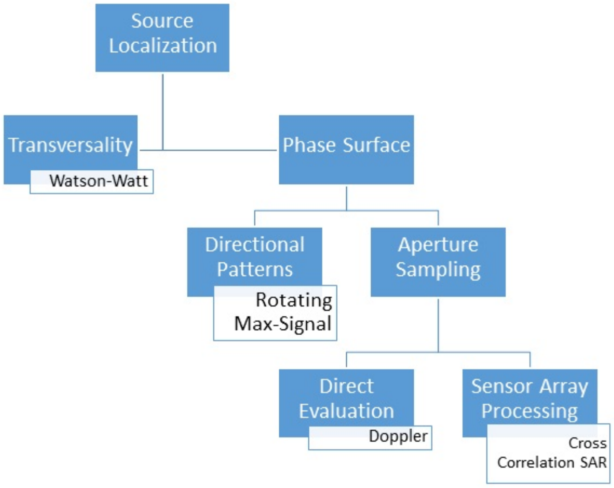

Figure 2.1: The broad categories of source localization techniques

The first category includes those methods which rely on the transversality of an electromagnetic wave's field vectors. These methods directly measure the direction in which the field vectors, either electric, magnetic, or both, are pointing. From this information the wave's direction of propagation can be determined by recalling that the direction of propagation is orthogonal to that of the field vectors. [6]

An early example of a technique in this category is the Watson-Watt method first developed in 1925. This method uses two crossed directional antennas to measure the magnitude of an arriving electromagnetic wave. These measured magnitudes are then mixed with a reference signal obtained from an omni-directional antenna. An arctangent may then be applied to the two results in order to obtain the arriving signal's bearing. [4, 6]

The second category of direction finding methods includes those techniques which measure the orientation of surfaces of equal phase. This category may be further subdivided into those methods relying on measurement of directional patterns and those relying on aperture sampling. [4]

A simple example of a system which relies on the measurement of directional patterns is that of a rotating maximal-signal direction finder. Here, an operator physically rotates a receiving antenna until the voltage output due to an arriving signal reaches a maximum. The bearing of the arriving signal can then be determined from the rotation angle of the antenna. This method can be automated and used for modern applications by the addition of a system which autonomously detects the antenna angle at the point of maximum received voltage and outputs a computed signal bearing. This allows for antennas which rotate at speeds much greater than the rate at which a human operator could identify the signal maximum or record its bearing. [4]

Aperture sampling techniques may be further subdivided into those relying on direct evaluation of the phase components and those using sensor array processing methods. An example of a direct evaluation technique is that of a Doppler direction finding system.

In such a system a rotating antenna measures the frequency of an incoming wave. This frequency is modulated with the rotational frequency of the antenna itself. If the antenna is rotating toward the source of the incoming wave the frequency of the wave is increased, if it is rotating away the frequency is decreased. From this frequency change a bearing for the incoming wave can be determined. In practice, systems set out several antenna elements arrayed in a circle and sample from them in sequence using diode switches to simulate the effect of a rotating antenna. In this way the speed of rotation of the simulated antenna element can exceed that which is practical for a physically rotating apparatus. [4]

The final class into which direction finding systems are subdivided are those which rely on sensor array processing. Broadly speaking these techniques were not possible before the advent of digital computers powerful enough to handle the necessary calculations in a short enough period of time. It is this category into which the work done in this dissertation will fall. [4]

2.1.1 The MUSIC Algorithm

Another well known method in the class of sensor array processing techniques is the MUltiple SIgnal Classification algorithm or MUSIC. The basic mathematical framework for MUSIC was developed by Schmidt in 1977 and independently by Bienvenu in 1979. It is perhaps the most widely studied of the modern source localization techniques and is widely used in many applications. A closely related technique referred to as ESPRIT uses a similar process to the original MUSIC algorithm but, when applicable, has performance advantages over the original algorithm. [4, 7–9]

In this subsection we will present the framework of the MUSIC algorithm and briefly examine the reason for the method's difficulty in handling highly correlated signals.

First, let there be N emitters in a scene of interest and let us observe this scene with an array of receiving antennas containing M elements. We model the transmitted signals as complex sinusoids with the n^{th} signal given by

$$s_n(t) = p_n e^{i\omega_n t}. \tag{2.1}$$

If the received signal at the first sensor is $x_1(t) = s(t)$ and it arrives at an angle θ then the signal recorded at sensor m is

$$x_m(t) = e^{-i\omega \frac{(m-1)d\sin(\theta)}{c_0}} s(t) \tag{2.2}$$

where d is the element separation and c_0 is the speed of light. Then the vector of all recorded signals at the M sensors can be written as $\mathbf{x}(t) = \mathbf{a}(\theta)s(t)$ where $\mathbf{a}(\theta)$ is called the steering vector. [7]

With N signals present we have $\mathbf{x}(t) = \mathbf{A}\mathbf{s}(t) + \mathbf{n}(t)$ where $\mathbf{n}(t)$ is the noise vector, the columns of the $M \times N$ matrix $\mathbf{A}$ are the $\mathbf{a}_n(t)$ steering vectors for the N received signals, and $\mathbf{s}(t)$ is the $N \times 1$ vector of the N signals. Thus, $\mathbf{x}(t)$ is a $M \times 1$ vector where the i^{th} element is comprised of linear combinations of the i^{th} component of each of the N steering vectors multiplied by the i^{th} signal. So, each element in $\mathbf{x}(t)$ is the sum over the product of all signals recorded at the corresponding array element with the appropriate delay and angle factor for that signal.

The MUSIC algorithm then computes the $M \times M$ correlation matrix

$$\mathbf{R}_{xx} = E[\mathbf{x}(t)\mathbf{x}^H(t)] = \mathbf{A}\mathbf{R}_{ss}\mathbf{A}^H + \mathbf{R}_{nn} \tag{2.3}$$

where $\mathbf{R}_{ss} = E[\mathbf{s}(t)\mathbf{s}^H(t)]$ is the signal correlation matrix. In the case of perfectly uncorrelated signals this matrix is the diagonal matrix $\mathbf{R}_{ss} = diag\{\sigma_1^2, \ldots, \sigma_N^2\}$. If some correlation exists between the signals but the matrix $\mathbf{R}_{ss}$ is still full column rank the MUSIC method will still work. [7]

However, if two or more signals are perfectly correlated so that $\mathbf{R}_{ss}$ is rank deficient the method fails in general and the signals cannot be resolved. In such cases methods, which are broadly referred to as “supper resolution," exist which attempt to process portions of the array independently in order to absorb the negative effects of this signal correlation. Doing so, however, causes one to lose some capability since the number of total array elements must be sacrificed to perform the processing, leading to a reduction in the number of emitters capable of being localized. [7]

Returning to equation (2.3), in the case of additive white Gaussian noise (AWGN), we can rewrite this expression as

$$\mathbf{R}_{xx} = E[\mathbf{x}(t)\mathbf{x}^H(t)] = \mathbf{A}\mathbf{R}_{ss}\mathbf{A}^H + \sigma_0^2\mathbf{I}. \tag{2.4}$$

The concept behind MUSIC for source localization is then to estimate the noise subspace from this expression of the available samples. This is done by identifying the eigenvalue/eigenvector pairs for $\mathbf{R}_{xx}$. The method then uses the fact that the signal subspace is orthogonal to the noise subspace to identify signal parameters including the angle of arrival. This can be accomplished as follows:

We know that the eigenvalues of $\mathbf{R}_{xx}$ are given by the solutions to the equation

$$|\mathbf{R}_{xx} - \lambda_i\mathbf{I}| = 0 \tag{2.5}$$

where, here $|\cdot|$ denotes the matrix determinant.

So, we have

$$|\mathbf{A}\mathbf{R}_{ss}\mathbf{A}^H + \sigma_0^2\mathbf{I} - \lambda_i\mathbf{I}| = |\mathbf{A}\mathbf{R}_{ss}\mathbf{A}^H + (\sigma_0^2 - \lambda_i)\mathbf{I}| = 0. \tag{2.6}$$

Thus, the eigenvalues of the matrix $\mathbf{A}\mathbf{R}_{ss}\mathbf{A}^H$ are given by $v_i = \lambda_i - \sigma_0^2$. To reiterate, this is under the assumption that the matrix $\mathbf{A}$ is comprised of linearly independent steering vectors and that the received signals are not highly correlated. In this case $\mathbf{R}_{ss}$ is non-singular. Under these conditions we have that, when $N < M$, the $M \times M$ matrix $\mathbf{A}\mathbf{R}_{ss}\mathbf{A}^H$ is positive semi-definite and of rank N. [10]

Thus, we will have $M - N$ eigenvalues of $\mathbf{A}\mathbf{R}_{ss}\mathbf{A}^H$ equal to zero. Since we have shown that the eigenvalues take the form $v_i = \lambda_i - \sigma_0^2$, we must have $M - N$ of the eigenvalues of $\mathbf{R}_{xx}$ equal to σ_0^2, which is the noise variance. We order the eigenvalues from largest to smallest which results in $\lambda_{M-N}, \ldots, \lambda_M = \sigma_0^2$. There remain N eigenvalues $\lambda_1, \ldots, \lambda_N$ to be determined.

In practice, due to the randomness of the additive noise in the receiving channel, when the correlation matrix $\mathbf{R}_{xx}$ is estimated from some finite set of real world data the noise eigenvalues $\lambda_{M-N}, \ldots, \lambda_M$ will not be exactly identical. Instead the user of the MUSIC algorithm must identify these eigenvalues as part of a closely spaced cluster around the smallest eigenvalue. The spread of the cluster is expected to decrease as the number of samples tends toward infinity with perfect equality only achieved in the limit.

Once a user has identified the cluster of noise eigenvalues their number may be counted in order to determine an estimate of the number of signals present in the data. In this way the user determines the number of signals to identify and localize with the rest of the algorithm. At this point, the number of signals present in the scene is assumed known for the purpose of localization. [7]

At this point we have determined the number of signals to be localized and have an eigenvalue associated with each signal. We then determine the eigenvectors for each eigenvalue according to $\mathbf{R}_{xx}\mathbf{e}_i - \lambda_i\mathbf{e}_\mathbf{i} = 0$. [10]

For the smallest eigenvalues, those associated with the noise subspace

$$\begin{aligned} \mathbf{R}_{xx}\mathbf{e}_i - \lambda_i\mathbf{e}_\mathbf{i} &= (\mathbf{A}\mathbf{R}_{ss}\mathbf{A}^H)\mathbf{e}_i + \sigma_0^2\mathbf{I}\mathbf{e}_i - \lambda_i\mathbf{e}_i \\ &= (\mathbf{A}\mathbf{R}_{ss}\mathbf{A}^H)\mathbf{e}_i + \sigma_0^2\mathbf{e}_i - \sigma_0^2\mathbf{e}_i = (\mathbf{A}\mathbf{R}_{ss}\mathbf{A}^H)\mathbf{e}_i = 0. \end{aligned} \tag{2.7}$$

Since $\mathbf{A}$ is a full rank matrix and we have postulated $\mathbf{R}_{ss}$ to be non-singular we must have $\mathbf{A}^H\mathbf{e}_i = 0$. Recall that the matrix $\mathbf{A}^H$ is made up of the steering vectors of the N signals present in the scene. Since the product of this matrix with the eigenvectors associated with the noise is zero we conclude that the noise subspace is orthogonal to the signal space defined by the steering vectors.

The direction of arrival (DOA) of the signals recorded at the array can then be estimated by forming a matrix of the eigenvectors associated with the noise subspace, call this matrix $\mathbf{U}_n$. The MUSIC algorithm then searches through all angles θ and plots the spatial spectrum according to the equation

$$P(\theta) = \frac{1}{\mathbf{a}^H(\theta)\mathbf{U}_n}. \tag{2.8}$$

When $\theta = \theta_i$, the direction of arrival of a signal, this function will have a peak. Determination of the N peaks of the function leads to detection of the angles of arrival of the N signals.

Unfortunately there are many drawbacks to this approach including computational time and the difficulty in distinguishing between highly correlated signals in the scene. The algorithm ESPRIT manages to overcome some of the problems but at the cost of twice the number of sensors and the correlated signals problems remain.

As mentioned previously, when the signal vector $\mathbf{s}(t)$ contains two or more highly correlated signals the resulting correlation matrix $\mathbf{R}_{ss}$ is not full column rank. As such, the rank of the signal subspace is below the number of signals to be localized. When this occurs the correlated signals cannot be distinguished from one another and the output of the algorithm may display a single displaced peak due to both of the correlated signals, rather than identifying the angle of arrival for each independently as is desired.

2.2 Time Difference of Arrival Localization Techniques

This dissertation will develop a new method of source localization which we are calling Synthetic Aperture Source Localization (SASL). This method will draw on established work in source localization which employs the cross correlation of signals to determine the time difference of arrival (TDOA) at two spatially separated receivers. Once the cross correlated data model has been developed we will employ the mathematical framework of Synthetic Aperture Radar (SAR) to form an image of the target scene. Our goal is to image the scene so that all of the Radio Frequency (RF) emitters are clearly reconstructed in their correct locations and with the correct relative intensities.

This image will be formed by means of a filtered backprojection operator. This operator resembles that used in x-ray tomographic imaging, Electrical Impedance Tomography (EIT), and traditional SAR methods. The signals received at two moving and geospatially separated receiving antennas will be cross correlated for each position of the antenna pair. The output of this cross correlation operation is then taken as the recorded data for a SAR-like image construction process. [2, 11]

This image construction process filters the cross-correlated data to reduce the appearance of artifacts and then backprojects the resulting filtered data into *image space* along the curves of equal Time Difference of Arrival (TDOA) for each position of the receiver pair. When the data is backprojected in this way, the superposition of all such projections interferes constructively in the image space locations corresponding to the emitter positions in the scene. In this manner an image of the locations and relative magnitudes of the RF emitters is reconstructed from the measurements of the emitted signals. This process will be discussed in greater detail in Section 3.1.5.

2.2.1 Estimation of the TDOA

As described above, the localization of a radiating source using information about the TDOA at two spatially separated receivers involves first processing the two received signals using a cross correlation function in order to get an estimate of the TDOA. We then process the TDOA estimate obtained in the first step in some way in order to obtain some estimate of the source's position in the scene of interest.

The mathematical foundations for determining TDOA measurements from the cross correlation of the received signals at two spatially separated receivers was first put forward by Knapp and Carter. Their 1976 paper demonstrated that the time argument at which the cross correlation function achieves its extrema is a maximum likelihood estimator (MLE) for the TDOA of the two signals. This important advancement over simple time difference calculations via subtraction allows for the determination of the TDOA without requiring any a priori knowledge of the time at which the signal was transmitted. [12, 13]

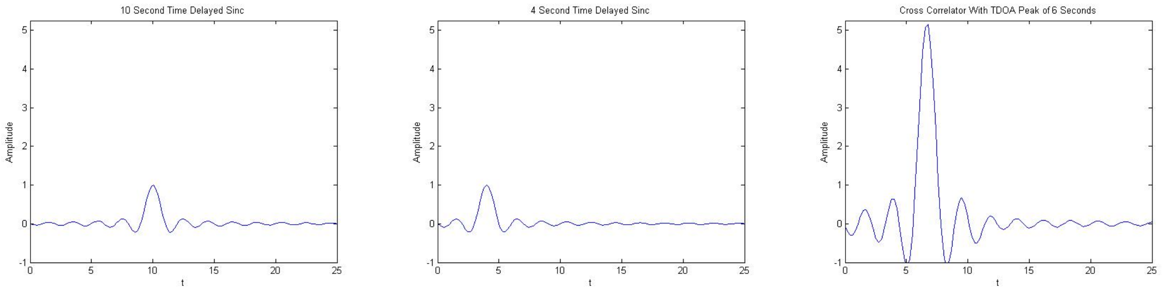

(a) A signal received at 10 seconds after listening begins

(b) A signal received at 4 seconds after listening begins

(c) The Cross Correlator has a peak at the TDOA

Figure 2.2: An example of the effect of Cross Correlation

This process can be demonstrated visually using a simple test case. Consider a sinc function transmitted at some unknown time t_0 from an emitter in a scene of interest and recorded at two geospatially separated receivers. The recorded signals as well as the result of cross correlating them is shown in Figure 2.2.

In Figure 2.2c we observe that the difference in the arrival times for the signal at each receiver can be clearly identified from the point at which the cross correlator achieves its maximum. Furthermore, the peak of the cross correlation function is almost an order of magnitude above that of the signal peaks. Thus the cross correlation process has the additional benefit of allowing for the identification of TDOAs for signals which may be difficult to pick out from the noise of a scene.

Early methods in applying a generalized cross correlation to the determination of TDOA were largely developed by researchers using sonar processing to locate acoustic sources. These early methods were adopted by the electromagnetics community for the estimation of the TDOA for arriving EM waves at passive receivers. However, Fowler and Hu have shown that the development of TDOA models based on cross correlation for the acoustic case does not translate perfectly into the electromagnetic one. [14]

In the acoustic case both the signal and the noise are modeled as a zero mean wide-sense stationary random process and are generally taken to be Gaussian in nature. These assumptions match the physical reality of the target emitters which early acoustic researchers were trying to locate. A ship's motor for instance can be taken as an acoustic source giving rise to a signal which is effectively a random Gaussian. However, in the electromagnetic case the assumption that the signal itself arises from a random process is often a poor one. [14]

Fowler and Hu demonstrated that electromagnetic sources, which are better modeled as deterministic signals, give rise to a different form of the MLE. In each case the MLE is a prefiltered version of the received signals which is then cross correlated. However the prefiltering is applied differently for acoustic sources than electromagnetic ones. In the acoustic case the prefilter relies on the spectral density of both the signal and the noise. In the electromagnetic case the prefiltering relies on the the noise spectral density alone. As such, the MLE for the electromagnetic case reduces to an unfiltered cross correlator whenever the noise can be considered white. The acoustic case requires both noise and signal to be white in order to achieve the same reduction. [14]

2.2.2 Localization of Sources by TDOA

Many established methods exist for performing source localization using measurements of TDOA. These methods are sometimes referred to as hyperbolic location systems, though the term TDOA systems is more common. [13]

Perhaps the simplest of these techniques is the classical method of triangulation. In a triangulation system a series of receivers detect the incoming signal and a calculation of the TDOA is computed for each receiver pair. Then, using each receiver pair as the foci, hyperbolas of equal TDOA may be drawn. The intersection of these hyperbolas is the location of the receiver. An example of this is seen in Figure 2.3. [13]

In this figure we have four receivers, each represented by a colored circle. We also have a single transmitter represented by a magenta square. The red and blue hyperbolas shown correspond to the TDOA curve drawn using the leftmost black circle as one foci and the red or blue, respectively, circle as the other foci. The third hyperbola, the one shown in black, is the TDOA curve for the rightmost circle paired with the red circle. While many points of intersection exist between one or more branches of each hyperbola with another hyperbola in the image, there is only a single point

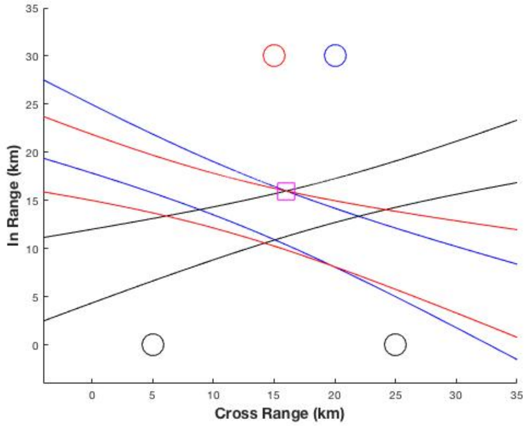

Figure 2.3: Triangulation: Four receivers are able to triangulate one emitter via intersection of TDOA curves.

at which all three hyperbolas intersect simultaneously, this is the location of the emitter which transmitted the signal.

Here we have plotted both branches of the three hyperbolas formed by drawing curves of equal TDOA. This amounts to a data set which is agnostic regarding whether the signal arrived at the red or the black receiver first. That is, we have assumed we know the magnitude of the TDOA, but not its sign. In practice, taking the cross correlation of the two recorded signals will yield a value for the TDOA which can be either positive or negative. This allows us to eliminate one branch from each of the hyperbolas shown, thereby simplifying the process of localizing the emitter to the intersection of just three curves instead of six.

The term *triangulation* comes from the classical case of an emitter transmitting a signal at a known time. In this case, circles of radius equal to the Time of Arrival (TOA) may be drawn centered upon each receiver. The emitter is then located at the intersection of these three circles. When the emitter transmits a signal at an unknown time it takes at least four receivers to localize it in the plane. Five or more receivers are required in a three dimensional geometry. Additional receivers are required to localize more than one emitter present in the scene. This becomes problematic as the number of emitters to be localized grows. [4]

Additionally, basic triangulation provides a location point for an emitter, but does not provide information regarding emitters relative strengths and cannot accurately reconstruct extended sources which cannot be accurately treated as point-like. Also, in the presence of noise, additional optimization techniques are required since the TDOA hyperbolas will not perfectly intersect at a single point. [11, 13]

In 1986 Norton and Linzer introduced a source localization method using backprojection based on previous work that had been published in the x-ray tomography literature. Their method used diametrically opposed receivers laid out in a circle around the region of interest to record incoming signals. They then cross correlated the signals and backprojected the resulting data along the lines from which it was collected. [11]

Norton and Linzer assumed that the sources were arrayed randomly and radiated isotropically. Under these conditions they showed that the imaging process was linear with regard to the source intensity and that complex and extended sources could be imaged quantitatively. These results were verified numerically by localizing a signal caused by breaking a glass capillary on a steel plate. They also demonstrated that the backprojection technique was capable of localizing sources from much lower signal to noise ratios (SNR) than triangulation or other traditional localization techniques. [11, 15]

This work has been extended to consider the minimum number of receivers required to localize an RF transmitter [16], as well as to consider the case of a single moving RF emitter. [17] Other research has been conducted in applying a fleet of UAVs to collect RF data and geolocate a single emitter of interest. However, this work does not involve a backprojection imaging process. [18, 19]

Work has also been done on the effectiveness of using the asymptotes of the TDOA hyperbolas rather than the full hyperbolas themselves to estimate the TDOA of received signals. Doing so results in a set of linear equations in the region far from the receivers. It has been shown that in certain circumstances this approximation can be used to precondition algorithms used in the methods above and thereby improve the results. [20]

As previously discussed, our method uses the cross correlated signals from a moving pair of receivers to form an image by use of a SAR-like backprojection technique. Work has been done in examining the mathematical similarities between the use of passive multistatic radar (PMR) systems, which seek to use the emitters in a scene of interest to image the scattering objects present in the scene, and the source localization problem. It has been shown that mathematical equivalences exist between the two when the scattering objects are modeled as RF emitters but that large differences in the signal strengths means that these equivalences are of limited use. [21]

It has been demonstrated that the cross correlation of the two received signals can be viewed in the SAR framework as an approximation to performing the traditional matched filtering operation which will be discussed in Chapter 3. Furthermore it has been shown that under the ideal conditions of a noiseless signal reception at one receiver and the absence of the direct path signal at the other receiver the cross correlated data achieves the same detection performance of the ideal matched filter in traditional PMR. [22]

2.3 Related Techniques

While the subject of this dissertation is the presentation of a new and unique method of source localization using a backprojection algorithm in the spirit of SAR imaging systems, certain closely related techniques have recently been proposed which rely on a similar theoretical framework to overcome the inherent limitations in the previously discussed methods.

In addition to the localization schemes previously discussed, methods based on the Angle of Arrival (AOA) and Frequency Difference of Arrival (FDOA) are also in broad use. Most of the more advanced forms of these methods however, have one or more shortcomings which cause the method to be inherently suboptimal. Indeed, Amar and Weiss demonstrate that fundamental limits on AOA techniques will lead to a suboptimal geolocation method in all cases. From this they conclude that new methods should be developed which move beyond the traditional approaches. [23]

Many traditional methods of localization based on AOA, FDOA, or TDOA can be grouped into a class of algorithms broadly referred to as “two step" methods.

The name two step comes from the fact that these algorithms first use the measurements at each individual receiver to calculate an estimation of the time delay, doppler frequency, angle of arrival (AOA) or so forth at each receiver independently. These independent estimates are then combined to form some estimation of the target’s true position in the scene. These methods fail to account for the fact that all calculated parameters, such as AOA, must arise from the same point. Thus, these methods can result in the calculation of AOA measurements which do not produce positions lines that all intersect at a since point. [24, 25]

Methods for performing these position estimations as a single step process have been proposed. Such methods are sometimes to as direct position determination methods. These methods utilize the measurements from all receiver stations simultaneously to maximize a cost function that depends upon the unknown position parameter. When the signal to noise ratio is low it has been shown that these methods outperform the traditional two step methods. However, such methods require higher communication bandwidth since the full observations, and not merely the parameter estimations, must be transmitted to the processing hub. [24–26]

Our method differs from these approaches in that we apply a backprojection technique based on the data recorded from moving receivers to form an image of the target scene from which the location of the emitters may be deduced. Weiss et al use the data from static receivers to estimate the position of an emitter via a cost function which is based upon the maximum likelihood (ML) estimator.

Chapter 3

THE MATHEMATICS OF SYNTHETIC APERTURE RADAR

3.1 Synthetic Aperture Radar

We turn now to a discussion of the mathematical framework of Synthetic Aperture Radar (SAR) that we will use to construct a quantitative image of the distribution of RF emitters in a scene of interest.

In 1951 Carl Wiley, then a mathematician with Goodyear Aircraft Company, invented SAR as a solution to a classic problem in radar imaging. The resolution achievable in a radar image can be measured in terms of both range and cross range dimensions. The resolution in the range direction, that is the direction in which the radar is aimed, depends on the bandwidth of the transmitted signal. The cross range resolution is inversely proportional to the size of the antenna, or aperture, being used to transmit the waveform. This phenomenon occurs because larger apertures give rise to smaller footprints on the ground. See Figure 3.1. [2,27,28]

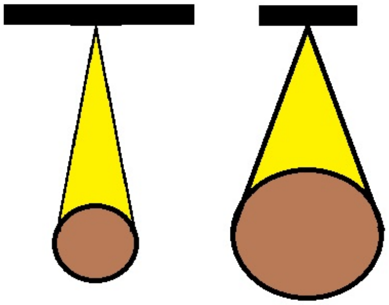

Figure 3.1: The antenna footprint is smaller for larger antennas

In real aperture imaging targets which are separated from each other in the “in-range" direction (see Figure 3.2a) can be resolved because the scattered wave takes longer to return to the radar antenna from objects farther away. However, all objects which are separated in the “Cross-Range" direction but share the same range distance from the radar cannot be resolved if their separation distance is less than the size of the antenna footprint (see Figure 3.2b). This is due to the fact that the scattered returns from all of these objects arrive at the radar at the same moment. [27, 28]

This can be understood mathematically. Let $\mathbf{x}$ be the variable describing a position in the scene, and let $T(\mathbf{x})$ be a function whose value at each point $\mathbf{x}$ is a model for how reflective the scene is at that point. That is, $T(\mathbf{x})$, called the scene reflectivity function, models the fraction of incident radar energy reflected at location $\mathbf{x}$ and measured at the receiving antenna.

Then the measured return at the radar for each time sample is the line integral of $T(\mathbf{x})$ over the curve of fixed iso-range contours corresponding to the wave travel distance for that time sample. Since this integration necessarily blurs out all objects located on the same iso-range curve, very narrow beamwidths are required to reduce the size of the illuminated region and thus achieve good cross-range resolution.

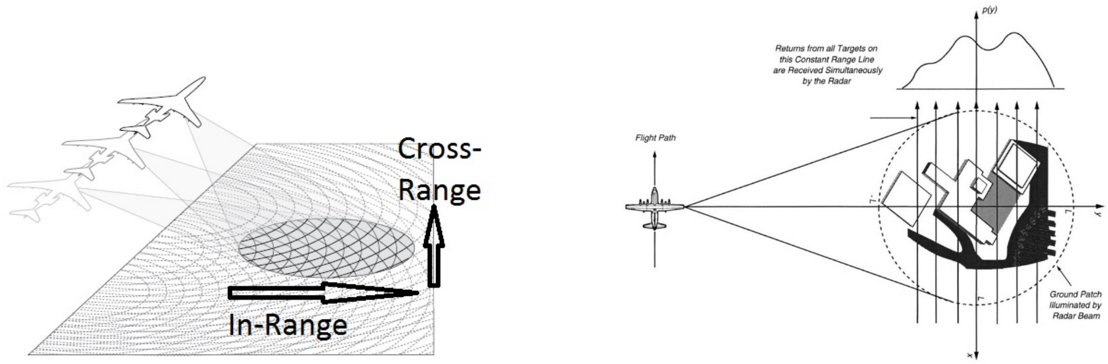

(a) In-Range and Cross-Range directions for a SAR image [2]

(b) A Cross Range ambiguity exists along iso-range contours. [27]

Figure 3.2

For a given target distance R in range and transmitted wavelength λ the achievable cross-range resolution (ΔCR) for a real-aperture imaging radar is given by:

$$\Delta CR \approx R\frac{\lambda}{D} \tag{3.1}$$

Where D is the aperture length. For a radar operating at a distance of $50km$ from its target and transmitting a 150 MHz wave (the center frequency of a wave which achieves a roughly $1m$ resolution in the range direction), we would require an antenna $1500m$ long to achieve a $1m$ cross-range resolution. This is clearly infeasible. [27, 28]

The SAR process overcomes this difficulty by placing a much smaller antenna on a moving platform. For our purposes, we will assume the platform is an aircraft flying over our scene of interest. The returns gathered by the platform from multiple locations along its flight path, or “looks," can be coherently combined in order to synthesize the return from an aperture which is the total length of the flight path. Using this process, resolutions as fine as $10cm$ are achievable using antennas which can be mounted beneath a standard aircraft. [2, 27, 28]

In the rest of the chapter we will present a brief introduction to the different SAR modalities that are applicable to this dissertation and how they relate to the method of Synthetic Aperture Source Localization presented in this dissertation.

3.1.1 Electromagnetic wave propagation

In all SAR regimes the waves under consideration are electromagnetic and therefore must satisfy Maxwell’s equations.

$$\nabla \times \mathcal{E}(t, \mathbf{x}) = -\frac{\partial \mathcal{B}(t, \mathbf{x})}{\partial t} \tag{3.2}$$

$$\nabla \times \mathcal{H}(t, \mathbf{x}) = \mathcal{J}(t, \mathbf{x}) + \frac{\partial \mathcal{D}(t, \mathbf{x})}{\partial t} \tag{3.3}$$

$$\nabla \cdot \mathcal{D}(t, \mathbf{x}) = \rho \tag{3.4}$$

$$\nabla \cdot \mathcal{B}(t, \mathbf{x}) = 0 \tag{3.5}$$

In this formulation, $\mathcal{E}$ is the electric field, $\mathcal{B}$ is the magnetic induction field, $\mathcal{D}$ is the electric displacement field, $\mathcal{H}$ is the magnetic field, $\mathcal{J}$ is the current density, and ρ is the charge density.

For our work, and indeed most airborne SAR applications, the propagation takes place in dry air, which can reasonably be modeled as free space. In free space both the charge and current densities are zero so that $\mathcal{J} = \rho = 0$, and the free space constitutive relations given by

$$\mathcal{D} = \epsilon_0 \mathcal{E} \tag{3.6}$$

$$\mathcal{B} = \mu_0 \mathcal{H} \tag{3.7}$$

hold. From these relations we may derive a simplified expression for the governing differential equation. We begin by taking the curl of (3.2) and substituting (3.7) into the result; this yields:

$$\nabla \times \nabla \times \mathcal{E}(t, \mathbf{x}) = \nabla \times \frac{-\partial \mathcal{B}(t, \mathbf{x})}{\partial t} = -\frac{\partial}{\partial t} \left(\nabla \times \mu_0 \mathcal{H} \right). \tag{3.8}$$

Then, noting $\mathcal{J} = 0$ and substituting (3.6) into (3.3) we find

$$\nabla \times H = \frac{\partial \epsilon_0 \mathcal{E}(t, \mathbf{x})}{\partial t} \tag{3.9}$$

so that

$$\nabla \times \nabla \times \mathcal{E}(t, \mathbf{x}) = \nabla(\nabla \cdot \mathcal{E}) - \nabla^2 \mathcal{E} = -\mu_0 \epsilon_0 \frac{\partial^2 \mathcal{E}}{\partial t^2} \tag{3.10}$$

where, in the second equality, we have applied the triple product identity. Since we have assumed $\rho = 0$ we have

$$\nabla \cdot \mathcal{D}(t, \mathbf{x}) = \nabla \cdot \epsilon_0 \mathcal{E}(t, \mathbf{x}) = 0 \tag{3.11}$$

thus $\nabla \cdot \mathcal{E} = 0$ and (3.10) reduces to

$$\nabla^2 \mathcal{E} = \mu_0 \epsilon_0 \frac{\partial^2 \mathcal{E}}{\partial t^2}. \tag{3.12}$$

Thus, we have shown that the electric field components satisfy the scalar wave equation when the assumption of free space propagation is valid. A similar derivation demonstrates the same expression holds for $\mathcal{H}$.

In a region far from any EM sources this equation can be rewritten as

$$\nabla^2 \mathcal{E} - \frac{1}{c_0^2}\frac{\partial^2 \mathcal{E}}{\partial t^2} = 0 \tag{3.13}$$

where $c_0 = 1/\sqrt{\mu_0 \epsilon_0}$ is the wave speed of an electromagnetic wave in free space.

When a scattering object is present in the scene we can consider the effect of the scattering to be a perturbation in the wave speed so that the effective wave speed $c(\mathbf{x})$ is given by

$$\frac{1}{c^2(\mathbf{x})} = \frac{1}{c_0^2} - T(\mathbf{x}). \tag{3.14}$$

When modeling a scene using we shall often assume that the scatterers in the scene can be modeled as a collection of point scatterers. [29]

The goal of a SAR imaging process is then to construct an image of the scene reflectivity function $T(\mathbf{x})$ from measurements of the scattered waves. Using this model, the governing equation for the waves present in the scene away from any sources is

$$\nabla^2 \mathcal{E}^{tot} - \frac{1}{c^2(\mathbf{x})}\frac{\partial^2 \mathcal{E}^{tot}}{\partial t^2} = 0. \tag{3.15}$$

In order to take account of the effects of the antennas, which transmit and receive the waves, it is necessary to add a source term to these equations. The governing equations of the incident and total fields for a SAR system are then

$$\nabla^2 \mathcal{E}^{in} - \frac{1}{c_0^2}\frac{\partial^2 \mathcal{E}^{in}}{\partial t^2} = j(t, \mathbf{x}) \tag{3.16}$$

$$\nabla^2 \mathcal{E}^{tot} - \frac{1}{c^2(\mathbf{x})}\frac{\partial^2 \mathcal{E}^{tot}}{\partial t^2} = j(t, \mathbf{x}) \tag{3.17}$$

where j is proportional to the time derivative of the current density on the antenna.The incident field can be solved for by convolving with the Green's function solution to (3.18). [30]

The solution to the scalar wave equation of interest to us is the outgoing Green's function satisfying

$$\nabla^2 g(t,\mathbf{x}) - \frac{1}{c_0^2}\frac{\partial^2 g(t,\mathbf{x})}{\partial t^2} = -\delta(t)\delta(\mathbf{x}) \tag{3.18}$$

and is explicitly given by

$$g(t,\mathbf{x}) = \frac{\delta(t - |\mathbf{x}|/c_0)}{4\pi|\mathbf{x}|}. \tag{3.19}$$

Once we have this Green's function solution, the solution to (3.16) is merely the convolution of this Green's function with the source term, $j(t,\mathbf{x}) * g(t,\mathbf{x})$. Thus

$$\mathcal{E}^{in}(t,\mathbf{x}) = -\int g(t-\tau,\mathbf{x}-\mathbf{y})j(\tau,y)d\tau d\mathbf{y} \tag{3.20}$$

$$= -\int \frac{\delta(t-\tau-\frac{|\mathbf{x}-\mathbf{y}|}{c_0})}{4\pi|\mathbf{x}-\mathbf{y}|} j(\tau,\mathbf{x})d\tau d\mathbf{y}. \tag{3.21}$$

We can rewrite (3.16) in the frequency domain as

$$(\nabla^2 + k^2)E^{in}(f,\mathbf{x}) = J(f,\mathbf{x}). \tag{3.22}$$

In the frequency domain we have the Green's function expression

$$G(f,\mathbf{x}) = \frac{e^{i2\pi k|\mathbf{x}|}}{4\pi|\mathbf{x}|} \tag{3.23}$$

where $k = f/c_0$.

We may solve (3.22) to obtain the following expression for the incident wave:

$$E^{in}(\mathbf{x}) = \int G(\mathbf{x}-\mathbf{y})J(\mathbf{y})d\mathbf{y} \approx \frac{e^{i2\pi k|\mathbf{x}-\mathbf{x_0}|}}{4\pi|\mathbf{x}-\mathbf{x_0}|} F\left(f, \widehat{\mathbf{x}-\mathbf{x_0}}\right). \tag{3.24}$$

Note that we have added a superscript to indicate that this is the field due to the incident wave, that is, the wave that is incident on the scattering elements in the scene before any scattering occurs. Here, $\mathbf{x}_0$ is the location of the transmitting antenna and $\widehat{\quad}$ denotes a unit vector. The function F

incorporates information about the transmitted waveform and transmitting antenna beam pattern. For more on the relationship between F and J see [2]. Here we have also taken advantage of the *far-field* approximation.

The far-field approximation is valid for $|x| \gg |y|$ and is given by

$$|x-y| = |x| - \hat{x}\cdot y + \mathcal{O}\left(\frac{|y|^2}{|x|}\right). \tag{3.25}$$

An expression for the scattered field may be obtained by subtracting (3.16) from (3.17) to obtain

$$\left(\nabla^2 - \frac{1}{c_0^2}\frac{\partial^2}{\partial t^2}\right)\mathcal{E}^{sc}(t,\mathbf{x}) = -T(\mathbf{x})\frac{\partial^2}{\partial t^2}\mathcal{E}^{tot}(t,\mathbf{x}), \tag{3.26}$$

which may be expressed in integral form as

$$\begin{aligned}\mathcal{E}^{sc}(t,\mathbf{x}) &= \int g(t-\tau,\mathbf{x}-\mathbf{z})T(\mathbf{z})\frac{\partial^2}{\partial \tau^2}\mathcal{E}^{tot}(\tau,\mathbf{z})d\tau d\mathbf{z} \qquad (3.27)\\ &= \int \frac{\delta(t-\tau-|\mathbf{x}-\mathbf{z}|/c_0)}{4\pi|\mathbf{x}-\mathbf{z}|}T(\mathbf{z})\frac{\partial^2}{\partial \tau^2}\mathcal{E}^{tot}(\tau,\mathbf{z})d\tau d\mathbf{z}. \qquad (3.28)\end{aligned}$$

This expression is known as the *Lippmann-Schwinger* integral equation. We note here that, since $\mathcal{E}^{tot}$ is the sum of both the incident and the scattered fields (3.28) is not an explicit formula for calculating $\mathcal{E}^{sc}$ but rather an equation that must be solved. [2]

Additionally (3.28) is nonlinear since $T(\mathbf{x})$ is multiplied by the right hand side term containing $\mathcal{E}^{sc}$. In order to linearize this equation we apply a simplification known as the *Born*, or single scattering, approximation.

The mathematical effect of the Born approximation is to replace $\mathcal{E}^{tot}$ with $\mathcal{E}^{in}$ in (3.28). It amounts to the approximation of the total field by the first term in an expansion of $\mathcal{E}^{tot}$ known as the *Neumann series*. From a physical standpoint, the Born approximation makes the assumption that all waves only scatter once before returning to the radar receiver. [2, 29]

Applying this approximation and solving the resulting integral equation yields the following frequency domain expression for the scattered field.

$$E^{sc} \approx -\int \frac{e^{i2\pi k|\mathbf{x}-\mathbf{z}|}}{4\pi|\mathbf{x}-\mathbf{z}|} T(\mathbf{z}) f^2 E^{in}(f,\mathbf{z}) d\mathbf{z} \tag{3.29}$$

We may now substitute our expression for the incident field into (3.29) and obtain the model

$$E^{sc} = \int \frac{e^{i2\pi k|\mathbf{x}-\mathbf{z}|}}{4\pi|\mathbf{x}-\mathbf{z}|} T(\mathbf{z}) f^2 \frac{e^{i2\pi k|\mathbf{z}-\mathbf{x_0}|}}{4\pi|\mathbf{z}-\mathbf{x_0}|} F\left(f, \widehat{\mathbf{z}-\mathbf{x_0}}\right) d\mathbf{z}. \tag{3.30}$$

3.1.2 Matched Filtering

Now, the reception and recording of any electromagnetic wave using a real (as opposed to a simulated) system involves the inclusion of some noise factor. This noise factor is typically considered to be added to the received waveform so that what is actually recorded is

$$S_{rec}(t) = E^{sc}(t) + n(t). \tag{3.31}$$

In an ideal case we would like to apply a filter to the recorded data which would completely eliminate the noise factor. This is not possible since the noise arises from a random process and cannot be deterministically modeled. Thus we must settle for a filter which maximizes the Signal to Noise Ratio (SNR).

We apply the filter $h(t)$ to the recorded signal S_{rec} via convolution. The signal and noise outputs after application of the filter are, respectively

$$\eta_s(t) = \int h(t-\tau) S_{rec}(\tau) d\tau = \int h(t-\tau) S(\tau - t') d\tau \tag{3.32}$$

$$\eta_n(t) = \int h(t-\tau) n(\tau) d\tau. \tag{3.33}$$

In the second equality above we have modeled the received signal as a time delayed version of the known transmitted signal. Taking the noise to be generated by a white Gaussian process we may write $E[n(t)\bar{n}(t')] = N\delta(t-t')$, where E denotes statistical expectation and N is the noise power.

Under these conditions the SNR is

$$SNR = \frac{|\eta_s(t)|^2}{E|\eta_n(t)|^2} \tag{3.34}$$

Our goal is to choose the filter $h(t)$ to maximize this expression.

Computing the expressions for both the numerator and denominator above we find

$$SNR = \frac{|\int h(t)s(-t)dt|^2}{N\int |h(t)|^2 dt}. \tag{3.35}$$

By definition

$$||h(t)||_2^2 = \int |h(t)|^2 dt. \tag{3.36}$$

The Cauchy-Swartz inequality states that, for given functions $f(t)$ and $h(t)$,

$$\left|\int h(t)\bar{f}(t)dt\right| \leq ||h||_2 \; ||f||_2 \tag{3.37}$$

where equality occurs iff $h(t) \propto f(t)$. Thus, the maximizing of (3.35) requires that $h(t) = \bar{s}(-t)$. That is, the best SNR occurs when our applied filter is a time reversed complex conjugated version of the transmitted signal. This is known as the *Matched Filter*. [2]

With these expressions in hand we now turn our attention to the different SAR modalities.

3.1.3 Monostatic SAR

In Monostatic SAR (MSAR) both the transmission and reception components of the SAR system are handled by the same antenna and only one platform is utilized. In practice some systems exist which are comprised of two antennas, one for transmission and one for reception, but the two elements are located so close together that their separation distance is negligible compared to the range to the target scene. Such systems are referred to as pseudo-monostatic and the phenomenology is very near that of the true monostatic case. In Section 3.1.4 we will contrast such systems with the Bistatic case in which the transmitting and receiving antennas are not collocated.

When the transmit and receive antennas are collocated, the point at which the scattered wave is measured is the same as the point at which the wave originated, namely $\mathbf{x}_0$. Thus, we evaluate (3.30) at $\mathbf{x}_0$ and obtain the following model for the collected signal

$$S(f, \mathbf{x}_0) = \int e^{i4\pi k|\mathbf{x_0} - \mathbf{z}|} A(f, \mathbf{x_0}, \mathbf{z}) T(\mathbf{z}) d\mathbf{z} \tag{3.38}$$

where the factor

$$A(f, \mathbf{x_0}, \mathbf{z}) = \frac{f^2 F_{rec}(k, \widehat{\mathbf{x_0} - \mathbf{z}}) F_t(k, \widehat{\mathbf{x_0} - \mathbf{z}})}{(4\pi|\mathbf{x_0} - \mathbf{z}|)^2} \tag{3.39}$$

contains information regarding the transmitting and receiving antenna beam patterns as well as geometric spreading factors. A may also include the effects of matched filtering on the received signal.

Up to this point we have considered the transmitting and receiving hardware to be stationary. We may now include the platform's flightpath into our model by parameterizing the antenna location for a given data collection point.

We will assume that our platform follows a known flight trajectory denoted by $\gamma(s)$ where s is referred to as the slow time variable. This is to distinguish it from t which is known as the fast time variable. In our model t measures the wave travel time over the course of a single transmit and receive cycle (one “look"), whereas s measures the platform location over the duration of the entire flight path. Substitution of the platform flightpath into our model produces the following expression for the data collected.

$$D(s, f) = \int e^{i4\pi k|\gamma(s) - \mathbf{z}|} A(f, s, \mathbf{z}) T(\mathbf{z}) d\mathbf{z} \tag{3.40}$$

This model assumes the *start-stop* approximation. This approximation takes the platform to be stationary throughout the duration of each look and to jump to the next collection point between looks. Although this is clearly not true in practice, the typical platform moves at speeds orders of magnitude slower than the wave travel speed so the effects of this approximation are negligible for most applications. [2, 28]

The time domain version of (3.40) is

$$d(s,t) = \int e^{-i2\pi f(t - r_M(s,\mathbf{x}))} A(\mathbf{x}, s, f) T(\mathbf{x}) d\mathbf{x} df \tag{3.41}$$

where

$$r_M(s,\mathbf{x}) = \frac{2|\gamma(s) - \mathbf{x}|}{c_0}. \tag{3.42}$$

Here r_M is twice the range from the radar platform to the point $\mathbf{x}$ in the scene. As will be seen later, the data collection for each fast time step amounts to a line integral of the scene reflectivity over a circle.

3.1.4 Bistatic SAR

We now turn to the case where the transmit and receive antennas are not collocated. If the transmitting antenna is located on one platform and the receiving antenna is located on another platform the system is called Bistatic. The more general case of Multistatic Synthetic Aperture Radar will not concern us in this research.

In a Bistatic SAR system (BiSAR) the two platforms are assumed to fly known, but independent flight paths. We denote these as $\gamma_T(s)$ and $\gamma_R(s)$ for the transmit and receive platforms respectively. In this case, replacing $\mathbf{x_0}$ with $\gamma_T(s)$ in (3.30) and solving for the field at location $\gamma_R(s)$ produces

$$d(s,t) = \int e^{-i2\pi f(t - r_B(s,\mathbf{x}))} A(\mathbf{x}, s, f) T(\mathbf{x}) d\mathbf{x} df \tag{3.43}$$

where

$$r_B(s,\mathbf{x}) = \frac{|\gamma_T(s) - \mathbf{x}|}{c_0} + \frac{|\gamma_R(s) - \mathbf{x}|}{c_0}. \tag{3.44}$$

Here r_B is referred to as the Bistatic Range and is the sum of the distance from the transmitting platform to the point $\mathbf{x}$ in the scene and the distance from $\mathbf{x}$ to the receiving platform. The lines of equal Bistatic Range in the scene are ellipses with foci at the transmitting and receiving platform locations. [31]

This SAR geometry which may be termed *active BiSAR* was nominally extended by Nicholas Willis in [32] to include the case of a passive receiver with what is termed an *emitter of opportunity*. Although a BiSAR set up was not explicitly investigated, the conditions under which a source located in the scene that is not under the direct control of the radar operator can be used as the transmitting platform for a bistatic radar data collection geometry were laid out. The term *hitchhiker* is often used to refer to such systems in the literature.

The initial work of Willis has been extended in [33] and [34] to include a full SAR backprojection method to image the scene radiance. This may be taken as an analog of the scene reflectivity function which is the target object in traditional BiSAR systems. This work, however, relies on certain statistical assumptions regarding the nature of both the transmitted signals and the scene reflectivity function.

3.1.5 Backprojection

The goal of traditional SAR imaging is form an image of the scene reflectivity function $T(\mathbf{x})$. This is accomplished by applying a backprojection operator to the data $d(s,t)$ obtained from (3.41) or (3.43) which projects the data into an image space and, over the course of many data collection angles, ultimately forms an image of the reflectivity function for the target scene. To this end, d can be viewed as a forward operator $\mathcal{W}$ acting on T, that is,

$$d(s,t) = \mathcal{W}\left\{T\right\}(s,t). \tag{3.45}$$

We then seek to apply an appropriate imaging operator $\mathcal{K}$ that will recover T from the recorded data.

The operator $\mathcal{K}$ which accomplishes this is reffered to as a filtered-backprojection (FBP) operator. This operator applies some filter Q to the data and then back-projects the result to obtain an image. The backprojection interferes constructively at points at which a scattering element is located. As we shall see in Section 4.4, we seek to choose the filter Q so as to minimize the appearance of artifacts in the image.

In general, if $d(s,t)$ is our data the FBP operator acts on d as

$$\begin{aligned} I(\mathbf{z}) = \mathcal{K}[d](\mathbf{z}) &:= \int e^{i2\pi f(t - r(s,\mathbf{z})/c_0)} Q(\mathbf{z}, f, s) d(s,t) df ds dt && (3.46) \\ &= \int e^{-i2\pi f r(s,\mathbf{z})/c_0} Q(\mathbf{z}, f, s) D(s,f) df ds && (3.47) \end{aligned}$$

where $D(s,f)$ is the frequency domain model of the data.

We can achieve an intuitive understanding of the action of $\mathcal{K}$ on d by examining the case where we chose $Q \equiv 1$. This amounts to the back projection of the data without any filtering. With $Q \equiv 1$ the image I becomes

$$\begin{aligned} I(\mathbf{z}) &= \int e^{i2\pi f(t - r(s,\mathbf{z})/c_0)} d(s,t) df ds dt && (3.48) \\ &= \int \delta(t - r(s,\mathbf{z})/c_0) d(s,t) ds dt && (3.49) \\ &= \int d(s, r(s,\mathbf{z})/c_0) ds. && (3.50) \end{aligned}$$

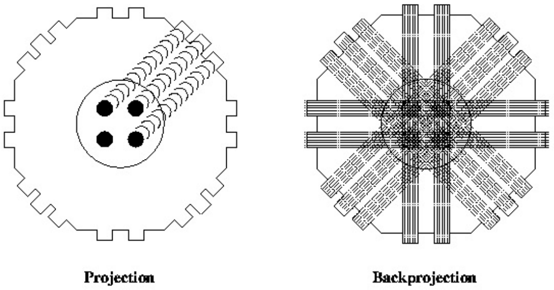

Figure 3.3: Backprojected radiation can image source elements inside a region of interest. [1]

Thus without any filtering, the application of the backprojection operator has the effect of projecting the recorded data onto those locations $\mathbf{z}$ which are at the correct travel time $r(s,\mathbf{z})/c_0$

from the receiving antenna at the time step s. In monostatic SAR the backprojection is done over circles for which the radius is the correct range from the radar defined by $r_M(s, \mathbf{z})$. For the case of BiSAR, $r_B(s, \mathbf{z})$ produces backprojection over the ellipses of correct bistatic range.

In Chapter 4 shall see that, for the case of a SASL data collection and backprojection process $r(s, \mathbf{z})/c_0$ yields backprojection over the hyperbolas of correct TDOA.

The backprojection process is illustrated graphically in Figure 3.3. Here four radiative source elements emit some form of radiation that is measured along the eight sides of the surrounding octagon. These measurements can be considered mathematically as projections of the two dimensional source region onto the one dimensional line over which the field strength is recorded.

The data collection process is illustrated on the left. Here each of the small squares represents a point at which the incident radiation is measured. The radiated waves for one such set of data collection points is shown.

The backprojection operation then projects these field measurements along the line running through the interior of the region from which the original data was recorded. In those regions of image space where a source is located, the backprojected data interfere constructively to build up an image of the radiating elements. This is shown in figure 3.3 on the right.

A clear difficulty with this process is the star-like artifact patterns that build up due to the backprojection. Filtering the data before backprojection by appropriate choice of Q in $\mathcal{K}$ can minimize the appearance of these artifacts.

An example of the process of filtered backprojection in Monostatic SAR is displayed in Figure 3.4.

It is clear from the images in Figure 3.4 that something odd is happening. The scattering objects have been reconstructed correctly, but a mirror image of the pair has been reconstructed as well. This is known in SAR terms as the left-right ambiguity. It arises due to the fact that, if an antenna's beam is centered at the ground beneath the radar there is no way to determine whether the contribution to the data comes from the left or right side of the craft. To eliminate this problem antennas are mounted so that they project and record data from only one side of the aircraft. This effectively eliminates such mirror points. [2]

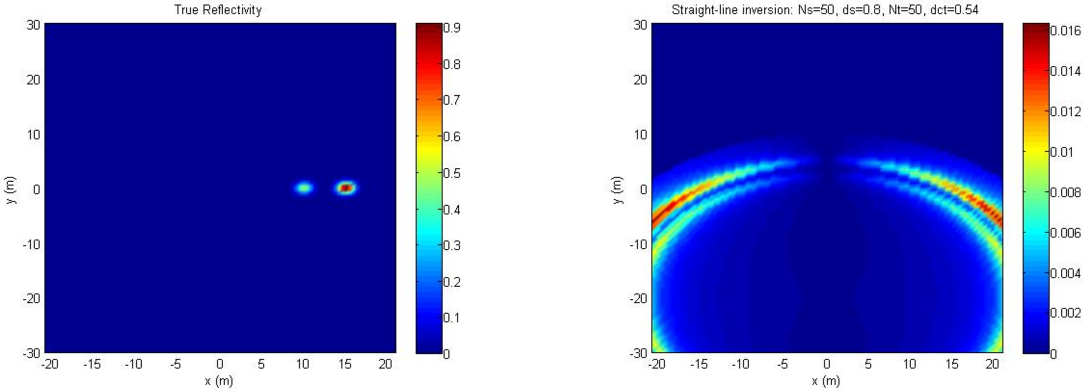

(a) Scene Truth: Two scatterers **(b)** The backprojected image from one slow time point

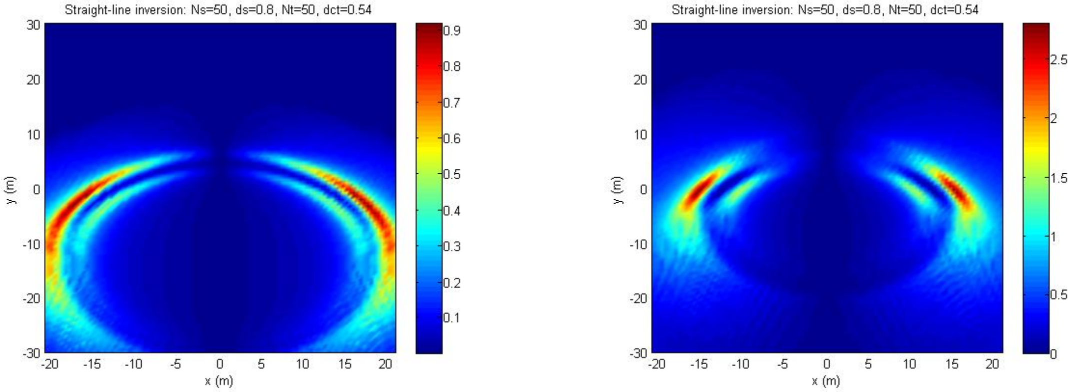

(c) The backprojected image from 10 slow time points **(d)** The backprojected image from 20 slow time points

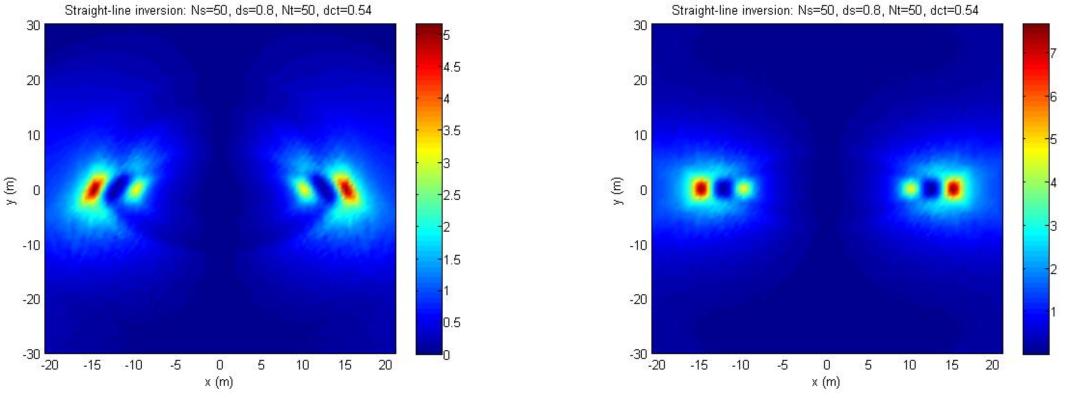

(e) The backprojected image from 30 slow time points **(f)** The backprojected image from 50 slow time points

Figure 3.4: A series of backprojection images for an increasing number of slow-time samples [2]

3.2 SAR Resolution

We conclude this chapter with a brief look at the resolution which is achievable in a SAR image for given data collection parameters. As was briefly discussed earlier, the resolution of a traditional monostatic system is limited by the beamwidth of the antenna or antennas performing the transmission and reception of the signal. As was previously discussed, the cross range resolution of such a system is approximately $\Delta_{CR} \approx R\frac{\lambda}{D}$. Where R is the range to the target, λ is the wavelength of the transmitted signal, and D is the size of the physical aperture.

If, as in Spotlight mode SAR, the target is visible throughout the length of the synthesized aperture, the cross range resolution achievable is given by

$$\Delta_{CR} = \frac{\lambda}{4\sin(\frac{\Delta\theta}{2})} \tag{3.51}$$

where $\Delta\theta$ is the angular interval over which the aperture is synthesized. [35]

From this it is clear that the resolution achievable in a traditional SAR image is dependent both on the transmitted waveform and on the duration of the flight path which synthesizes the aperture.

The Fourier resolution of a SAR image can be defined as the main lobe width of the impulse response. This is also known as null-to-null resolution and is shown graphically in Figure 3.5b . [35] [2]

The resolution which can be attained in a back projection image is ultimately dependent on the *data collection manifold* (DCM), that is, the set of data which is collected by the receiving antenna. The data collection manifold is a region in Fourier space which is defined by the range of the variables in the phase of the data model. As seen in Figure 3.5a the data collection manifold is the a sector of an annulus.

As the range of the receiving antennas to the target increases, the data collection manifold becomes more rectangular over equal flight path lengths. If we assume the manifold may be approximated by a rectangle we can factor the impulse response as

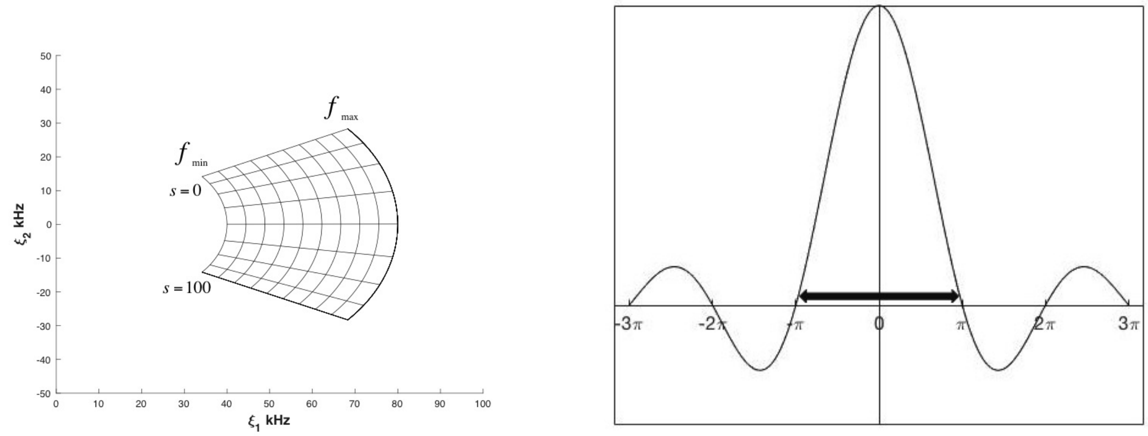

(a) The data collection manifold for a 20km aperture with $20MHz$ bandwidth signal with f_c = 30MHz.

(b) The peak width distance for a standard sinc function

Figure 3.5: Diagram of a DCM and the Null-to-Null width

$$L(\mathbf{z},\mathbf{x}) = \int e^{i2\pi(\mathbf{z}-\mathbf{x})\cdot\xi} d\xi \approx \int e^{i2\pi(z_1-x_1)\xi_1} d\xi_1 \int e^{i2\pi(z_2-x_2)\xi_2} d\xi_2. \tag{3.52}$$

The resolution of the image can then be considered by examining the cross-range and in-range components separately. We can apply these same principals to our formation of a SASL image. We will explore these ideas more fully in chapter 5 when we consider the numerical simulation of SASL images. [35]

Chapter 4

SYNTHETIC APERTURE SOURCE LOCALIZATION IN TWO DIMENSIONS

4.1 Introduction

Our work is fundamentally different from the SAR modalities described above in that we are seeking to reconstruct an image, not of the scene reflectivity function $T(\mathbf{x})$ but rather of what may be termed the source intensity function, which we denote by $V(\mathbf{x})$. Here $V(\mathbf{x})$ is the spatial dependence, that is time invariant representation, of the time dependent source function $j(\mathbf{x}, t)$ which gives rise to the electromagnetic fields emanating from a scene of interest. Simply put, we are trying to image the locations of RF emitters in a target scene using measurements of the direct path EM fields they transmit, rather than imaging scattering objects in the scene from measurements of a reflected wave incident on them. The relations of these functions will be made precise in the derivations to follow.

In this chapter we will lay the foundations of the SASL method using certain statistical assumptions about the recorded signals which will make the data easier to use in our image formation process. The most important assumption will be that the correlation between signals arriving from different emitters is negligible. This is is the assumption which the MUSIC algorithm and other similar approaches require in order to image sources without artifacts. Under these conditions we will build up a backprojection model for the SASL process and then show numerical results for our method in Chapter 5.

Then, in Chapter 7 we will return to the data model and derive a new form of the expressions shown in this chapter which do not rely on the statistical assumptions we invoke here. This will dramatically complicate the effort when the signals emitted from the scene are highly correlated. We will show that in the case of uncorrelated signals the more complex data model reduces to the simpler statistical version derived here and we will examine in depth the impact the additional terms have on the resulting SASL image.

4.2 Derivation of the SASL Data Model

If a target scene contains some distribution of sources described by the source function $j(\mathbf{x}, t)$ then those sources will produce a field satisfying the scalar wave equation

$$\nabla^2 \mathcal{E} - \frac{1}{c_0} \frac{\partial \mathcal{E}}{\partial t^2} = j(\mathbf{x}, t). \tag{4.1}$$

In the time domain, the statistical structure of the source function j will be of the form

$$u(\mathbf{x}_1, \mathbf{x}_2; t_1, t_2) = \mathbb{E}[j(\mathbf{x}_1, t_1) j(\mathbf{x}_2, t_2)] \tag{4.2}$$

where $\mathbb{E}[\cdot]$ is the statistical expectation and $(\mathbf{x}_i, t_i)$ is the spatiotemporal measurement point for the field $\mathcal{E}$. The first work in adapting this model to electromagnetic source localization from the existing literature in acoustics was done by Linzer and Norton. We follow their approach here in deriving our statistical data model. [11, 12]

We assume that this statistical structure can be considered as stationary over the duration of fast time measurements so that we can rewrite u as

$$u(\mathbf{x}_1, \mathbf{x_2}; \tau_{12}) = u(\mathbf{x}_1, \mathbf{x}_2; t_1, t_2) \tag{4.3}$$

where $\tau_{12} = t_1 - t_2$. This can be thought of physically as an estimation of the time delay of the reception between a signal at two spatially separated receivers. Furthermore, if we assume that the field is spatially and temporally incoherent, that is

$$\mathbb{E}[j(\mathbf{x_1}, t) j(\mathbf{x_2}, t)] = 0 \tag{4.4}$$

$$\mathbb{E}[j(\mathbf{x}, t) j(\mathbf{x}, t')] = 0 \tag{4.5}$$

for $\mathbf{x}_1 \neq \mathbf{x}_2$ and $t \neq t'$, then $u(\mathbf{x})$ may be written as

$$u(\mathbf{x}_1, \mathbf{x}_2; \tau_{12}) = V(\mathbf{x}_1)\delta(\mathbf{x}_1 - \mathbf{x}_2)b(\tau_{12}). \tag{4.6}$$

This is may be called the *separability assumption*. Such incoherence will likely not hold in practice for situations involving scenes with emitters transmitting highly similar waveforms or waveforms with significant low frequency components. In Chapter 6 we will return to these and other assumptions to examine how they may be relaxed or removed through the use of a non-statistical model.

In simple terms, we are assuming that signals transmitted from different emitters in the target scene are not correlated with each other, or that this correlation is weak enough to be neglected. One expects that in most scenes under surveillance users will not transmit highly correlated waveforms since doing so would make it difficult for the users themselves to distinguish between the signals and thus reduce the effectiveness of the transmitter.

However, it has been shown that making such an assumption, even under measurement circumstances which severely violate it, does not degrade the fundamental performance of the model beyond the production of additional artifacts in the data. We will explore these artifacts and what can be done to mitigate their effects in Chapter 7. [11]

Furthermore, as we shall see below, this model can also be viewed from the perspective that one receives and records the signals from target emitters “one at a time," correlates them separately, and superimposes the result. As such the model remains an accurate representation of the data recorded for even highly correlated signals if an *a priori* method, such as voice recognition, exists for separating the data recorded from different sources in the scene.

By Fourier transform, the equivalent formulation of equation (4.6) in the frequency domain is given by

$$U(\mathbf{x}_1, \mathbf{x}_2; f) = V(\mathbf{x_1})\delta(\mathbf{x_1} - \mathbf{x_2})B(f) \tag{4.7}$$

In practice of course, we do not have knowledge of $j(\mathbf{x}, t)$ and so we must use field measurements to estimate any quantities derived from it. We approximate the function $u(\mathbf{x_1}, \mathbf{x_2}; \tau_{12})$ with the cross correlation of two field measurements $\hat{\mathcal{E}}(\mathbf{x_1}, t)$ and $\hat{\mathcal{E}}(\mathbf{x_2}, t + \tau_{12})$ given by

$$\hat{u}(\mathbf{x_1}, \mathbf{x_2}; \tau_{12}) = \int \hat{\mathcal{E}}(\mathbf{x_1}, t)\hat{\mathcal{E}}(\mathbf{x_2}, t + \tau_{12})dt. \tag{4.8}$$

In order to form a SAR-like data model which will allow for the formation of SAR-like images, we introduce a windowing function, $h(t - s)$, which separates the recorded data into time segments of duration T. The length of T is then taken to be the length of one look at the scene. The data separated in this way is then treated as a single, ‘slow time’, data collection point. The measurements within one such slow time collection are measured in ‘fast time.’ So that slow time records the inter-look duration while fast time records the intra-look durations between instantaneous samples.

In theory h is a smooth cut-off function which takes the value 1 on the interval $[0, T]$ and 0 outside of it. In practice a variety of smooth windowing functions are available and the optimal choice may vary depending on a variety of factors. Use of a Hamming or Tukey window is common in signal processing as these windows lower the effect of signal sidelobes and lead to a reduction in numerical processing artifacts while also possessing desirable Fourier transform properties. [36]

We also introduce the notation $\gamma_1(s)$ and $\gamma_2(s)$ which denote the slow time measurement positions along the flight paths of our two receivers. We assume γ_1, γ_2 are known deterministic functions.

To visually simplify the resulting calculations, with a sight abuse of notation, we write

$$s_1(s, t) = \hat{\mathcal{E}}(\gamma_1(s), t)) \tag{4.9}$$

so that $s_1(s, t)$ is the signal measurement received at the first receiver at position $\gamma_1(s)$ and fast time t. We then have the time domain data model given by

$$d(s,t) = s_1(s,t) \star s_2(s,t) = \int s_1(s,\tau)s_2(s,t+\tau)h(\tau - s)d\tau \tag{4.10}$$

where $\star$ is an operator denoting the windowed cross correlation. For more on the cross correlation function and its Fourier transform see Appendix A.

Taking the Fourier transform of (4.10) with respect to t we obtain an expression for our approximation to $U(\mathbf{x}_1, \mathbf{x}_2; f)$, the frequency domain representation of the data. The result, denoted by D, is also known as the power spectral density. [11, 12]

Here we have

$$D(s,f) = \mathbb{E}\left[\bar{S}_1(s,f)S_2(s,f)\right] \tag{4.11}$$

where $S_i(s,f) = \mathcal{F}\{s_i(s,t)\}$.

Recall from the previous chapter that

$$E(\mathbf{y}, f) = \int G(\mathbf{y} - \mathbf{x}, f)J(\mathbf{x}, f)d\mathbf{x}. \tag{4.12}$$

We therefore write

$$S_i(s,f) = \int G(\gamma_i(s) - \mathbf{x}, f)J(\mathbf{x}, f)d\mathbf{x}. \tag{4.13}$$

Substitution into equation (4.11) produces

$$D(s,f) = \mathbb{E}\left[\int \bar{G}(\gamma_1(s) - \mathbf{x}, f)\bar{J}(\mathbf{x}, f)G(\gamma_2(s) - \mathbf{x}', f)J(\mathbf{x}', f)d\mathbf{x}'d\mathbf{x}\right] \tag{4.14}$$

$$= \int \bar{G}(\gamma_1(s) - \mathbf{x}, f)G(\gamma_2(s) - \mathbf{x}', f)E\left[\bar{J}(\mathbf{x}, f)J(\mathbf{x}', f)\right] d\mathbf{x}'d\mathbf{x}. \tag{4.15}$$

However,

$$\mathbb{E}\left[\bar{J}(\mathbf{x}, f)J(\mathbf{x}', f)\right] = U(\mathbf{x}, \mathbf{x}'; f) = V(\mathbf{x})\delta(\mathbf{x} - \mathbf{x}')B(f), \tag{4.16}$$

so

$$D(s,f) = \int \bar{G}(\gamma_1(s)-\mathbf{x},f)G(\gamma_2(s)-\mathbf{x}',f)V(\mathbf{x})\delta(\mathbf{x}-\mathbf{x}')B(f)d\mathbf{x}'d\mathbf{x} \tag{4.17}$$

$$= \int \bar{G}(\gamma_1(s)-\mathbf{x},f)G(\gamma_2(s)-\mathbf{x},f)V(\mathbf{x})B(f)d\mathbf{x}. \tag{4.18}$$

Substituting in our expression for $G(\mathbf{x},f)$ from Chapter 3 we have

$$D(s,f) = \int \frac{e^{i2\pi f|\gamma_1(s)-\mathbf{x}|/c_0}}{4\pi|\gamma_1(s)-\mathbf{x}|}\frac{e^{-i2\pi f|\gamma_2(s)-\mathbf{x}|/c_0}}{4\pi|\gamma_2(s)-\mathbf{x}|}V(\mathbf{x})B(f)d\mathbf{x} \tag{4.19}$$

$$= \int \frac{e^{i2\pi f r(s,\mathbf{x})/c_0}}{(4\pi)^2|\gamma_1(s)-\mathbf{x}||\gamma_2(s)-\mathbf{x}|}V(\mathbf{x})B(f)d\mathbf{x} \tag{4.20}$$

where $r(s,\mathbf{x}) = |\gamma_1(s)-\mathbf{x}| - |\gamma_2(s)-\mathbf{x}|$. Here $B(f)$ is assumed known and $V(\mathbf{x})$ is the unknown spatial dependence which we are attempting to image through field measurements. Although $B(f)$ is not known in practice it can be estimated directly from the power spectrum of the recorded signals. We will return to this estimation in Chapter 7. [11]

Under these assumptions the time domain form of the data model may be written as

$$d(s,t) = \int e^{i2\pi f(t-r(s,\mathbf{x})/c_0)}A(s,\mathbf{x})V(\mathbf{x})df\,d\mathbf{x} \tag{4.21}$$

where

$$A(\mathbf{x},s,f) = \frac{B(f)}{(4\pi)^2|\gamma_1(s)-\mathbf{x}||\gamma_2(s)-\mathbf{x}|} \tag{4.22}$$

4.3 The Case of a Single Emitter in the Scene

We can obtain some insight into equation (4.21) by examining the simple case in which the scene consists of a single transmitter located at the point $\mathbf{x_0}$ radiating a waveform $p(t)$. For this case our source function is given by

$$j(\mathbf{x},t) = p(\mathbf{x},t)\delta(\mathbf{x}-\mathbf{x_0}). \tag{4.23}$$

Our data model is then

$$D(s,f) = \int \bar{G}(\gamma_1(s)-\mathbf{x},f)G(\gamma_2(s)-\mathbf{x}',f)\mathbb{E}\left[\bar{J}(\mathbf{x},f)J(\mathbf{x}',f)\right]d\mathbf{x}'d\mathbf{x} \tag{4.24}$$

$$= \int \bar{G}(\gamma_1(s)-\mathbf{x},f)G(\gamma_2(s)-\mathbf{x}',f)\mathbb{E}\left[\bar{P}(\mathbf{x},f)P(\mathbf{x}',f)\delta(\mathbf{x}-\mathbf{x_0})\delta(\mathbf{x}'-\mathbf{x_0})\right]d\mathbf{x}'d\mathbf{x} \tag{4.25}$$

$$= \int \bar{G}(\gamma_1(s)-\mathbf{x},f)G(\gamma_2(s)-\mathbf{x}',f)\bar{P}(\mathbf{x},f)P(\mathbf{x}',f)\delta(\mathbf{x}-\mathbf{x}')d\mathbf{x}'d\mathbf{x} \tag{4.26}$$

$$= \int \frac{e^{i2\pi f r(s,\mathbf{x})/c_0}}{(4\pi)^2|\gamma_1(s)-\mathbf{x}||\gamma_2(s)-\mathbf{x}|}\left|P(\mathbf{x},f)\right|^2 d\mathbf{x}. \tag{4.27}$$

By Fourier transform the corresponding time domain model is

$$d(s,t) = \int e^{i2\pi f(t-r(s,\mathbf{x})/c_0)}\frac{[p(s,t)\star p(s,t)]}{(4\pi)^2|\gamma_1(s)-\mathbf{x}||\gamma_2(s)-\mathbf{x}|}df\,d\mathbf{x}. \tag{4.28}$$

where, $p(s,t)\star p(s,t)$ is an autocorrelation of the recorded signal. In this way we see that, in the case of a single emitter, the data model consists of the cross correlation of the transmitted waveform and propagation factors associated with the transmission of the electromagnetic wave to the receivers.

4.3.1 Multiple Transmitters

We can expand upon this by considering a scene in which many point-like transmitters are present. We consider a scene in which N such transmitters emit signals recorded by the two receivers. Our source function is then given by

$$j(\mathbf{x},t) = \sum_{n=1}^{N} p_n(\mathbf{x},t)\delta(\mathbf{x}-\mathbf{x_n}). \tag{4.29}$$

The expectation function of (4.29) in our data model is then

$$\mathbb{E}\left[\bar{j}(\mathbf{x},f)j(\mathbf{x}',f)\right] = \mathbb{E}\left[\sum_{n=1}^{N}\bar{p}_n(\mathbf{x},t)\delta(\mathbf{x}-\mathbf{x_n})\sum_{m=1}^{N}p_m(\mathbf{x}',t)\delta(\mathbf{x}'-\mathbf{x_m})\right] \tag{4.30}$$

$$= \mathbb{E}\left[\sum_{n=1}^{N}\bar{p}_n(\mathbf{x},t)p_n(\mathbf{x}',t)\delta(\mathbf{x_n}-\mathbf{x}') + \sum_{n=1}^{N}\sum_{m\neq n}\bar{p}_n(\mathbf{x},t)p_m(\mathbf{x}',t)\delta(\mathbf{x}-\mathbf{x_n})\delta(\mathbf{x}'-\mathbf{x_m})\right] \tag{4.31}$$

The effect of the assumption of signal incoherence which we have made above amounts in this case to assuming that the effect of the “cross terms" on the expectation function can be neglected. We thus have the sum of cross correlations of each of the transmitted waveforms as the basis of our derived data model. As previously mentioned, we will return to examine the effect of a non-zero contribution of the cross term sum

$$\sum_{n=1}^{N} \sum_{m \neq n} \bar{p}_n(\mathbf{x}, t) p_m(\mathbf{x}', t) \delta(\mathbf{x} - \mathbf{x_n}) \delta(\mathbf{x}' - \mathbf{x_m}) \tag{4.32}$$

in Chapter 7. Now that we have formulated a model for the data recorded from a scene of interest we turn to the problem of constructing an image of the source intensity function.

4.4 Backprojection and Analysis of The Imaging Operator

In order to image the source intensity function $V(\mathbf{x})$ we apply a backprojection operator as seen in Section 3.1.5. Thus we have

$$I(\mathbf{z}) = \mathcal{K}[d](\mathbf{z}) = \int e^{i2\pi f(t - r(s,\mathbf{z})/c_0)} Q(\mathbf{z}, s, f) d(s, t) df ds dt \tag{4.33}$$

$$= \int e^{-i2\pi f r(s,\mathbf{z})/c_0} Q(\mathbf{z}, s, f) D(s, f) df ds \tag{4.34}$$

We may now turn our attention to an analysis of the imaging operator $\mathcal{K}$ and to the determination of the filter Q to be applied.

Carrying out the Fourier transform in the time domain version of the data model derived in Eqn (4.21) we find,

$$D(s, f) = \int e^{i2\pi f r(s,\mathbf{x})/c_0} A(\mathbf{x}, s, f) V(\mathbf{x}) d\mathbf{x} \tag{4.35}$$

substitution into (4.34) produces:

$$I(\mathbf{z}) = \int e^{i2\pi f[r(s,\mathbf{x}) - r(s,\mathbf{z})]/c_0} Q(\mathbf{z}, f, s) A(\mathbf{x}, s, f) V(\mathbf{x}) d\mathbf{x} df ds. \tag{4.36}$$

We can rewrite this expression as

$$I(\mathbf{z}) = \mathcal{L}\left[V\right](\mathbf{z}) = \int L(\mathbf{z},\mathbf{x})V(\mathbf{x})d\mathbf{x} \tag{4.37}$$

where

$$L(\mathbf{z},\mathbf{x}) = \int e^{i2\pi f(r(s,\mathbf{x})-r(s,\mathbf{z}))}Q(\mathbf{z},f,s)A(\mathbf{x},s,f)dfds. \tag{4.38}$$

In the mathematics community L is referred to as the Point Spread Function (PSF) while in the engineering parlance the term ambiguity function is more common. We will use the mathematics convention in this dissertation.

The point spread function is fundamentally a description of how blurred out a point in the scene becomes when it is imaged via the FBP technique. Under ideal circumstances we would desire to have L approximate the action of a delta function as nearly as possible.

That is, we would like to have

$$L(\mathbf{z},\mathbf{x}) \approx \delta(\mathbf{z}-\mathbf{x}) = \int e^{i2\pi(\mathbf{z}-\mathbf{x})\cdot\xi}d\xi \tag{4.39}$$

If L were exactly the delta function the image reconstruction would be perfect. Our goal in this analysis will be to apply an appropriate change of variables followed by a judicious choice of the filter Q in order to make the relationship in (4.39) as close to equality as possible.

To determine how closely L matches the ideal delta function we apply a stationary phase analysis in s and f to the PSF to determine the critical points which contribute the bulk of the integral's value. A more detailed look at the method of stationary phase is presented in Appendix B.

The points at which the phase of L is stationary are those for which,

$$\partial_f\left(\frac{f}{c_0}[r(s,\mathbf{x})-r(s,\mathbf{z})]\right) := 0 \Rightarrow r(s,\mathbf{x}) = r(s,\mathbf{z}) \tag{4.40}$$

$$\partial_s\left(\frac{f}{c_0}[r(s,\mathbf{x})-r(s,\mathbf{z})]\right) := 0 \Rightarrow h(s,\mathbf{x}) = h(s,\mathbf{z}) \tag{4.41}$$

where

$$h(s, \mathbf{x}) = \frac{f}{c_0} \left(\frac{(\gamma_1(s) - \mathbf{x})}{|\gamma_1(s) - \mathbf{x}|} \cdot \dot{\gamma_1}(s) - \frac{(\gamma_2(s) - \mathbf{x})}{|\gamma_2(s) - \mathbf{x}|} \cdot \dot{\gamma_2}(s) \right) \tag{4.42}$$

The first condition amounts to a restriction that the points $\mathbf{x}$ and $\mathbf{z}$ must lie on the same line of TDOA while the second equation is a condition on the Frequency Difference of Arrival (FDOA) of the two points.

One solution of (4.40) and (4.41) is, the point $\mathbf{x} = \mathbf{z}$, that is those points in image space which correspond to the same location in the scene. As we saw in the case of the monostatic reconstruction process in Figure 3.4, whether additional critical points exist is determined by factors relating to the physical geometry of the platform and the antenna beam patterns. For the present consideration we will assume that the collection apparatus is aligned in such a way that $\mathbf{x} = \mathbf{z}$ is the only critical point satisfying (4.40) and (4.41). We will return to justify this assumption in Chapter 7.

In order to force the phase of L to match that of the delta function in a region around $\mathbf{x} = \mathbf{z}$ we apply the *Stolt* change of variables which is defined as

$$(f, s) \to \xi = \frac{f}{c_0} \Xi(s, \mathbf{x}, \mathbf{z}) \tag{4.43}$$

where we have defined

$$\Xi(s, \mathbf{x}, \mathbf{z}) = \int_0^1 \nabla r(s, \mathbf{z} + \mu(\mathbf{x} - \mathbf{z})) d\mu \tag{4.44}$$

For a detailed justification of the Stolt change of variables see Appendix C. [2]

Applying this change of variables allows us to make the substitution $r(s, \mathbf{x}) - r(s, \mathbf{z}) = \frac{c_0}{f} \xi \cdot (\mathbf{x} - \mathbf{z})$ in the phase of L which results in

$$L(\mathbf{x}, \mathbf{z}) = \int e^{i2\pi\xi \cdot (\mathbf{x} - \mathbf{z})} Q(\mathbf{z}, f(\xi), s(\xi)) A(\mathbf{x}, s(\xi), f(\xi)) \eta^{-1} d\xi \tag{4.45}$$

where

$$\eta^{-1} = \left| \frac{\partial(f, s)}{\partial \xi} \right| \tag{4.46}$$

is the reciprocal of $\eta = \left|\frac{\partial \xi}{\partial(s,f)}\right|$ which is referred to as the *Beylkin* determinant for the PSF. [2,29]

A more detailed analysis of this factor and how it is implemented in the numerical simulations can be seen in Appendix D.1.

Thus, an approximate expression for the image $I(\mathbf{z})$ formed by application of the FBP operator $\mathcal{K}$ is given by

$$I(\mathbf{z}) \approx \int \exp\left[i2\pi\xi \cdot (\mathbf{x} - \mathbf{z})\right] Q(\mathbf{z}, f(\xi), s(\xi)) A(\mathbf{x}, s(\xi), f(\xi)) |\eta^{-1}| V(\mathbf{x}) d\mathbf{x} d\xi \tag{4.47}$$

We may interpret this expression, not as a formula from which the image will be computed but rather as a useful approximation on which to base our choice of the filter Q. It is this task to which we now turn.

4.4.1 Determination of Q and the Reconstruction Formula

Our determination of the filter Q is informed by our desire to have the PSF match the form of a delta function in the region of $\mathbf{x} = \mathbf{z}$. In (4.47) we have already matched the phase of the delta function. We would like for the rest of the integrand of (4.47) to multiply out to 1. That is, we would like to choose Q in such a way that it is the reciprocal of the rest of the combined elements of the integrand.

Two problems with this choice exist. First, Q is a function of $\mathbf{z}$ while A is a function of $\mathbf{x}$. Secondly, there are large regions in which the function A is zero. These include areas of the scene which are outside the antenna beam and those frequencies which are outside the frequency band of the receiving antenna. [2]

Since the leading order contribution to the integral comes from those points for which $\mathbf{x} = \mathbf{z}$ we can approximate $A(s, f, \mathbf{x})$ by $A(s, f, \mathbf{z})$. We thus define Q in terms of the value of A evaluated at the image point $\mathbf{z}$ rather than the scene point $\mathbf{x}$.

We solve the division by zero problem by introducing a function χ which acts as a smooth cut off function preventing division by zero. Here $\chi(s, f, \mathbf{z}) = \begin{cases} 1 & \xi \in \Omega \\ 0 & \xi \notin \Omega \end{cases}$ where $\Omega = \{\xi \mid A(s, f, \mathbf{z}) \neq 0\}$.

Here Ω is known as the *data collection manifold*. Using χ and our approximation to A our choice of Q is then

$$Q(f,s,\mathbf{z}) = \frac{\chi(s,f,\mathbf{z})}{A(s,f,\mathbf{z})}\eta = \frac{\chi(s,f,\mathbf{z})A^*(s,f,\mathbf{z})}{|A(s,f,\mathbf{z})|^2}\eta \tag{4.48}$$

Substitution of (4.48) into (4.34) produces the following reconstruction formula based on the collected data

$$I(\mathbf{z}) = \int e^{-i2\pi f r(s,\mathbf{z})/c_0} \frac{\chi(\mathbf{z},s,f)A^*(\mathbf{z},s,f)}{|A(\mathbf{z},s,f)|^2}\eta D(s,f) df ds \tag{4.49}$$

We now turn our attention to numerical simulations of example scenes of interest.

Chapter 5

NUMERICAL SIMULATIONS

5.1 Introduction and Approximations

Here we consider a series of numerically simulated test cases. We simulate the reception of signals from a target scene of interest at two platforms as described in chapter 4 and form the back projection image from the resulting cross correlated data. For computational simplicity we consider a two dimensional case in which the receivers travel in the same plane as the emitters. In chapter 8 we will examine how a three dimensional data collection geometry relates to the two dimensional examples simulated here and simulate a three dimensional data collection.

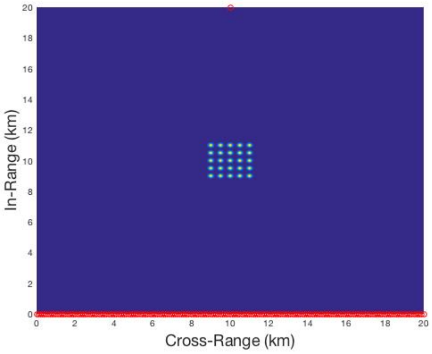

Figure 5.1: The data collection geometry

In this chapter we will consider a bistatic geometry in which the first receiver is stationary throughout the data collection process. That is, we take $\gamma_1(s) \equiv (\gamma_{1x}, \gamma_{1y})$ for all s where γ_{1x}, γ_{1y} are constants. The second receiver travels along a straight line flight path which, for simplicity, we take to be the x-axis.

The target scene is a 2km $\times$2km region at a 10km stand off distance from each receiver at the nearest point of their flight paths. This situation is illustrated in Figure 5.1. In this image the center dots correspond to emitter locations and the red circles at the bottom of the image and the one red circle at the top are the slow time locations along the flight path of the receivers. In the following images we will show images displaying only the center square in which the emitters are located.

We begin by examining the reconstruction of RF emitters which are transmitting various chirped waveforms. A chirp is the most commonly used radar waveform. Radars operate most efficiently when transmitting constant amplitude signals and a chirp is a constant amplitude signal whose frequency varies linearly over time. [2]

A chirp therefore takes the form

$$p(t) = e^{i2\pi(f_{min}t+\alpha t^2/2)}u_{[0,T]} \tag{5.1}$$

where α is the *chirp rate* and $u_{[0,T]}$ is a cut off function which is 1 in the range $t \in (0,T)$ and 0 outside of it. Here T is the length of time the radar is transmitting. If T_0 is the length of time for which the radar is turned off before it begins transmitting again the ratio $T/(T+T_0)$ is referred to as the radar's *duty cycle*.

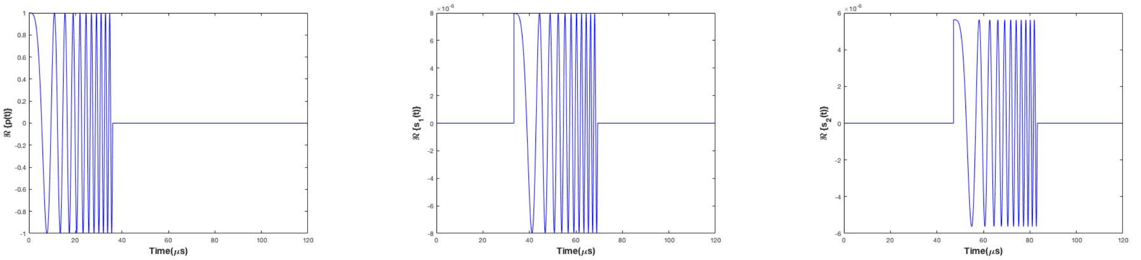

(a) Chirp transmitted at $t = 0$ **(b)** The chirp received at $\gamma_1(s)$ **(c)** The chirp received at $\gamma_2(s)$

Figure 5.2: The transmitted and received signals

Figure 5.2a shows an example of a transmitted chirped waveform. Figures 5.2b and 5.2c show the time delayed and attenuated version of the chirp which is received at two spatially separated receivers. In this example the emitter is located at the center of the target scene at the point $(10km, 10km)$ and the two receivers are located at $\gamma_1(s) = (10km, 20km)$ and $\gamma_2(s) = (0km, 0km)$.

Figure 5.3 shows the result of cross correlating these two received signals. Here we see that the peak of the cross correlation occurs at the expected TDOA of roughly $-13.84\mu s$.

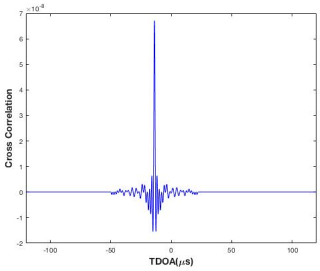

Figure 5.3: The Cross-Correlation of the two recorded chirps

The total data collected from a scene of interest is then the collection of the values of the cross correlation of the recorded signals for each slow time sample point.

Unless otherwise specified we assume that the moving receiver is traveling at a speed of $200m/s$. This is consistent with the air speed of the DC-8 platform used in the joint JPL/NASA AIRSAR program which collected data from 1988-2004. [37] The sample rate of the fast time data is approximately 40MHz. We consider only attenuation due to geometric spreading and do not consider any additional attenuation which may be due to atmospheric effects.

5.1.1 Image Overview

The reconstructed images in this chapter follow the radar engineer's convention of displaying reconstructions on a decibel scale with the highest point on the image at 0db. We use the radar engineers decibel convention which is a $10\log_{10}$ scale. This is illustrated in Figure 5.4a and Figure 5.4b.

The resulting image is then cleaned up for improved visualization by setting all values below a cut off threshold to that threshold. The value of this threshold will be made more precise when the issue of noisy signals is considered in Chapter 9. Below shows the effect of setting a threshold of -12db on the image reconstruction. Thus, we are suppressing any contributions which are roughly

(a) The back-projected image on a linear scale **(b)** The back-projected image on a db scale

Figure 5.4: The effect of db scaling

15 times weaker than the peak contribution. This effect is shown in Figure 5.5c Heat maps of the image before and after the conversion to a db scale are shown in Figures 5.5b and 5.5c.

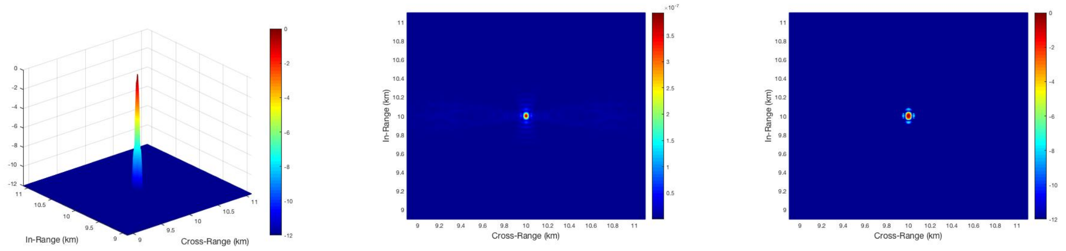

(a) The thresholded db image **(b)** A heat map of the image on a linear scale **(c)** A heat map of the image on a db scale

Figure 5.5: db scaling of the SASL image

5.2 Imaging a Single Emitter

The simplest imaging case consists of a single emitter located somewhere in the target scene. Here we consider the case of an emitter located at the point $e_1 = (10, 10)$, where the distance is measured in km. The receiver in motion flies along a straight line path from $(0, 0)$ to $(20, 0)$ while collecting 200 evenly spaced samples of the target scene. Our stationary receiver is located at the point $\gamma_2 = (10, 20)$. In each figure below we see the improvement of the back projected image as the platform continues to traverse a longer flight path, allowing more data to be back projected onto the image.

In Figures 5.6c, 5.6f, and 5.6i we see clear refinement of the resulting image when additional data is added to the back projection by means of a longer aperture. However in Figures 5.6l and 5.6o these improvements seem to have reached a point for which continuing to add additional data does not appear to have nearly as profound an effect on the quality of the resulting image.

Particularly we note the difference in the refinement of the back projection in the range and cross-range directions. Upon a quick visual examination, the localization of the emitter in the range direction appears to have reached its limit between 5km and 10km of data, however, the cross-range improvements continue for another few km. Indeed, in figure 5.6c we note that the cross-range smearing of the target spans the entire image while the range ambiguity is only about 1km. We will address the question of factors which effect the resolution achievable in our image in Section 5.4

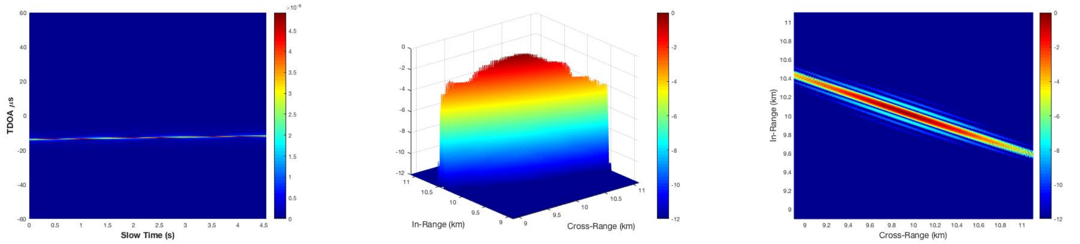

(a) The data collected over the first 1km **(b)** The surface reconstruction **(c)** The back projected heat map

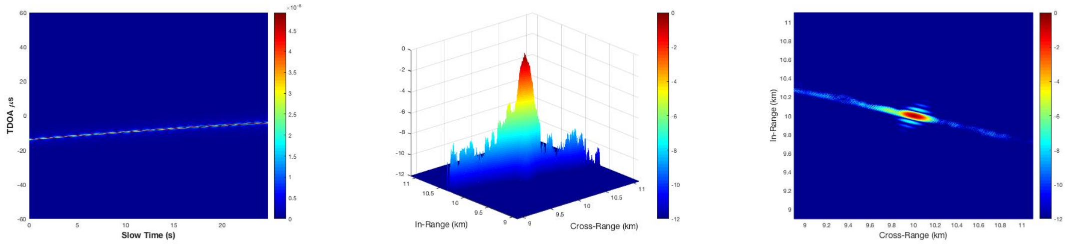

(d) The data collected over the first 5km **(e)** The surface reconstruction **(f)** The back projected heat map

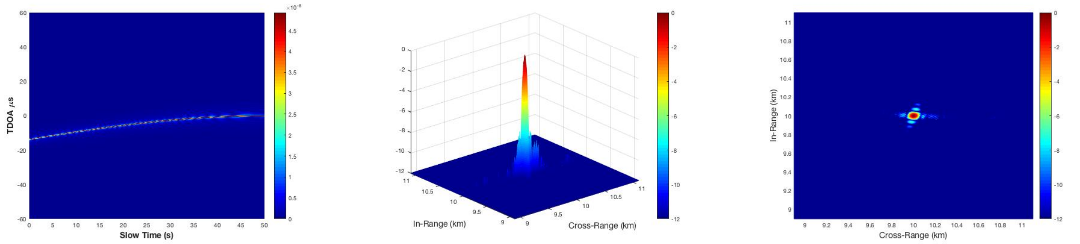

(g) The data collected over the first 10km **(h)** The surface reconstruction **(i)** The back projected heat map

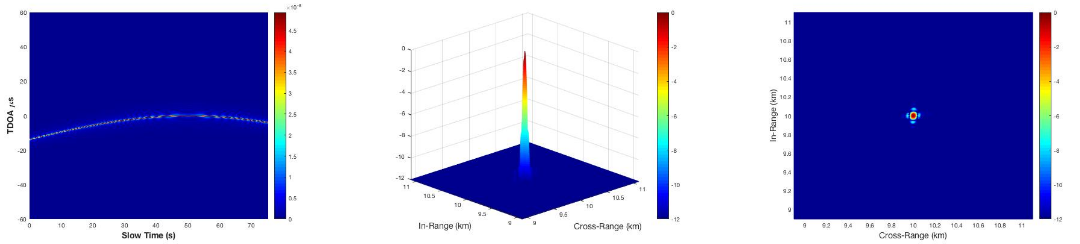

(j) The data collected over the first 15km **(k)** The surface reconstruction **(l)** The back projected heat map

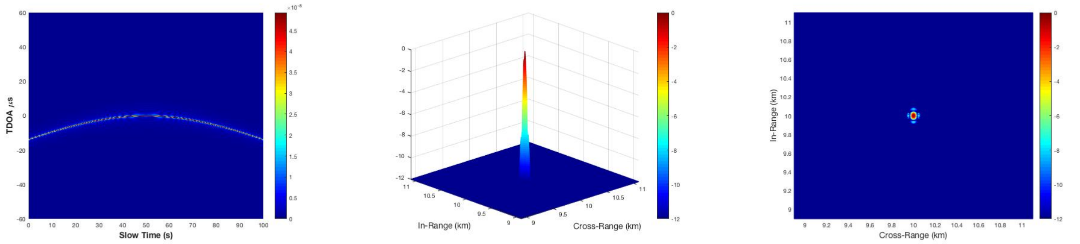

(m) The data collected over the first 20km **(n)** The surface reconstruction **(o)** The back projected heat map

Figure 5.6: The backprojected image for various lengths of synthetic aperture.

5.3 Multiple Emitters

We turn now to the case in which there are several emitters which are located inside our target scene. Here we consider the case in which we have 9 total emitters in the scene spaced equally apart in a $2km$ square scene whose center is $10km$ from the center of the flight path for the moving platform. In this example all of the emitters are transmitting chirped pulses with a $20MHz$ bandwidth and center frequencies of $40Mhz$ with a duty cycle of 2×10^{-5} seconds. While a scene containing several equally spaced emitters transmitting perfectly identical waveforms is unlikely to be encountered in practice this simulation will allow us to gain a basic understanding of the SASL image which we will build upon in further chapters.

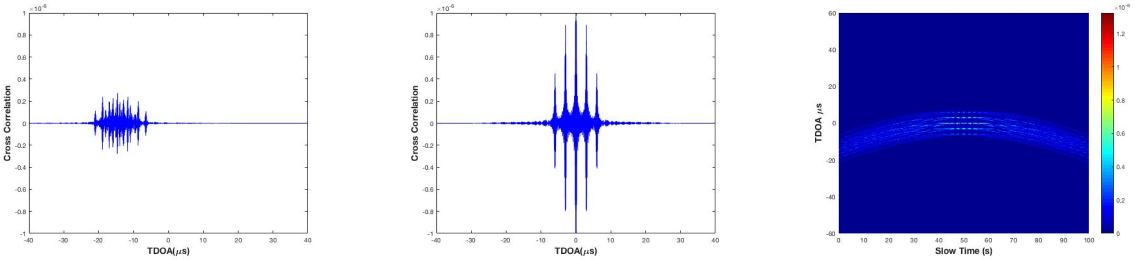

(a) Data from $\gamma_2(s) = (0, 0)$ **(b)** Data from $\gamma_2(s) = (10, 0)$ **(c)** Data from the entire flight

Figure 5.7: The cross correlation data for a scene with multiple emitters

In Figures 5.7a and 5.7b we see the cross correlated data for two different points along the flight path of the moving receiver. In Figure 5.7a there are 9 visually discernible peaks in the data slice corresponding to the signals received from different emitters in the scene. However, in Figure 5.7b we see only 5.

This occurs because at the first data collection point the two receivers are located such that the TDOA for each emitter is measurably different. However, midway through the data collection the moving receiver is located exactly opposite the stationary receiver along the x-axis. Thus a large number of path lengths from the emitters to the receivers are identical. When two emitters are located such that the TDOA of the emitted signal is identical for a given slow time step the

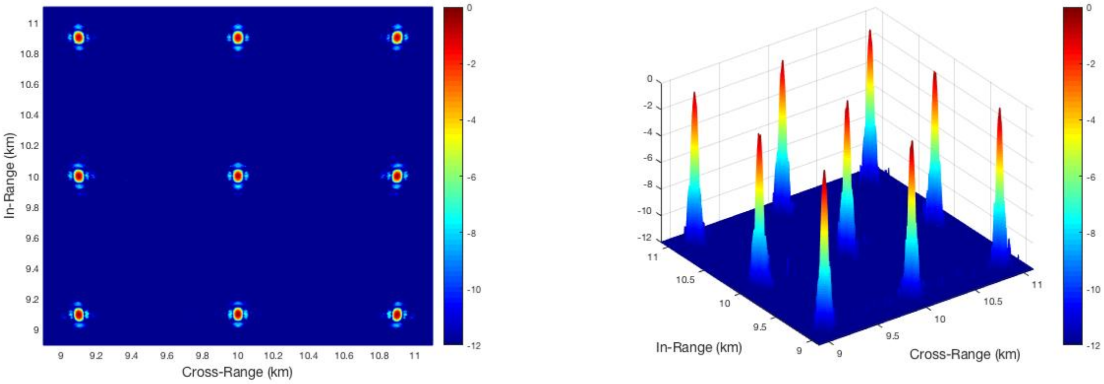

(a) The SASL image of a grid of 9 emitters

(b) A 3D mesh of the SASL image

Figure 5.8

contribution to the data due to those emitters cannot be distinguished. Figure 5.7c displays the data collected over a full 20km flight path.

Applying our backprojection scheme to this data we form the images scene in Figures 5.8a and 5.8b. We see all of the emitters in the target scene have a corresponding peak in the back projected image which occurs at the correct location in the scene.

Although all of the emitters in this example are reconstructed correctly and no obvious artifacts are present, we have chosen a scene in which the emitters are widely spaced geographically compared to their relative size in the SASL image. Recalling the series of images produced in 5.6 we can ask what parameters affect our ability to distinguish between closely spaced emitters and whether it matters if they are separated in the range or the cross-range directions. In the following sections we will derive a measure of the image resolution and explore the effect that various parameter changes cause.

5.4 The SASL Image Resolution

We turn now to the consideration of the resolution which is achievable for given data collection parameters. In Chapter 3 the resolution of a traditional monostatic system was briefly discussed. As a reminder we saw that, the cross range resolution of such a system is

$$\Delta_{CR} = \frac{\lambda}{4\sin(\frac{\Delta\theta}{2})} \tag{5.2}$$

where R is the range to the target, λ is the wavelength of the transmitted signal, and $\Delta\theta$ is the angular interval over which the aperture is synthesized. Recall also that the range resolution was found to be a function of the signal bandwidth. [35]

Thus the resolution achievable in a traditional SAR image is dependent both on the transmitted waveform and on the duration of the flight path which synthesizes the aperture. We expect that an analysis of the resolution of the SASL image reconstruction will demonstrate similar dependencies.

As has been previously mentioned, the resolution which can be attained in a back projection image is ultimately dependent on the *data collection manifold* (DCM), that is, the set of data which is collected by the receiving antenna. The data collection manifold is a region in Fourier space which is defined by the range of the variables (ξ_1, ξ_2) in the phase of the data model. [35]

In Chapter 4 we demonstrated that, by appropriate choice of the filter Q and use of the Stolt change of variables, the leading contribution to the point spread function for a critical point $\mathbf{x} = \mathbf{z}$ is

$$L(\mathbf{z}, \mathbf{x}) = \int e^{i2\pi(\mathbf{z}-\mathbf{x})\cdot\xi} d\xi \tag{5.3}$$

where $\xi = \frac{f}{c_0}\Xi(s, \mathbf{x}, \mathbf{z})$. In Appendix D.1 it is shown that

$$\Xi(s, \mathbf{z}, \mathbf{z}) = \begin{bmatrix} 1 & 0 & \partial\psi/\partial z_1 \\ 0 & 1 & \partial\psi/\partial z_2 \end{bmatrix} \left(\frac{(\gamma_2(s) - \mathbf{z})}{|\gamma_2(s) - \mathbf{z}|} - \frac{(\gamma_1(s) - \mathbf{z})}{|\gamma_1(s) - \mathbf{z}|} \right) \tag{5.4}$$

so that for the two dimensional system under consideration here we have

$$\begin{bmatrix} \Xi_1 \\ \Xi_2 \end{bmatrix} = \begin{bmatrix} (\gamma_{2x}(s) - z_x)/R_2 - (\gamma_{1x}(s) - z_x)/R_1 \\ (\gamma_{2y}(s) - z_y)/R_2 - (\gamma_{1y}(s) - z_y)/R_1 \end{bmatrix} \tag{5.5}$$

where $R_i = |\gamma_i(s) - \mathbf{z}|$.

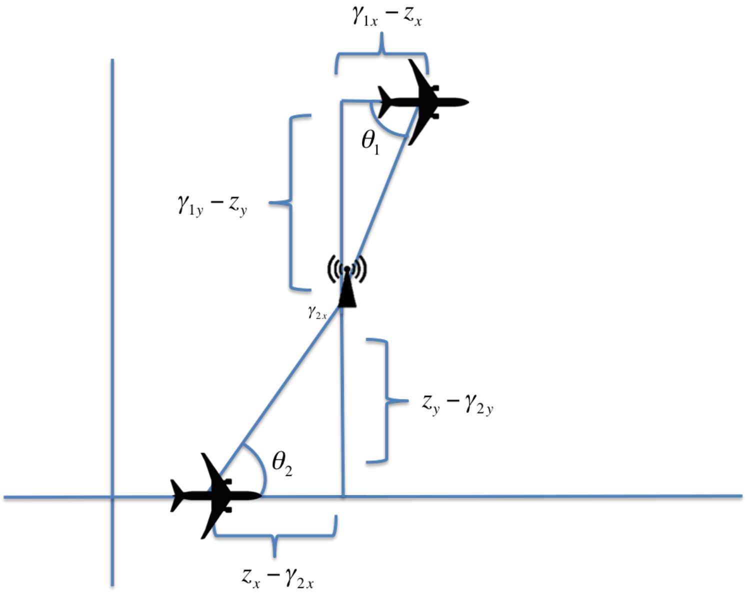

Figure 5.9: A diagram of the variables associated with one slow time look

Thus, for the particular geometry shown in Figure 5.9, under the change of variables $(f, s) \rightarrow \xi = \frac{f}{c_0}\Xi(s, \mathbf{x}, \mathbf{z})$ we have

$$\xi_1 = \frac{f}{c_0}\big(\cos(\theta_2(s)) - \cos(\theta_1(s))\big) \tag{5.6}$$

$$\xi_2 = \frac{f}{c_0}\big(\sin(\theta_2(s)) - \sin\theta_1(s))\big) \tag{5.7}$$

where γ_{ij} and θ_i are as shown in Figure 5.9.

This provides a useful tool for examining the DCM for this flight path, namely, we can view changes to the length of the flight path as providing either fewer or more angles of view over which the target emitter is observed. While the exact angle representation shown here does not generalize to all possible flight paths, the intuition regarding the effect on the DCM provides a useful framework for considering this problem moving forward. However, in Chapter 7 we will see that the size of the DCM is not the only factor impacting the quality of the final image.

The data collection manifold for an emitter located at the scene center, that is $(10km, 10km)$, transmitting a chirped waveform with a bandwidth of $20MHz$ and a center frequency of $30MHz$, with receiver flight paths defined in section 5.2 is shown in Figure 3.5a

We are interested in determining a formula to measure the resolution of a SASL image from the data collected. Recall that in Chapter 3 we demonstrated that we could find an approximate formulate for the null-to-null resolution by assuming that the DCM is approximately rectangular in regions far from the receivers. This allows us to write our expression of the impulse response as

$$L(\mathbf{z},\mathbf{x}) = \int e^{i2\pi(\mathbf{z}-\mathbf{x})\cdot\xi} d\xi \approx \int e^{i2\pi(z_1-x_1)\xi_1} d\xi_1 \int e^{i2\pi(z_2-x_2)\xi_2} d\xi_2 \tag{5.8}$$

and thereby consider the range and cross range resolutions separately. We shall begin in section with a consideration of the cross range resolution.

5.4.1 The Cross Range Resolution

To determine the resolution of the backprojected image in the cross-range direction we consider a pair of points which differ only in their cross-range, that is azimuthal, coordinate. Then $\mathbf{z}-\mathbf{x} = (z_1 - x_1, 0)$ and so $L(\mathbf{z},\mathbf{x})$ reduces to

$$L(\mathbf{z},\mathbf{x}) = \int e^{i2\pi(z_1-x_1)\xi_1} d\xi_1 \tag{5.9}$$

Recalling that

$$\int_{-b}^{b} e^{i\rho x} dx = \frac{2\sin(b\rho)}{\rho} = 2b\,\mathrm{sinc}(b\rho) \tag{5.10}$$

we have the impulse response as

$$L(\mathbf{z},\mathbf{x}) = 2b\,\mathrm{sinc}\big(b2\pi(z_1 - x_1)\big) \tag{5.11}$$

where b is determined by the data collection manifold. Taking the resolution to be the null-to-null distance we have a resolution of $\frac{2\pi}{b}$, where b is half the bandwidth of the data collection manifold in the ξ_1 direction. It then remains only to determine b from the data collection manifold, that is, to determine the range of values of ξ_1 which lie in the manifold and therefore contribute to the integral.

From (5.6), for a point $\mathbf{x} = (x_x, x_y)$ in the scene, we have

$$\xi_1 = \frac{f}{c_0}\big((\gamma_{2x}(s) - z_x)/R_2 - (\gamma_{1x}(s) - z_x)/R_1\big) = \lambda\big(\cos(\theta_2(s)) - \cos(\theta_1(s))\big) \tag{5.12}$$

since γ_{1x} is constant, the range of ξ_1 is determined by the range of γ_{2x} and f. It is clear that the largest possible range of ξ_1, and therefore the best possible resolution would be achieved for values of $\theta_2 \in (-\pi, \pi)$, that is for an infinitely long flight path.

Of course this is impossible for many reasons, not least of which being that as the platform moves farther away from the emitter, the attenuation of the signal will eventually become too great for the platform to detect it. Thus we conclude that resolution improves for longer flight paths as long as the emitter remains within the range of the receiving antenna's ability to record the signal. Antenna beam patterns will play a significant role in determining this factor for physical systems.

The range of ξ_1 for the data collection described above is then

$$\begin{aligned} \Delta\xi_1 &= \frac{\lambda}{R}\big(\max\{\gamma_{2x}(s)\} - \min\{\gamma_{2x}(s)\}\big) \\ &= \frac{30 \times 10^6 \ Hz}{c_0 \cdot 10000m} 20000m \end{aligned} \tag{5.13}$$

where R is the range to the emitter from the center of the synthesized aperture.

Recalling that b is half the range of ξ_1 this yields a resolution of

$$\Delta_{CR} = \frac{2\pi}{b} \approx 63m. \tag{5.14}$$

In order to fully understand this number we must recall that the quantities of “range" and “cross range" resolution are derived with respect to the synthesized aperture. That is, the cross range resolution is the resolution in the direction orthogonal to the line between the aperture center and the scene center. As shown in Figure 5.10b, when the synthesized aperture is to the left of the scene center the cross range direction is not aligned with the x, y axis of the scene as displayed in Figure 5.22c. The effects of this alignment will become more apparent in a later example.

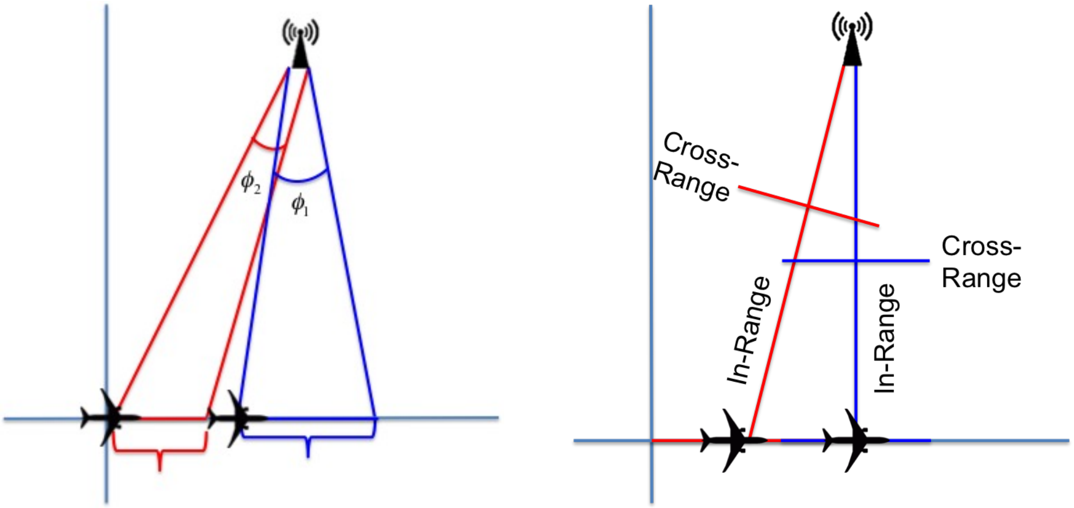

(a) A centered and left-centered flight path **(b)** The In-Range and Cross-Range directions

We can show the how this resolution affects the resulting image by considering what happens as two emitters in the scene of interest are moved gradually closer together in the cross range direction.

In Figures 5.11 through 5.13 we see that two emitters are easily separated at $100m$, begin to blur into one another but remain distinguishable at $80m$, but ultimately are reconstructed as one elongated peak at a separation of $60m$. This closely matches our expectations based upon the calculated cross range resolution.

Our expression for the resolution of the reconstructed emitters leads us to the conclusion that we can improve upon the separability of closely spaced emitters when the emitters transmit waveforms of higher frequency. We consider the case in which the two emitters under consideration have identical characteristics as those in Figures 5.11 through 5.13, but transmit at a center frequency of $50MHz$, that is, $20MHz$ higher than the previous case.

We calculate the approximate resolution for a $50MHz$ center frequency transmitted signal as

$$\Delta_{CR} = \frac{2\pi}{b} = 2\pi \left(\frac{50 \times 10^6 \ Hz}{2c_0 \cdot 10000m} 20000m \right)^{-1} \approx 38m \tag{5.15}$$

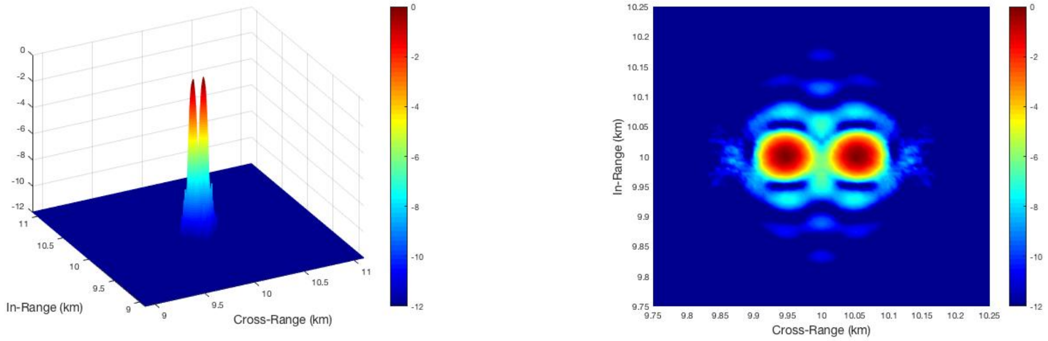

Figure 5.11: A 100m separation

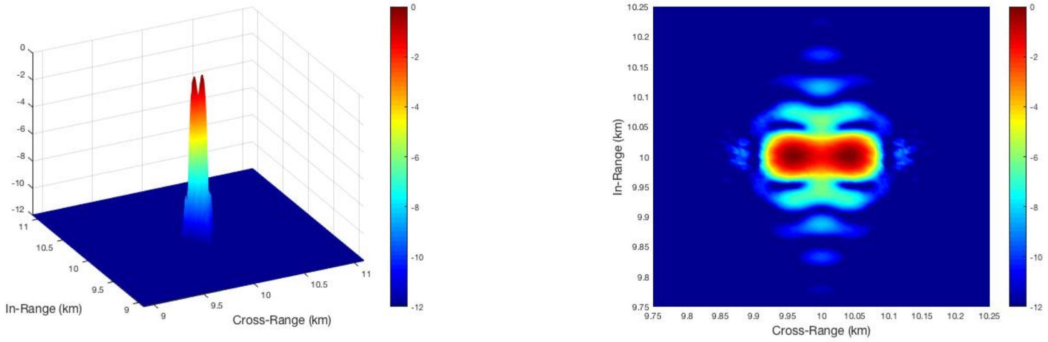

Figure 5.12: An 80m separation

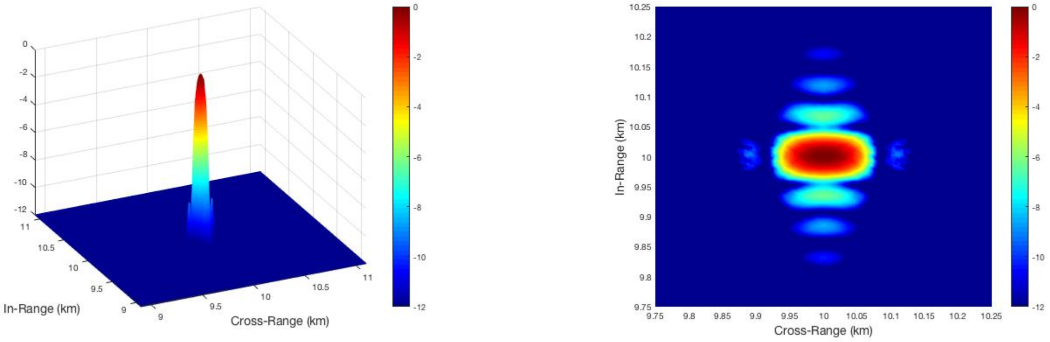

Figure 5.13: A 60m separation

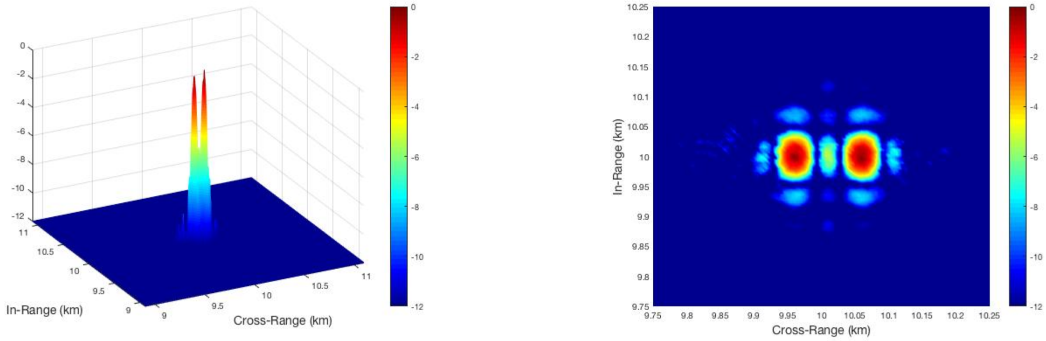

Figure 5.14: An 80m separation

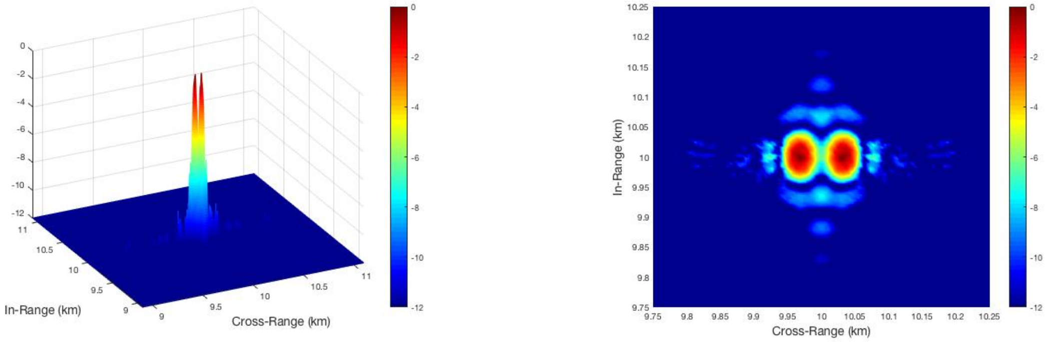

Figure 5.15: A 60m separation

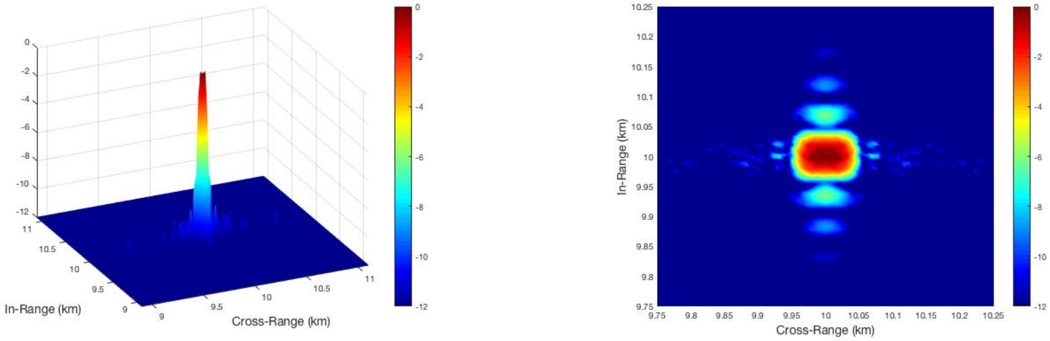

Figure 5.16: A 40m separation

which is consistent with the simulations shown in Figures 5.14 through 5.16. In these images we see that two emitters are easily distinguished at $80m$, are still well separated at $60m$ and are blurring together significantly at $40m$.

We can see the effect that this has on the overall scene reconstruction by examining Figure 5.17. We see that increasing the carrier frequency of the transmitted signals has a marked effect on the overall image quality of the reconstructed scene.

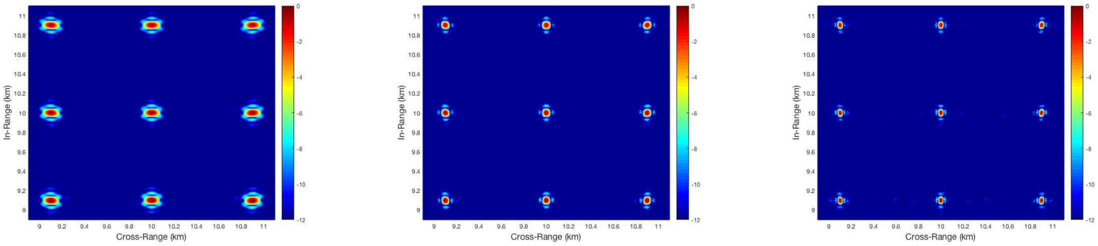

(a) $f_c = 20MHz$ Signal **(b)** $f_c = 40MHz$ Signal **(c)** $f_c = 60MHz$ Signal

Figure 5.17: The image resolution improves with increasing carrier frequency

Carrier frequency is, however, not the only component of the resolution expression. In (5.13) we see that the data collection manifold is dependent on the range from the synthesized aperture to the target emitter and on the total length of the synthesized aperture. We will consider how each of these two parameters impact the resulting image construction.

First we shall look at how the range of aspect angles of the target emmiter which are viewed by the receiver affects the resulting image we are capable of constructing. We begin by examining the data collection manifolds for two emitters in the scene with identical characteristics, and which are both located on the same cross range line in the image, but are separated in range by $1.9km$ so that one emitter is significantly closer to the moving receiver than the other. The emitter which is located closer to the receiver will be viewed by the receiver over a larger collection of angles than will the emitter which is farther away.

In Figure 5.18 we have the data collection manifolds for two emitters separated by $1.9km$ in range. Here we see that the DCM is smaller for the emitter which was viewed from fewer angles, that is, the receiver which was farther away from the aperture. The resolution in the backprojected image for each emitter is calculated to be

$$\Delta_{CR}(15,14) = \frac{2\pi}{b} = 2\pi \left(\frac{30 \times 10^6 \ Hz}{2c_0 \cdot 9050m} 20000m \right)^{-1} \approx 57m \tag{5.16}$$

$$\Delta_{CR}(15,16) = \frac{2\pi}{b} = 2\pi \left(\frac{30 \times 10^6 \ Hz}{2c_0 \cdot 10950m} 20000m \right)^{-1} \approx 69m \tag{5.17}$$

The effect on the reconstructed image is shown in Figure 5.19.

Here we have four emitters located symmetrically across from each other along the same cross range line with the second pair of emitters $1.9km$ farther away from the synthesized aperture than the first. We see that, at a separation distance of $70m$, the first pair of emitters are distinguishable in the reconstruction, however the second pair of emitters are not. This is consistent with the resolution we have derived for this carrier frequency at these ranges.

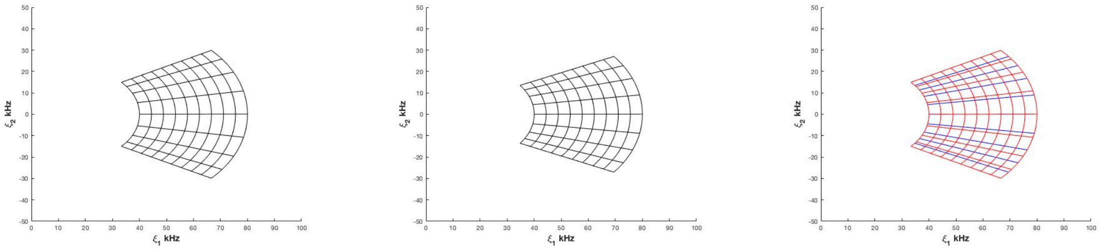

(a) The DCM for $e_1 = (10, 8.9)$ **(b)** The DCM for $e_1 = (10, 10.9)$ **(c)** The two DCMs overlaid

Figure 5.18: The effect on the DCM of receivers separated in the range direction

As shown in Figure 5.20, the range of angles over which the emitter is viewed is necessarily smaller for emitters which are farther away from the moving receiver. Thus, an increase in the range from the synthesized aperture to the target emitter results in a smaller data collection manifold, even if the emitter is visible to the receiving antenna throughout the duration of the data collection.

If a receiver flies along a flight path for which certain points in the scene of interest are always much farther away than other points in the scene, any emitters at those locations will be

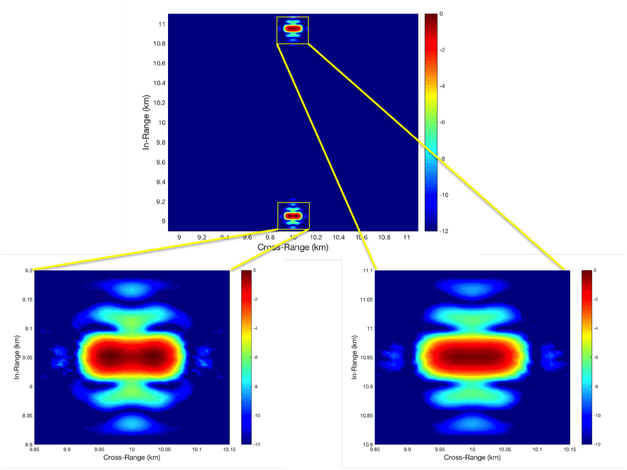

Figure 5.19: Emitters nearer the synthesized aperture are reconstructed with better resolution

reconstructed with corresponding lower fidelity than will closer emitters. This occurs because the receiver has viewed such emitters from fewer angles.

It may be prudent therefore to observe large scenes from flight paths which are curved in order to increase the number of aspect angles over which all points in the scene are viewed. We return to this observation in Chapter 9 where the effects of flight path parameters are considered more fully.

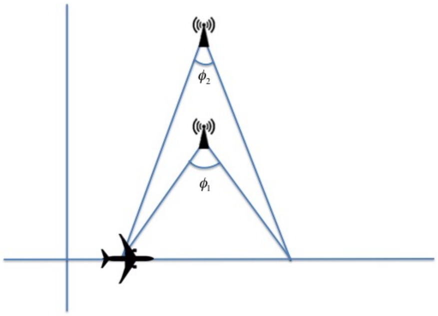

Figure 5.20: The range of angles over which data are collected is smaller for emitters farther away

From equation (5.13) it is also clear that the data collection manifold, and therefore the cross range resolution of the backprojected image, is dependent on the length of the flightpath. Thus shorter flight paths lead to smaller DCMs and therefore to lower resolution images. This can also be thought of in the context of Figure 5.20. Shorter flight paths lead to fewer angles over which the emitter is viewed, and therefore to a smaller data collection manifold and worse resolution. This is essentially the effect which we had already observed taking place in the images of Figure 5.6. We can now make these observations precise.

In the above reconstructions we have observed the images achievable with data collected from a flight path of $20km$ for which the synthesized aperture is centered on the the scene center. We now consider how a shorter flight path reduces the image quality. We first consider the backprojected image which results in a flight path one quarter as long at that previously considered.

For a $30MHz$ carrier frequency emitter observed from a flight path of just $5km$ we have

$$\Delta_{CR}(10,10) = \frac{2\pi}{b} = 2\pi\left(\frac{30 \times 10^6\ Hz}{2c_0 \cdot 10000m} 5000m\right)^{-1} \approx 251m. \tag{5.18}$$

Whereas for the same emitter observed from a $20km$ flight path the cross range resolution is

$$\Delta_{CR}(10,10) = \frac{2\pi}{b} = 2\pi\left(\frac{30 \times 10^6\ Hz}{2c_0 \cdot 10000m} 20000m\right)^{-1} \approx 63m. \tag{5.19}$$

In Figure 5.21 we see how two emitters located $200m$ are well separated in the image created using the data from a $20km$ long data collection flight but are blurring into a single peak when imaged using the data from a flight path of only $5km$.

This matches the experience we have developed already, namely, that longer flight paths produce a longer synthetic aperture from which we image our scene. As was first discussed in Chapter 3, the longer the aperture size the better the cross range resolution achievable in the resulting image. We are now simply able to put a number to this intuitive understanding which allows us to grasp a quantitative understanding of the magnitude of this effect.

While we understand that the aperture length affects the cross range resolution according to equation (5.13), our previous analysis of this equation assumed that the flight path was always centered on the scene center. A natural extension of our analysis so far is to answer the question: what affect will be had on the image if the synthesized aperture is off center from the scene under surveillance?

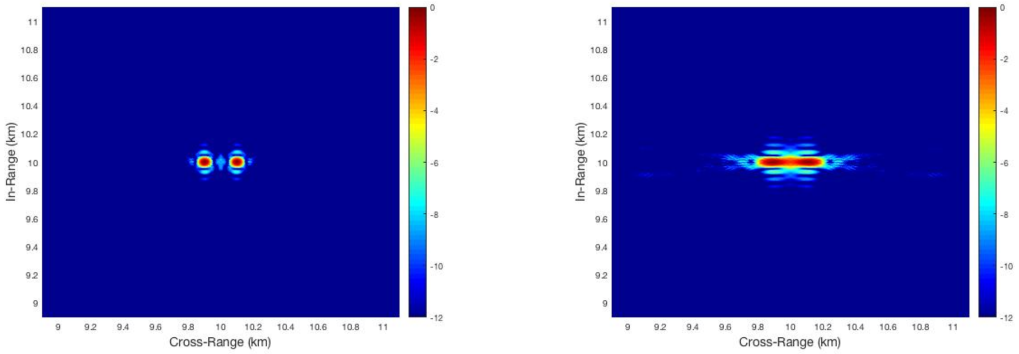

Figure 5.21: Shorter flight paths produce less resolved images

In Figure 5.22 we see the effect of having a short flight path which is not centered on the scene center. In Figure 5.22b we have an image created from the data gathered along a $5km$ flight path in which the moving receiver traverses the points $\gamma_2(s) = (7.5, 0)$ to $\gamma_2(s) = (12.5, 0)$. This is contrasted with the image in Figure 5.22c which is created using the data gathered along the flight path $\gamma_2(s) = (0, 0)$ to $\gamma_2(s) = (5, 0)$.

The data collection manifold for the emitter located in the scene center is shown for each of these cases in figures 5.22d through 5.22f. For clarity, the data collection geometries for both the centered and the left centered flight paths described are diagramed in Figure 5.10a.

Despite using data collections of the same total length we find: in the left centered image the emitters are not reconstructed as well as in the centered image, and the reconstructed emitters appear skewed with respect to the x, y axis. Both of these effects can be explained by returning to equation (5.13). The calculated cross range resolutions for each of the flight paths described here are

$$\text{centered} \rightarrow \Delta_{CR}(10, 10) = \frac{2\pi}{b} = 2\pi \left(\frac{30 \times 10^6 \ Hz}{2c_0 \cdot 10000m} 5000m \right)^{-1} \approx 251m \tag{5.20}$$

$$\text{left centered} \rightarrow \Delta_{CR}(10, 10) = \frac{2\pi}{b} = 2\pi \left(\frac{30 \times 10^6 \ Hz}{2c_0 \cdot 12500m} 5000m \right)^{-1} \approx 314m. \tag{5.21}$$

Since the left centered flight path synthesizes an aperture whose center is farther away from the scene center the number of angles which are viewed by the receiver is less. As a result the overall

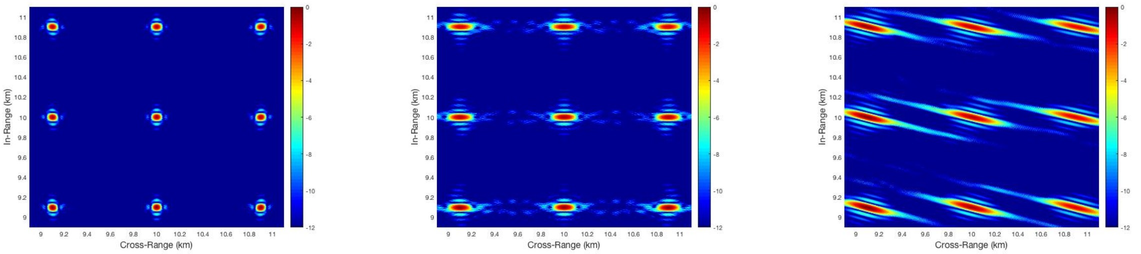

(a) SASL Image for a $20km$ flight path **(b)** SASL Image for a centered $5km$ flight path **(c)** SASL Image for a left centered $5km$ flight path

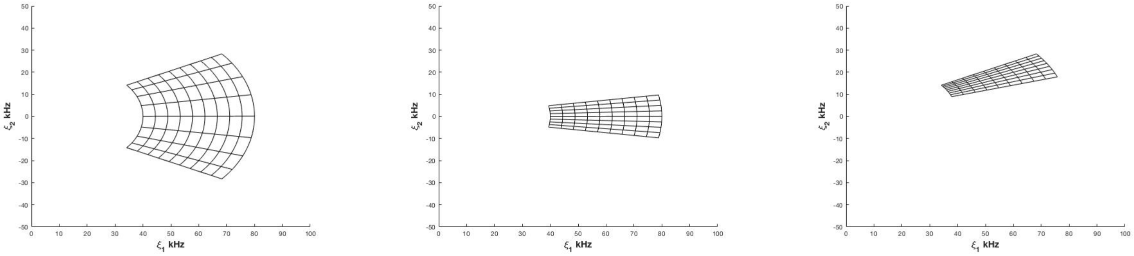

(d) A $20km$ flight path **(e)** A centered $5km$ flight path **(f)** A left centered $5km$ flight path

Figure 5.22: The backprojected images from different data collections

resolution of the image is negatively impacted. This is shown graphically in Figure 5.10a. The left centered flight path shown in red records data over a smaller range of angles than does the centered blue path. This narrows the data collection manifold as seen in Figures 5.22e and 5.22f.

Furthermore, as we previously made note of in our discussion of figures 5.10a and 5.10b, the cross range direction is dependent on the orientation of the flight path of the receiver. When the flight path is to the left of the scene center the cross range direction is not aligned with the x, y axis of the scene. Thus the reconstructed emitters have a skewed appearance in the resulting SASL image.

As a final note on the achievable cross range resolution for target emitters of interest we consider the resolution for an FM radio broadcast tower. In the United States such towers operate with center frequencies in the $88MHz$ to $108MHz$ range with a bandwidth of $200kHz$. The cross range resolution of a station operating on the frequency 95.0 FM is then $\Delta_{CR}(10, 10) \approx 20m$ when imaged from a $20km$ flight path at a range of $10km$ to the radio tower which we take to be at or near the scene center. [38]

5.4.2 The Range Resolution

We turn now to the other component of the image quality, the range resolution. From our argument in section 5.4 the range resolution of the constructed SASL image is determined by the range of

$$\xi_2 = \frac{f}{c_0}\big((\gamma_{2y}(s) - z_y)/R_2 - (\gamma_{1y}(s) - z_y)/R_1\big) = \frac{f}{c_0}\big(\sin(\theta_2(s)) - \sin\theta_1(s))\big) \tag{5.22}$$

where $R_i = |\gamma_i(s) - \mathbf{z}|$ and θ_i is as shown in Figure 5.9. For the flight path described above we have γ_{2y} and γ_{1y} constant. Furthermore, noting that, as in (5.13) we use the distance to the scene center from the midpoint of the synthesized aperture for $|\gamma_i(s) - \mathbf{z}|$, we see that the measure of the resolvability of target emitters in the range direction is dependent upon the range of values of f, that is, on the bandwidth of the transmitted waveform.

For the data collection geometry in Figure 5.9 and assuming the use of a baseband signal, that is, one for which $f_{min} = 0$ we have

$$\max\{\xi_2\} = \frac{f_{max}}{c_0}R_T = \frac{2f_{max}}{c_0} \tag{5.23}$$

$$\min\{\xi_2\} = \frac{f_{min}}{c_0}R_T = 0 \tag{5.24}$$

for a point at the scene center, where $R_T = \frac{R_1R_2}{R_2(\gamma_{1y}-z_y)-R_1(\gamma_{2y}-z_y)}$ is the total range dependence.

Taking max$\{\xi_2\}$ and min$\{\xi_2\}$ as our limits of integration we have

$$\int_0^{\frac{2f}{c_0}} e^{i2\pi(z_2-x_2)\xi_2}d\xi_2 = \frac{e^{2\pi i2f/c_o(z_2-x_2)} - e^0}{2\pi i(z_2 - x_2)} \tag{5.25}$$

$$= \frac{e^{2\pi i2f_c/c_o(z_2-x_2)+2\pi i2B_w/c_o(z_2-x_2)} - e^{2\pi i2f_c/c_o(z_2-x_2)-2\pi i2B_w/c_o(z_2-x_2)}}{2\pi i(z_2 - x_2)} \tag{5.26}$$

$$= e^{2\pi i2f_c/c_o(z_2-x_2)}\sin(4\pi B_w(z_2 - x_2)/c_0)\frac{1}{\pi(z_2 - x_2)} \tag{5.27}$$

$$= e^{2\pi i2f_c/c_o(z_2-x_2)}\frac{4B_w}{c_0}\text{sinc}(4\pi B_w(z_2 - x_2)/c_0) \tag{5.28}$$

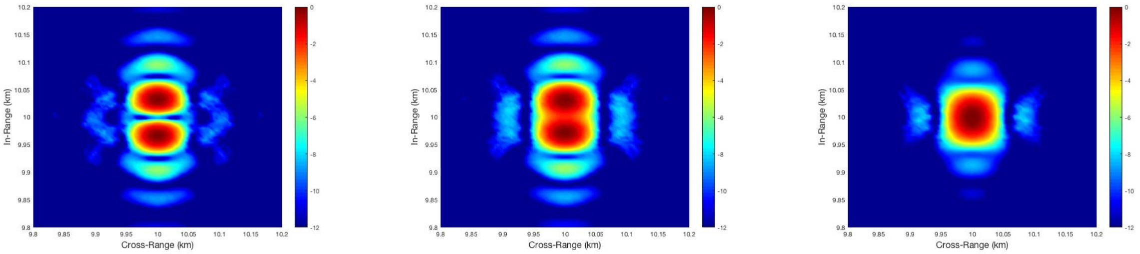

(a) A $50m$ separation **(b)** A $45m$ separation **(c)** A $40m$ separation

Figure 5.23: The resolvability of emitters transmitting a $20Mhz$ bandwidth chirp

Where B_w is the bandwidth of the transmitted signal. Noting that $|e^{2\pi i 2f_c/c_o(z_2-x_2)}| = 1$ we have that $b = 2B_w/c_0$. Thus the resolution in the range direction for a baseband signal for which $B_w = f_{max}$ is $\Delta_{IR} \approx \frac{2\pi c_0}{2f_{max}}$. Generalizing to non-baseband signals we have that the resolution in the range direction is then

$$\Delta_{IR} \approx \frac{\pi c_0}{B_w}. \tag{5.29}$$

For the data collection geometry in Figure 5.9 and a $20MHz$ bandwidth we have

$$\Delta_{IR}(10,10) = \frac{\pi c_0}{20 \times 10^6} \approx 47m. \tag{5.30}$$

In Figure 5.23 we see that two emitters transmitting a $20MHz$ signal are resolvable at a in range separation of $50m$, blurring at $45m$ and completely indistinguishable by $40m$, which is consistent with our resolution calculation.

Similarly in Figure 5.24 we see that emitters which are transmitting a higher bandwidth signal, in this case a $30MHz$ chirp, are resolvable at closer distances. In Figure 5.24a we see that the emitters are easily separable at $45m$. In 5.24b we see that they remain distinguishable but are beginning to blur together at $37m$. Finally in 5.24c once a $30m$ separation is reached the two appear as one peak.

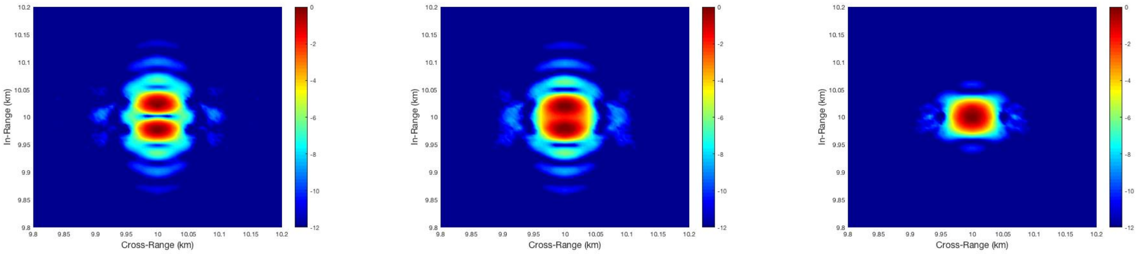

(a) A $45m$ separation **(b)** A $37m$ separation **(c)** A $30m$ separation

Figure 5.24: The separability of emitters transmitting a $50Mhz$ chirp

These results are consistent with the calculation that the range resolution is given by

$$\Delta_{IR}(10,10) = \frac{\pi c_0}{30 \times 10^6} \approx 31m \tag{5.31}$$

Just as we saw for the cross range case, the greater resolution in the range direction is due to a larger data collection manifold. This is easily seen in Figure 5.25. It is clear that the signal with the larger bandwidth produces a much wider DCM which, as we have seen, leads to finer resolution images.

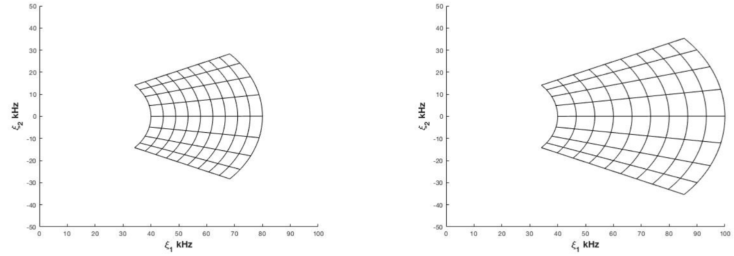

(a) A $20MHz$ bandwidth **(b)** A $30MHz$ bandwidth

Figure 5.25: The DCM for two chirp signals with $f_c = 30MHz$

Now that the concept of image resolution has been thoroughly considered in the ideal case we can begin to examine the effects of the cross terms on our images.

Chapter 6

A NON-STATISTICAL MODEL FOR SASL

6.1 Introduction

We now return the various assumptions made in Chapter 4. There, we assumed certain statistical properties about the transmitted signals. Most notably we assumed that the contribution of cross term correlations in the data are either negligible or else, that the signals from different emitters can be separated prior to the calculation of the cross correlation.

Each receiver records the superposition of the waves incident on it at any given fast time step. Therefore, it is not trivial, and indeed it can be quite difficult or even impossible, to determine the contributions that each emitter in the scene makes to the recorded signal a priori. Often, additional information about the signals in the scene is needed in order to perform any kind of signal separation before localization. Furthermore, although we expect the sources in a typical scene to be uncorrelated, there may be scenes of interest which contain highly correlated sources that we desire to image.

Thus, we seek to perform the cross correlation operation without any *a priori* separation under conditions in which various emitters are, or could be, highly correlated. Doing so increases the difficulty of the reconstruction. Our previous data model took the form of the superposition of the cross correlation matrices for the signal transmitted from each emitter. This assumed that the data from each emitter could be separated *a priori* from all of the others which, as we have said, is unlikely to be true for highly correlated sources.

In broad terms, our current model will take the form of the cross correlation of the superposition of the data recorded from each emitter. That is,

$$d_{old}(s,t) \Longrightarrow \sum_i S_i^{(1)}(s,t) \star S_i^{(1)}(s,t) \quad \text{vs.} \quad d_{new}(s,t) \Longrightarrow \sum_i S_i^{(1)}(s,t) \star \sum_j S_j^{(2)}(s,t) \tag{6.1}$$

where $\star$ denotes the cross correlation and $S_i^{(k)}$ is the signal recorded at the k^{th} receiver due to the i^{th} emitter.

We shall proceed to derive a fresh model of the data in terms of the cross correlation of two received signals without considering the expectation of the source terms. This will allow us to separate the contribution to the data of the correlation of an emitted signal at one receiver with its counterpart recorded at the other receiver from those contributions which arise from the correlation of an emitted signal recorded at one receiver with a different signal recorded at the other receiver. Previously we have assumed that such correlations are negligible.

Let $S_i(t)$ be the signal recorded at the i^{th} receiver. Then

$$\begin{aligned} S_1(\mathbf{x}, t) &= \int \frac{j\left(\mathbf{y}, t - \frac{|\mathbf{x}-\mathbf{y}|}{c_0}\right)}{4\pi|\mathbf{x}-\mathbf{y}|} d\mathbf{y} && (6.2) \\ &= \int e^{2\pi i f |\mathbf{x}-\mathbf{y}|/c_0} e^{-2\pi i f t} \frac{J(\mathbf{y}, f)}{4\pi|\mathbf{x}-\mathbf{y}|} d\mathbf{y} df && (6.3) \end{aligned}$$

$$S_2(\mathbf{x}', t) = \int e^{2\pi i f' |\mathbf{x}'-\mathbf{y}'|/c_0} e^{-2\pi i f' t} \frac{J(\mathbf{y}', f')}{4\pi|\mathbf{x}'-\mathbf{y}'|} d\mathbf{y}' df' \qquad (6.4)$$

where $j(\mathbf{y}, t)$ is the source function for an emitter located at $\mathbf{y}$ of the scalar wave equation

$$\left(\nabla^2 - \frac{1}{c_0^2}\frac{\partial}{\partial t^2}\right)\mathcal{E}(\mathbf{x}, t) = j(\mathbf{y}, t) \qquad (6.5)$$

describing the electromagnetic waves created by a distribution of sources in the scene of interest and $(\mathbf{x}, t)$, $(\mathbf{x}', t)$ are the two spatiotemporal locations at which the signals are recorded.

We then take our data collected from the scene to be the cross correlation of these two signals. That is

$$\begin{aligned} d(\mathbf{x},\mathbf{x}',t) = \int & e^{2\pi i f\left(\tau - \frac{|\mathbf{x}-\mathbf{y}|}{c_0}\right)} e^{-2\pi i f'\left(t+\tau-\frac{|\mathbf{x}'-\mathbf{y}'|}{c_0}\right)} \\ & \times \frac{\bar{J}(\mathbf{y},f)J(\mathbf{y}',f')}{(4\pi)^2|\mathbf{x}-\mathbf{y}||\mathbf{x}'-\mathbf{y}'|} d\mathbf{y}d\mathbf{y}'dfdf'd\tau \end{aligned} \tag{6.6}$$

$$\begin{aligned} = \int & e^{-2\pi i f\left(\frac{|\mathbf{x}-\mathbf{y}|}{c_0}\right)} e^{-2\pi i f'\left(t-\frac{|\mathbf{x}'-\mathbf{y}'|}{c_0}\right)} \\ & \times \frac{\bar{J}(\mathbf{y},f)J(\mathbf{y}',f')}{(4\pi)^2|\mathbf{x}-\mathbf{y}||\mathbf{x}'-\mathbf{y}'|} d\mathbf{y}d\mathbf{y}'dfdf' \int e^{2\pi i\tau(f-f')}d\tau. \end{aligned} \tag{6.7}$$

Performing the τ and f' integration we have

$$d(\mathbf{x},\mathbf{x}',t) = \int e^{-2\pi i f\left(\frac{|\mathbf{x}-\mathbf{y}|}{c_0}\right)} e^{-2\pi i f'\left(t-\frac{|\mathbf{x}'-\mathbf{y}'|}{c_0}\right)} \frac{\bar{J}(\mathbf{y},f)J(\mathbf{y}',f')}{(4\pi)^2|\mathbf{x}-\mathbf{y}||\mathbf{x}'-\mathbf{y}'|}\delta(f-f')d\mathbf{y}d\mathbf{y}'dfdf' \tag{6.8}$$

$$= \int e^{-2\pi i f\left(\frac{|\mathbf{x}-\mathbf{y}|}{c_0}\right)} e^{-2\pi i f\left(t-\frac{|\mathbf{x}'-\mathbf{y}'|}{c_0}\right)} \frac{\bar{J}(\mathbf{y},f)J(\mathbf{y}',f)}{(4\pi)^2|\mathbf{x}-\mathbf{y}||\mathbf{x}'-\mathbf{y}'|}d\mathbf{y}d\mathbf{y}'df \tag{6.9}$$

$$= \int e^{-2\pi i f\left(t+\frac{|\mathbf{x}-\mathbf{y}|}{c_0}-\frac{|\mathbf{x}'-\mathbf{y}'|}{c_0}\right)} \frac{\bar{J}(\mathbf{y},f)J(\mathbf{y}',f)}{(4\pi)^2|\mathbf{x}-\mathbf{y}||\mathbf{x}'-\mathbf{y}'|}d\mathbf{y}d\mathbf{y}'df. \tag{6.10}$$

As in Chapter 4 we apply the start-stop approximation. That is, we assume the measurement points $\mathbf{x}, \mathbf{x}'$ can be considered stationary throughout the duration of one “look" of time T. As seen previously this can be accomplished mathematically by application of a windowing function. Taking as before $\gamma_1(s)$ and $\gamma_2(s)$ to be the slow time functions of our receiver locations we can rewrite the data expression above as

$$d(s,t) = \int e^{-2\pi i f(t-r(s,\mathbf{y},\mathbf{y}')/c_0)}\bar{J}(\mathbf{y},f)J(\mathbf{y}',f)A(s,\mathbf{y},\mathbf{y}')d\mathbf{y}d\mathbf{y}'df. \tag{6.11}$$

where

$$r(s,\mathbf{y},\mathbf{y}') = |\boldsymbol{\gamma_2}(\mathbf{s})-\mathbf{y}'| - |\boldsymbol{\gamma_1}(\mathbf{s})-\mathbf{y}| \tag{6.12}$$

and $A(s,\mathbf{y},\mathbf{y}')$ accounts for geometric spreading factors and windowing. If the field being measured is due to a single antenna radiating an EM field as the result of a signal sent to it then the source function takes the form

$$J(\mathbf{x},f) = P(f)g(\mathbf{x}). \tag{6.13}$$

In the case of a radar, $g(\mathbf{x})$ is the time derivative of the current distribution over the antenna and $P(f)$ is the waveform sent to the antenna. As discussed previously, the particular waveform sent to the antenna can take a wide variety of forms, however a chirped waveform is the most common in radar transmission. [2, 30]

Thus, in the case of a single radiating antenna present in the scene our data takes the form

$$d(s,t) = \int e^{-2\pi i f(t - r(s,\mathbf{y},\mathbf{y}')/c_0)} A(s,\mathbf{y},\mathbf{y}')\bar{P}(f) g(\mathbf{y}) P(f) g(\mathbf{y}') d\mathbf{y} d\mathbf{y}' df. \tag{6.14}$$

We assume that the antenna can be treated as a point source so that $g(\mathbf{y}) = \delta(\mathbf{x_0} - \mathbf{y})$ where $\mathbf{x}_0$ is the antenna location. Whenever the physical radiating source is smaller than the resolution of the SASL image this approximation should not degrade image quality. As seen in Chapter 5, the resolution achieved when imaging a US FM radio tower is on the order of 30m. The physical footprint of such a tower is typically on the order of meters.

Under this approximation we have

$$\begin{aligned} d(s,t) &= \int e^{-2\pi i f(t - r(s,\mathbf{y},\mathbf{y})/c_0)} A(s,\mathbf{y},\mathbf{y})\bar{P}(f) P(f) \delta(\mathbf{y} - \mathbf{x_0}) d\mathbf{y} df & (6.15) \\ &= \int e^{-2\pi i f(t - r(s,\mathbf{y},\mathbf{y})/c_0)} A(s,\mathbf{y},\mathbf{y}) |P(f)|^2 V(\mathbf{y}) d\mathbf{y} df. & (6.16) \end{aligned}$$

This matches the form of the data model derived for a single emitter under the previous assumptions.

We now consider the form of the data when multiple emitters are present. To do so we extend our previous source function to the case of N point-like emitters each transmitting its own waveform. We thus have

$$J(\mathbf{x}, f) = \sum_{n=1}^{N} P_n(f) \delta(\mathbf{x} - \mathbf{x_n}) \tag{6.17}$$

where $\mathbf{x_n}$ is the location of the n^{th} receiver. Our data is then modeled by

$$
\begin{aligned}
d(s,t) = \int e^{-2\pi i f(t - r(s,\mathbf{y},\mathbf{y}')/c_0)} A(s,\mathbf{y},\mathbf{y}') \\
\times \sum_{n=1}^{N} \bar{P}_n(f)\delta(\mathbf{y}-\mathbf{x_n}) \sum_{m=1}^{N} P_m(f)\delta(\mathbf{y}'-\mathbf{x_m}) d\mathbf{y} d\mathbf{y}' df.
\end{aligned}
\tag{6.18}
$$

We can then separate the contribution to the data from those terms which are the correlation of the two copies of a signal from one emitter recorded at each platform and those terms which result from the correlation of two signals which were emitted from different points in the scene. Doing so produces

$$
\begin{aligned}
d(s,t) = \int e^{-2\pi i f(t - r(s,\mathbf{y},\mathbf{y}')/c_0)} A(s,\mathbf{y},\mathbf{y}') \Bigg(\sum_{n=1}^{N} \bar{P}_n(f)\delta(\mathbf{y}-\mathbf{x_n}) P_n(f)\delta(\mathbf{y}'-\mathbf{x_n}) \\
+ \sum_{n=1}^{N} \sum_{m\neq n} \bar{P}_n(f)\delta(\mathbf{y}-\mathbf{x_n}) P_m(f)\delta(\mathbf{y}'-\mathbf{x_m}) \Bigg) d\mathbf{y} d\mathbf{y}' df.
\end{aligned}
\tag{6.19}
$$

$$
\begin{aligned}
&= \int e^{-2\pi i f(t - r(s,\mathbf{y},\mathbf{y})/c_0)} A(s,\mathbf{y},\mathbf{y}) \sum_{n=1}^{N} |P_n(f)|^2 \delta(\mathbf{y}-\mathbf{x_n}) d\mathbf{y} df \\
&+ \int e^{-2\pi i f(t - r(s,\mathbf{y},\mathbf{y}')/c_0)} A(s,\mathbf{y},\mathbf{y}') \sum_{n=1}^{N} \sum_{m\neq n} \bar{P}_n(f) P_m(f) \delta(\mathbf{y}'-\mathbf{x_m}) \delta(\mathbf{y}-\mathbf{x_n}) d\mathbf{y} d\mathbf{y}' df.
\end{aligned}
\tag{6.20}
$$

$$
= d_D(s,t) + d_C(s,t) \tag{6.21}
$$

where

$$
d_D(s,t) = \sum_{n=1}^{N} \int e^{-2\pi i f(t - r(s,\mathbf{y},\mathbf{y})/c_0)} A(s,\mathbf{y},\mathbf{y}) |P_n(f)|^2 \delta(\mathbf{y}-\mathbf{x_n}) d\mathbf{y} df \tag{6.22}
$$

is the data due to the correlation of each emitted signal with itself. Here we have chosen the subscript D to denote the fact that these are the *diagonal* terms as opposed to the off diagonal *cross terms.* These diagonal terms may be thought of as the “correct" emitter data, or the data we would collect if there were no correlation between signals emitted from different sources. Equivalently, these terms are the data we would record if we were able to separate the data contributions from each emitter before the correlation operation was performed. The second term

$$d_C(s,t) = \int e^{-2\pi i f(t - r(s,\mathbf{y},\mathbf{y}')/c_0)} A(s,\mathbf{y},\mathbf{y}') \sum_{n=1}^{N} \sum_{m \neq n} \bar{P}_n(f) P_m(f) \delta(\mathbf{y}' - \mathbf{x_m}) \delta(\mathbf{y} - \mathbf{x_n}) d\mathbf{y} d\mathbf{y}' df \tag{6.23}$$

is then the contribution of the cross terms, that is, those terms wherein a signal from one emitter is cross correlated with the signal from a different emitter. In our previous model we had essentially assumed $d_C(s,t) = 0$. As previously argued, this is likely a good approximation for scenes which can be assumed to contain a variety of emitters transmitting fairly dissimilar signals. However, as we shall see, this model fails to capture reality when highly correlated signals may be present in the target scene.

Our current goal is to consider these cross terms and to make definite statements regarding their contribution to the image under a wide variety of situations. We first motivate this discussion with a few numerical examples. Here we record the signals from several emitters in the scene at each receiver. We then cross correlate the superposition of all such received signals. Finally we backproject the resulting data using our previously derived imaging operator, that is, the operator we constructed assuming that the cross term contribution to the data is zero in each case.

6.2 Numerical Examples

First we consider the case in which the transmitted signals are dissimilar, having different bandwidths, center frequencies, and duty cycles. In this first example we have a scene which contains nine emitters transmitting signals with center frequencies in the range of $10MHz$ to $50MHz$ and bandwidths between $10MHz$ and $20MHz$. We display the resulting data and backprojected images for this scene which result from two differing data collections. First we use our previous model for the data collection, that is assuming the signal contributions are separable before any processing is done. Second, we process the more general model for which we assume such separation is impossible a priori. The resulting images are displayed side by side in figures 6.1a and 6.1b.

The leftmost figure shows the result when our simulation performs the correlation prior to the superposition of the signals, that is assuming that the signals can be separated in the data a priori, thus ensuring that $d_C(s,t) = 0$ by construction. The right hand simulation performs the superposition of the signals prior to the correlation so that our data takes the form $d(s,t) = d_D(s,t) + d_C(s,t)$ where $d_C(s,t)$ is not necessarily zero.

First, we have the recorded forward data sets shown side by side in Figure 6.1. Here it is immediately apparent that when the contribution of the individual emitters cannot be separated a priori the resulting data set is messier and more cumbersome. Indeed in Figure 6.1a the curves of the data from individual emitters are visually discernible along the edges and visual inspection alone suggests the presence of nine emitters in the scene. In Figure 6.1b however, no such conclusions can be drawn due to the presence of the cross term artifacts.

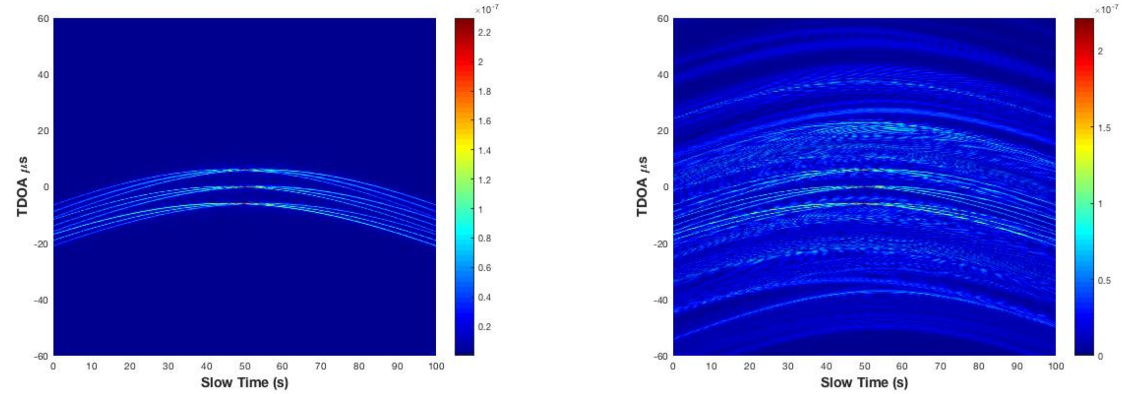

(a) Assuming separability

(b) Cross correlating without separation

Figure 6.1: The total data set for each case

The resulting backprojected images are shown in Figures 6.2a and 6.2b. Here we find that, despite including the contribution to the data set which arises from correlation of different emitters in the scene, the resulting image remains highly accurate with few additional artifacts.

We conclude from this that the prior assumption that the cross terms can be neglected is a fair one for situations in which the emitters in a target scene transmit waveforms which are relatively dissimilar in bandwidth, carrier frequency, and so forth.

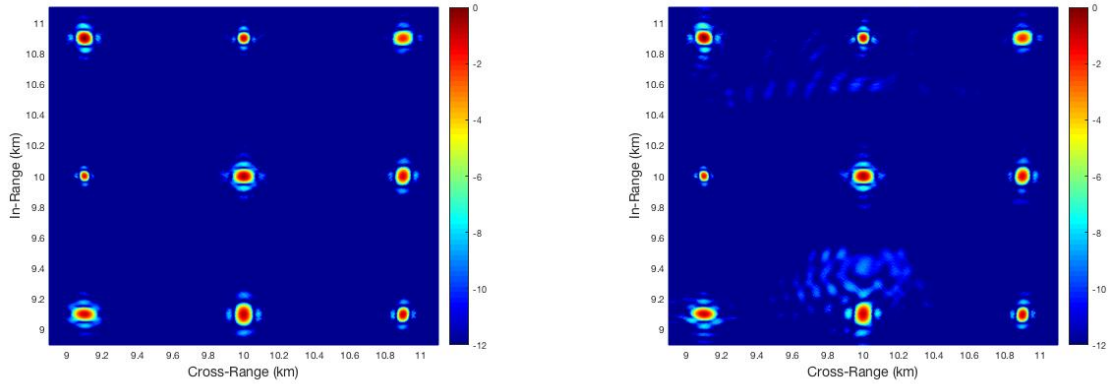

(a) Assuming separability

(b) Cross correlating without separation

Figure 6.2: The backprojected image of the target scene

Recall that we have argued previously that this assumption should accurately reflect the situation in many target scenes. We expect that operators of any emitters in a scene will intentionally transmit waveforms which are different from those transmitted by other operators in the same scene in order to distinguish their own signals from the signals of the surrounding emitters. Were they to do otherwise the utility of their own signals to whatever use they are employing them would be limited.

However, we may ask how the reconstructed image is impacted when several emitters in a scene transmit identical or highly similar waveforms. Below we simulate an example in which nine emitters in a target scene, located at the same points as those in the previous case, emit identical chirps. Since the waveforms are identical and are transmitted simultaneously we expect that the correlation between the signals arriving from different emitters should approximate a worst case scenario providing insight into the limitations of our methods. For this example these chirps have center frequency $f_c = 30MHz$ and bandwidth $b_w = 20MHz$.

The resulting data sets, assuming the signals are separable and not separable respectively, are shown in Figures 6.3a and 6.3b. Once again we see that the cross terms have a significant presence in the dataset when we correlate the signal data without separating contributions from separate emitters.

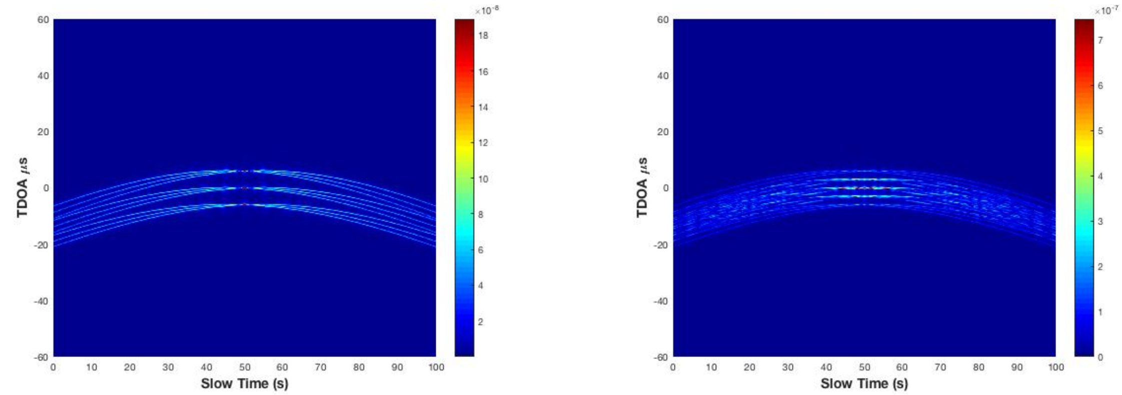

(a) Assuming separability

(b) Cross correlating without separation

Figure 6.3: The total data set for each case

Unlike in the previous example however, the backprojection images which result from the use of the two data sets are significantly different. In Figure 6.4a the emitters are clearly distinguishable and no phantoms or excessive artifacts are present. In Figure 6.4b however, several artifacts and phantom emitters are present in the reconstructed scene and these phantoms appear to be on par with the strength of the true emitters in the scene. Furthermore some of the true emitters appear slightly more blurred more than in Figure 6.4a, and in the locations where emitters overlap phantoms, the emitter strengths are incorrectly increased with respect to the strength of the reconstruction of the emitters along the top and bottom of the scene.

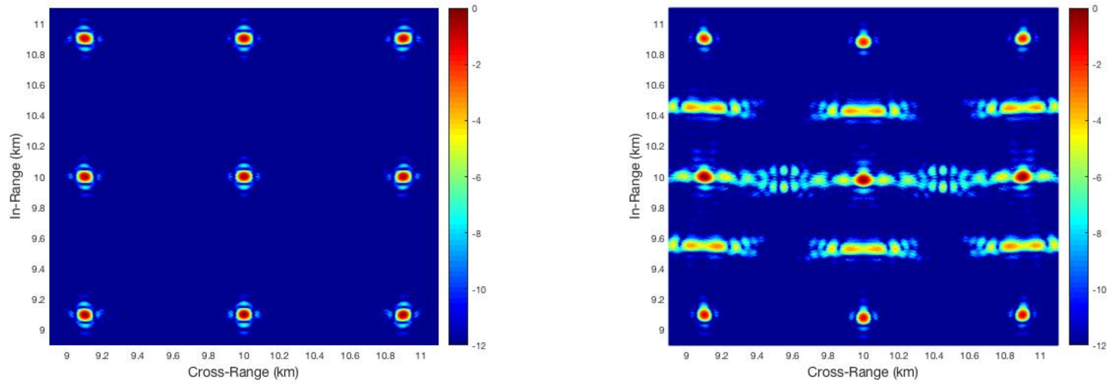

(a) Assuming separability

(b) Cross correlating without separation

Figure 6.4: The backprojected image of the target scene

We conclude that when a scene contains several identical emitters the current method performs poorly in localizing each one without producing additional phantom localizations. We are thus motivated to build a rigorous foundation for the analysis of these cross terms. We are interested in what can be shown regarding where and when they will appear in the image. We will also be interested in any method which can be shown to minimize their strength. This begins by examining what can be said regarding how the cross terms in the data are projected into the image space.

6.3 The Two Emitter Case

We begin with the simplest case in which cross term effects can cause phantoms to appear in the image, that is, the two emitter case. For the general case of two point-like emitters located at $\mathbf{e_1}, \mathbf{e_2}$ in the scene transmitting arbitrary waveforms our data model takes the form

$$d(s,t) = d_D(s,t) + d_C(s,t) \tag{6.24}$$

$$\begin{aligned} &= \int e^{-2\pi i f(t - r(s,\mathbf{y},\mathbf{y})/c_0)} A(s,\mathbf{y},\mathbf{y}) \sum_{n=1}^{2} |P_n(f)|^2 \delta(\mathbf{y} - \mathbf{e_n}) d\mathbf{y} df \\ &+ \int e^{-2\pi i f(t - r(s,\mathbf{y},\mathbf{y}')/c_0)} A(s,\mathbf{y},\mathbf{y}') \sum_{n=1}^{2} \sum_{m \neq n} \bar{P}_n(f) P_m(f) \delta(\mathbf{y}' - \mathbf{e_m}) \delta(\mathbf{y} - \mathbf{e_n}) d\mathbf{y} d\mathbf{y}' df. \end{aligned} \tag{6.25}$$

So the cross term data contribution takes the form

$$\begin{aligned} d_C(s,t) = &\int e^{-2\pi i f(t - r(s,\mathbf{y},\mathbf{y}')/c_0)} A(s,\mathbf{y},\mathbf{y}') \\ &\times \left(\bar{P}_1(f) P_2(f) \delta(\mathbf{y}' - \mathbf{e_1}) \delta(\mathbf{y} - \mathbf{e_2}) + \bar{P}_2(f) P_1(f) \delta(\mathbf{y}' - \mathbf{e_2}) \delta(\mathbf{y} - \mathbf{e_1}) \right) d\mathbf{y} d\mathbf{y}' df. \end{aligned} \tag{6.26}$$

Our two primary concerns with regards to the creation of phantoms in the SASL image will be: their location and their strength relative to that of the emitters. We first consider the phantom location.

If we consider each term in $d_C(s,t)$ individually we note that integration in the first term produces the phase expression

$$\phi_{e_1e_2} = -2\pi i f \left(t - \frac{|\gamma_2(s) - \mathbf{e_2}|}{c_0} + \frac{|\gamma_1(s) - \mathbf{e_1}|}{c_0} \right). \tag{6.27}$$

If we compare this to the phase in the term from $d_E(s,t)$ which is due to the emitter at $\mathbf{e_2}$ we have instead

$$\phi_{e_2} = -2\pi i f \left(t - \frac{|\gamma_2(s) - \mathbf{e_2}|}{c_0} + \frac{|\gamma_1(s) - \mathbf{e_2}|}{c_0} \right). \tag{6.28}$$

The data term due to $\mathbf{e_2}$ can thus be thought of as the line integral of the source power spectrum $|P_2(f)|^2$ over the hyperbola of TDOA defined by the emitter location $\mathbf{e_2}$ with foci $\gamma_1(s), \gamma_2(s)$. This leads to an interpretation of the data term due to the cross correlation of the signals from $\mathbf{e_1}$ and $\mathbf{e_2}$ as the line integral of the product $\bar{P}_2(f)P_1(f)$ over some hyperbola defined by the location of the two emitters and two receivers for that particular slow time look.

We thus expect that when the backprojection is performed, the data due to the $\mathbf{e_2}$ term will then be projected onto the hyperbola described by ϕ_{e_2}. As previously discussed, all such hyperbolas interfere constructively in the location of the emitter leading to a synthetic aperture image of the target emitter. We further expect that the cross term data will be projected onto this other hyperbola ϕ_{e_1,e_2}, along which no emitter is present, which will lead to the creation of a phantom in the final image if the projections of several slow time looks overlap along these cross term hyperbolas and the magnitude of the cross terms being projected is high compared to the true emitter terms.

Thus, taking our image coordinate to be $\mathbf{z}$, we expect the phantom backprojection for a single slow time sample will thus be onto the hyperbola

$$|\gamma_2(s) - \mathbf{z}| - |\gamma_1(s) - \mathbf{z}| = |\gamma_2(s) - \mathbf{e_2}| - |\gamma_1(s) - \mathbf{e_1}|. \tag{6.29}$$

6.4 Formation of the Image

We turn now to the derivation and analysis of the back projection operator which shall act on our data to form the final image. We begin our analysis by forming a filtered backprojection operator L to create the image I from the collected data $d(s,t)$.

$$I(\mathbf{z}) = L[d](\mathbf{z}) = \int e^{i2\pi(t-r(s,\mathbf{z},\mathbf{z})/c_0)} Q(s,f,\mathbf{z}) d(s,t) ds dt df \tag{6.30}$$

Substituting our expression for $d(s,t)$ into (6.30) we have

$$I(\mathbf{z}) = \int e^{i2\pi(t-r(s,\mathbf{z},\mathbf{z})/c_0)} e^{-2\pi i f'(t-r(s,\mathbf{y},\mathbf{y}')/c_0)} Q(s,f,\mathbf{z}) A(s,\mathbf{y},\mathbf{y}') \bar{J}(\mathbf{y},f') J(\mathbf{y}',f') d\mathbf{y} d\mathbf{y}' df ds dt df'. \tag{6.31}$$

Here we make an assumption that the product of the source terms may be written as

$$\bar{J}(\mathbf{y},f') J(\mathbf{y}',f') = T(\mathbf{y},\mathbf{y}') B(f'). \tag{6.32}$$

The justification for this assumption and its effects will be laid out below. For the moment we consider the function $T(\mathbf{y},\mathbf{y}')$ to be the source density function we wish to reconstruct for our image. We will reconsider this choice in 6.6.2. However, we first demonstrate that the backprojection operator can be put into a pseudodifferential operator form, and thus benefit from the results of microlocal analysis when considering the source to be the cross term contaminated product $\bar{J}(\mathbf{y},f')J(\mathbf{y}',f')$.

Carrying out the integration in t we have

$$I(\mathbf{z}) = \int e^{i2\pi(f' r(s,\mathbf{y},\mathbf{y}') - f r(s,\mathbf{z},\mathbf{z}))/c_0} Q(s,f,\mathbf{z}) A(s,\mathbf{y},\mathbf{y}') T(\mathbf{y},\mathbf{y}') B(f') \delta(f-f') d\mathbf{y} d\mathbf{y}' df df' ds \tag{6.33}$$

$$= \int e^{i2\pi \frac{f}{c_0}(r(s,\mathbf{y},\mathbf{y}') - r(s,\mathbf{z},\mathbf{z}))} Q(s,f,\mathbf{z}) A(s,\mathbf{y},\mathbf{y}') T(\mathbf{y},\mathbf{y}') B(f) d\mathbf{y} d\mathbf{y}' df ds. \tag{6.34}$$

The kernel of this operator is then

$$K(\mathbf{y},\mathbf{y}',\mathbf{z}) = \int e^{i2\pi \frac{f}{c_0}(r(s,\mathbf{y},\mathbf{y}') - r(s,\mathbf{z},\mathbf{z}))} Q(s,f,\mathbf{z}) A(s,\mathbf{y},\mathbf{y}') B(f) df ds. \tag{6.35}$$

As in the previous case, we would like to choose the filter Q so that K is as close to a delta function as possible. That is, we hope to find a choice of Q so that $K \approx \int e^{i2\pi(x-z)\cdot\xi} d\xi$ at least around those points which contribute most to the image $I(\mathbf{z})$.

6.5 Forming an FIO Model of the Data via Change of Variables

We first must tackle the problem that the phase of K is a function of more than 3 variables. In this section we will consider a change of variables into an elliptic coordinate system by noting that $|\gamma_1(s) - \mathbf{y}| - |\gamma_2(s) - \mathbf{y}'|$ defines a family of hyperbolas in the plane. That is, for each fixed $\gamma_1(s), \gamma_2(s), \mathbf{y}$ the variable $\mathbf{y}'$ defines a unique hyperbola.

By performing this change of variables we will be able to demonstrate that the collected data can be put into the form of a Fourier Integral Operator (FIO) which will make the data amenable to micro local analysis. It is hoped that this form of the data will provide useful insights into the behavior of cross term effects. However, we will see that, due to the presence of the Jacobian which arises from the change of variables, the imaging operator is largely intractable under this change of variables.

However, this will be to our benefit as we only desire to reconstruct the emitter locations correctly in the image and are not interested in an operator which focuses the effects of the cross terms. In section 6.7 we shall return to the data model and demonstrate that this same analysis can be performed without the following change of variables if we consider only the diagonal terms as desirable data and form a backprojection operator without considering it's effect on the cross term contributions.

In chapter 7 we will then examine how the cross terms are backprojected into the image using this 'diagonal terms only' model to formulate the imaging operator. It is hoped that in the course of future work greater insight into the cross term effects can be gained by connecting the insights from the change of variables model to the more useful and mathematically tractable diagonal terms only filter which is derived in section 6.7 and used throughout the rest of this document.

To this end we begin our analysis of the data by performing the change of variables $(\mathbf{y},\mathbf{y}') \to (\mathbf{u},\mathbf{v})$ defined by

$$|\gamma_2(s)-\mathbf{y}| - |\gamma_1(s)-\mathbf{y}'| = |\gamma_2(s)-\mathbf{u}| - |\gamma_1(s)-\mathbf{u}| \tag{6.36}$$

$$|\gamma_2(s)-\mathbf{y}| + |\gamma_1(s)-\mathbf{y}'| = |\gamma_2(s)-\mathbf{v}| + |\gamma_1(s)-\mathbf{v}|. \tag{6.37}$$

Credit for the idea to use this change of variables to examine the FIO form of the operator goes to Dr. James Given of NRL [39].

The PSF can then be written as

$$\begin{aligned} K(\mathbf{u},\mathbf{v},\mathbf{z}) &= \int e^{i2\pi\frac{f}{c_0}(|\gamma_2(s)-\mathbf{u}|-|\gamma_1(s)-\mathbf{u}|-|\gamma_2(s)-\mathbf{z}|+|\gamma_1(s)-\mathbf{z}|)} \\ &\quad \times Q(s,f,\mathbf{z})A(s,\mathbf{u},\mathbf{v})B(f)\mathcal{J}[(\mathbf{y},\mathbf{y}')\to(\mathbf{u},\mathbf{v})]df\,ds \end{aligned} \tag{6.38}$$

$$= \int e^{i2\pi\frac{f}{c_0}(r(s,\mathbf{u},\mathbf{u})-r(s,\mathbf{z},\mathbf{z}))}Q(s,f,\mathbf{z})A(s,\mathbf{u},\mathbf{v})B(f)\mathcal{J}[(\mathbf{y},\mathbf{y}')\to(\mathbf{u},\mathbf{v})]df\,ds. \tag{6.39}$$

Where $\mathcal{J}[(\mathbf{y},\mathbf{y}' \to (\mathbf{u},\mathbf{v})]$ is the Jacobian due to the change of variables. We can then seek the critical points of K, that is, those points which most contribute to the value of the integral, by performing a Stationary Phase analysis. We introduce the large parameter β by writing $f = \beta\tilde{f}$ so that

$$K(\mathbf{u},\mathbf{v},\mathbf{z}) = \int e^{i2\pi\beta\tilde{f}(r(s,\mathbf{u},\mathbf{u})-r(s,\mathbf{z},\mathbf{z}))/c_0}Q(s,f,\mathbf{z})A(s,\mathbf{u},\mathbf{v})B(f)\mathcal{J}[(\mathbf{y},\mathbf{y}')\to(\mathbf{u},\mathbf{v})]df\,ds \tag{6.40}$$

is a rapidly oscillating integral.

The largest contribution to K then comes from the critical points at which the phase is stationary. These are the points satisfying

$$\frac{d}{df}\phi(s,f) = \frac{2\pi}{c_0}\left[r(s,\mathbf{u},\mathbf{u}) - r(s,\mathbf{z},\mathbf{z})\right] = 0 \tag{6.41}$$

$$\frac{d}{ds}\phi(s,f) = \frac{2\pi f}{c_0}\left[h(s,\mathbf{u},\mathbf{u}) - h(s,\mathbf{z},\mathbf{z})\right] = 0 \tag{6.42}$$

where

$$h(s,\mathbf{u},\mathbf{u}) = \frac{\gamma_1(s)-\mathbf{u}}{|\gamma_1(s)-\mathbf{u}|}\cdot\dot{\gamma}_1(s) - \frac{\gamma_2(s)-\mathbf{u}}{|\gamma_2(s)-\mathbf{u}|}\cdot\dot{\gamma}_2(s). \tag{6.43}$$

The condition in equation (6.41) amounts to a statement that the points $\mathbf{u}$ and $\mathbf{z}$ must lie on the same TDOA curve. This is easily shown by conversion to an elliptic coordinate system. Taking the receiver locations $\gamma_1(s), \gamma_2(s)$ as our foci we define the change of coordinates

$$u_1 = a\cosh(\mu_u)cos(\nu_u) = a\sigma_u\tau_u \tag{6.44}$$

$$u_2 = a\sinh(\mu_u)sin(\nu_u) = a\sqrt{(\sigma_u^2-1)(1-\tau_u^2)} \tag{6.45}$$

with $\mathbf{z} \to (\sigma_z, \tau_z)$ defined analogously. Then

$$r(s,\mathbf{u},\mathbf{u}) = r(s,\mathbf{z},\mathbf{z}) \Longrightarrow 2a\tau_u = 2a\tau_z \tag{6.46}$$

where the curves of constant τ form hyperbolas in the plane. [40]

Thus, the TDOA at the platform locations $\gamma_1(s), \gamma_2(s)$ must be the same for $\mathbf{u}$ as for $\mathbf{z}$ for each critical point.

The condition

$$h(s,\mathbf{u},\mathbf{u}) = h(s,\mathbf{z},\mathbf{z}) \tag{6.47}$$

can be rewritten as

$$\hat{R}_1(\mathbf{u})\cdot\mathbf{v}_1 - \hat{R}_2(\mathbf{u})\cdot\mathbf{v}_2 = \hat{R}_1(\mathbf{z})\cdot\mathbf{v}_1 - \hat{R}_2(\mathbf{z})\cdot\mathbf{v}_2 \tag{6.48}$$

where $\hat{R}$ is the unit vector from the receiving platform to the target point and $\mathbf{v}$ is the platform velocity. Note that we have used $\mathbf{v}$ as a spatial variable and $\mathbf{v}_i$ as a velocity. The subscript will thus denote the velocity and no subscript will denote the spatial variable. The two instances are not used together in our equations, so there should be no chance for confusion as to which is meant.

Here $\hat{R} \cdot \mathbf{v}_i$ is the down range component of the velocity for for the i^{th} platform which gives rise to a Doppler shift in the transmitted signal. Thus the condition in equation (6.42) amounts to a statement that the difference in the Doppler shifts at each platform from $\mathbf{u}$ and $\mathbf{z}$ must be the same. That is, (6.42) is a condition on the Frequency Difference of Arrival or FDOA.

While the isodoppler curves for an arbitrary flight path can be quite complicated the situation is considerably more straightforward for the case in which one receiver is stationary. If we take $\gamma_1(s) \equiv (u_1, u_2)$ constant then the condition simplifies to

$$\hat{R}_2(\mathbf{u}) \cdot \mathbf{v}_2 = \hat{R}_2(\mathbf{z}) \cdot \mathbf{v}_2. \tag{6.49}$$

Therefore the critical points must lie on the curves defined by

$$\hat{R}_2(\mathbf{u}) \cdot \mathbf{v}_2 = c \tag{6.50}$$

for c is some constant.

We assume for the present that the only critical point is then $\mathbf{u} = \mathbf{z}$. We then desire that in the neighborhood of $\mathbf{u} = \mathbf{z}$ the PSF behaves like $\int e^{i2\pi(\mathbf{u}-\mathbf{z})\cdot\xi}$. We thus perform the Stolt change of variables seen previously by writing

$$f(r(s, \mathbf{u}, \mathbf{u}) - r(s, \mathbf{z}, \mathbf{z})) = (\mathbf{u} - \mathbf{z}) \cdot \Xi(\mathbf{u}, \mathbf{z}, s, f) \tag{6.51}$$

where

$$\Xi(\mathbf{u}, \mathbf{z}, s, f) = \int \nabla r(s, \mathbf{z} + \mu(\mathbf{u} - \mathbf{z})) d\mu \tag{6.52}$$

and defining

$$(f, s) \longrightarrow \xi = \frac{f}{c_0} \Xi(\mathbf{u}, \mathbf{z}, s, f). \tag{6.53}$$

Our Point Spread Function is then

$$K(\mathbf{u},\mathbf{v},\mathbf{z}) = \int e^{i2\pi(\mathbf{u}-\mathbf{z})\cdot\xi} Q(\xi(s),\xi(f),\mathbf{z})A(\xi(s),\mathbf{u},\mathbf{v})B(\xi(f))\mathcal{J}[(\mathbf{y},\mathbf{y}') \to (\mathbf{u},\mathbf{v})]\eta^{-1}d\xi \tag{6.54}$$

where

$$\eta^{-1} = \left|\frac{\partial(f,s)}{\partial\xi}\right| \tag{6.55}$$

is the reciprocal of the Belkin determinant as seen previously.

The imaging operator is then approximately

$$\begin{aligned} I(\mathbf{z}) \approx \int & e^{i2\pi(\mathbf{u}-\mathbf{z})\cdot\xi} Q(\xi(s),\xi(f),\mathbf{z})A(\xi(s),\mathbf{u},\mathbf{v}) \\ & \times B(\xi(f))\mathcal{J}[(\mathbf{y},\mathbf{y}') \to (\mathbf{u},\mathbf{v})]\eta^{-1}V(\mathbf{u},\mathbf{v})d\xi d\mathbf{u}d\mathbf{v}. \end{aligned} \tag{6.56}$$

As before we shall base our choice of the filter Q off of this estimate of the image I.

6.6 Determination of the Filter

As previously stated, we desire to have the PSF approximate a delta function near the critical points so that the singularities in the image are reconstructed as sharply as possible. To this end we desire to chose Q so that the factors in the PSF multiple to equal 1. That is, we desire to choose Q so that it is nearly the reciprocal of the other factors in the PSF.

However, the simple choice of

$$Q(\xi(s),\xi(f),\mathbf{z}) = \frac{1}{A(\xi(s),\mathbf{u},\mathbf{v})B(\xi(f))\mathcal{J}[(\mathbf{y},\mathbf{y}') \to (\mathbf{u},\mathbf{v})]\eta^{-1}} \tag{6.57}$$

has three problems.

First, the function A is a function of the scene variables $\mathbf{u},\mathbf{v}$ while the filter Q is a function of the image point $\mathbf{z}$. The second is that there are regions where the function A is zero. These include any regions outside of the observed scene. Finally, the function $B(f)$ is not known to the operator forming the filter.

We first consider the problem of the unknown function $B(f)$. While $B(f)$ is not known, the frequency content of the signals which it represents can be estimated from the collected data.

Recall that we have assumed a data model in which

$$\bar{J}(\mathbf{y}, f)J(\mathbf{y}', f) = T(\mathbf{y}, \mathbf{y}')B(f). \tag{6.58}$$

However, using the antenna model of the source function we have

$$\bar{J}(\mathbf{y}, f)J(\mathbf{y}', f) = \sum_{n=1}^{N}\sum_{m=1}^{n} \bar{P}_n(f)P_m(f)\delta(\mathbf{y} - \mathbf{y_n})\delta(\mathbf{y}' - \mathbf{y_m}). \tag{6.59}$$

So we expect the function $B(f)$ in our model to behave like

$$B(f) \approx \sum_{n=1}^{N}\sum_{m=1}^{M} \bar{P}_n(f)P_m(f). \tag{6.60}$$

We cannot know the sum in equation (6.60) since the signal waveforms are unknown and beyond our control. However, we can gain an insight into this problem by examining what can be determined regarding $B(f)$ in the single emitter case.

6.6.1 Estimating emitter power spectral density

If only one emitter, located at $\mathbf{y_0}$, is present in the scene transmitting the waveform $P(f)$ then the cross correlated data takes the form

$$\begin{aligned} d(s,t) &= \int e^{-2\pi i f(t - r(s,\mathbf{y},\mathbf{y}')/c_0)} A(s,\mathbf{y},\mathbf{y}')|P(f)|^2\delta(\mathbf{y}-\mathbf{y_0})\delta(\mathbf{y}'-\mathbf{y_0})d\mathbf{y}d\mathbf{y}'df & (6.61)\\ &= \int e^{-2\pi i f(t - r(s,\mathbf{y},\mathbf{y})/c_0)} A(s,\mathbf{y},\mathbf{y})B(f)T(\mathbf{y})d\mathbf{y}df. & (6.62)\end{aligned}$$

The signal recorded at one receiver is given by

$$s_1(s,t) = \int e^{-i2\pi f(t - |\gamma_1(s) - \mathbf{y}|/c_0)} \frac{P(f)\delta(\mathbf{y}-\mathbf{y_0})}{4\pi|\gamma_1(s) - \mathbf{y}|} d\mathbf{y}df. \tag{6.63}$$

We may then take the autocorrelation of this signal. Denoting the autocorrelation by $\mathcal{A}$ we have

$$\begin{aligned}\mathcal{A}(s,t) = s_1(s,t) \star s_1(s,t) = \int & e^{i2\pi f(\tau - |\gamma_1(s)-\mathbf{y}|/c_0)} e^{-i2\pi f'(t+\tau-|\gamma_1(s)-\mathbf{y}|/c_0)} \\ & \times \frac{\bar{P}(f)\delta(\mathbf{y}-\mathbf{y_0})}{4\pi|\gamma_1(s)-\mathbf{y}|} \frac{P(f)\delta(\mathbf{y}'-\mathbf{y_0})}{4\pi|\gamma_1(s)-\mathbf{y}'|} d\mathbf{y}' d\mathbf{y} df df' d\tau\end{aligned} \tag{6.64}$$

$$= \int e^{i2\pi f(-|\gamma_1(s)-\mathbf{y}|/c_0)} e^{-i2\pi f(t-|\gamma_1(s)-\mathbf{y}|/c_0)} \frac{|P(f)|^2 \delta(\mathbf{y}-\mathbf{y_0})}{(4\pi|\gamma_1(s)-\mathbf{y}|)^2} d\mathbf{y} df \tag{6.65}$$

$$= \int e^{-i2\pi f t} \frac{B(f)}{(4\pi|\gamma_1(s)-\mathbf{y_0}|)^2} df = \mathcal{F}^{-1}\left\{ \frac{B(f)}{(4\pi|\gamma_1(s)-\mathbf{y_0}|)^2} \right\}. \tag{6.66}$$

Thus,

$$\mathcal{F}\left\{\mathcal{A}(s,t)\right\} = \frac{B(f)}{(4\pi|\gamma_1(s)-\mathbf{y_0}|)^2}. \tag{6.67}$$

Note that we have carried out the integrations of the two delta functions, which are over different variables $\mathbf{y}$ and $\mathbf{y}'$. Since the variables of integration are different in each delta function the difficulties involved with the theoretical question of the mathematical meaning of a squared delta function never arises.

We see that in the single emitter case, $B(f)$ can be extracted from the signal data by Fourier transforming the autocorrelation function. The factor $(4\pi|\gamma_1(s)-\mathbf{y_0}|)^2$ is constant for a single slow time look and can be treated as a simple scale factor which is absorbed into the data. Additionally, in the case that the first receiver is stationary, $\gamma_1(s) =$ constant, the scale factor is constant over all slow time looks.

We generalize the results obtained above for the case of several emitters in the scene. Autocorrelation of the signal recorded at one receiver produces

$$\begin{aligned}\mathcal{A}(s,t) = \int e^{-i2\pi f t} & \left(\sum_{n=1}^{N} \frac{|P_n(f)|^2 \delta(\mathbf{y}-\mathbf{y_n})}{(4\pi|\gamma_1(s)-\mathbf{y}|)^2} \right. \\ & \left. + \sum_{n=1}^{N} \sum_{m\neq n} \frac{\bar{P}_n(f) P_m(f) \delta(\mathbf{y}-\mathbf{y_n}) \delta(\mathbf{y}'-\mathbf{y_m})}{(4\pi)^2|\gamma_1(s)-\mathbf{y}||\gamma_2(s)-\mathbf{y}'|} \right) d\mathbf{y} d\mathbf{y}' df\end{aligned} \tag{6.68}$$

$$= \mathcal{F}^{-1}\left\{ \sum_{n=1}^{N} \frac{|P_n(f)|^2}{(4\pi|\gamma_1(s)-\mathbf{y_n}|)^2} + \sum_{n=1}^{N}\sum_{m\neq n} \frac{\bar{P}_n(f)P_m(f)}{(4\pi)^2|\gamma_1(s)-\mathbf{y_n}||\gamma_2(s)-\mathbf{y_m}|} \right\}. \tag{6.69}$$

Thus, setting $\tilde{B}(f) = \mathcal{F}\{\mathcal{A}(s,t)\}$ provides a scaled estimate of the spectral content of the signal which can be used to unambiguously define a filter Q to be applied in the imaging operator. While $\tilde{B}(f)$ provides less information for us to construct the filter than does the perfect matched filter employed in traditional SAR we must be satisfied with something less than a perfect estimate of the spectral content since we assume that the emitted waveforms are unknown and inseparable in our recorded data.

We turn now to the second problem with the chosen filter, that the filter is a function of the image variable $\mathbf{z}$ while the geometric spreading factors in A are a function of the scene variables. Recall that the geometric spreading factors take the form

$$A(s,\mathbf{y},\mathbf{y}') = \frac{1}{(4\pi)^2|\gamma_1(s)-\mathbf{y}||\gamma_2(s)-\mathbf{y}'|}. \tag{6.70}$$

Furthermore, we have said that the bulk of the image integral comes from those points satisfying $\mathbf{u} = \mathbf{z}$. Where $\mathbf{u}$ is defined by $|\gamma_2(s)-\mathbf{y}| - |\gamma_1(s)-\mathbf{y}'| = |\gamma_2(s)-\mathbf{u}| - |\gamma_1(s)-\mathbf{u}|$. Thus the critical points satisfy $|\gamma_2(s)-\mathbf{y}| - |\gamma_1(s)-\mathbf{y}'| = |\gamma_2(s)-\mathbf{z}| - |\gamma_1(s)-\mathbf{z}|$. We have already seen in equation (6.20) that those terms which account for true emitter locations, and thus are most desirable to reconstruct correctly, satisfy $\mathbf{y} = \mathbf{y}'$. We thus evaluate the geometric spreading terms for $\mathbf{y} = \mathbf{y}' = \mathbf{z}$ so that we calculate $A(s,\mathbf{z},\mathbf{z})$ for the purposes of determining Q.

Finally, we account for any regions in which the function A is zero by application of a smooth cutoff function $\chi(s,f,\mathbf{z})$ which is equal to one over the data collection manifold and zero outside it. Our filter then takes the form

$$Q(s,f,\mathbf{z}) = \frac{\chi(s,f,\mathbf{z})\eta}{A(s,\mathbf{z},\mathbf{z})\tilde{B}(f)\mathcal{J}[(\mathbf{y},\mathbf{y}') \to (\mathbf{u},\mathbf{v})]} \tag{6.71}$$

The imaging operator then takes the form

$$I(\mathbf{z}) = \int e^{-i2\pi r(s,\mathbf{z},\mathbf{z})/c_0} \frac{\chi(s,f,\mathbf{z})\eta}{A(s,\mathbf{z},\mathbf{z})\tilde{B}(f)\mathcal{J}[(\mathbf{y},\mathbf{y}') \to (\mathbf{u},\mathbf{v})]} D(s,f)dsdf. \tag{6.72}$$

So that we have shown that the backprojection operator can be put into a pseudodifferential form to act on the entire data set $D(s, f)$ with the filter Q chosen as above.

However, this filter was chosen under the assumption that we desire to reconstruct the function $T(\mathbf{y}, \mathbf{y}')$ as accurately as possible. We examine the effect of this through a microlocal analysis of the imaging operators effects on the diagonal and cross terms in the data.

6.6.2 Microlocal Analysis of the Data Terms

We have shown that the imaging operator K can be written in the form of a pseudodifferential operator, abbreviated ΨDO. Pseudodifferential operators have what is known as the *pseudolocal* property. If K is a ψDO then WF$(Ku) \subseteq$ WF(u), where $WF(\cdot)$ denotes the wave front set. Thus singularities are reconstructed in their correct locations provided that they were visible to the receivers during the data collect. [**?**, 2]

We have seen that the operator K can be written as

$$K(\mathbf{z}, \mathbf{u}, \mathbf{v}) = \int e^{i2\pi(\mathbf{u}-\mathbf{z})\cdot\xi} \mathbb{A} d\xi \tag{6.73}$$

where $\mathbb{A}$ contains the filter and other amplitude factors which do not influence the location of the backprojection. Thus we can consider $K \propto \int e^{i2\pi(\mathbf{u}-\mathbf{z})\cdot\xi} d\xi$ sufficient for this portion of our analysis.

When K operates on a diagonal term we have that $T(\mathbf{u}, \mathbf{v}) = T(\mathbf{u}, \mathbf{u})$, so that T does not depend on $\mathbf{v}$, and $\mathbf{u} = \mathbf{y}$ so that the image of the diagonal term, $I_d(\mathbf{z})$, is

$$I_d(\mathbf{z}) \propto \int e^{i2\pi(\mathbf{u}-\mathbf{z})\cdot\xi} T(\mathbf{u}, \mathbf{v}) d\xi d\mathbf{u}\mathbf{v} \tag{6.74}$$

$$= \int e^{i2\pi(\mathbf{y}-\mathbf{z})\cdot\xi} T(\mathbf{y}, \mathbf{y}) d\xi d\mathbf{y} = T(\mathbf{z}, \mathbf{z}). \tag{6.75}$$

Thus, diagonal terms are acted on so that contributions to the data which come from true emitters in the scene are backprojected in the image to reconstruct the emitters in the correct location.

However, when the operator K acts on cross terms the result is different. If we form an image from the first term in the cross term data $d_C(s,t)$ derived above we have

$$I_c(\mathbf{z}) \propto \int e^{i2\pi(\mathbf{u}-\mathbf{z})\cdot\xi} T(\mathbf{u},\mathbf{v}) d\xi = \int T(\mathbf{z},\mathbf{v}) d\mathbf{v}. \tag{6.76}$$

Thus, the contribution to the image from a cross term is not proportional to the value of the source density function at the corresponding point in the scene, but rather is proportional to the integral of T over the variable v for that image point.

This is not a difficulty, indeed this is actually to our benefit. Although the cross correlated data contains both diagonal and cross terms the cross terms merely clutter the image with undesirable phantoms. Our true desire is not to reconstruct the function $T(\mathbf{y},\mathbf{y}')$ containing both real and phantom emitter contributions as accurately as possible, but rather to form an image of the function $V(\mathbf{y})$ containing only the diagonal terms which arise from actual emitter locations. That is, we would like to image the function

$$V(\mathbf{y}) = \sum_{n=1}^{N} |P_n(f)|^2 \delta(\mathbf{y} - \mathbf{e_n}) \tag{6.77}$$

from the data which gives us $T(\mathbf{y},\mathbf{y}')$. Since V is merely the diagonal terms of T the two functions are related by $T(\mathbf{y},\mathbf{y}') = V(\mathbf{y}) +$ cross terms.

6.7 The Diagonal Terms Filter

We can thus return to our previous work demonstrating that the data can be written as $d(s,t) = d_D(s,t) + d_C(s,t)$ to formulate a filter which is best suited to the imaging of the diagonal terms. We do this by taking $d_D(s,t)$ to be the data we desire to collect and treat the cross term data $d_C(s,t)$ as a nonrandom noise-like term that produces undesirable corruptions in the image, rather than as a portion of a source function to be reconstructed. We write

$$I(\mathbf{z}) = \int e^{i2\pi(t-r(s,\mathbf{z}))}Q(s,f,\mathbf{z})\left[d_D(s,t)+d_C(s,t)\right]dsdt \tag{6.78}$$

$$= \int e^{i2\pi(t-r(s,\mathbf{z}))}Q(s,f,\mathbf{z})d_D(s,t)dsdt + \int e^{i2\pi(t-r(s,\mathbf{z}))}Q(s,f,\mathbf{z})d_C(s,t)dsdt. \tag{6.79}$$

Then, under the previous assumptions we have

$$I(\mathbf{z}) = \int K(\mathbf{y},\mathbf{z})V(\mathbf{y})d\mathbf{y} + \int K(\mathbf{y},\mathbf{z})[\text{cross terms}]d\mathbf{y} \tag{6.80}$$

where

$$K(\mathbf{y},\mathbf{z}) = \int e^{i2\pi\frac{f}{c_0}(r(s,\mathbf{y})-r(s,\mathbf{z}))}Q(s,f,\mathbf{z})A(s,\mathbf{y})B(f)dfds. \tag{6.81}$$

As before we seek to define Q so that K is as close as possible to a delta function so that we may reconstruct $V(\mathbf{y})$ as accurately as possible. Taking $\mathbf{y}$ in place of $\mathbf{u}$ in our previous stationary phase argument we find that our critical points must satisfy

$$r(s,\mathbf{y}) = r(s,\mathbf{z}) \tag{6.82}$$

$$\hat{R}_1(\mathbf{y})\cdot\mathbf{v}_1 - \hat{R}_2(\mathbf{y})\cdot\mathbf{v}_2 = \hat{R}_1(\mathbf{z})\cdot\mathbf{v}_1 - \hat{R}_2(\mathbf{z})\cdot\mathbf{v}_2. \tag{6.83}$$

These curves can be quite complicated for an arbitrary flight path. For the case $\gamma_1(s) = \mathbf{x_0}$, for some constant $\mathbf{x_0}$, these critical points then lie at the intersection of the hyperbolas defined by $r(s,\mathbf{y}) = r(s,\mathbf{z})$ and the curves $\hat{R}_2(\mathbf{y})\cdot\mathbf{v}_2 = \hat{R}_2(\mathbf{z})\cdot\mathbf{v}_2$, where $\hat{R}_2(\mathbf{y})$ is the unit vector in the direction of $\mathbf{y}$ from the platform whose flightpath is $\gamma_2(s)$.

For example, in the flight path which we have been simulating the moving receiver travels along the x-axis so that the y components of both the position vector $\gamma_2(s)$ and $\mathbf{v_2}$ are zero. With $\gamma_1(s)$ held constant as well the FDOA condition reduces to

$$\frac{(\gamma_{2x}(s)-y_x)v_{2x}}{|\gamma_2(s)-\mathbf{y}|} = \frac{(\gamma_{2x}(s)-z_x)v_{2x}}{|\gamma_2(s)-\mathbf{z}|}. \tag{6.84}$$

Here $\gamma_{2x}(s)$ is the x component of the flight path and y_x is the x component of the two dimensional scene variable $\mathbf{y}$. Under these conditions the TDOA and FDOA are far simpler. We plot two examples of these curves for a receive position corresponding to $\gamma_2(s) = (7.5, 0)$ and $\gamma_2(s) = (17, 0)$ in Figure 6.5.

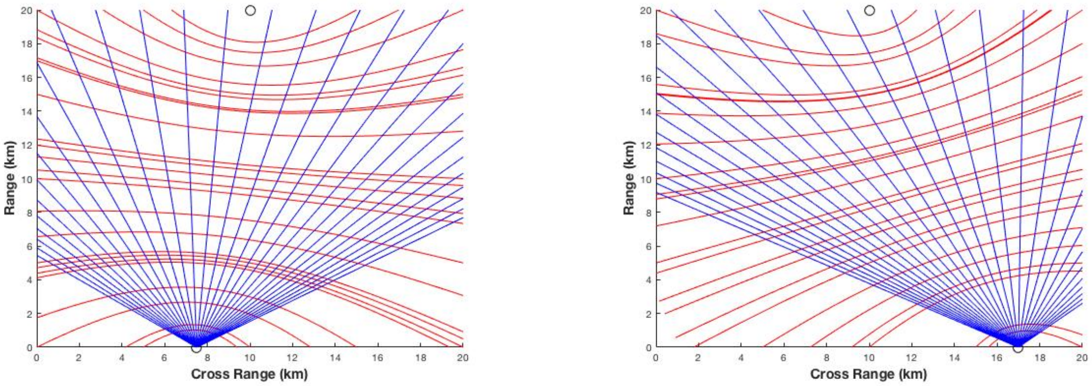

(a) The TDOA and FDOA curves for $\gamma_2(s) = (7.5, 0)$ **(b)** The TDOA and FDOA curves for $\gamma_2(s) = (17, 0)$

Figure 6.5: The TDOA Curves (Red) and FDOA Curves (Blue) for two different points along the flight path of the moving receiver. The circles denote receiver positions.

From Figure 6.5 it is clear that the only point of intersection of the two sets of curves which lies in our target scene is the point $\mathbf{y} = \mathbf{z}$. Although the TDOA and FDOA curves can be far more difficult to plot for a complex flight path we assume for the present that this critical point condition will hold for more complicated sets of curves as well.

As before, we desire that K behave like a delta function near these critical points. To this end we apply the Stolt change of variables previously discussed. Doing so puts K into the form of a ΨDO, provided that A satisfies the symbol estimate. Taking η to be the Beylkin determinant we have

$$K(\mathbf{y}, \mathbf{z}) = \int e^{i2\pi(\mathbf{y}-\mathbf{z})\cdot\xi} Q(s, f, \mathbf{z}) A(s, \mathbf{y}) B(f) \eta^{-1} d\xi. \tag{6.85}$$

We then choose Q to be the reciprocal of all of the non-phase factors in the integrand so that their product will be approximately equal to unity in those regions near a critical point. As before, to accomplish this we evaluate A at the point $\mathbf{y} = \mathbf{z}$ and we make the substitution $B(f) \approx \tilde{B}(f)$

where $\tilde{B}$ is the measured power spectrum of the recorded signals. Our filter is then

$$Q(s, f, \mathbf{z}) = \frac{\chi(s, f, \mathbf{z})\eta}{A(s, \mathbf{z})\tilde{B}(f)} \tag{6.86}$$

where χ is smooth cut off function preventing division by zero.

Applying this filter to our imaging operator produces

$$I(\mathbf{z}) = \int e^{i2\pi(t-r(s,\mathbf{z}))} \frac{\chi(s, f, \mathbf{z})\eta}{A(s, \mathbf{z})\tilde{B}(f)} D(s, f) ds\, df \tag{6.87}$$

In section 6.6.2 we discovered that the filter we had derived resulted in the imaging operator acting on the data to reconstruct the source function with the correct intensity in those regions where an emitter was located. We can apply the same analysis to this version of the imaging operator.

Using the same method as we did in section 6.6.2 we have

$$I_d(\mathbf{z}) \propto \int e^{i2\pi(\mathbf{y}-\mathbf{z})\cdot\xi} V(\mathbf{y}) d\xi d\mathbf{y} = V(\mathbf{z}) \tag{6.88}$$

Thus, K acts on $D_D(s, t)$ to reconstruct the diagonal terms of the data in their correct location and orientation, just as we intended that it should. The analysis of how K acts to backproject the cross terms is, as was alluded to by our results in section 6.6.2, more complicated. It is this subject which we will take up in the next chapter.

Chapter 7

THE EFFECT OF CROSS TERMS IN THE DATA

7.1 Locating the Cross Term Phantoms

Now that we have an expression for the imaging operator to be applied to the data we can return to the question of when and where cross term phantoms appear in the final image. We saw in section 6.6 that the bulk of their contribution to the image occurs at the points $\mathbf{z}$ satisfying $|\gamma_2(s) - \mathbf{y}| - |\gamma_1(s) - \mathbf{y}'| = |\gamma_2(s) - \mathbf{z}| - |\gamma_1(s) - \mathbf{z}|$.

This is consistent with our earlier observation that the cross terms in the data model have the same form as the diagonal emitter terms but with the data collection appearing to take place along hyperbolas defined by $|\gamma_2(s) - \mathbf{y}| - |\gamma_1(s) - \mathbf{y}'| = \text{constant}$. Since every cross term is the result of exactly two emitters in the scene, we can restrict our analysis to the two emitter case. The multi-emitter case then follows easily as the sum over the cross term effects of all pairs of emitters present.

As seen in section 6.3 the cross terms in the data model for a scene containing two emitters are given by

$$\begin{aligned} d_C(s,t) = &\int e^{-2\pi i f(t - r(s,\mathbf{y},\mathbf{y}')/c_0)} A(s,\mathbf{y}) \bar{P}_1(f) P_2(f) \delta(\mathbf{y}' - \mathbf{e_1}) \delta(\mathbf{y} - \mathbf{e_2}) d\mathbf{y} d\mathbf{y}' df \\ &+ \int e^{-2\pi i f(t - r(s,\mathbf{y},\mathbf{y}')/c_0)} A(s,\mathbf{y}) \bar{P}_2(f) P_1(f) \delta(\mathbf{y}' - \mathbf{e_2}) \delta(\mathbf{y} - \mathbf{e_1}) d\mathbf{y} d\mathbf{y}' df. \end{aligned} \tag{7.1}$$

For simplicity we consider just the first term, the analysis of the second term is identical. Additionally, the amplitude terms A and Q do not alter the location of the backprojection and so we neglect them in this analysis. The backprojection operator acts on the first term of $d_C(s,t)$ to yield

$$I(\mathbf{z}) = \int e^{i2\pi \frac{f}{c_0}(r(s,\mathbf{y},\mathbf{y}')-r(s,\mathbf{z},\mathbf{z}))} \bar{P}_1(f)P_2(f)\delta(\mathbf{y}'-\mathbf{e_1})\delta(\mathbf{y}-\mathbf{e_2})d\mathbf{y}d\mathbf{y}'df\,ds. \tag{7.2}$$

$$= \int e^{i2\pi \frac{f}{c_0}(r(s,\mathbf{e_2},\mathbf{e_1})-r(s,\mathbf{z},\mathbf{z}))} \bar{P}_1(f)P_2(f)df\,ds. \tag{7.3}$$

Thus, the cross term phantom results in a backprojected return along the hyperbola

$$|\gamma_2(s)-\mathbf{z}| - |\gamma_1(s)-\mathbf{z}| = |\gamma_2(s)-\mathbf{e_2}| - |\gamma_1(s)-\mathbf{e_1}| \tag{7.4}$$

for each slow time step s. This backprojection will have amplitude $\mathbb{A}_{e_1e_2}(s)$ given by

$$\mathbb{A}_{e_1e_2}(s) = Q(s,f,\mathbf{z})A(s,\mathbf{e_2},\mathbf{e_1})\bar{P}_1(f)P_2(f). \tag{7.5}$$

We note here that the location of the cross term backprojection for a given slow time step is a function of the location of both emitters and both receivers. We have seen in the previous data model that the backprojections interfere constructively in regions in which an emitter is located and destructively elsewhere. We can ask whether a similar process occurs when cross terms are present in the data.

Our analysis of the backprojections of the diagonal and cross terms so far has indicated that, while the diagonal terms will be focused up in the final image regardless of the receiver flightpath, the location of the cross term phantoms depends on receiver trajectory. Thus, over a long flight path, the cross term phantoms should blur out across the image while the diagonal terms will focus up ever more sharply. Thus, over a sufficiently long aperture, the phantom contribution to the image should be reduced well below the level of the diagonal terms using the backprojection scheme devised above.

We first illustrate this phenomenon with a numerical example and then present a proof that the cross term hyperbolas will not result in a focused phantom point while the diagonal terms will focus at the location of the emitter.

In Figure 7.1 we show the hyperbolas for a the flight path we have previously been simulating. That is for $\gamma_2(s)$ beginning at $(0,0)$ and traveling to $(20,0)$ while $\gamma_1(s)$ remains stationary at $(10,20)$. The hyperbolas shown are the backprojection curves from $1.5km$ intervals along this path for the case of the diagonal data term for a single emitter in Figure 7.1a and for a cross term in Figure 7.11b. In both figures the circles indicate the emitter positions.

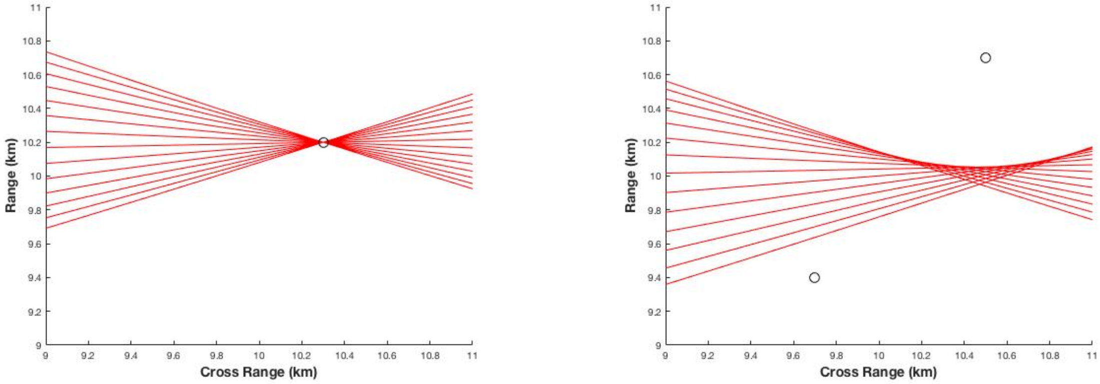

(a) The diagonal backprojections

(b) The cross-term backprojections

Figure 7.1: Backprojection hyperbolas for a diagonal and cross term case

In this example it is clear that, while every diagonal term backprojection intersects at the location of the emitter, none of the cross term backprojections shown cross the location of either of the emitters which produced the cross term in the data. Furthermore, the cross term hyperbolas do not intersect each other at a unique point. Rather their intersections are blurred out over a curve in the image. This would lead to progressively weaker phantom appearance in the image as compared to the emitter image over time.

This leads us to ask whether it can be shown that this behavior occurs in general for all emitter locations and receiver trajectories. To this end we consider the envelope of the family of backprojection hyperbolas for each data term.

7.1.1 The Backprojection Envelope

Mathematically the *envelope* of a family of curves is defined as: *A curve which touches all of the curves of a family and which is touched at every point by a curve of the family.* In simpler terms, the envelope of a family of curves is the limit of the set of all points at which “infinitely close" members of the family intersect each other. For a single parameter family, this means two curves whose single parameter differ only by an infinitesimal ϵ. [41, 42]

Thus, the envelope is not the set of all points at which two members of a family intersect one another. Rather it is the limiting set of the intersection of nearby curves of a family. It is elsewhere defined as the curve which touches all members of a family of one parameter curves tangentially and is touched tangentially at every point by a member of the family. We may also extend this interpretation to the degenerate case in which the ‘curve’ is a single point through which every member of the family passes. [41–43]

If, for some data term, we can demonstrate that the envelope of the family of backprojection curves is a single point, that is, that all such curves overlap at a single location, then those backprojections will constructively interfere in the image producing a strong peak. If, on the other hand, the backprojection curves of another term do not intersect at a single point we will have shown that any phantoms due to the backprojection imaging process from that term will gradually blur out along some curve in the image as the receiver moves along its flight path.

First we note the following theorem: *If the curves of the family $f(x, y, C) = 0$ have no singular points, the curve defined by the system of equations $f(x, y, C) = 0, \quad f'_C(x, y, C) = 0$ is the envelope of the family provided it also has no singular points*. [41–43]

The backprojection hyperbolas for a term in the data collection are the family of curves

$$f(\mathbf{z}, s, \mathbf{e_i}, \mathbf{e_j}) = |\gamma_2(s) - \mathbf{z}| - |\gamma_1(s) - \mathbf{z}| - |\gamma_2(s) - \mathbf{e_i}| + |\gamma_1(s) - \mathbf{e_j}| \tag{7.6}$$

Differentiating with respect to the parameter s we have

$$
\begin{aligned}
f'(\mathbf{z}, s, \mathbf{e_i}, \mathbf{e_j}) = \frac{(\gamma_2(s) - \mathbf{z}) \cdot \dot{\gamma}_2(s)}{|\gamma_2(s) - \mathbf{z}|} - \frac{(\gamma_1(s) - \mathbf{z}) \cdot \dot{\gamma}_1(s)}{|\gamma_1(s) - \mathbf{z}|} \\
- \frac{(\gamma_2(s) - \mathbf{e_i}) \cdot \dot{\gamma}_2(s)}{|\gamma_2(s) - \mathbf{e_i}|} + \frac{(\gamma_1(s) - \mathbf{e_j}) \cdot \dot{\gamma}_1(s)}{|\gamma_1(s) - \mathbf{e_j}|}.
\end{aligned}
\tag{7.7}
$$

Since the first receiver is stationary, $\gamma_1(s)$ is constant and thus $\dot{\gamma}_1(s) = 0$ so that

$$
f'(\mathbf{z}, s, \mathbf{e_i}, \mathbf{e_j}) = \frac{(\gamma_2(s) - \mathbf{z}) \cdot \dot{\gamma}_2(s)}{|\gamma_2(s) - \mathbf{z}|} - \frac{(\gamma_2(s) - \mathbf{e_i}) \cdot \dot{\gamma}_2(s)}{|\gamma_2(s) - \mathbf{e_i}|}. \tag{7.8}
$$

Thus the envelope is the curve satisfying the system of equations given by

$$
|\gamma_2(s) - \mathbf{z}| - |\gamma_1(s) - \mathbf{z}| - |\gamma_2(s) - \mathbf{e_i}| + |\gamma_1(s) - \mathbf{e_j}| = 0 \tag{7.9}
$$

$$
\frac{(\gamma_2(s) - \mathbf{z}) \cdot \dot{\gamma}_2(s)}{|\gamma_2(s) - \mathbf{z}|} - \frac{(\gamma_2(s) - \mathbf{e_i}) \cdot \dot{\gamma}_2(s)}{|\gamma_2(s) - \mathbf{e_i}|} = 0. \tag{7.10}
$$

Note that neither equation has any singular points since we assume that the platform is separated some distance from the scene. Thus $\gamma_2(s) \neq \mathbf{z}$ and $\gamma_2(s) \neq \mathbf{e_i}$. This is required on physical grounds already and not a limitation to the theory.

We define a *focused point* of a family of curves as: a point through which every member of the family passes. We shall first prove that if such a point exists for the family of backprojection hyperbolas in our model then it is unique. Thus, if all the backprojections for a data term constructively interfere at a point they do not constructively interfere at any other point in the scene. Once uniqueness is demonstrated we will examine existence.

For simplicity of notation we shall allow $\mathbf{e_i}$ to refer both to the location of the i^{th} emitter in the scene as well as shorthand to reference the emitter itself and do the same with the receiver located at $\gamma_i(s)$ at slow time step s.

Theorem 1: *Let two receivers observe a scene with one in motion and the other stationary. If the receiver in motion flies any flightpath through or around the target scene for which its velocity vector is not aimed directly at the the stationary receiver then: If the family of hyperbolas, over* *which a data term is backprojected according to the imaging operator defined in equation* (6.87)*, has a* focused point, *that focused point is unique.*

Proof: Let the signals produced by two emitters $\mathbf{e_1}$ and $\mathbf{e_2}$ give rise to a term in the cross correlated data as previously discussed. Let $\mathbf{z_0}$ be a focused point of the family of backprojection hyperbolas formed when this term is filtered and backprojected to form the image as described by equation (6.87). Then, as previously shown, these hyperbolas are described by the one parameter family of equations given by

$$|\gamma_2(s) - \mathbf{z}| - |\gamma_1(s) - \mathbf{z}| = |\gamma_2(s) - \mathbf{e_2}| - |\gamma_1(s) - \mathbf{e_1}|. \tag{7.11}$$

Note here that the argument for the symmetrical case for the cross term in which $\mathbf{e_1}$ and $\mathbf{e_2}$ are interchanged is identical and that the diagonal case $\mathbf{e_1} = \mathbf{e_2}$ is merely a degenerate version of the cross term case. Thus we need only examine this form of the family of hyperbolas in order to exhaust the analysis of the backprojection families for all data terms.

Then,

$$|\gamma_2(s) - \mathbf{z_0}| - |\gamma_1(s) - \mathbf{z_0}| = |\gamma_2(s) - \mathbf{e_2}| - |\gamma_1(s) - \mathbf{e_1}|. \tag{7.12}$$

for all values s by definition of a focused point.

So, $\mathbf{z}_0$ is intersected by every member of the family of curves trivially and so by definition, a member of the envelope of the family.

Since $\mathbf{z_0}$ is an envelope point for every curve in the family and $\dot{\gamma}_1(s) = 0$, $\mathbf{z_0}$ also satisfies,

$$\frac{(\gamma_2(s) - \mathbf{z_0}) \cdot \dot{\gamma}_2(s)}{|\gamma_2(s) - \mathbf{z_0}|} - \frac{(\gamma_2(s) - \mathbf{e_i}) \cdot \dot{\gamma}_2(s)}{|\gamma_2(s) - \mathbf{e_i}|} = 0 \tag{7.13}$$

for all s, due to the envelope theorem given above.

Now, assume there exists another point in the image $\mathbf{z_1} \neq \mathbf{z_0}$, which is is also focused point for the envelope of the family. Then

$$|\gamma_2(s_1) - \mathbf{z_1}| - |\gamma_1(s_1) - \mathbf{z_1}| = |\gamma_2(s_1) - \mathbf{e_2}| - |\gamma_1(s_1) - \mathbf{e_1}| \tag{7.14}$$

and

$$|\gamma_2(s_2) - \mathbf{z_1}| - |\gamma_1(s_2) - \mathbf{z_1}| = |\gamma_2(s_2) - \mathbf{e_2}| - |\gamma_1(s_2) - \mathbf{e_1}| \tag{7.15}$$

for some value of s_1 which is a particular realization of s, and s_2, the slow time data collection point succeeding s_1. This must be true since, by definition of the focused point, $\mathbf{z_1}$ must lie on all hyperbolas in the family. Furthermore,

$$\frac{(\gamma_2(s_1) - \mathbf{z_1}) \cdot \dot{\gamma}_2(s_1)}{|\gamma_2(s_1) - \mathbf{z_1}|} - \frac{(\gamma_2(s_1) - \mathbf{e_2}) \cdot \dot{\gamma}_2(s_1)}{|\gamma_2(s_1) - \mathbf{e_2}|} = 0 \tag{7.16}$$

for some value of s_1.

Since $\mathbf{z_0}$ is a focused point, it also satisfies

$$|\gamma_2(s_1) - \mathbf{z_0}| - |\gamma_1(s_1) - \mathbf{z_0}| = |\gamma_2(s_1) - \mathbf{e_2}| - |\gamma_1(s_1) - \mathbf{e_1}| \tag{7.17}$$

$$|\gamma_2(s_2) - \mathbf{z_0}| - |\gamma_1(s_2) - \mathbf{z_0}| = |\gamma_2(s_2) - \mathbf{e_2}| - |\gamma_1(s_2) - \mathbf{e_1}| \tag{7.18}$$

Therefore,

$$|\gamma_2(s_1) - \mathbf{z_0}| - |\gamma_1(s_1) - \mathbf{z_0}| = |\gamma_2(s_1) - \mathbf{z_1}| - |\gamma_1(s_1) - \mathbf{z_1}| \tag{7.19}$$

$$|\gamma_2(s_2) - \mathbf{z_0}| - |\gamma_1(s_2) - \mathbf{z_0}| = |\gamma_2(s_2) - \mathbf{z_1}| - |\gamma_1(s_2) - \mathbf{z_1}| \tag{7.20}$$

Since $\gamma_1(s_1) = \gamma_1(s_2)$ because $\gamma_1(s)$ is constant, it is clear that $|\gamma_1(s_1) - \mathbf{z_0}| = |\gamma_1(s_2) - \mathbf{z_0}|$ and $|\gamma_1(s_1) - \mathbf{z_1}| = |\gamma_1(s_2) - \mathbf{z_1}|$. So that, by subtraction of (7.20) from (7.19) we have

$$|\gamma_2(s_1) - \mathbf{z_0}| - |\gamma_2(s_2) - \mathbf{z_0}| = |\gamma_2(s_1) - \mathbf{z_1}| - |\gamma_2(s_2) - \mathbf{z_1}| \tag{7.21}$$

which may be rewritten as

$$|\gamma_2(s_1) - \mathbf{z_0}| - |\gamma_2(s_1) - \mathbf{z_1}| = |\gamma_2(s_2) - \mathbf{z_0}| - |\gamma_2(s_2) - \mathbf{z_1}|. \tag{7.22}$$

Thus, the difference in the distance from the second receiving platform to each of the points must be equal as the platform moves from $\gamma_2(s_1)$ to $\gamma_2(s_2)$. Since we have postulated that $\mathbf{z_0} \neq \mathbf{z_1}$ the platform must move along some hyperbola with the two focused points as the foci. This can be more clearly seen by setting $|\gamma_2(s_1) - \mathbf{z_0}| - |\gamma_2(s_1) - \mathbf{z_1}| = C$ where C is constant.

Essentially, by setting $|\gamma_2(s_1) - \mathbf{z_0}| - |\gamma_2(s_1) - \mathbf{z_1}|$ equal to a constant we are examining a specific realization of the single point s_1 along the flight path of $\gamma_2(s)$. Thus, with a fixed (but arbitrary) choice for s_1 the condition is

$$|\gamma_2(s) - \mathbf{z_0}| - |\gamma_2(s) - \mathbf{z_1}| = C \tag{7.23}$$

in the region around s_2. Recall $\mathbf{z_0}$ and $\mathbf{z_1}$ are also fixed. Allowing s to vary around s_1 it is clear that this equation traces out a portion of a hyperbola with foci $\mathbf{z_0}$ and $\mathbf{z_1}$ and containing the point $\gamma_2(s_1)$. Thus, in physical terms, this condition constrains the flight path of the moving receiver to some hyperbola in the plane in the region around the time step s_1.

If we allow the perpendicular bisector of the line segment joining $\mathbf{z_0}$ and $\mathbf{z_1}$ to form the x-axis of a new coordinate system and the line between $\mathbf{z_0}$ and $\mathbf{z_1}$ to form the y-axis, the receiving platform must follow a flight path like the examples shows in Figure 7.2.

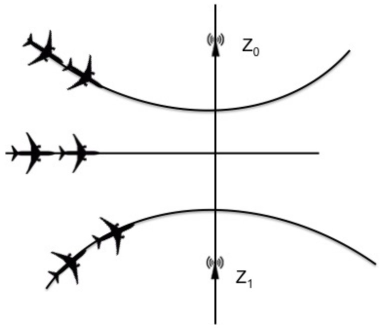

Figure 7.2: The coordinate system defined by the two focused points

It is certainly possible for the moving receiver to fly any other flight path, however, if it does so then we have reached a contradiction and our conclusion is already proven. Thus we assume that the receiver is constrained to such a flight path.

We now take into consideration the effect of the position of the stationary receiver on the existence of the hypothesized second focused point $\mathbf{z}_1$.

In equation (7.19) we demonstrated that a necessary condition for $\mathbf{z_1}$ to be in the envelope of the backprojection family given that $\mathbf{z_0}$ is a focused point is that

$$|\gamma_2(s_1) - \mathbf{z_0}| - |\gamma_1(s_1) - \mathbf{z_0}| = |\gamma_2(s_1) - \mathbf{z_1}| - |\gamma_1(s_1) - \mathbf{z_1}|. \tag{7.24}$$

However, we have now gone further and shown that, for a second focused point to exist, the flight path of the moving receiver must be constrained to one of a family of hyperbolas in the plane. That is, $|\gamma_2(s) - \mathbf{z_0}| - |\gamma_2(s) - \mathbf{z_1}| = C$ for some constant C. Therefore equation (7.19) implies

$$|\gamma_1(s) - \mathbf{z_0}| - |\gamma_1(s) - \mathbf{z_1}| = |\gamma_2(s) - \mathbf{z_0}| - |\gamma_2(s) - \mathbf{z_1}| = C. \tag{7.25}$$

Thus, for $\mathbf{z}_1$ to be a focused point of the family, the stationary receiver $\gamma_1(s)$ must also lie on the same hyperbola that constrains the flight path of $\gamma_2(s)$. In practice this should be easily avoided. However, we can go further and show that of the infinite number of hyperbolas in this family, only the degenerate case, that is, the the case for which $C = 0$ and the 'hyperbola' is actually a straight line flight path pointed directly at the stationary receiver, allows for the existence of a second focused point.

Using the coordinate system set up in figure 7.2, let $\gamma_2(s)$ and $\gamma_1(s)$ be on some hyperbola in the family for some fixed constant C. The data collection for one point along this path is shown graphically in figure 7.3. In this figure the black hyperbola is the flight path of the receiver in motion and the stationary receiver is located at a point on this hyperbola. The location of the stationary receiver is denoted by the radar dish and the location of the moving receiver by the clipart airplane.

Recall that, because $\mathbf{z}_0$ is a focused point of the family of backprojections and therefore lies on every hyperbola in the family, the backprojection hyperbola for any location of $\gamma_2(s)$ is defined by

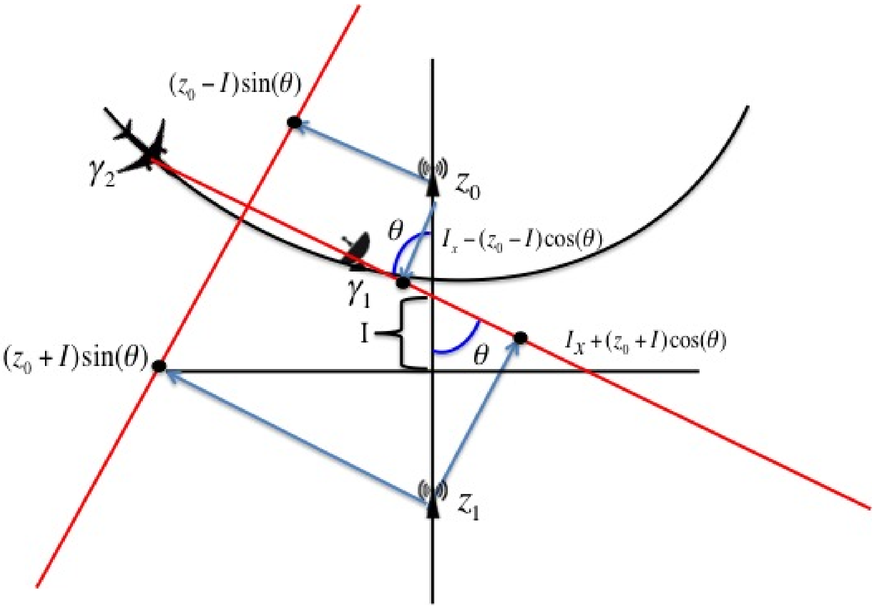

Figure 7.3: The position requirements for a mirror point to be in the envelope of the backprojection family.

$$|\gamma_2(s) - \mathbf{z}| - |\gamma_1(s) - \mathbf{z}| = |\gamma_2(s) - \mathbf{z_0}| - |\gamma_1(s) - \mathbf{z_0}|. \tag{7.26}$$

Since one branch of a hyperbola is a concave curve any line in the plane may intersect it in at most two points. Specifically to our interest, the y-axis of the coordinate system defined by the line segments $\overline{\mathbf{z_0 z_1}}$ can intersect the backprojection hyperbola in at most two points. We know that one of these points is $\mathbf{z}_0$. We have hypothesized that the other point of intersection is the point $\mathbf{z_1}$, for all locations of the receiver $\gamma_2(s)$.

We shall show that, when γ_2 and γ_1 are on a hyperbola defined by the foci $\mathbf{z_0}$ and $\mathbf{z_1}$, then a second hyperbola (the hyperbola of TDOA for the two receivers shown in figure 7.4) containing $\mathbf{z_0}$ cannot contain $\mathbf{z_1}$ unless the line $\overline{\gamma_2\gamma_1}$ between the two receivers makes a right angle with the y-axis defined by $\mathbf{z_0 z_1}$. Since the only hyperbola for which this is true at *all* points is the degenerate hyperbola which forms the x-axis of the system shown in 7.3 this is the only flight path which can produce a second focused point in the image.

First, note that for any hyperbola, all of the points of the curve are contained between the asymptotes. These asymptotes pass through the origin. Thus, when we consider the hyperbola to which the receivers are confined, the line $\overline{\gamma_2\gamma_1}$ between the two receivers must have a slope whose

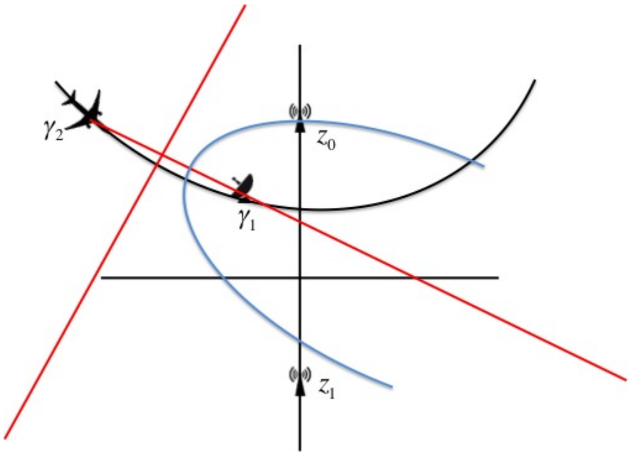

Figure 7.4: The hyperbola of TDOA for the receiver positions shown in figure 7.3.

magnitude is less than the magnitude of the slope of the asymptotes and must intersect the y-axis of the $\overline{\mathbf{z_0 z_1}}$ coordinate system above the x-axis as shown in 7.3.

We thus denote by I the magnitude of the distance from the origin of the $\overline{\mathbf{z_0 z_1}}$ coordinate axis to the point of intersection with the line $\overline{\gamma_2\gamma_1}$ and note that I is strictly positive whenever the two receivers are on a non-degenerate hyperbola as shown in 7.3.

We now define a second coordinate system based upon the location of the two receivers γ_2 and γ_1. Here we denote the axes as $\tilde{x}$ and $\tilde{y}$ to prevent confusion with the $\overline{\mathbf{z_0 z_1}}$ coordinates. Let the $\tilde{x}$-axis be defined as the line $\overline{\gamma_2\gamma_1}$ passing through the receivers and let the $\tilde{y}$-axis be the perpendicular bisector of the line segment $\overline{\gamma_2\gamma_1}$.

Then, as shown in figure 7.3, the $\tilde{x}$-axis intersects the y-axis at an angle $0 \leq \theta < \frac{\pi}{2}$. The $(\tilde{x}, \tilde{y})$ coordinates of $\mathbf{z_0}$ and $\mathbf{z_1}$ are

$$\mathbf{z_0} = \big(I_x - (z_0 - I)\cos(\theta), (z_0 - I)\sin(\theta)\big) \tag{7.27}$$

$$\mathbf{z_1} = \big(I_x + (z_0 + I)\cos(\theta), (z_0 + I)\sin(\theta)\big). \tag{7.28}$$

Here we have denoted by I_x the distance along the $\tilde{x}$-axis at which the line $\overline{\mathbf{z_0 z_1}}$ crosses, and in a slight abuse of notation we have used z_0 to denote the the magnitude $|\mathbf{z_0}| = |\mathbf{z_1}|$.

Now since γ_1 and γ_2 are equally spaced across the $\tilde{y}$-axis we can define an elliptical coordinate system by

$$\tilde{x} = a\cosh(\mu)\cos(\nu) \tag{7.29}$$

$$\tilde{y} = a\sinh(\mu)\sin(\nu) \tag{7.30}$$

where a is half the distance between γ_1 and γ_2. In an elliptical coordinate system such as (7.30) hyperbolas are given by lines of constant $|\nu|$ with the half of the hyperbola above the $\tilde{x}$ axis given by $0 < \nu$ and the half below the $\tilde{x}$-axis given by $-\nu < 0$ as shown in figure 7.5.

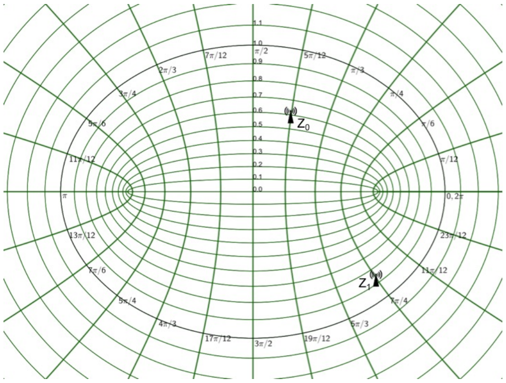

Figure 7.5: The lines of an elliptical coordinate system.

Now, if $\mathbf{z_0}$ and $\mathbf{z_1}$ lie on the same hyperbola of TDOA we must have

$$\tilde{\mathbf{z}}_0 = (a\cosh(\mu_0)\cos(\nu_0), a\sinh(\mu_0)\sin(\nu_0)) \tag{7.31}$$

$$\tilde{\mathbf{z}}_1 = (a\cosh(\mu_1)\cos(-\nu_0), a\sinh(\mu_1)\sin(-\nu_0)). \tag{7.32}$$

Combining the representations of the locations of $\mathbf{z_0}$ and $\mathbf{z_1}$ then, we have

$$\tilde{z}_{0x} = a\cosh(\mu_0)\cos(\nu_0) = I_x - (z_0 - I)\cos(\theta) \tag{7.33}$$

$$\tilde{z}_{0y} = a\sinh(\mu_0)\sin(\nu_0))) = (z_0 - I)\sin(\theta) \tag{7.34}$$

$$\tilde{z}_{1x} = a\cosh(\mu_1)\cos(-\nu_0) = I_x + (z_0 + I)\cos(\theta) \tag{7.35}$$

$$\tilde{z}_{1y} = a\sinh(\mu_1)\sin(-\nu_0) = (z_0 + I)\sin(\theta). \tag{7.36}$$

Noting that $\cos(-x) = \cos(x)$ and $\sin(-x) = -\sin(x)$ we have

$$a\cosh(\mu_0)\cos(\nu_0) + z_0\cos(\theta) = I_x + I\cos(\theta) \tag{7.37}$$

$$a\cosh(\mu_1)\cos(\nu_0) - z_0\cos(\theta) = I_x + I\cos(\theta) \tag{7.38}$$

$$- a\sinh(\mu_0)\sin(\nu_0) + z_0\sin(\theta) = I\sin(\theta) \tag{7.39}$$

$$- a\sinh(\mu_1)\sin(\nu_0) - z_0\sin(\theta) = I\sin(\theta). \tag{7.40}$$

Therefore

$$a\cosh(\mu_0)\cos(\nu_0) + z_0\cos(\theta) = a\cosh(\mu_1)\cos(\nu_0) - z_0\cos(\theta) \tag{7.41}$$

$$- a\sinh(\mu_0)\sin(\nu_0) + z_0\sin(\theta) = -a\sinh(\mu_1)\sin(\nu_0) - z_0\sin(\theta). \tag{7.42}$$

Rearranging terms produces

$$2z_0\cos(\theta) = a\cos(\nu_0)\big(\cosh(\mu_1) - \cosh(\mu_0)\big) \tag{7.43}$$

$$2z_0\sin(\theta) = a\sin(\nu_0)\big(\sinh(\mu_0) - \sinh(\mu_1)\big). \tag{7.44}$$

Note that when $\theta = 0$, the receivers γ_1 and γ_2 are equally spaced across the y-axis and the hyperbola of TDOA is the straight line forming the y-axis of the $\overline{\mathbf{z_0 z_1}}$ coordinate axis. At this point then, the hyperbola of TDOA clearly hits both $\mathbf{z_1}$ and $\mathbf{z_0}$. This is true for all flight paths constrained by (7.26). However, since $\mathbf{z_1}$ is a focused point only if it is hit by *every* hyperbola of

TDOA we can simply note that $\theta = 0$ will satisfy the condition in equation (7.26) and constrain our analysis to those points for which $\theta \neq 0$.

Since, for the geometry shown in figure 7.3, $0 < \theta < \frac{\pi}{2}$ and $0 < \nu_0 < \frac{\pi}{2}$ so that $0 < \cos(\theta)$ and $0 < \cos(\nu_0)$ equation (7.43) implies that we have that $\cosh(\mu_1) > \cosh(\mu_0)$. Since μ is strictly positive this implies $\mu_1 > \mu_0$. Likewise $0 < \sin(\theta)$ and $0 < \sin(\nu_0)$, thus we must have $0 < \big(\sinh(\mu_0) - \sinh(\mu_1)\big)$. However, since $\sinh(x)$ is a positive monotonic function in the first quadrant and $\mu_0 < \mu_1$ this is false!

Note that we have examined the geometry shown in 7.3 in explicit detail. The case in which the receivers are located on the opposite side of the y-axis is merely a mirror case where θ is measured from the right instead of the left side. The case in which the two receivers lie below the x-axis instead of above it is likewise identical. Indeed, since we have arbitrarily determined the positive direction of the y axis to begin with it is possible to simply define the side of the x-axis on which the two receivers lie as the positive y direction.

We have therefore reached a contradiction and it cannot be true that $\mathbf{z}_1$ is on the same hyperbola of TDOA as $\mathbf{z_0}$ when $0 < \theta$. Since the only hyperbola for which $\theta = 0$ for all points along the flightpath is the degenerate case of the x-axis it must be that $\gamma_2(s)$ and $\gamma_1(s)$ are confined to this straight line. Any other flight path will not produce a second focused point.

Thus, for the case of γ_1 stationary we must have $\mathbf{z_1}$ and $\mathbf{z_0}$ on the same circle centered at $\gamma_1(s_1)$ and the moving receiver flying directly toward or away from the stationary receiver during the entire data collection. This is illustrated in Figure 7.6.

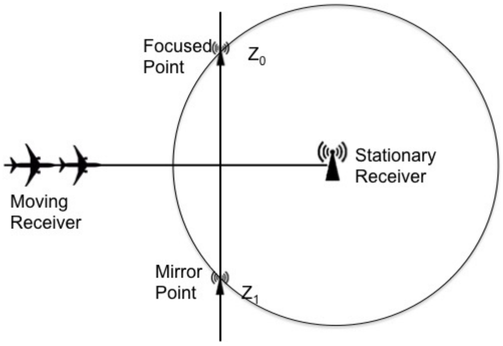

Figure 7.6: The position requirements for a mirror point to be in the envelope of the backprojection family.

Thus, the only situation in which $\mathbf{z_1}$ is a member of the envelope of the backprojection family is when the platform in motion flies a data collection which is along the perpendicular bisector of the line segment joining the two points. Since the point $\mathbf{z_1}$ is not specified a priori, we must rephrase this statement in order to capture its true meaning.

First, define the *mirror point* of a given focused point for time step s_1 as that point which is the reflection of the focused point across the line in the plane which passes through the moving receiver's position along the vector defining the receiver's velocity. For example, in Figure 7.6, the point $\mathbf{z_1}$ is the mirror point of the focused point $\mathbf{z_0}$ for the flight path along the x-axis.

Then, what we have proven is that: if there is a focused point $\mathbf{z_0}$ in the SASL image and the moving receiver flies a straight line flight path aimed directly at (or away from) the stationary receiver, then there will be a second focused point in the image at the location of the mirror point of $\mathbf{z_0}$. Henceforth we shall assume that our receivers are constrained to avoid flying this one highly specific flight path.

Thus, whenever a focused point exists in the family of backprojections it is unique regardless of the data collection flight path unless for the entire data collection the moving receiver flies directly toward or away from the stationary receiver's position. □

We can illustrate how the location of the stationary receiver, with respect to the flight path of the moving receiver, influences the existence of additional points in the envelope of the family of backprojection curves by examining some numerical examples of the backprojection hyperbolas for a scene containing a single emitter with various locations for the stationary receiver. These results are shown in Figure 7.7.

Here, as we have already proven, we see that when the receiver in motion flies a flight path directly toward or away from the stationary receiver (Figures 7.7f and 7.7b respectively), the back-projection curves intersect at the mirror point of the emitter in the scene. However, when the same flight path is flown with the stationary receiver in position 2, 3, or 4, the curves will constructively interfere only at the location of the emitter.

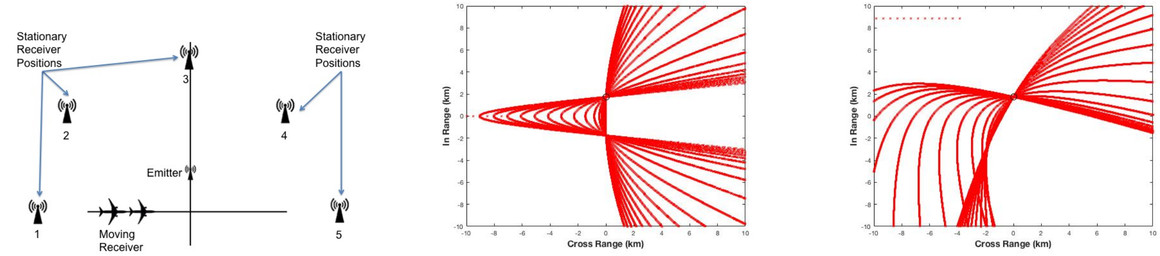

(a) Graphic of the flight path and 5 example positions for the stationary receiver.

(b) Position 1

(c) Position 2

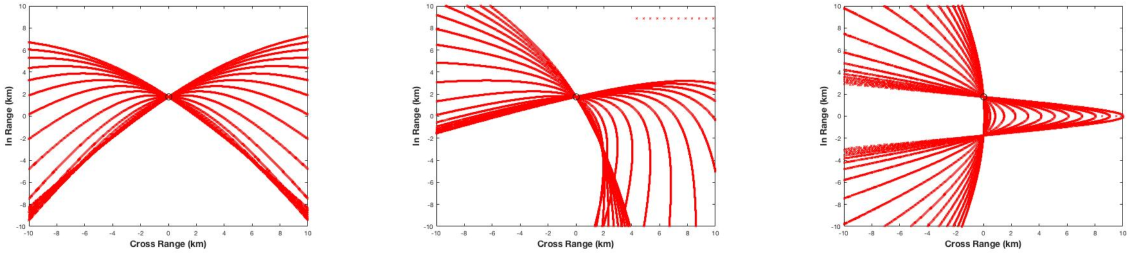

(d) Position 3

(e) Position 4

(f) Position 5

Figure 7.7: Examples of the families of backprojection hyperbolas for a single emitter scene with various hypothesized locations for the stationary emitter.

We note here that the existence or nonexistence of such mirror point artifacts in the image depends only on the relative locations and flight paths of the two receivers, which are known and under the control of the data collection designer. Therefore, since the flight paths which give rise to these extra points in the envelope of the family of backprojection curves are highly restrictive and should be easily avoided by an operator with very little restriction on the data collection process, we shall henceforth assume in our examples and discussion that these flight paths are avoided. Thus, we may assume that if a focused point exists due to a data term, it is unique.

Now that we have a full understanding of the uniqueness of a focused point in the SASL image we are prepared to prove that the only such points will be the emitter positions.

Theorem 2: *If, as described in the data collection model above, one receiver is stationary and not in a direct line with the moving receiver's flight path, the only focused points for all backprojection hyperbolas in the image given by equation* (6.87) *are the emitter locations regardless of the flight path of the second receiver.*

We shall prove this theorem by exhausting the possible cases in which the receiver/emitter geometries can be set up. We first examine the diagonal terms and then move to the cross terms.

Proof: *Case 1: The diagonal terms.*

The contribution to the image of any diagonal term in the data takes the form

$$\int e^{i2\pi(t-r(s,\mathbf{z}))} Q(s,f,\mathbf{z}) d_D(s,t) ds dt \tag{7.45}$$

where $d_D(s,t)$ is the data term being backprojection onto the image. Thus, a diagonal term projects the product $Q(s,f,\mathbf{z})d_D(s,t)$ onto the image for each set of receiver positions $\gamma_1(s), \gamma_2(s)$. In the case of a diagonal term, the data from only one emitter is present by definition, let the position of this emitter be $\mathbf{e_1}$. As previously shown these backprojections are over the hyperbolas defined by

$$|\gamma_2(s) - \mathbf{z}| - |\gamma_1(s) - \mathbf{z}| = |\gamma_2(s) - \mathbf{e_1}| - |\gamma_1(s) - \mathbf{e_1}|. \tag{7.46}$$

It is clear that, for all times along the flight path, this equation has the trivial solution $\mathbf{z} = \mathbf{e_1}$. Thus, all backprojections constructively interfere at the point in the image corresponding to the emitter's location and it is a focused point in the resulting image. Since a focused point is unique by the previous theorem, the only focused points resulting from the diagonal terms are at the locations of the emitters corresponding to those terms.

Case 2: The cross terms.

It has already been seen that, in the case of a diagonal term, one focused point exists and it exists at the location of an emitter. For a given cross term, three outcomes may be possible. Either that a focused point exists and exists at the location of one of the two emitters, that a focused point exists and exists at some location in the image at which there is no emitter, or else that no focused points exist in the resulting image due to the cross term.

Subcase I A: We consider first the possibility that a focused term exists at the location of one of the two emitters present in the scene.

Let $\mathbf{e_1}, \mathbf{e_2}$ be the location of two emitters in the scene. Then the contribution to the image for each of the cross terms from such emitters takes the form

$$\int e^{i2\pi(t-r(s,\mathbf{z}))} Q(s,f,\mathbf{z}) d_C(s,t) ds dt. \tag{7.47}$$

where $d_C(s,t)$ is the data term resulting from either the correlation of the signal at emitter $\mathbf{e_1}$ with the signal at emitter $\mathbf{e_2}$ or vise versa. Without loss of generality we will examine the case in which the term under consideration arises from the correlation of the signal emitted by $\mathbf{e_1}$ and received at the receiver at $\gamma_1(s)$ with the signal emitted by $\mathbf{e_2}$ and received at the receiver at $\gamma_2(s)$ at time s.

As we have seen, this results in the backprojection of the product $Q(s,f,\mathbf{z})d_C(s,t)$ along the hyperbola defined by

$$|\gamma_2(s) - \mathbf{z}| - |\gamma_1(s) - \mathbf{z}| = |\gamma_2(s) - \mathbf{e_2}| - |\gamma_1(s) - \mathbf{e_1}|. \tag{7.48}$$

Assume that there exists a focused point for these backprojections and let that point be denoted $\mathbf{z_0}$ where $\mathbf{z_0} = \mathbf{e_1}$ or $\mathbf{z_0} = \mathbf{e_2}$.

We first consider the case where $\mathbf{z_0} = \mathbf{e_2}$, that is, the case in which a focused point occurs at the location of the emitter whose signal was recorded at the moving receiver. We shall handle the case for which $\mathbf{z_0} = \mathbf{e_1}$ in *Subcase I B*.

Since $\mathbf{z_0}$ is a focused point

$$|\gamma_2(s) - \mathbf{z_0}| - |\gamma_1(s) - \mathbf{z_0}| = |\gamma_2(s) - \mathbf{e_2}| - |\gamma_1(s) - \mathbf{e_1}|. \tag{7.49}$$

for all time steps s. Since $\mathbf{z_0} = \mathbf{e_2}$ we have

$$|\gamma_1(s) - \mathbf{z_0}| = |\gamma_1(s) - \mathbf{e_1}| \tag{7.50}$$

which implies

$$|\gamma_1(s) - \mathbf{e_2}| = |\gamma_1(s) - \mathbf{e_1}| \tag{7.51}$$

for all s, since we have postulated $\mathbf{z_0} = \mathbf{e_2}$. This is true if and only if the two emitters lie on the same circle centered at the stationary receiver.

Thus, a focused point for the cross term data exists at the location of the emitter whose signal was received at the moving receiver whenever the second emitter is equidistant to the stationary receiver. If the two are not equidistant then equation (8.35) is a contradiction and no such focused point exists.

Subcase I B: Now consider the analogous case in which $\mathbf{z_0} = \mathbf{e_1}$. Similarly in this case we find that $\mathbf{z_0}$ must satisfy

$$|\gamma_2(s) - \mathbf{z_0}| = |\gamma_2(s) - \mathbf{e_2}| \tag{7.52}$$

for all s. This equation states that the distance from the moving receiver to the focused point at $\mathbf{z_0}$ is equal to the distance from the receiver to the emitter at $\mathbf{e_2}$, whose signal it is receiving at all points along its flight path. Since $\mathbf{z_0} = \mathbf{e_1}$ we thus have the condition

$$|\gamma_2(s) - \mathbf{e_1}| = |\gamma_2(s) - \mathbf{e_2}| \tag{7.53}$$

for all s.

However, since we have postulated that there are two emitters so that $\mathbf{e_1} \neq \mathbf{e_2}$ and that $\gamma_2(s_1) \neq \gamma_2(s_2)$ for any time step s_1 because γ_2 is in motion, this is possible only in the case in which the moving receiver flies a path straight along the perpendicular bisector of the line segment joining $\mathbf{e_1}$ and $\mathbf{e_2}$. In the rare case that the moving receiver flies a flight path exactly between two emitters in the scene, then there will be a focused point due to the cross term of the two emitters at the point corresponding to the location of the emitter whose signal was received at the stationary emitter.

Thus, when we consider the possibility of the backprojection image containing a focused point due to a cross term at the location of one of the emitters we find: if two emitters are equidistant from the stationary receiver, then each emitter is the focused point of the backprojection of the cross term in which that emitter's signal is the signal received at the moving receiver. Similarly, if the moving receiver flies a straight line flight path exactly between two emitters so that it is always equidistant from both of them, then each emitter is the focused point of the backprojection of the cross term in which that emitter's signal is the signal received at the stationary receiver.

Otherwise, there are no focused points at the location of either emitter due to the cross terms. In these cases, since a focused point is unique, no other focused points exist in the image due to that data term.

Subcase II: Now assume that there exists a focused point in the image due to a cross term which is not located at an emitter's position. Let this point be denoted by $\mathbf{z_0}$ where $\mathbf{z_0} \neq \mathbf{e_1} \neq \mathbf{e_2}$. As above we must have that

$$|\gamma_2(s) - \mathbf{z_0}| - |\gamma_1(s) - \mathbf{z_0}| = |\gamma_2(s) - \mathbf{e_2}| - |\gamma_1(s) - \mathbf{e_1}|. \tag{7.54}$$

for all s. As seen previously if $\mathbf{z_0}$ is a focused point it must also satisfy

$$\frac{(\gamma_2(s) - \mathbf{z_0}) \cdot \dot{\gamma}_2(s)}{|\gamma_2(s) - \mathbf{z_0}|} = \frac{(\gamma_2(s) - \mathbf{e_2}) \cdot \dot{\gamma}_2(s)}{|\gamma_2(s) - \mathbf{e_2}|} \tag{7.55}$$

for all s.

As seen in the proof of our first theorem, these conditions can be rewritten as

$$|\gamma_2(s) - \mathbf{z_0}| - |\gamma_2(s) - \mathbf{e_2}| = |\gamma_1(s) - \mathbf{z_0}| - |\gamma_1(s) - \mathbf{e_2}|. \tag{7.56}$$

Since $\gamma_1(s), \mathbf{e_2}$ and $\mathbf{z_0}$ are constants we have

$$|\gamma_2(s) - \mathbf{z_0}| - |\gamma_2(s) - \mathbf{e_2}| = C \tag{7.57}$$

for C is constant.

In the proof of Theorem 1, we showed these conditions are met if and only if the moving receiver flies a flight trajectory directly along the perpendicular bisector of the line segment joining the two points $\mathbf{z_0}$ and $\mathbf{e_2}$. Otherwise we have reached a contradiction and no such focused point exists.

However, if the moving receiver flies a flight path directly along the perpendicular bisector of the line segment joining the two points $\mathbf{z_0}$ and $\mathbf{e_2}$, then its distance to each of those points is equal at all times, thus $|\gamma_2(s) - \mathbf{z_0}| = |\gamma_2(s) - \mathbf{e_2}|$. Therefore $C = 0$. But the constant C is given by the equation

$$C = |\gamma_1(s) - \mathbf{z_0}| - |\gamma_1(s) - \mathbf{e_2}|. \tag{7.58}$$

So, if $C = 0$ then $|\gamma_1(s) - \mathbf{z_0}| = |\gamma_1(s) - \mathbf{e_2}|$. Thus the distance from the stationary receiver to the emitter $\mathbf{e_2}$ and the cross term focused point $\mathbf{z_0}$ is equal. Since $\mathbf{e_2} \neq \mathbf{z_0}$ by assumption we have that $\mathbf{z_0}$ and $\mathbf{e_2}$ lie on the same circle centered on the stationary receiver γ_1.

Combining this requirement with the one that the moving receiver fly directly between the two points leaves us with the moving receiver flying a flight path either directly toward or away from the stationary receiver as was shown in Figure 7.6.

Thus the only focused point which can exist at a location other than the true location of an emitter due to a cross term is a mirror point which is caused by flying the one flight path we have disallowed.

Conclusion: The cross terms do not produce focused points in the image except for certain specific geometries. Those geometries are: 1) When two emitters are equidistant from the stationary receiver. In this case the cross term due to the signal received by the moving receiver and cross correlated with the signal received at the stationary receiver will focus at the emitter which transmitted the signal recorded at the moving receiver. 2) When two emitters are at all times equidistant from the moving receiver, that is, when the moving receiver flies a trajectory along a straight line between two emitters. In this case, the cross term due to the signal recorded at the stationary receiver and cross correlated with the one received at the moving receiver will focus at the location of the emitter whose signal was received by the stationary receiver.

Thus, excluding the flight path in a direct line with the stationary receiver, the only focused points for any family of back projection hyperbolas in the image are the emitter locations, regardless of the flight path of the moving receiver. Furthermore, with the exception of a few special cases, the focused points will be due to the diagonal terms in our data. □

We have thus proven that persistent peaks in the final image, due to all data terms, will be those points which correspond to the location of an emitter in the scene. The contribution to the final image of the cross terms then will be to gradually blur out along the envelope of the family of backprojections as the receiver travels along its path.

We can further illustrate these effects with some numerical simulations.

7.2 Numerical Examples

We consider first the case in which two emitters are equidistant from the stationary receiver. In figure 7.8 we show examples of some of the hyperbolas in the family of backprojection curves for the two cross terms which arise from the emitters shown. In these examples we continue to use our previous flight path geometry in which the stationary receiver is located at $\gamma_1(s) \equiv (10, 20)$ while the receiver in motion travels from $\gamma_2(s_0) = (0, 0)$ to $\gamma_2(s_T) = (20, 0)$.

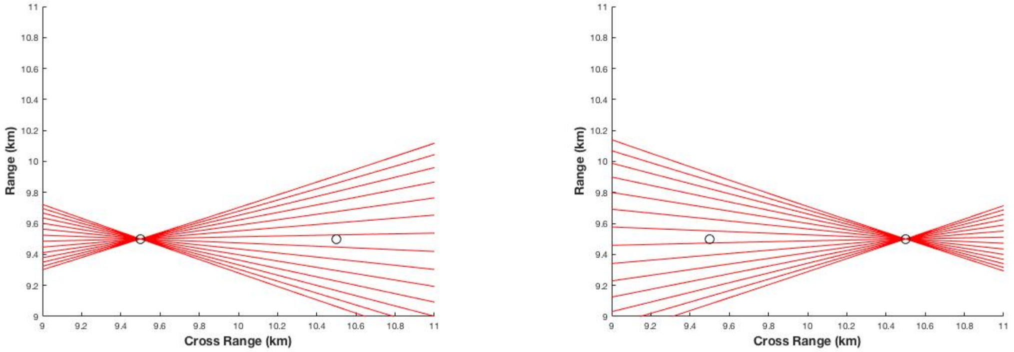

(a) Examples from the family of curves for the left-most emitter.

(b) Examples from the family of curves for the right-most emitter.

Figure 7.8: The families of backprojection curves for the two cross terms arising from two emitters equidistant from the stationary receiver.

Here we can see that, as we have proven, when the two emitters present in the scene are equidistant from the stationary emitter, the cross term backprojections will constructively interfere at the locations of the two emitters. In such a case, the peaks in the image corresponding to the location of the two emitters will be strengthened by the cross term effects and no phantom streaks will appear in the final image.

The simulated SASL image for this scene is shown in figure 7.9. As predicted the emitters appear clearly with no evidence of any phantom effects from the cross terms present in the data.

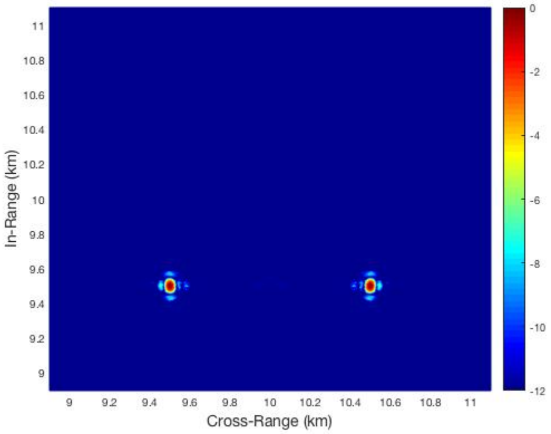

Figure 7.9: The SASL image for two emitters at (9.5, 9.5) and (10.5, 9.5) with receivers located at (10,20) and flying from (0,0) to (20,0).

The effect of the addition of the cross terms can be clearly seen by examining the image which results from the backprojection of our current data model with that which results from the data when the signals are assumed to be separable prior to the cross correlation. In the separable case the cross terms are not present in the data. When the two images are displayed on the same scale, the result is that the peaks are lower in the image generated from the separable data because the cross terms contribute to their height. This is seen in figure 7.10.

Next we consider the case in which two emitters are located in the scene but are not located equidistant from the stationary receiver. A collection of some of the curves in the family of back-projections is shown for both cross terms for an example of this case in figure 7.11.

In figure 7.11a we display examples of the family of curves for the case in which the signal from the emitter at $\mathbf{e_1} = (9.7, 9.4)$ is received at the moving receiver. In figure 7.11b we display

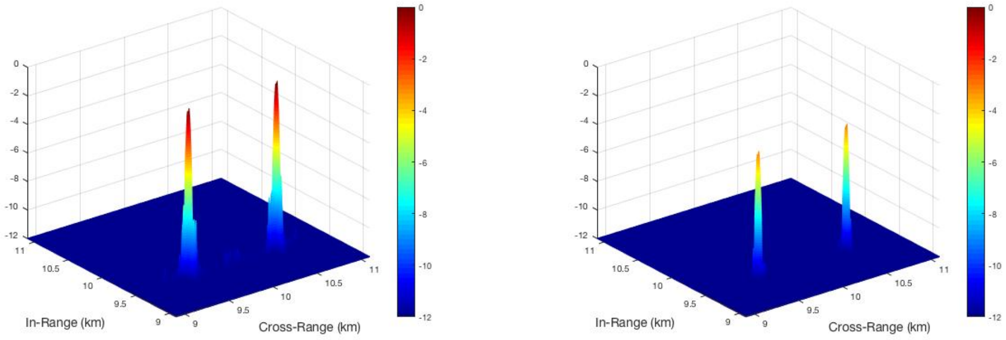

(a) The cross term case. **(b)** The seperable case.

Figure 7.10: Comparison of the separable and non-separable cases for two emitters equidistant from the stationary receiver.

curves from the case in which it is the emitter at $\mathbf{e_2} = (10.5, 10.7)$ whose signal is received at the moving receiver.

In both cases it is clear that the envelope of the family is non-degenerate and that, therefore, no focused point exists. Thus, we expect that as the flight path lengthens, the impact of the cross terms in the creation of phantoms will be gradually diminished leaving the peaks at the emitter locations standing out.

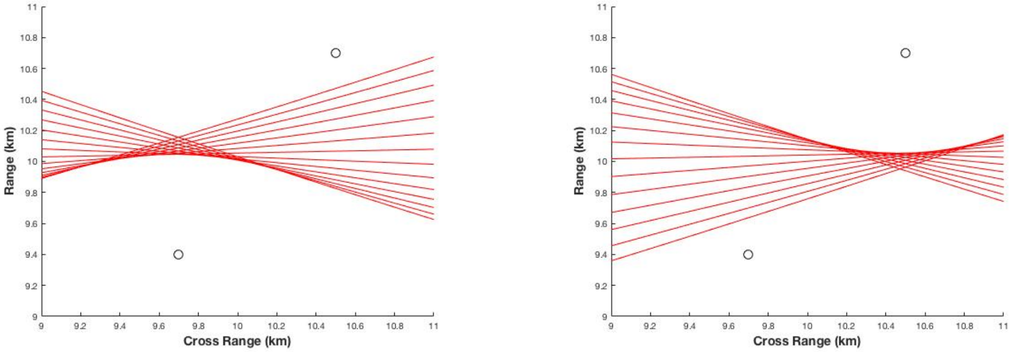

(a) Examples from the family of curves for $\mathbf{e_1} = (9.7, 9.4)$ received at $\gamma_2(s)$. **(b)** Examples from the family of curves for $\mathbf{e_2} = (10.5, 10.7)$ received at $\gamma_2(s)$.

Figure 7.11: Examples from the families of the backprojection curves for two cross terms.

Figure 7.12 shows the progression of images which result from gradually longer data collections of two emitters positioned at the same locations seen in figure 7.11. In figure 7.12a the contributions from the cross and diagonal terms appear to be of roughly equal strength. As the aperture lengthens the cross term phantoms at first forms the semblance of a peak between the two emitters; however as predicted, as the data collection lengthens the peak blurs and the effects of the cross terms are gradually spread along the envelope of the family of curves reducing their impact on the overall image.

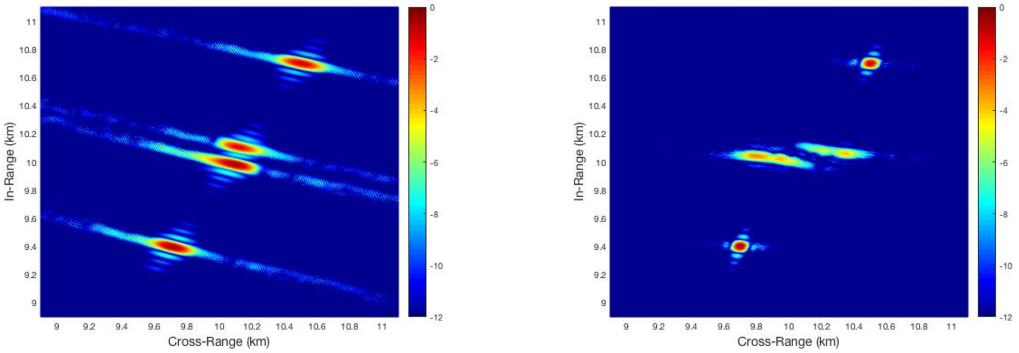

(a) $\gamma_2(s) = (0,0)$ to $(5,0)$ **(b)** $\gamma_2(s) = (0,0)$ to $(10,0)$.

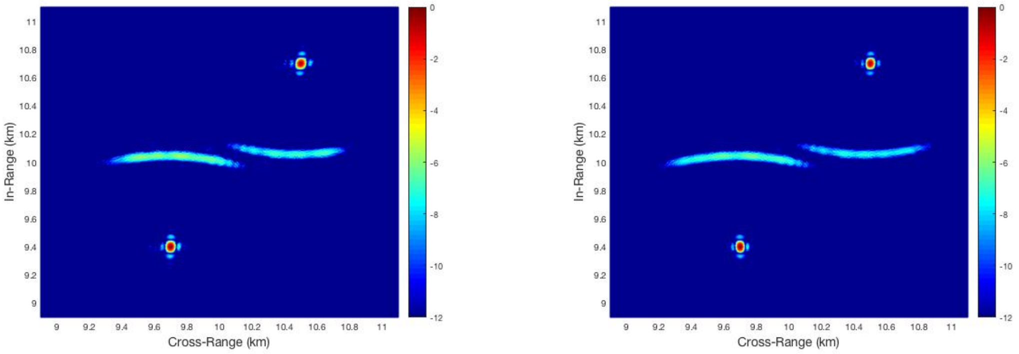

(c) $\gamma_2(s) = (0,0)$ to $(15,0)$ **(d)** The full $20km$ flight path.

Figure 7.12: SASL images for two emitters with a gradually lengthening data collection.

We now examine a combination of the last two cases. In this example we have three emitters in the scene which form a triangle so that two of the emitters are equidistant from the stationary receiver whilst the third is located between them and closer to the stationary receiver. This example is shown in figure 7.13. Here, as before, we witness that the effect of the cross terms in the creation of phantoms in the image is significant for short data collections, however, as the data collection lengthens these effects gradually disappear in the finial image. However, it is important to note in

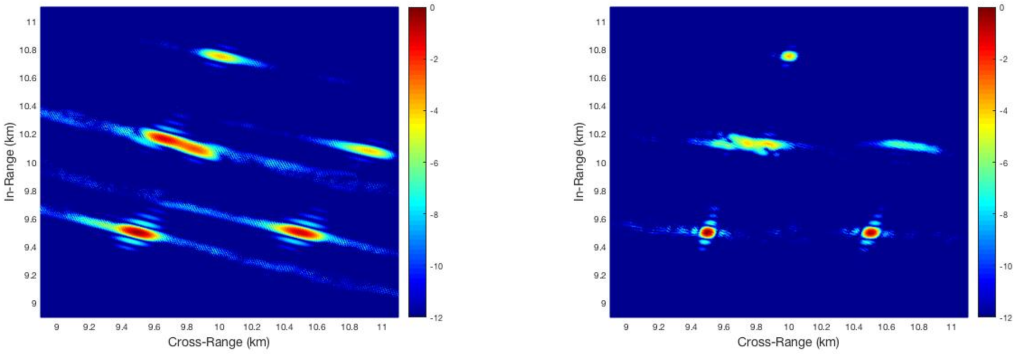

(a) $\gamma_2(s) = (0,0)$ to $(5,0)$ **(b)** $\gamma_2(s) = (0,0)$ to $(10,0)$.

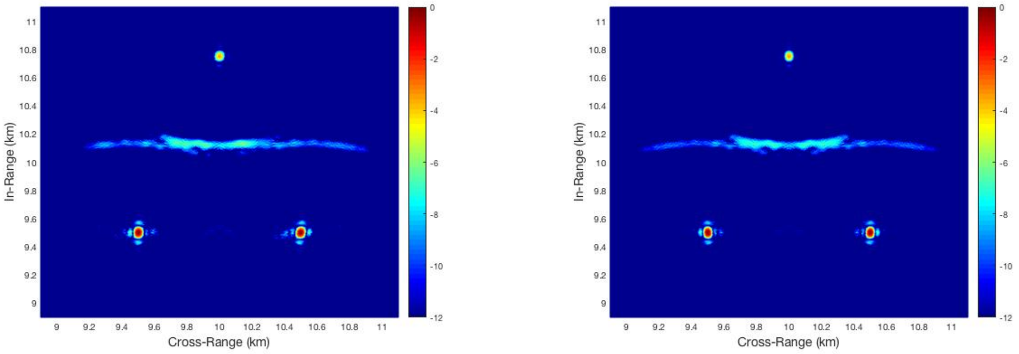

(c) $\gamma_2(s) = (0,0)$ to $(15,0)$ **(d)** The full $20km$ flight path.

Figure 7.13: SASL images for three emitters with a gradually lengthening data collection.

figure 7.13d that the focusing effect of the cross terms at the location of the emitters causes the two emitters in the lower portion of the image to have significantly higher peaks than that seen for the upper emitter.

This could lead one to believe that the two emitters near the bottom of the image are transmitting a significantly stronger signal. In fact, in this example, the strength of all three emitters is identical, the extra height of the lower peaks in this case is merely an artifact of their positions relative to the stationary emitter.

Chapter 8

THREE DIMENSIONAL SASL

In previous chapters we have examined and simulated only a two dimensional version of the source localization problem in which the receivers are constrained to a flight path in the ground plane. This was done for simplicity in introducing the subject as well as for numerical efficiency in simulating the SASL imaging process. We shall now consider the three dimensional case in greater detail and examine how a truly three dimensional geometry affects the formulation of the SASL image.

First we note that all previous analytical work in deriving the model of the data terms and the backprojected image has been done in a dimensionally agnostic way so that the equations apply equally well to a two dimensional planar geometry embedded in a three dimensional medium as they do to the case in which the receivers fly in some three dimensional space above the ground plane.

As a brief reminder of this previous work, recall that our data is modeled by the equation

$$d(s,t) = \int e^{-i2\pi i f(t - r(s,\mathbf{y},\mathbf{y}')/c_0)} A(s,\mathbf{y},\mathbf{y}') T(\mathbf{y},\mathbf{y}') d\mathbf{y} d\mathbf{y}' df \tag{8.1}$$

which can be rewritten as a sum of diagonal terms corresponding to the emitter locations and cross terms which have undesirable effects on the final product. In this way we rewrite $d(s,t)$ as

$$d(s,t) = \int e^{-i2\pi i f(t - r(s,\mathbf{y})/c_0)} A(s,\mathbf{y}) V(\mathbf{y}) d\mathbf{y} df \tag{8.2}$$

$$+ \int e^{-i2\pi i f(t - r(s,\mathbf{y},\mathbf{y}')/c_0)} A(s,\mathbf{y},\mathbf{y}') W(\mathbf{y},\mathbf{y}') d\mathbf{y} d\mathbf{y}' df \tag{8.3}$$

where $W(\mathbf{y},\mathbf{y}') = T(\mathbf{y},\mathbf{y}') - V(\mathbf{y})$.

We then use the backprojection scheme derived in Chapter 7 to obtain the image

$$I(\mathbf{z}) = \int e^{i2\pi(t-r(s,\mathbf{z}))} \frac{\chi(s,f,\mathbf{z})\eta}{A(s,\mathbf{z})\tilde{B}(f)} D(s,f)dsdf. \tag{8.4}$$

In Chapter 7 we demonstrated that, for a two dimensional data collection geometry, this image is built up from the projection of the data along the hyperbolas satisfying

$$|\gamma_2(s) - \mathbf{z}| - |\gamma_1(s) - \mathbf{z}| = |\gamma_2(s) - \mathbf{e_i}| - |\gamma_1(s) - \mathbf{e_j}| \tag{8.5}$$

where $\mathbf{e_i}$ and $\mathbf{e_j}$ correspond to the location of emitters in the scene and we proved certain properties for the families of such hyperbolas. We shall now examine the effect of allowing the flight paths $\gamma_1(s)$ and $\gamma_2(s)$ to contain a height component. We will first examine the case in which the two receivers fly at some height h above a flat ground plane. We will then move to examining the case where one receiver is a stationary ground based platform and the other flies at some constant height h above the ground. We leave the more general case of receivers with a varying height component for future work.

It should be clear that, for a given s, equation (8.5) defines a hyperboloid in three dimensions with the foci being the location of the two receivers. For simplicity in the following calculations, for a particular time s_1 defining two receiver positions $\gamma_1(s_1)$ and $\gamma_2(s_1)$, let a coordinate axis be defined such that $\gamma_1(s_1) = (-d, 0, 0)$ and $\gamma_2(s_1) = (d, 0, 0)$ where

$$2d = |\gamma_1(s_1) - \gamma_2(s_1)| \tag{8.6}$$

in the original coordinate setting of the scene. Then the hyperboloid of TDOA defined by (8.5) can be written in canonical form as

$$\frac{x^2}{a^2} - \frac{y^2}{b^2} - \frac{z^2}{b^2} = 1 \tag{8.7}$$

where a is half the TDOA

$$2a = |\gamma_2(s) - \mathbf{e_i}| - |\gamma_1(s) - \mathbf{e_j}| \tag{8.8}$$

and b is given by

$$b^2 = d^2 - a^2 \tag{8.9}$$

[43,44].

Let both receivers fly at a constant height h above the ground plane. In our coordinate system then the ground plane is located at $-h$. Then, the intersection of the ground plane with the hyperboloid of TDOA can be derived as follows:

$$\frac{x^2}{a^2} - \frac{y^2}{b^2} - \frac{h^2}{b^2} = 1 \tag{8.10}$$

$$\frac{x^2}{a^2} - \frac{y^2}{b^2} = 1 + \frac{h^2}{b^2} \tag{8.11}$$

$$\frac{x^2}{a^2(1+\frac{h^2}{b^2})} - \frac{y^2}{b^2(1+\frac{h^2}{b^2})} = 1 \tag{8.12}$$

which is the canonical form of a hyperbola, $\frac{x^2}{A^2} - \frac{y^2}{B^2} = 1$, with $A^2 = a^2(1+\frac{h^2}{b^2})$ and $B^2 = b^2(1+\frac{h^2}{b^2})$.

Thus, as we had previously stated without proof, the intersection of the three dimensional surface of TDOA with the ground plane is a hyperbola. Thus, in the three dimensional case, as in the two dimensional case, the set of backprojections will be a family of hyperbolas in the the plane.

The foci of the intersection hyperbola can be derived from equation (8.52). Using the fact that $B^2 = D^2 - A^2$, where D is half the distance between foci in the ground plane, we have

$$D^2 = B^2 + A^2 = b^2 + h^2 + a^2 + a^2\frac{h^2}{b^2} \tag{8.13}$$

$$= d^2 + h^2 + \frac{a^2h^2}{d^2 - a^2}. \tag{8.14}$$

Substitution of our expression for d and a produces

$$\begin{aligned} D^2 = &\left(\frac{1}{2}|\gamma_1(s) - \gamma_2(s)|\right)^2 + h^2 \\ &+ \frac{2h^2\left(\frac{1}{2}(|\gamma_2(s) - \mathbf{e}_i| - |\gamma_1(s) - \mathbf{e}_j|\right)^2}{|\gamma_1(s) - \gamma_2(s)| - (\frac{1}{2}(|\gamma_2(s) - \mathbf{e}_i| - |\gamma_1(s) - \mathbf{e}_j|)^2}. \end{aligned} \tag{8.15}$$

Recall that $2D$ is the distance between the foci of the hyperbola in the plane. Note that, since h^2 and $\frac{a^2h^2}{d^2-a^2}$ are strictly positive, equation (8.14) implies that $D \geq d$, with equality occurring only in the case $h = 0$. Thus the distance between the foci of the the intersection hyperbola will always be greater than the distance between the two receivers unless the receivers are located in the ground plane. Furthermore, the difference in these distances increases as the height of the receivers increases.

Since the ground plane intersects the hyperboloid at a slope of zero with respect to the axis defined by the two receivers, the foci of the intersection hyperbola must lie on the same axis. Thus, we can determine the location of the foci of the hyperbola of equal TDOA in the ground plane by simply taking the projection of $\gamma_1(s)$ and $\gamma_2(s)$ into the ground plane, call these projections $\tilde{\gamma}_1(s)$ and $\tilde{\gamma}_2(s)$ respectively, and adding the vector of length D from the center point $\frac{1}{2}(\tilde{\gamma}_1(s) + \tilde{\gamma}_2(s))$ in the direction of each of the two projected receiver positions. This will give us foci locations which will better allow us to characterize the family of backprojections. Heuristically, these foci positions at the positions which would give rise to the hyperbola of TDOA in the ground plane if the receivers were located in the two dimensional ground plane rather than above it at height h.

Information about how these families of hyperbolas behave with respect to the two dimensional case may aid in the construction of optimal flight paths which is something we hope to pursue in future work.

Mathematically these foci positions can be written as

$$\Gamma_1(s) = \frac{1}{2}(\gamma_1(s) + \gamma_2(s)) + D \cdot \frac{\gamma_1(s) - \gamma_2(s)}{|\gamma_1(s) - \gamma_2(s)|} \tag{8.16}$$

$$\Gamma_2(s) = \frac{1}{2}(\gamma_1(s) + \gamma_2(s)) + D \cdot \frac{\gamma_2(s) - \gamma_1(s)}{|\gamma_1(s) - \gamma_2(s)|} \tag{8.17}$$

where we have used $\Gamma_1(s)$ and $\Gamma_2(s)$ to denote the positions of the foci associated with the receivers γ_1 and γ_2 respectively. The first consequence of these expressions is that the focus location Γ_1 will depend not only on γ_1 but also on the position of γ_2. Thus, if γ_1 is stationary and γ_2 is in motion, then the location of the focus Γ_1, will also be in motion, even though γ_1 is not.

We hope that a characterization of this motion may help us to better understand the backprojection families and thereby to choose flight paths which are better suited to the scene on observation. Some of our initial efforts to characterize this behavior are discussed in Appendix E.

An important question however, is whether this motion has any bearing on our previous proofs which demonstrated that the only persistent peaks in the SASL image would be the location of the emitters in the scene. Before proceeding to numerical simulations of various data collection geometries in three dimensions, and the resulting SASL images produced, we first prove two corollaries to our previous theorems. These corollaries demonstrate that the previous results in two dimensions hold in the three dimensional case when one receiver is either a stationary ground based receiver or a hovering receiver.

Corollary to Theorem 1: *Let two receivers observe a scene from a three dimensional flight path with one in motion and the other stationary and let the receiver in motion fly at a constant height h above the ground plane. If the receiver in motion flies any flightpath through or around the target scene for which its velocity vector is not aimed directly at the the stationary receiver then: If the family of hyperbolas, over which a data term is backprojected according to the imaging operator defined in equation* (6.87)*, has a* focused point, *that focused point is unique.*

Proof: From the proof of Theorem 1 we have that

$$|\gamma_2(s_1) - \mathbf{z_0}| - |\gamma_2(s_1) - \mathbf{z_1}| = |\gamma_2(s_2) - \mathbf{z_0}| - |\gamma_2(s_2) - \mathbf{z_1}| \tag{8.18}$$

where $\mathbf{z_0}$ is a focused point in the SASL image and $\mathbf{z_1}$ is a hypothesized second focused point.

In three dimensions this implies that the difference in the distance from the second receiving platform to each of the points is equal as the platform moves from $\gamma_2(s_1)$ to $\gamma_2(s_2)$. Since we have postulated that $\mathbf{z_0} \neq \mathbf{z_1}$ the platform must move along some hyperboloid with the two focused points as the foci.

As before, this can be more clearly seen by setting $|\gamma_2(s_1) - \mathbf{z_0}| - |\gamma_2(s_1) - \mathbf{z_1}| = C$ where C is constant. This is just a specific realization of a single point along the flight path of $\gamma_2(s)$. Then we have

$$|\gamma_2(s) - \mathbf{z_0}| - |\gamma_2(s) - \mathbf{z_1}| = C \tag{8.19}$$

where $\mathbf{z_0}$ and $\mathbf{z_1}$ are fixed.

Allowing s to vary around s_2 it is clear that this equation traces out a portion of a hyperboloid with its vertex in the ground plane, foci at the locations $\mathbf{z_0}$ and $\mathbf{z_1}$, and containing the point $\gamma_2(s_2)$. Thus, in physical terms, this condition constrains the flight path of the moving receiver to be on the two dimensional surface of some hyperboloid rising out of the ground plane.

If we allow the perpendicular bisector of the line segment joining $\mathbf{z_0}$ and $\mathbf{z_1}$ to form the x-axis of a new coordinate system and the line between $\mathbf{z_0}$ and $\mathbf{z_1}$ to form the y-axis, the receiving platform must follow a flight path constrained to the surface of some hyperboloid like the one shown in Figure 8.1.

Note in Figure 8.1 that, although the hyperboloid will extend below the ground plane we can safely constrain our receiver to the half of the hyperboloid located above it, though this fact will not figure into our proof. Note also that the hyperboloid shown is merely a single example of the infinite number of such hyperboloids which satisfy our conditions at this point. We will soon see, that only one such member of this family of hyperboloids satisfies all the constraints that we may place on this family, and that this hyperboloid will be the degenerate case of a plane located between the two focused points.

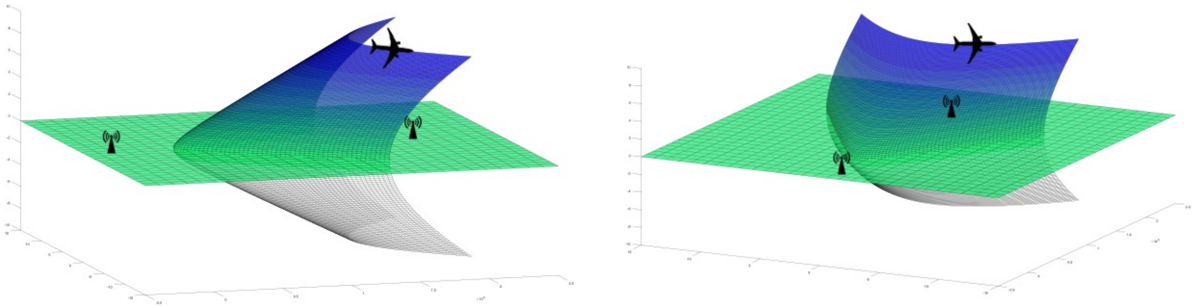

(a) A side view of the scene.

(b) A frontal view of the scene.

Figure 8.1: An example of a hyperboloid surface constraining the flight path. The light green plane here denotes the ground plane on which the emitters are located.

As mentioned in our proof of the first theorem, it is certainly possible for the moving receiver to fly any other flight path, however, if it does so then we have reached a contradiction and our conclusion is already proven. Thus we assume that the receiver's flight path is constrained to one of these surfaces.

In equation (7.19) we demonstrated that a second necessary condition for $\mathbf{z_1}$ to be in the envelope of the backprojection family given that $\mathbf{z_0}$ is a focused point is that

$$|\gamma_2(s_1) - \mathbf{z_0}| - |\gamma_1(s_1) - \mathbf{z_0}| = |\gamma_2(s_1) - \mathbf{z_1}| - |\gamma_1(s_1) - \mathbf{z_1}|. \tag{8.20}$$

However, we have now gone further and shown that, for a second focused point to exist, the flight path of the moving receiver must be constrained to one of a family of hyperboloids intersecting the ground plane. That is, $|\gamma_2(s) - \mathbf{z_0}| - |\gamma_2(s) - \mathbf{z_1}| = C$ for some constant C. Therefore equation (8.20) implies

$$|\gamma_1(s) - \mathbf{z_0}| - |\gamma_1(s) - \mathbf{z_1}| = |\gamma_2(s) - \mathbf{z_0}| - |\gamma_2(s) - \mathbf{z_1}| = C. \tag{8.21}$$

Thus, for $\mathbf{z}_1$ to be a focused point of the family, the stationary receiver $\gamma_1(s)$ must also lie on the same hyperboloid that constrains the flight path of $\gamma_2(s)$. In practice this should be easily avoided. However, as before, we can go further and show that of the infinite number of hyperboloids in this family, only the degenerate case, that is, the the case for which $C = 0$ and the 'hyperboloid' is actually a plane which contains both receivers at all points along the flight path, allows for the existence of a second focused point.

First let the stationary receiver γ_1 be at a height h above the ground so that it hovers at the same height as the moving platform. Then we may define a coordinate system similar to that defined in chapter 7. This is shown in figure 8.2.

Here the coordinates shown in black are defined by the line $\overline{\mathbf{z_0}\mathbf{z_1}}$ with the ground plane defined as the plane for which $z = 0$, where z is the third axis of the coordinate system. As in chapter 7, we can define a second coordinate system shown in red using the locations of the two stationary

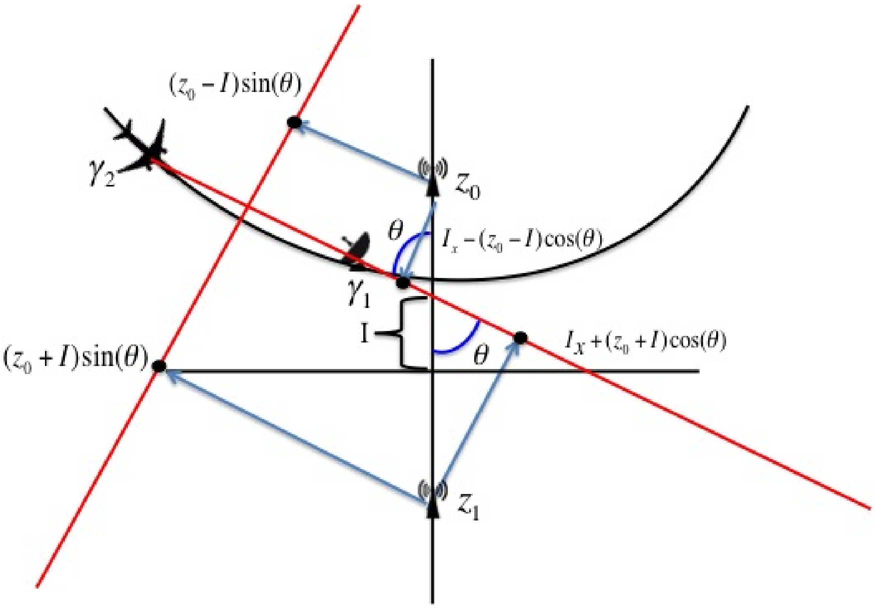

Figure 8.2: A top down view of a two coordinate system representations of the scene under observation.

receivers. We denote this second coordinate system by $(\tilde{x}, \tilde{y}, \tilde{z})$. As before, since γ_2 and γ_1 are located on the same hyperboloid at the same height, the angle θ that the $\tilde{x}$-axis intersects the y-axis with must be between 0 and $\pi/2$.

The location of the two focused points with respect to this second coordinate system are given by

$$\mathbf{z_0} = \big(I_x - (z_0 - I)\cos(\theta),\ (z_0 - I)\sin(\theta),\ 0\big) \tag{8.22}$$

$$\mathbf{z_1} = \big(I_x + (z_0 + I)\cos(\theta),\ (z_0 + I)\sin(\theta),\ 0\big). \tag{8.23}$$

Similarly to our proof of Theorem 1, we may define an elliptic cylindrical coordinate system (μ, ν, z) based on γ_2 and γ_1. Where

$$\tilde{x} = a\cosh(\mu)\cos(\nu) \tag{8.24}$$

$$\tilde{y} = a\sinh(\mu)\sin(\nu) \tag{8.25}$$

$$\tilde{z} = z. \tag{8.26}$$

In order for $\mathbf{z_1}$ to be a focused point it must be true that it lies on the same hyperbola of intersection formed by the hyperboloid of TDOA and the ground plane as $\mathbf{z_0}$ for all locations of $\gamma_2(s)$. In our elliptic cylindrical coordinate system, $z_{0z} = z_{1z} = 0$ because the ground plane is flat and both emitters are located on the ground. Thus, for $\mathbf{z_1}$ to be a focused point we must have

$$\tilde{\mathbf{z}}_\mathbf{0} = (a\cosh(\mu_0)\cos(\nu_0), a\sinh(\mu_0)\sin(\nu_0)) = \big(I_x - (z_0 - I)\cos(\theta), (z_0 - I)\sin(\theta), 0\big) \tag{8.27}$$

$$\tilde{\mathbf{z}}_\mathbf{1} = (a\cosh(\mu_1)\cos(-\nu_0), a\sinh(\mu_1)\sin(-\nu_0)) = \big(I_x + (z_0 + I)\cos(\theta), (z_0 + I)\sin(\theta), 0\big) \tag{8.28}$$

However, this is the same condition which we examined in our proof of Theorem 1 in chapter 7 (see equations (7.33)-(7.36)). There we found that these equations imply that $\theta = 0$ for all points along the flight path and that $\theta = 0$ implies that the hyperboloid on which the two receivers lie is the flat plane which bisects the line segment $\overline{\mathbf{z_0}\mathbf{z_1}}$ and meets the ground plane at a right angle.

The case in which the stationary receiver is not at the same height as the moving receiver is only slightly more complicated. In the case in which the moving and stationary receivers are confined to the same hyperboloid, but do not necessarily occupy the same height in the scene a few additional details need to be explained. As previously mentioned, when the receiver in motion is constrained to fly at a constant height h within the hyperboloid defined by $|\gamma_2(s) - \mathbf{z_0}| - |\gamma_2(s) - \mathbf{z_1}| = C$, its path must follow along some hyperbola at a height above the ground plane; let this height be h_2.

Similarly, regardless of its height, the stationary receiver must also be on some hyperbola at a height h_1 above the ground plane not necessarily equal to h_2. Note that we could have $h_1 = 0$ for the case in which our stationary receiver is located on a short tower near our scene of interest for example. This situation is shown graphically in figure 8.3.

This more expansive data collection geometry can be broken down into a few broad cases. By treating each of these cases in turn we can show that in every case the resulting data collection geometry can be shown to produce an equivalent set of conditions on the locations of $\mathbf{z_0}$ and $\mathbf{z_1}$ to those found in equations (8.27) and (8.28).

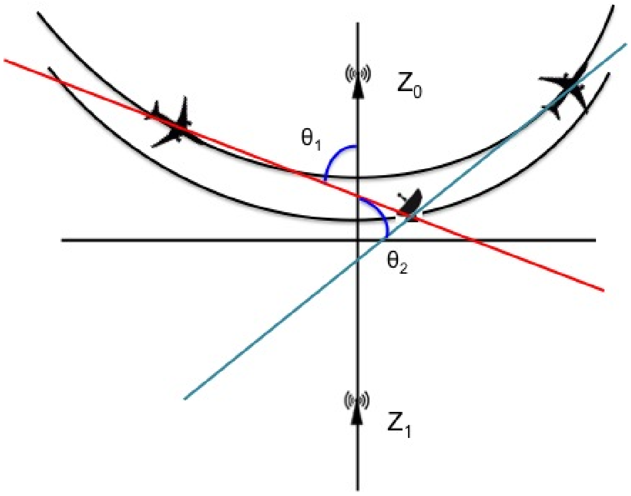

Figure 8.3: The two hyperbolas on which the receivers are located within the hyperboloid constraining the receiver locations. These hyperbolas are projections onto the ground plane of constant-elevation flight paths on the hyperboloid.

The cases can be broken down as follows. First the stationary receiver must be either at a higher or a lower elevation in z than the moving receiver. Second, the two receivers must be either on the same, or opposite sides of the y-axis. Throughout this analysis we shall assume that the receivers lie on hyperbolas above the x-axis. Since the hyperbolas which lie below the x-axis are symmetric to those above the axis, and the orientation of the axis was arbitrarily determined to begin with, this does not reduce the generality of the proof.

First, we consider the case in which the stationary receiver is at a lower elevation than the moving one and the two are on opposite sides of the y-axis. This is pictured in figure 8.3 with the red line drawn between the two receivers.

Here, it is clear that whenever the stationary receiver is on the opposite side of the y-axis from the moving receiver, the angle that the line between the receivers projected onto the (x, y) plane makes with the y-axis will be non-zero for all but at most one point (that point being a time at which $\gamma_{2y}(s) = \gamma_{1y}(s)$) and the point of intersection with the y-axis will be above the x-axis. Whenever the stationary receiver is at a lower elevation than the moving receiver, this angle will be less than $\pi/2$. In this case our argument from the equal height case carries over exactly.

Secondly, we consider the case in which the stationary receiver is at a lower elevation than the moving one and the two are on the same side of the $y$axis. This situation is pictured in figure 8.3 with the blue line drawn between the two receivers.

In this case, the intersection of the line between $\gamma_2(s)$ and $\gamma_1(s)$ with the y-axis may, depending on the location of the two receivers, fall below the x-axis rather than above it. This is also easily handled. If the line intersects the y-axis below the origin we simply replace I with $-I$. Similarly we now have I_x on the negative side of the $\tilde{x}$-axis so that we will have $-I_x + (z_0 - (-I))\cos(\theta)$ rather than $I_x - (z_0 - I)\cos(\theta)$ whenever the $\tilde{x}$-axis intersects the y-axis at a point when $\tilde{x}$ is less than zero. These two changes merely change the overall sign in our expressions for $\tilde{z}_{0x}$ and $\tilde{z}_{1x}$. Thus, by merely canceling a -1 on each side of equation (8.29) we have

$$a\cosh(\mu_0)\cos(\nu_0) + z_0\cos(\theta) = a\cosh(\mu_1)\cos(\nu_0) - z_0\cos(\theta) \tag{8.29}$$

$$-a\sinh(\mu_0)\sin(\nu_0) + z_0\sin(\theta) = -a\sinh(\mu_1)\sin(\nu_0) - z_0\sin(\theta). \tag{8.30}$$

Which are exactly the same two conditions arrived at in equations (7.41) and (7.42) which we found led to a contradiction. Thus, in this case also, the two receivers must lie on the bisecting plane of $\overline{\mathbf{z_0 z_1}}$.

Now we consider the case in which the stationary receiver is at a higher elevation that the moving one. When the stationary receiver is at some height $h_1 > h_2$, then it will be located on a hyperbola whose projection onto the ground plane is at a larger value of y. That is to say, the stationary receiver will be on a hyperbola which is closer to $\mathbf{z_0}$ than the moving receiver. This is the opposite of the situation pictured in figure 8.3.

First we consider the case when the two receivers are on the same side of the y-axis. In this case, there will still be a portion of the moving receiver's flight path for which $0 < \theta_1 < \pi/2$. Specifically this will occur whenever $\gamma_{2y}(s) > \gamma_{1y}(s)$. If the moving receiver is at any time at a point with a greater value of y than the stationary one this alone is enough to cause a contradiction.

This forces our two receivers to be located on the same plane bisecting the line $\overline{\mathbf{z_0 z_1}}$ as was the case for the equal height scenario. This is shown in figure 8.4.

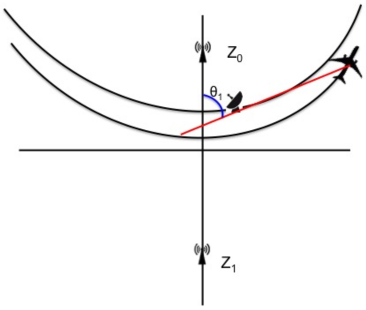

Figure 8.4: A stationary receiver at a higher elevation in z will still produce an acute angle for the second coordinate axis when the moving receiver is at a higher value of y along its flight path.

However, for some locations along this flight, the angle shown in figure 8.4 will be greater than $\pi/2$. This is not a problem. It is a simple matter to point out that whenever the angle shown in figure 8.4 is greater than $\pi/2$ then the angle on the opposite side of the y-axis will be between 0 and $\pi/2$. This is shown in figure 8.5. We simply define the angle shown in figure 8.5 to be θ and define the set of coordinates $(\tilde{x}, \tilde{y})$ according to this angle. Thus, in either case, θ is limited to the range we have already considered. Thus, all of the trigonometric identities we have used continue to hold and the proof by contradiction remains valid.

As seen in figure 8.5, this continues to hold true in the final case in which the moving receiver is on the opposite side of the y-axis as the stationary one.

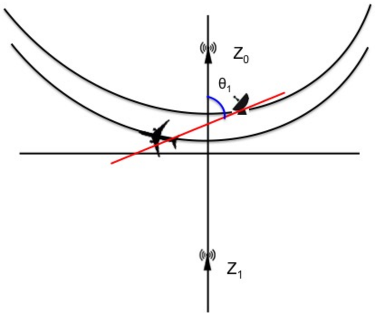

Figure 8.5: A stationary receiver at a higher elevation in z will still produce an acute angle for the second coordinate axis when the moving receiver is at a lower value of y along its flight path.

Thus, regardless of the height of the stationary receiver, in order for a second focused point to appear in the image, the two receivers must be confined to the same plane bisecting the line $\overline{\mathbf{z_0 z_1}}$. Since both receivers have known trajectories which are under the control of the data collection designer, we can safely assume that this one highly specific data collection path can be avoided.

Thus if the receiver in motion flies at a constant height above the ground plane, whenever a focused point exists in the family of backprojections it is unique and the envelope contains only that point regardless of the data collection flight path unless for some portion of the flight path the moving receiver flies directly toward or away from the stationary receiver's position. □

Having now extended the proof of uniqueness to the three dimensional data collection case we turn to the question of existence. Here we extend the second theorem to demonstrate that, as in the two dimensional geometry previously considered, the only focused points in the image will be emitter locations.

Corollary to Theorem 2: *If, as described in the data collection model of Corollary 1, one receiver is stationary and not in the same vertical plane with the moving receiver's flight path, the only focused points for all backprojection hyperbolas in the image given by equation* (8.4) *are the emitter locations regardless of the flight path of the second receiver.*

We shall prove this theorem by exhausting the possible cases in which the receiver/emitter geometries can be set up. We first examine the diagonal terms and then move to the cross terms.

Proof: *Case 1: The diagonal terms.*

The contribution to the image of any diagonal term in the data takes the form

$$\int e^{i2\pi(t-r(s,\mathbf{z}))}Q(s,f,\mathbf{z})d_D(s,t)dsdt \tag{8.31}$$

where $d_D(s,t)$ is the data term being backprojection onto the image.

In theorem 2 we proved that the only focused points resulting from the diagonal terms are at the locations of the emitters corresponding to those terms regardless of data collection geometry. We will here consider only the cross terms.

In theorem 2 we also demonstrated that for a given cross term, three outcomes may be possible, namely either that a focused point exists and exists at the location of one of the two emitters, that a focused point exists and exists at some location in the image at which there is no emitter, or else that no focused points exist in the resulting image due to the cross term.

Subcase I A: We consider first the possibility that a focused term exists at the location of one of the two emitters present in the scene.

Let $\mathbf{e_1}, \mathbf{e_2}$ be the location of two emitters in the scene. Then the contribution to the image for each of the cross terms from such emitters takes the form

$$\int e^{i2\pi(t-r(s,\mathbf{z}))} Q(s,f,\mathbf{z}) d_C(s,t) ds dt. \tag{8.32}$$

where $d_C(s,t)$ is the data term resulting from either the correlation of the signal at emitter $\mathbf{e_1}$ with the signal at emitter $\mathbf{e_2}$ or vis versa. Without loss of generality we will examine the case in which the term under consideration arises from the correlation of the signal emitted by $\mathbf{e_1}$ and received at the receiver at $\gamma_1(s)$ with the signal emitted by $\mathbf{e_2}$ and received at the receiver at $\gamma_2(s)$ at time s.

As we have seen, this results in the backprojection of the product $Q(s,f,\mathbf{z})d_C(s,t)$ along the hyperbola which is the intersection of the ground plane and the hyperboloid defined by

$$|\gamma_2(s) - \mathbf{z}| - |\gamma_1(s) - \mathbf{z}| = |\gamma_2(s) - \mathbf{e_2}| - |\gamma_1(s) - \mathbf{e_1}|. \tag{8.33}$$

Assume that there exists a focused point for these backprojections and let that point be denoted $\mathbf{z_0}$ where $\mathbf{z_0} = \mathbf{e_1}$ or $\mathbf{z_0} = \mathbf{e_2}$.

We first consider the case where $\mathbf{z_0} = \mathbf{e_2}$, that is, the case in which a focused point occurs at the location of the emitter whose signal was recorded at the moving receiver. We shall handle the case for which $\mathbf{z_0} = \mathbf{e_1}$ in *Subcase I B*.

Since $\mathbf{z_0}$ is a focused point

$$|\gamma_2(s) - \mathbf{z_0}| - |\gamma_1(s) - \mathbf{z_0}| = |\gamma_2(s) - \mathbf{e_2}| - |\gamma_1(s) - \mathbf{e_1}|. \tag{8.34}$$

for all time steps s. Since $\mathbf{z_0} = \mathbf{e_2}$ we have

$$|\gamma_1(s) - \mathbf{z_0}| = |\gamma_1(s) - \mathbf{e_1}| \tag{8.35}$$

which implies

$$|\gamma_1(s) - \mathbf{e_2}| = |\gamma_1(s) - \mathbf{e_1}| \tag{8.36}$$

for all s, since we have postulated $\mathbf{z_0} = \mathbf{e_2}$. This is true if and only if the two emitters lie on the same sphere centered at the stationary receiver. Since we assume that the emitters are located within the same flat ground plane this condition amounts to a restriction of the location of the two emitters to a circle in the ground plane centered at the x, y coordinates of the stationary receiver.

Thus, a focused point for the cross term data exists at the location of the emitter whose signal was received at the moving receiver whenever the second emitter is equidistant to the stationary receiver. If the two are not equidistant then equation (8.35) is a contradiction and no such focused point exists.

Subcase I B: Now consider the analogous case in which $\mathbf{z_0} = \mathbf{e_1}$. Similarly in this case we find that $\mathbf{z_0}$ must satisfy

$$|\gamma_2(s) - \mathbf{z_0}| = |\gamma_2(s) - \mathbf{e_2}| \tag{8.37}$$

for all s. This equation states that the distance from the moving receiver to the focused point at $\mathbf{z_0}$ is equal to the distance from the receiver to the emitter at $\mathbf{e_2}$, whose signal it is receiving at all points along its flight path. Since $\mathbf{z_0} = \mathbf{e_1}$ we thus have the condition

$$|\gamma_2(s) - \mathbf{e_1}| = |\gamma_2(s) - \mathbf{e_2}| \tag{8.38}$$

for all s.

However, since we have postulated that there are two emitters so that $\mathbf{e_1} \neq \mathbf{e_2}$ and that $\gamma_2(s_1) \neq \gamma_2(s_2)$ for any time step s_1 because γ_2 is in motion, this is possible only in the case in which the moving receiver flies a path contained entirely within the plane which bisects the line segment joining $\mathbf{e_1}$ and $\mathbf{e_2}$ and is perpendicular to the ground plane. In the rare case that the moving receiver flies a flight path exactly between two emitters in the scene in this manner, then there will be a focused point due to the cross term of the two emitters at the point corresponding to the location of the emitter whose signal was received at the stationary emitter.

Thus, as was the case in the two dimensional data collection geometry, when we consider the possibility of the backprojection image containing a focused point due to a cross term which arises at the location of one of the emitters we find: if two emitters are equidistant from the stationary receiver, then each emitter is the focused point of the backprojection of the cross term in which that emitter's signal is the signal received at the moving receiver. Similarly, if the moving receiver flies a flight path in the bisecting plane so that it is at all times exactly between two emitters with respect to the ground plane so that it is always equidistant from both of them, then each emitter is the focused point of the backprojection of the cross term in which that emitter's signal is the signal received at the stationary receiver.

Otherwise, there are no focused points at the location of either emitter due to the cross terms. In these cases, since a focused point is unique, no other focused points exist in the image due to that data term.

Subcase II: Now assume that there exists a focused point in the image due to a cross term which is not located at an emitter's position. Let this point be denoted by $\mathbf{z_0}$ where $\mathbf{z_0} \neq \mathbf{e_1} \neq \mathbf{e_2}$. As seen in the proof of our first theorem, this implies

$$|\gamma_2(s) - \mathbf{z_0}| - |\gamma_2(s) - \mathbf{e_2}| = |\gamma_1(s) - \mathbf{z_0}| - |\gamma_1(s) - \mathbf{e_2}|. \tag{8.39}$$

If $\mathbf{z_0}$ is a focused point it must also satisfy

$$\frac{(\gamma_2(s) - \mathbf{z_0}) \cdot \dot{\gamma}_2(s)}{|\gamma_2(s) - \mathbf{z_0}|} = \frac{(\gamma_2(s) - \mathbf{e_2}) \cdot \dot{\gamma}_2(s)}{|\gamma_2(s) - \mathbf{e_2}|} \tag{8.40}$$

for all s.

Since $\gamma_1(s), \mathbf{e_1}$ and $\mathbf{z_0}$ are constants we have

$$|\gamma_2(s) - \mathbf{z_0}| - |\gamma_2(s) - \mathbf{e_2}| = C \tag{8.41}$$

for C is constant.

In the conclusion to the proof of the corollary to Theorem 1, we showed these conditions are met if and only if the moving receiver flies a flight trajectory constrained to a plane bisecting the line segment joining the two points $\mathbf{z_0}$ and $\mathbf{e_2}$ and making a right angle with the ground plane. Otherwise we have reached a contradiction and no such focused point exists.

However, if the moving receiver flies entirely within this plane, then its distance to each of those points is equal at all times, thus $|\gamma_2(s) - \mathbf{z_0}| = |\gamma_2(s) - \mathbf{e_2}|$. Therefore $C = 0$. But the constant C is given by the equation

$$C = |\gamma_1(s) - \mathbf{z_0}| - |\gamma_1(s) - \mathbf{e_2}|. \tag{8.42}$$

If $C = 0$ then $|\gamma_1(s) - \mathbf{z_0}| = |\gamma_1(s) - \mathbf{e_2}|$. Thus the distance from the stationary receiver to the emitter $\mathbf{e_2}$ and the cross term focused point $\mathbf{z_0}$ is equal. Since $\mathbf{e_2} \neq \mathbf{z_0}$ by assumption we have that $\mathbf{z_0}$ and $\mathbf{e_2}$ lie on the same sphere centered on the stationary receiver γ_1.

Combining this requirement with the one that the moving receiver fly directly between the two points leaves us with the moving receiver flying a flight path either directly toward or away from the stationary receiver with respect to its x, y position in the ground plane. Thus the only focused point which can exist at a location other than the true location of an emitter due to a cross term is a mirror point which is caused by flying a flight path we have disallowed.

Conclusion: The cross terms do not produce focused points in the image except for certain specific geometries. Those geometries are: 1) When two emitters are equidistant from the stationary receiver. In this case the cross term due to the signal received by the moving receiver and cross correlated with the signal received at the stationary receiver will focus at the emitter which transmitted the signal recorded at the moving receiver. 2) When two emitters are at all times equidistant from the moving receiver, that is, when the moving receiver flies a trajectory constrained to a plane between two emitters that makes a right angle with the ground plane. In this case, the cross term due to the signal recorded at the stationary receiver and cross correlated with the one received at the moving receiver will focus at the location of the emitter whose signal was received by the stationary receiver.

Thus, excluding flight paths which travel directly toward or away from the stationary receiver with respect to the ground plane dimensions of the receiver positions, the only focused points for any family of back projection hyperbolas in the image are the emitter locations, regardless of the flight path of the moving receiver. Furthermore, with the exception of a few special cases, the focused points will be due to the diagonal terms in our data. □

We have thus extended the previous two proofs to show that persistent peaks in the final image, due to all data terms, will be those points which correspond to the location of an emitter in the scene for arbitrary flight paths in three dimensions provided one receiver is stationary. As before, the contribution to the final image of the cross terms will be to gradually blur out along the envelope of the family of backprojections as the receiver travels along its path. We will now turn to the numerical simulation of several flight paths for which these corollaries hold.

8.1 Numerical Examples

We begin by examining the cases in which the stationary receiver hovers above the ground plane at the same height as the moving receiver. We will examine this case for different heights above the ground plane. In this case the receivers may be drones such as the common quadcopter model which have the capability to hover at arbitrary locations above the ground plane.

We will then consider the case of a stationary ground based receiver such as a radar located on a short tower or other ground based platform. We will then conclude by briefly examining the case in which the previously stationary receiver flies a short flight path which results in a stationary focus for the family of backprojections. We examine this final case as an example for future work of what may be possible with two receivers flying complimentary flight paths.

In the following examples the stationary receiver is located at $\gamma_1(s) = (10km, 20km, h)$ and the moving receiver flies from $\gamma_2(s_0) = (0km, 0km, h)$ to $\gamma_2(s_T) = (20km, 0km, h)$ where h is the height of the flight path. The scene is a $2km \times 2km$ square located at the center of the moving receiver's flight path and equidistant between receivers at the midpoint of the flight. This flight path geometry is illustrated in in figure 8.6.

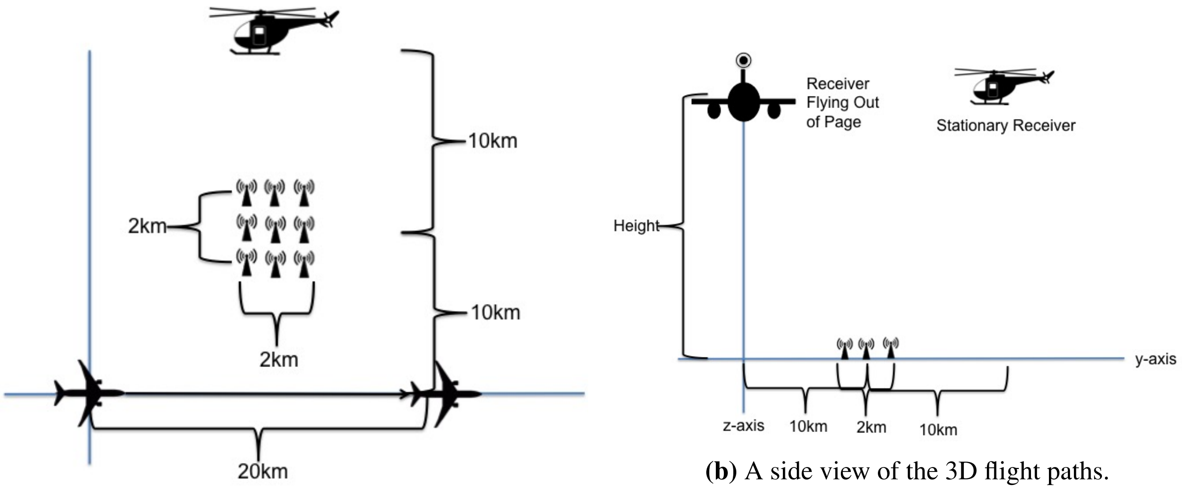

(a) A top view of the 3D flight paths.

(b) A side view of the 3D flight paths.

Figure 8.6: A diagram of the three dimensional data collection geometry.

Using a height of $1km$ and flying the flight paths discussed above we observe a scene containing two emitters transmitting identical waveforms as described in Chapter 7. Processing the data according to our model and performing the backprojection over the hyperboloid of equal TDOA according to equation (8.4) we construct the SASL image shown in figure 8.7a. We can contrast this image with the image shown in figure 8.7b. In this second image the flight paths are the same, however, the two receivers are located at a height of $5km$ rather than $1km$.

We note that in figure 8.7b the cross term phantom effects are worse than in figure 8.7a and the resolution is slightly worse as well. We can use the mathematical framework for image resolution derived in section 5.4 to explain these effects.

Recall here that the range direction runs along the image y-axis and the cross range direction is along the x-axis. Using the parameters above in the resolution formulas we developed, we find

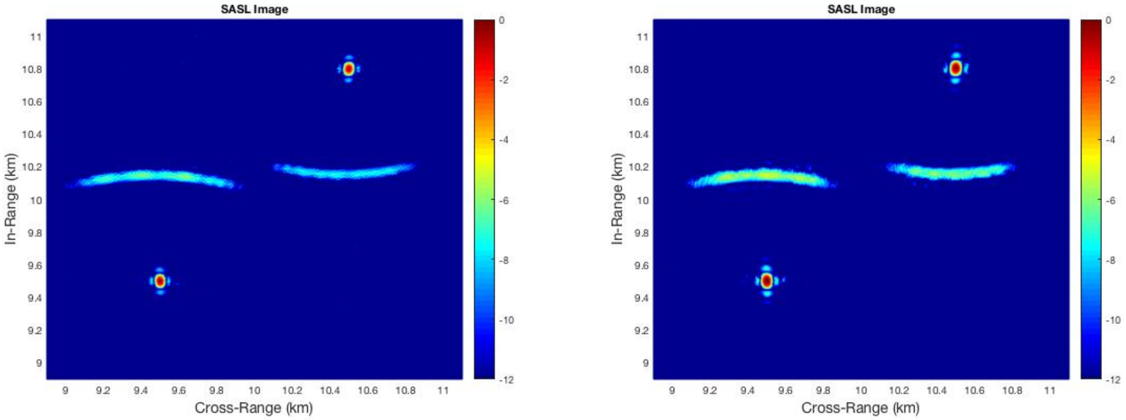

(a) Receiver height at $1km$

(b) Receiver height at $5km$

Figure 8.7: A scene with two emitters imaged from a flight path above the ground plane.

that the cross range resolution for the $1km$ height flight path, after algebraic simplification, is

$$\Delta_{CR}(h = 1km) = \frac{2\pi c_0}{f} \left(\frac{\Delta(\gamma_{2x}(s))}{2|\gamma_2(s) - \mathbf{z}|} \right)^{-1} = 8.9 \frac{c_0}{f} \approx 67m. \tag{8.43}$$

The cross range resolution for the the $5km$ heigh flight path is

$$\Delta_{CR}(h = 5km) = \frac{2\pi c_0}{f} \left(\frac{\Delta(\gamma_{2x}(s))}{2|\gamma_2(s) - \mathbf{z}|} \right)^{-1} = 9.4 \frac{c_0}{f} \approx 71m. \tag{8.44}$$

Similarly, the range resolution for each case can be computed as

$$\Delta_R(h = 1km) = \frac{2\pi c_0}{B_w} \left(\frac{(\gamma_{2y}(s) - \mathbf{z}_y)}{2|\gamma_2(s) - \mathbf{z}|} - \frac{(\gamma_{1y}(s) - \mathbf{z}_y)}{2|\gamma_1(s) - \mathbf{z}|} \right)^{-1} \approx 94m \tag{8.45}$$

and

$$\Delta_R(h = 5km) = \frac{2\pi c_0}{B_w} \left(\frac{(\gamma_{2y}(s) - \mathbf{z}_y)}{2|\gamma_2(s) - \mathbf{z}|} - \frac{(\gamma_{1y}(s) - \mathbf{z}_y)}{2|\gamma_1(s) - \mathbf{z}|} \right)^{-1} \approx 106m. \tag{8.46}$$

Thus, not surprisingly, the increase in height, which leads to a corresponding increase in distance to the target, reduces the achieved resolution. However, simply moving the receivers closer to the target in the range direction will not completely compensate for this loss of resolution. If we fly a third flight path, this time with both receivers $1.3km$ closer to the scene center in the range component of their coordinates so that the total distance to the target emitters is the same as that for the first flight path, our calculated resolutions are

$$\Delta_{CR}(h = 5km, \text{closer range}) = \frac{2\pi c_0}{f}\left(\frac{\Delta(\gamma_{2x}(s))}{2|\gamma_2(s) - \mathbf{z}|}\right)^{-1} = 9.4\frac{c_0}{f} \approx 67m \tag{8.47}$$

and

$$\Delta_{IR}(h = 5km, \text{closer range}) = \frac{2\pi c_0}{B_w}\left(\frac{(\gamma_{2y}(s) - \mathbf{z}_y)}{2|\gamma_2(s) - \mathbf{z}|} - \frac{(\gamma_{1y}(s) - \mathbf{z}_y)}{2|\gamma_1(s) - \mathbf{z}|}\right)^{-1} \approx 109m. \tag{8.48}$$

Here we see that the reduction in the range component of the distance, which leads to an increase in the angular coverage, improves the cross range resolution to match that of the flight path with a height of $1km$. However, this change also makes the range resolution slightly worse than the resolution loss already experienced due to the increase in the distance to the target. The reason for this is clear from equation (5.29). The reduction in the range distance decreases the quantify $\gamma_{2y}(s) - \mathbf{z}_y$ which has a deleterious effect on the resolvability of targets in range. These affects can be seen visually by comparing the images produced from each of these two flight paths.

In figure 8.8 we compare the two $5km$ height flight paths so far discussed. As predicted we see that the cross range resolution is improved when the receivers are moved closer to the scene center in the range component of the flight path, but that the range resolution suffers slightly from the change. The overall effect on the phantoms appears to be a slight reduction in their presence, but not to the levels seen in figure 8.7a.

Thus we conclude that, when possible, for a given distance to the target scene in range and for a given length of synthetic aperture, a better image is produced by receivers flying closer to the ground plane since this produces a larger aperture from which we image the scene.

8.1.1 Tower and Drone Collection

Having established the fundamental effects of a three dimensional data collection and examined their relation to the two dimensional cases already examined we now consider the image produced

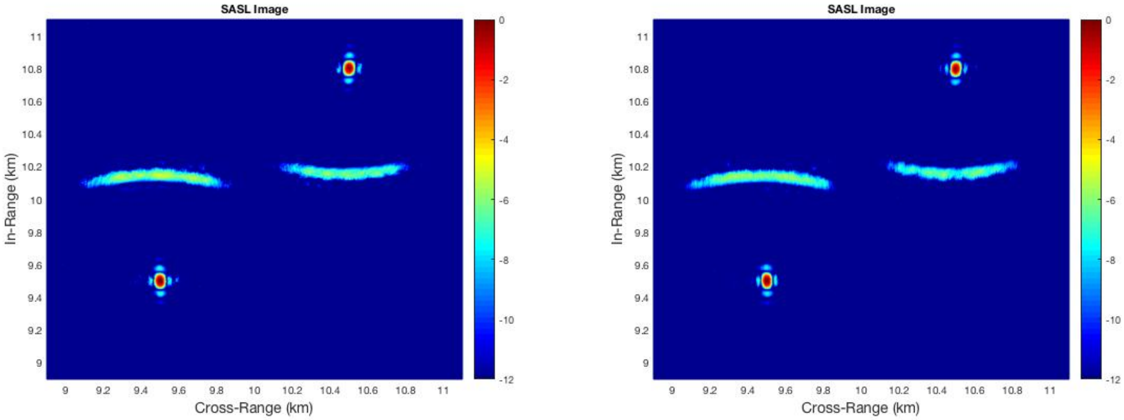

(a) Receiver height at $5km$ and $10km$ from the scene center in range **(b)** Receiver height at $5km$ and $8.7km$ from the scene center in range

Figure 8.8: A scene with two emitters imaged from flight paths at equal heights above the ground plane.

with data collected from a low flying drone and a stationary receiver located in the ground plane on a fixed tower. This flight path is shown graphically in figure 8.9.

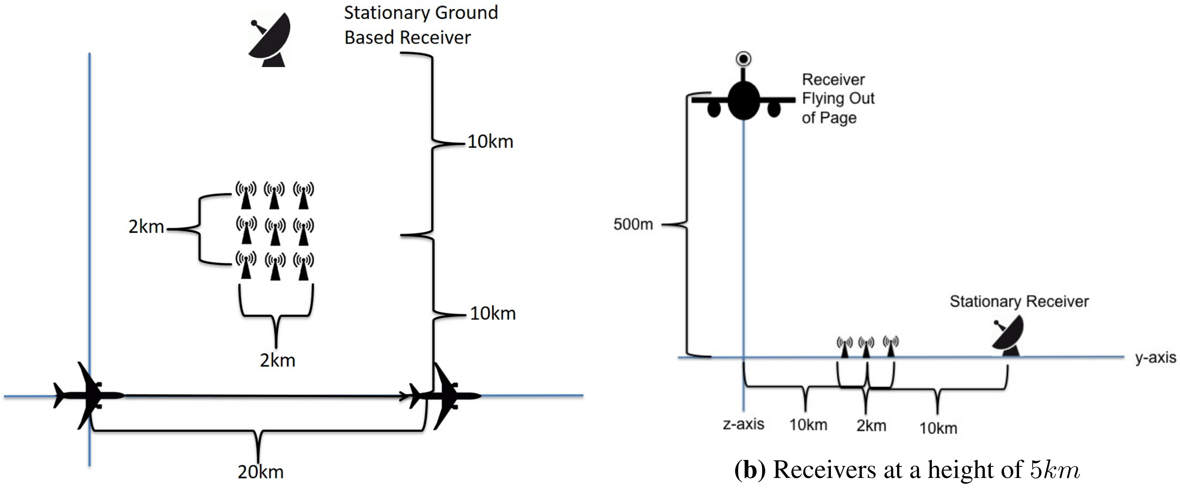

(b) Receivers at a height of $5km$

(a) Receivers at a height of $1km$

Figure 8.9: A data collection using one moving receiver and one ground based receiver.

Starting from equation (8.7) we can derive the expression for the intersection of the hyperboloid of TDOA and the ground plane. In our earlier example, the ground plane was located at a constant height $-h$ below both receivers so that the intersection occurred in the plane $z = -h$. In this case the intersecting plane has a more complicated expression.

Since the stationary receiver is located in the ground plane and the moving receiver is located at a fixed height h above the ground plane, when the coordinate system is defined by the location of the two receivers according to $\gamma_1(s) \equiv (d, 0, 0)$ and $\gamma_2(s) \equiv (-d, 0, 0)$, the equation for the ground plane can be expressed as $z = f(x)$ for some function f.

Here, we know that the ground plane contains the points $(d, 0, 0)$ and $(-d, 0, -h)$. From this we can find the expression of the ground plane as

$$z = f(x) = \frac{h}{2d}x - \frac{h}{2}. \tag{8.49}$$

Thus the curve of intersection is defined by

$$\frac{x^2}{a^2} - \frac{y^2}{b^2} - \frac{(\frac{h}{2d}x - \frac{h}{2})^2}{b^2} = 1 \tag{8.50}$$

$$\frac{x^2}{a^2} - \frac{y^2}{b^2} - \frac{h^2x^2}{4d^2b^2} + \frac{h^2x}{2db^2} = 1 + \frac{h^2}{2b^2} \tag{8.51}$$

$$\frac{x^2(4d^2b^2 - a^2h^2)}{4a^2d^2b^2} - \frac{y^2}{b^2} + \frac{h^2x}{2db^2} = 1 + \frac{h^2}{2b^2}. \tag{8.52}$$

We can determine the kind of conic section this expression defines by examining the discriminant. [44]

In this case the discriminant is given by

$$\mathcal{D} = \frac{4d^2b^2 - a^2h^2}{4a^2d^2b^2}\frac{1}{b^2}. \tag{8.53}$$

So, $\mathcal{D} > 0$ if

$$d^4 - d^2a^2 - a^2h^2 > 0. \tag{8.54}$$

Substituting $y^2 + h^2 = a^2$ where y is the distance to the target emitter in the ground plane we find that we require

$$-\frac{h^4}{d^2} - (1 + \frac{y^2}{d^2})h^2 + d^2 - y^2 > 0. \tag{8.55}$$

For the data collection geometry we have defined this occurs whenever $h < 13789m$. Once our receiver drone flies above this height the intersection of the hyperboloid with the ground plane becomes elliptical instead of hyperbolic. This height ceiling will increase as total receiver stand off from the target emitter increases. As such, it is not a fundamental limit of our method. By flying farther from the target in the ground plane range direction the receiver can increase its height without violating this ceiling.

For our purposes $13000m$ is more than an order of magnitude greater than the height we are examining. As such we can safely consider the TDOA curves to be hyperbolas in the ground plane at all times during the data collect.

The resulting SASL image is shown in figure 8.10. We see that, despite the analytic expression for the backprojections being far more complicated than in any case previously considered, the resulting SASL image closely matches those of the other data collections so far considered in this chapter.

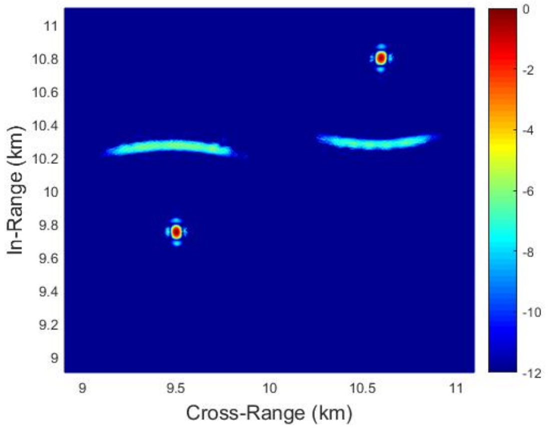

Figure 8.10: The SASL image from a ground based and arial receiver pair.

8.1.2 A Two Moving Receiver Example

Recall that it has yet to be determined if a truly stationary receiver is desirable, or if a second moving receiver provides an advantage in the quality of the SASL image. We have focused on the case of a stationary receiver in this document because doing so greatly simplifies the analytic proof of certain properties of the backprojection. This allows us to make definitive statements regarding the method's utility and provide proofs of certain phenomena in the SASL image.

When both receivers are in motion the frequency difference of arrival curves become far more complicated which adds additional layers of difficulty to the stationary phase arguments we have previously made. We leave as future work the analytic analysis of these more difficult curves which may determine whether having one receiver held at a stationary point provides some imaging benefit, or if some benefit may be obtained by having such a receiver fly a complementary flight path with respect to the second receiver.

As a first step toward examination of such potential complimentary flight paths we conclude this chapter with a simulated case in which the second receiver flies a flight path which produces one fixed focus for all backprojection hyperbolas in the ground plane. Recall that a hovering craft cannot reasonably approximate a stationary point in the ground plane with respect to the backprojection hyperbolas when that receiver's height is well above the plane.

A stationary focus position can be achieved however, by flying a flight path which exactly compensates for the movement of the focus of the hyperbola in the ground plane with respect to the backprojections produced. In this way, we illustrate how a realistic flight scenario in three dimensions can reproduce the same backprojection family seen in the two dimensional model worked through in Chapter 7.

As seen in equation (8.16), the location of the foci of the backprojection hyperbola in the plane is a deterministic function of the two receiver positions. We assume that both receiver trajectories are known and under the control of the operator. Under these conditions, it is possible to design a flight path for the first receiver which exactly compensates for the motion of the focus of the backprojection curve with respect to the scene center which is caused by the flight path of the second receiver.

In this manner, the first receiver can fly a short flight path nearly parallel to that of the second receiver which results in the focus position, Γ_1, remaining fixed. In such a case, the family of backprojections mimics that of the examples previously seen in the two dimensional simulations.

As a simple example of what such a path looks like, consider the case shown in figure 8.11. In this figure the blue line represents the flight path of the first receiver, that is, the receiver we have previously taken to be stationary. The second receiver flies a straight line flight path $20km$ long at a height of $5km$ from a starting location of $(0km, 0km, 5km)$ to an ending point at $(20km, 0km, 5km)$. Note again that this path is well below (with respect to the y-axis) the visible patch of the plane shown in figure 8.11.

By flying along the blue trajectory, a distance of roughly $1km$, at a height of $5km$ the first receiver compensates for the effects of the motion of the second receiver on the position of the foci in the ground plane resulting in a stationary location for the focus at $\Gamma_1 \equiv (10km, 21km)$ represented by the red X.

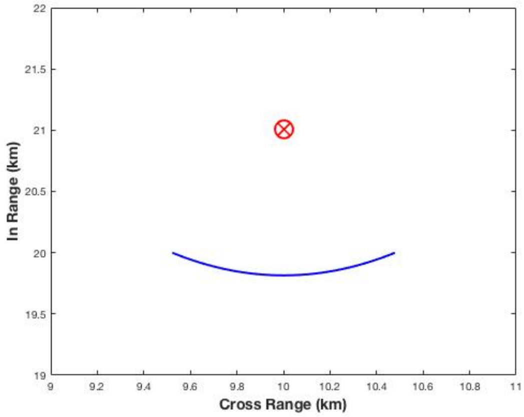

Figure 8.11: A receiver which flies a carefully designed flight path can compensate for the apparent motion caused by the second receiver resulting in a stationary focus.

A diagram of this flight path is shown in figure 8.12. In this example, both of our receivers are in motion along a physically realizable path in three dimensional space which produces a targeted result, in this case a stationary point for the family of backprojections. We make no claim that producing a stationary focus point for the family has a significant benefit in image quality.

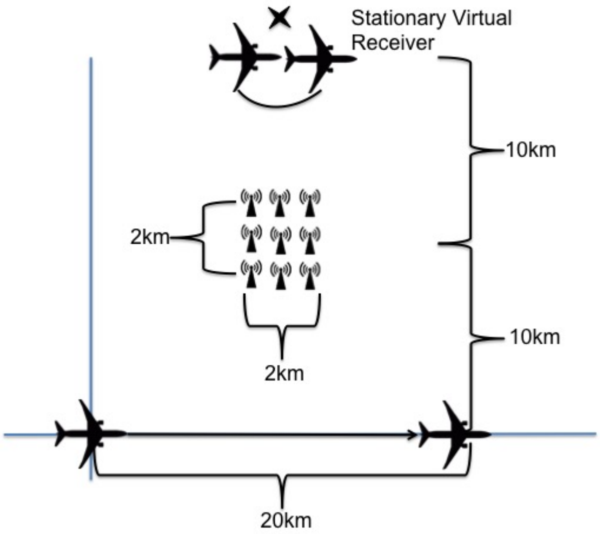

Figure 8.12: Diagram of the flight path which compensates from the virtual motion of a hovering receiver.

We illustrate it here merely to showcase the kind of complementary flight paths which it will be possible to design with the full characterization of the family of backprojections we have derived above. We leave for future work the determination of the most desirable characteristics to be targeted in the determination of the flight path.

For completeness in our simulations we consider both the case when the two receivers are flying at a height of $1km$ above the ground plane and the case in which they are $5km$ up. The images produced from these flight paths are simulated in figure 8.13. In each of these cases it is difficult to detect a large difference between this case and the case of the hovering receiver.

This is consistent with our observations in Appendix E that the change in the focus location is rather small in comparison to the motion due to the flight path of the second receiver. As such, we should not expect that this ‘motion compensation’ flight path would have a strong impact on either improving or deteriorating the quality of the image.

Indeed, as we have said, there may be nothing desirable about having such a stationary focus for the family of backprojections. We have concluded with this case merely as a simple example of how a detailed knowledge of the nature of the family of backprojection curves may aid our investigation into the more complicated flights paths which are possible when both receivers are in motion. It may be possible to construct more detailed flight paths for the two receivers which

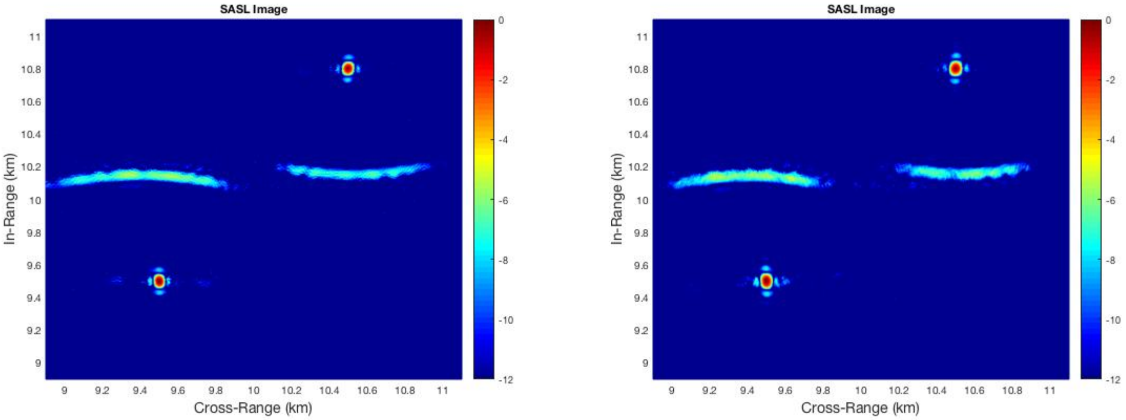

(a) Receivers at a height of $1km$

(b) Receivers at a height of $5km$

Figure 8.13: The case of both receivers in motion with one flying so as to produce a stationary virtual focus, for two different heights above the ground plane

maximize the angles viewed for the scene under surveillance or take account of a priori knowledge of the scene to maximize final image quality. We leave the investigation of such possibilities to future work.

Now that we have built a robust model of three dimensional data collection and simulated the creation of SASL images from three dimensional flight paths we will turn to the final step in providing a theoretical demonstration of the feasibility and utility of this approach, the creation of a SASL image from noisy signals.

Chapter 9

SASL WITH NOISY SIGNALS

Now that we have simulated our source localization procedure using a realizable three dimensional data collection we will turn our attention to the impact of noise on our ability to image, and thereby localize, target emitters in a scene of interest.

Random thermal motion of charged particles,whose temperature is above zero Kelvin, causes all objects in the universe to emit electromagnetic waves. These waves are referred to as thermal noise and are always present in the reception of any real-world EM signal. While all objects, including extraterrestrial ones, contribute to the noise present in a received signal, the thermal noise generated by a radar's own internal components usually dominates the contribution of all other sources of grey body radiation if the radar operates at frequencies in the microwave range or above. [28]

Environmental noise arises from everything visible to the radar, including the Sun, the ground, and galactic sources entering through the atmosphere. At frequencies below 1GHz cosmic noise is a significant contributor to the total noise level, but is a minor source of interference at frequencies above this. The nearness of the sun makes it a significant contributor to the environmental noise level, however, this effect can be mitigated by antenna gain if the receiving antennas are not pointed toward the sun's position. [28]

For our purposes we shall assume that the internal noise of the receiver systems dominates the environmental noise to a level where environmental effects can be safely neglected. Thermal noise in the receiver is well modeled by white noise, that is, noise for which the expected value obeys $E[n(t)\bar{n}(t')] = P_n\delta(t-t')$, where P_n is the noise power. Such noise is uniformly distributed over all radar frequencies, though only noise in the range of frequencies capable of being detected by our antennas will have an impact on our ability to form an image of the target emitters. [2, 28]

The standard way to describe the effect of noise on the received signal is the Signal-to-Noise Ratio (SNR). This is the ratio between the signal power and noise power at the receiver. The noise power at the receiver will be proportional to the receiver bandwidth since, as we have just stated, the noise is equally distributed across all frequencies. Thus an increase in the range of the frequencies recorded by the receiver corresponds to an increase in noise power.

Since the noise impacting the signal is created by the thermal motion of charged particles within the receiver, the receiver's internal temperature is also proportional to the power of the recorded noise. Thus we have that the noise power P_n is related to the receiver bandwidth and temperature by

$$P_n = kT_sB \tag{9.1}$$

where k is a constant of proportionality. For our case it turns out that when B is measured in Hertz and T_s in Kelvin k is Boltzmann's constant, that is $k = 1.38 \times 10^{-23}$ watt-sec/K. [28]

The power of the recorded signal is similarly given by

$$P_r = \frac{P_tG_tG_r}{(4\pi)^2R^2} \tag{9.2}$$

where P_t is the transmitted power, G_t and G_r are the gains of the transmitting and receiving antennas respectively, and R is the range from the emitting antenna to the receiving one. [28]

If the system consists of both an isotropic transmitting and receiving antenna the signal power is simply

$$P_r = \frac{P_t}{(4\pi)^2R^2}. \tag{9.3}$$

Thus, the SNR for a signal recorded at an isotropically receiving antenna which was transmitted from an isotropic antenna somewhere in the scene is given by

$$SNR = \frac{P_t}{(4\pi)^2R^2kT_sB}. \tag{9.4}$$

The post processing power of a recorded signal is can be measured by calculation of the integral $P_t = \left[\int h(t)\bar{s}(-t)\right]^2$ where $h(t)$ is the filter we apply to the recorded signal. In our case, the filter for the signal recorded at receiver $\gamma_2(s)$ is the signal recorded at $\gamma_1(s)$ and we apply the filter via cross correlation. The peak of the resulting cross correlation function is then the signal power for the recorded slow time position s.

Similarly the post processing noise power for each look is determined by applying the same correlation process but to the noise signal alone. Thus one applies the same filter to the noise present at the receiving antenna. We then measure the noise power as $P_n = E|\eta_n(\tau)|^2 = \sigma_n^2$ where σ_n^2 is the variance and $\eta_n(\tau)$ is the post processed noise.

Mathematically we have

$$\text{SNR} = \frac{|\eta_s(\tau)|^2}{E|\eta_n(\tau)|^2} = \frac{|\eta_s(\tau)|^2}{\sigma_n^2} \tag{9.5}$$

where

$$\eta_n(\tau) = \int h(\tau - t')n(t')dt' \tag{9.6}$$

and

$$\eta_s(\tau) = \int h(\tau - t')s(t' - \tau)dt' \tag{9.7}$$

for some applied filter $h(t)$.

Numerically this can be accomplished by simulating a signal reception at some time step s_1 and generating a random noise vector of the same length, call this vector $n(t)$. We store both the signal and noise vectors separately for the calculation of the SNR. The two are then added together in order to form the noisy data measurement.

We then process the noisy data in order to form the SASL image. Simultaneously, we process the noiseless data and the data vector containing the noise only in a manner identical to that of the noisy data. We can then measure the SNR in the post processing data by measuring the peak power of the signal and divide by the variance of the noise vector.

This can also be done for the SASL image as a whole to determine the SNR of the final image once all of the slow time snap shots have been integrated into the image. The SNR for the final image should be higher than that measured in the single look SNR calculations since each look should add further improvement in the image SNR. Once this has been done it becomes possible to set the output SNR to any desired level by judiciously adjusting the input power of the noise.

We can accomplish this by carefully tracking the effect of multiplying the input noise by a scaling constant. Recall that the noise power is measured by var$(\eta_n(\tau))$, so the power of the same noise when multiplied by some constant C before signal processing is then

$$\begin{aligned}\tilde{P}_n &= \text{var}\left(\int h(\tau - t')(Cn(t'))dt'\right) = \text{var}\left(C\int h(\tau - t')n(t')dt'\right)\\ &= C^2\text{var}\left(\int h(\tau - t')n(t')dt'\right) = C^2\text{var}(\eta_n(\tau) = C^2 P_n.\end{aligned} \tag{9.8}$$

Thus, the resulting SNR is given by

$$\text{SNR} = \frac{P_s}{C^2 P_n}. \tag{9.9}$$

By simple algebra we can then determine the appropriate scaling of the noise in order to set the output SNR to any desired value as

$$C = \sqrt{\frac{P_s}{(\text{SNR})P_n}}. \tag{9.10}$$

All of this analysis holds true for a traditional active SAR imaging system, for a SASL imaging system however, there is a complication.

The traditional method of measuring SNR described here assumes that one is dealing with purely additive noise and a deterministic filter which is applied to the received signal, traditionally this is the matched filter we encountered in Chapter 3. In our problem however, the role of the filter is played, not by a time reversed copy of the transmitted signal, but by the copy of the signal which is recorded at the second receiver. This copy is of course a noise contaminated version of the transmitted signal.

Thus, when we apply our filter to the additive noise present in the signal recorded at receiver γ_1, the result is

$$\eta_n(s,\tau) = \int h(\tau - t')n(t')dt' = [s_2(s,t) + n_2(t)] \star n_1(t) = s_2(s,t) \star n_1(t) + n_1(t) \star n_2(t). \tag{9.11}$$

Thus, our filter has a random component due to the presence of noise which causes the noise to behave multiplicatively in the processed result, not simply additively as we have previously assumed. This greatly complicates the application of traditional noise measurement methodologies to the calculation of the post processing SNR. An analysis of these complications is beyond the scope of this work and is left to future efforts.

We can, however, safely calculate the input SNR, that is, the SNR before any signal processing is done, and measure our noise contributions rigorously using this method. We can also carry out the numerical SNR calculations described above and achieve a non-rigorous measure of the post processing noise both for the single-look processing step, and for the SASL image as a whole. It is important to remember though, that while these calculations hold a heuristic value in giving the reader an idea of the noise level present in each portion of the SASL imaging process leading to the final image output, only the input SNR level is strictly supported by the established theory of additive noise.

As an example of the additional complications posed by the noise present in what may be termed the *reference channel*, that is the source of the signal which we use in place of the traditional matched filter, we can complete the same analysis carried out in equation (9.8) for the cross correlation case.

With $P_n = \text{var}\left([s_2(s,t) + n_2(t)] \star n_1(t)\right)$ we have

$$\begin{aligned}\tilde{P}_n &= \text{var}\left(\int h(\tau - t')(Cn(t'))dt'\right) = \text{var}\left([s_2 + Cn_2(t)] \star Cn_1(t)\right) \\ &= \text{var}\left(C^2 n_1(t) \star n_2(t) + Cn_1(t) \star s_2(t)\right) = C^4 \text{var}\left(n_1(t) \star n_2(t) + \frac{1}{C} n_1(t) \star s_2(t)\right) \\ &\approx C^4 \text{var}\left(n_1(t) \star n_2(t) + n_1(t) \star s_2(t)\right) = C^4 P_n.\end{aligned} \tag{9.12}$$

So we expect that we can achieve a close approximation to our desired post processing SNR by setting

$$C = \sqrt[4]{\frac{P_s}{(\text{SNR})P_n}}. \tag{9.13}$$

For each of the images below we perform the input SNR measurement according to

$$\text{SNR}_{\text{In}} = \frac{|s_1^H(t) s_1(t)|^2}{|n_1^H(t) n_1(t)|^2} \tag{9.14}$$

where $s_1(t)$ is the signal recorded at receiver γ_1 for a single slow time step and $n_1(t)$ is the additive noise applied to the signal for the same slow time look. We can then average these measurements over all slow time positions to arrive at measurement of the input signal to noise ratio.

For each image we also report a measurement of the 'single look' SNR for the cross correlated data, and an SNR for the final SASL image. We do this by measuring the peak power of the result of cross correlating the noiseless signal recorded at γ_1 with the signal data recorded at receiver γ_2; this value becomes our $|\eta_s(\tau)|^2$. We then measure the noise power by processing the noise signal present in the receiver channel γ_1 with the signal data recorded at receiver γ_2 and take the variance of the result. This becomes our σ_n^2. The ratio of these two quantities is then the reported single look post processing SNR.

It is important to reiterate that this value is provided for heuristic purposes. We are here applying the theory of purely additive noise to a case in which there are multiplicative factors involved. As previously stated, this provides a useful metric for the purposes of introducing the ideas of system performance for the purposes of this dissertation, but a fully detailed analysis of the noise present in the post processing stage is beyond the scope of our work.

We also measure the average noise power present in the final image using a similar process and report the resulting SNR measurement for heuristic purposes. In each case the SNR is given in decibels and in each image we continue with the convention of setting the peak point in the image to a decibel level of 0.

Now that we have established the methods for our calculation of the noise levels present in the signal reception we can visually examine the affect of various levels of noise on the images. We begin by imaging a scene with a single emitter and build up to the case of multiple emitters. We take the receivers to be both in motion flying along the flight path described in figure 8.12 at a height of $1km$ above the ground plane.

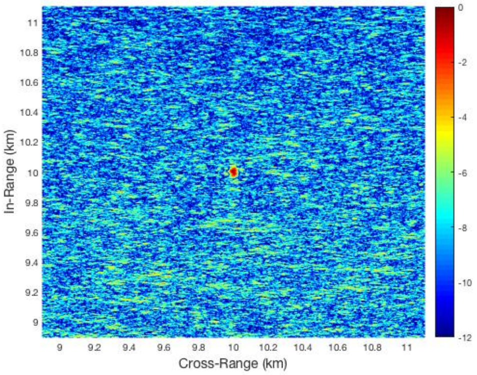

(a) The SASL image with:
An Input SNR of -43.7db
A single look SNR of -4.9db
An image SNR of 9.5db

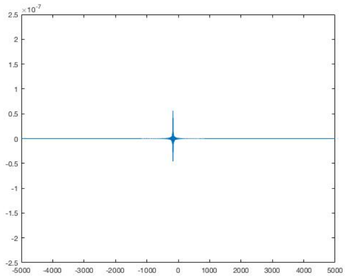

(b) The noiseless cross correlated signal

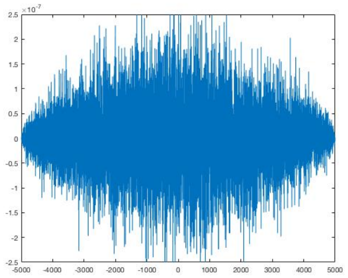

(c) The post processing noise

Figure 9.1: A single emitter scene with a high noise level.

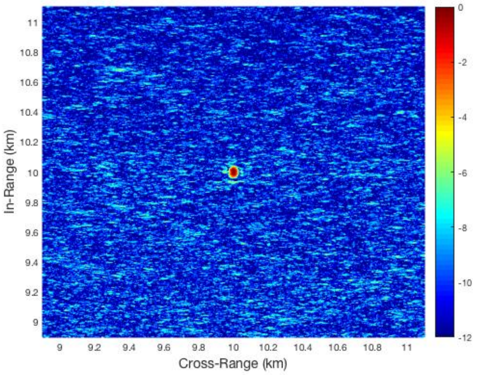

(a) The SASL image with:
An Input SNR of -38.8db
A single look SNR of 0.1db
An image SNR of 12.0 db

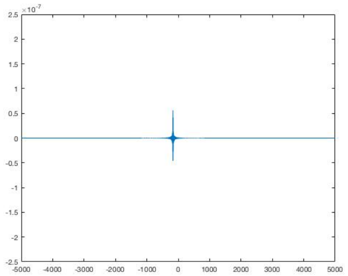

(b) The noiseless cross correlated signal

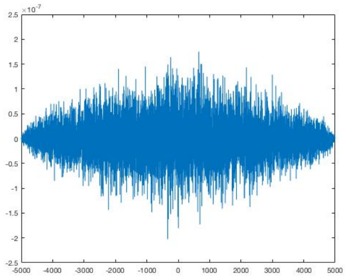

(c) The post processing noise

Figure 9.2: A single emitter scene with a moderate noise level.

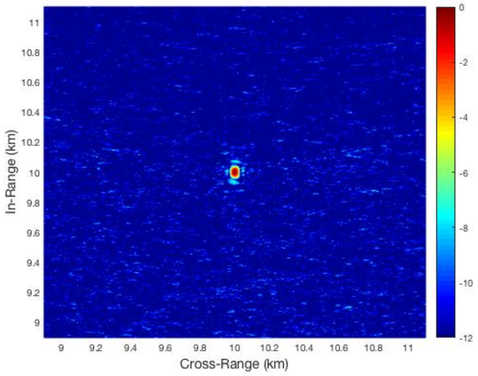

(a) The SASL image with:
An Input SNR of -29.3db
A single look SNR of 9.8db
An image SNR of 17.24db

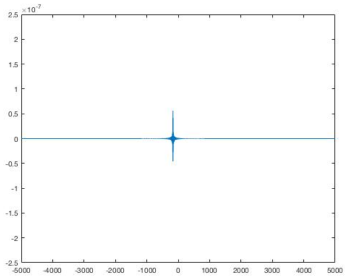

(b) The noiseless cross correlated signal

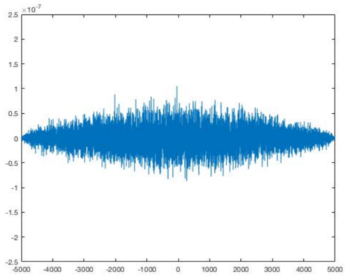

(c) The post processing noise

Figure 9.3: A single emitter scene with a low noise level.

We can also examine how the image of a target scene appears when multiple emitters are present and the signal reception is noisy. In figure 9.4 we image a target scene containing 5 identical transmitting antennas in the presence of the same input noise level shown in figures 9.1 - 9.3.

In these images we see that the emitters are distinguishable from the noise, though not easily at an input SNR of around -44db. At this level of the noise the distortion of the image is on par with the artifacts present from the cross term phantoms. As the noise level is reduced the cross term phantoms begin to dominate the distortion due to the presence of noise in the signal reception. By the time an input SNR of around -30db is reached the impact of the noise on the image is negligible compared to that of the artifacts from the cross term effects.

We saw in chapter 7 that increasing the length of the synthetic aperture reduces the strength of the cross term contributions to the image. One can ask whether increasing the length of the synthetic aperture provides an improvement in the SASL image degradation due to noise. In the images below we compare three different data collection geometries. These data collection geometries are shown in the diagrams of figure 9.5.

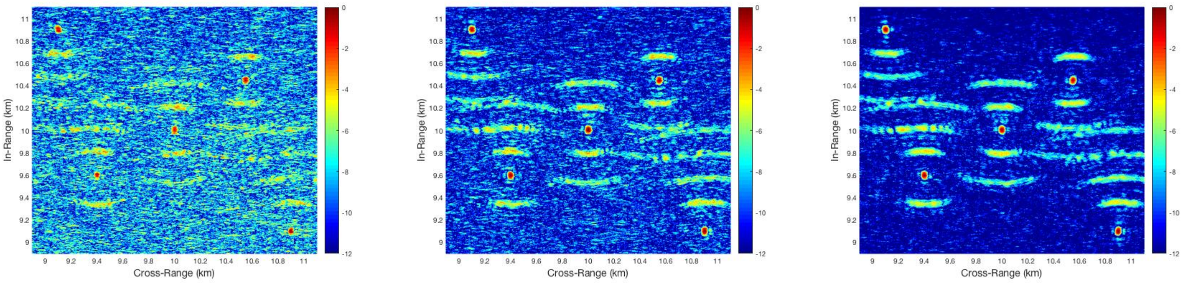

(a) An Input SNR of -43.7db **(b)** An Input SNR of -38.8db **(c)** An Input SNR of -29.3db

Figure 9.4: A target scene containing five identical emitters for three levels of noise.

In the following cases we will use these different data collection parameters to examine the effect on the image of two separate factors. First, we will compare the image formed from the data collected using the flight path shown in figure 9.5a to that formed from the data gathered from the flight path in figure 9.5b and 9.5c in order to determine the effects of flying a longer flight path with a broader angle diversity of the target scene.

Then, we will compare the images created from the data collected in the flight paths shown in figure 9.5b and figure 9.5c to determine the effect of flying the same flight path, but taking more slow time samples as the receiver moves along the flight path.

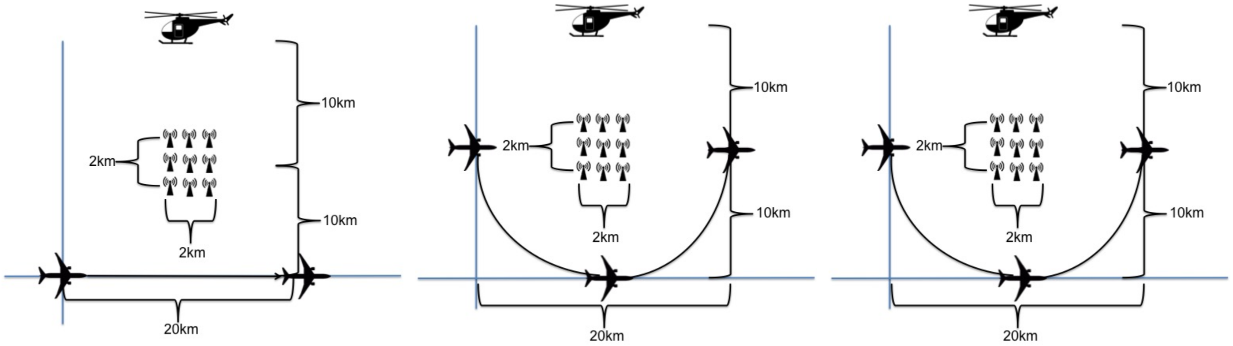

(a) A flight path with 200 slow time samples **(b)** A flight path with 200 slow time samples **(c)** A flight path with 400 slow time samples

Figure 9.5: The three data collection geometries we are investigating. Note that (B) and (C) are identical flight paths, but (C) contains twice the number of samples that (B) does.

We begin our analysis by imaging our target scene using the three flight paths described in figure 9.5 under the condition of a noiseless data collection. In figure 9.6 observe that, just as we had already demonstrated in chapter 7, when the flight path is lengthened the image resolution is improved and the appearance of the cross terms is reduced.

What is important to note here is that the SASL image shown in figure 9.6b is barely distinguishable from that shown in figure 9.6c. Both are much more clear than the image in figure 9.6a. This is a result of the longer synthetic aperture used to form the image. We observe that the use of twice as many samples along this flight path has little discernible effect on the image formed, especially compared to the difference made by the flight path used. Thus, we conclude that, in the noiseless case, the length of the aperture is crucial to image formation, but the number of slow time samples along the flight path is relatively unimportant.

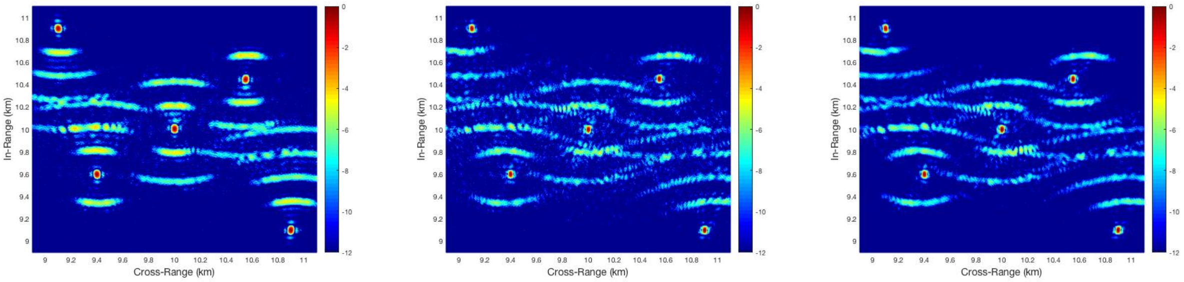

(a) The image created from the flight path shown in figure 9.5a

(b) The image created from the flight path shown in figure 9.5b

(c) The image created from the flight path shown in figure 9.5c

Figure 9.6: Three images of the same target scene with zero noise for three different data collections.

We contrast this finding with the conclusions which can be drawn from the images in figure 9.7. Here we form three images of the target scene using exactly the same flight path parameters used to form the images in figure 9.6. However, in this second example the images are formed in the presence of -43.7db SNR input noise which contaminates the signal reception.

In this example we see that, as expected, the image in figure 9.7b is better than the one in figure 9.7a. However, in addition to this, we find that the image in figure 9.7c is significantly better than its counterpart in figure 9.7b.

Additional samples along the flight path integrate coherently in our image. Since the noise in each measurement is incoherent and uncorrelated with the noise in the previous measurement, the more samples taken along the flight path, the better the image formed in the presence of noise.

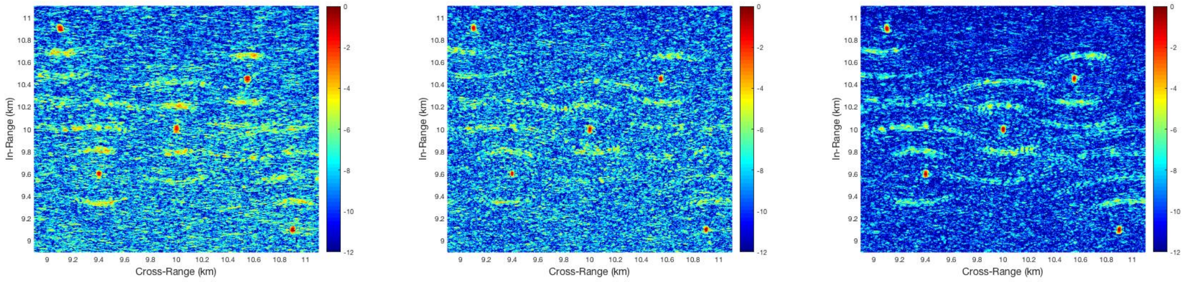

(a) Flight path (A)

(b) Flight path (B)

(c) Flight path (C)

Figure 9.7: The same target scene with an input SNR of -43.7db for three different data collections.

As a result of this analysis we conclude that, all other factors being equal, flying a longer flight trajectory and taking additional samples along that flight path will lead to improved image quality and therefore better emitter detection and localization. A quantitative analysis of the degree of improvement for each additional sample along the flight path will only become possible once a rigorous analysis of the post processing SNR is completed. Due to the highly complicated nature of the interaction of the noise signal with the data processing steps in the SASL imaging process this is left to future work.

Chapter 10

CONCLUSIONS AND FUTURE WORK

10.1 Conclusions

In this work we have briefly overviewed the state of the art in source localization techniques and presented a new method, Synthetic Aperture Source Localization (SASL). This new method requires at least two spatially separated receivers, of which at least one must be in motion. We have shown that this method is able to image multiple sources in a scene simultaneously, though a sizable synthetic aperture must be formed in order to do so. In this way the method is able to improve upon other methods which are currently employed, such as MUSIC, in the domains in which it is appropriate.

We have also seen that the use of the SASL imaging technique produces undesirable phantoms in the image when two or more receivers are highly correlated with one another. We have proven that, under relatively mild conditions within the control of the system operator, these phantoms can be minimized by flying progressively longer flight paths. Furthermore, we have shown that such phantoms will not form persistent peaks in the image at locations other than the locations of true emitters.

We have shown that the method is capable of imaging target emitters in the presence of noise and that the effect of noise on the ability to localize target emitters can be reduced by increasing the number of samples taken along the chosen flight path.

10.2 Future Work

A significant body of work remains to be done in order to fully characterize the use of this method and determine its efficacy in source localization. Among the remaining work to be accomplished are several natural next steps which, if accomplished would round out the theory presented in this thesis and improve the ground truth fidelity of the modeling work produced herein.

Firstly, we have assumed throughout this dissertation that the locations of the two receiving platforms are known with perfect accuracy. In practice this will not be the case and some position errors will be present. Thankfully, a great body of work already exists in correcting for these errors in traditional SAR systems. A future effort will be to leverage this work to make the SASL imaging method more robust to discrepancies in the position of the receivers along the flight path.

Second, although we have thoroughly examined the case of a three dimensional flight path data collection for the case of two receivers at constant height above a flat ground plane, this is not entirely realistic. A future effort will be to rigorously characterize flight paths in which both receivers fly trajectories of varying heights above a non-flat ground plane. This will require significant effort to determine the TDOA and FDOA curves and will lead to a reexamination of the stationary phase argument under these general conditions.

Third, it is the current belief of the author that cross term phantom backprojections, even in the case of correlated emitters, can be shown to be at worst no stronger than the equivalent backprojection of the more powerful of the two emitters under consideration. This could lead to a proof that, in addition to the non-focusing behavior already demonstrated, the cross terms phantoms will always be below the peak height of the strongest emitter in a two emitter scene. This too shall be investigated at a future date along side a more detailed analysis of the overall power of the cross terms in the image.

Fourth, while we have proven that the envelope of the family of backprojections is degenerate for diagonal terms and that it is non-degenerate for cross terms under certain conditions, this proof was done under rather restrictive flight path assumptions. A future effort will be to prove that these results hold under more general flight paths in which both receivers are in motion along arbitrary trajectories. With this will naturally come an effort to determine if complementary flight paths can be chosen that optimize the resulting SASL image and minimize the appearance of phantoms for arbitrarily placed emitters in a scene.

Finally, we have assumed throughout this work that all emitters and receivers are operating isotropically and that emitters transmit throughout the duration of the flight path, although they may be turning on and off at various times during our data collection. In practice many emitters of interest will be operating with significant gain along the bore sight of the antenna beam pattern with negligible energy transmitted along various trajectories leading out from the antenna location. A more thorough study of the SASL image which we are capable of forming under such conditions is warranted.

In addition to these efforts a good deal of investigative work remains to be done on the characterization of noise in the SASL measurements and how the processing of the recorded signals affects the resulting SNR of the final image. This will require a great deal more research into the processing of noise when the noise behaves multiplicatively. The hope is that further investigation into this aspect of the problem will provide avenues to more rigorously characterize the performance behavior of the system in a wide variety of circumstances.

Various extensions of this work may also be considered. Among them, the use of some form of automatic recognition algorithm, whether deterministic, statistical, or based upon a machine learning approach, to recognize target emitters in a scene of interest from a SASL image. If such a method were developed it may open the door to combining work done in finding optimal flight paths for given target geometries with an AI or gametheoretic approach in real time. Such a system may be able to take a partially formed SASL image, determine the likely location of a number of emitters in the scene, and autonomously adjust its flight plan in order to maximize localization of the hypothesized emitters in the final SASL product.

It is the author's hope and intention to tackle several of these challenges in the coming years ultimately leading toward deeper understanding and presentation of the theory of SASL imaging than is possible in this document given the scope of the effort to be completed.

Bibliography

[1] Anders Johan Nygren. Filtered back projection, 1997 Referenced April 2016. http://www.owlnet.rice.edu/~elec539/Projects97/cult/node2.html.

[2] Margaret Cheney and Brett Borden. *Fundamentals of radar imaging*, volume 79. Siam, 2009.

[3] K.C. Ho and Y.T. Chan. Solution and performance analysis of geolocation by tdoa. *IEEE Transactions on Aerospace and Electronic Systems*, 29, 1993.

[4] Rohde & Schwarz. Introduction into theory of direction finding. Technical report, Radiomonitoring & Radiolocation, 2010/2011.

[5] F. Nebeker. *Dawn of the Electronic Age: Electrical Technologies in the Shaping of the Modern World, 1914 to 1945*. John Wiley & Sons, 2009.

[6] W. Read. Review of conventional tactical radio direction finding systems. Technical report, Defense Research Establishment Ottawa, May 1989.

[7] Fawwaz Alsubaie. Multiple signal classification for determining direction of arrival of frequency hopping spread spectrum signals. Master's thesis, Air Force Institute of Technology, 2014.

[8] R. Roy and T. Kailath. Esprit-estimation of signal parameters via rotational invariance techniques. *IEEE Transactions of Acoustics, Speech, and Signal Processing*, 37, July 1989.

[9] Ralph O. Schmidt. Multiple emitter location and signal parameter estimation. *IEEE Transactions on Antennas and Propagation*, AP-34(3), 1986.

[10] Alan J. Laub. *Matrix Analysis for Scientists and Engineers*. Society for Industrial and Applied Mathematics, 2005.

[11] Stephen J Norton and Melvin Linzer. Backprojection reconstruction of random source distributions. *The Journal of the Acoustical Society of America*, 81(4):977–985, 1987.

[12] Charles H. Knapp and Clifford G. Carter. The generalized correlation method for estimation of time delay. *Acoustics, Speech and Signal Processing, IEEE Transactions on*, 24(4):320–327, 1976.

[13] Don J Torrieri. Statistical theory of passive location systems. *IEEE Transactions on Aerospace and Electronic Systems*, 20(2):183, 1984.

[14] Mark L Fowler and Xi Hu. Signal models for tdoa/fdoa estimation. *Aerospace and Electronic Systems, IEEE Transactions on*, 44(4):1543 – 1550, 2008.

[15] Stephen J Norton, Bradley J Carr, and Alan J. Witten. Passive imaging of underground acoustic sources. *The Journal of the Acoustical Society of America*, 119(5):2840–2847, 2006.

[16] Somaieh Beladi and Pubudu N Pathirana. Tdoa based transmitter localization with minimum number of receivers and power measurements. In *Control, Automation, Robotics and Vision, 2008. ICARCV 2008. 10th International Conference on*, pages 1259–1264. IEEE, 2008.

[17] Ling Wang and Birsen Yazici. Passive imaging of a non-cooperative moving rf emitter using sparsely distributed receivers. In *Radar Conference (RADAR), 2013 IEEE*, pages 1–4. IEEE, 2013.

[18] Paul Scerri, Robin Glinton, Sean Owens, David Scerri, and Katia Sycara. Geolocation of rf emitters by many uavs. In *AIAA Infotech @ Aerosapce 2007 Conference and Exhibit*, page 2858, 2007.

[19] Robert J Bamberger, Jay G Moore, Ravi P Goonasekeram, and David H Scheidt. Autonomous geolocation of rf emitters using small, unmanned platforms. *Johns Hopkins APL technical digest*, 32(3):636, 2013.

[20] Samuel P Drake and Kutluyil Doğançay. Geolocation by time difference of arrival using hyperbolic asymptotes. In *Acoustics, Speech, and Signal Processing, 2004. Proceedings.(ICASSP'04). IEEE International Conference on*, volume 2, pages ii–361. IEEE, 2004.

[21] Daniel E Hack, Lee K Patton, Braham Himed, and Michael A Saville. On the applicability of source localization techniques to passive multistatic radar. In *Signals, Systems and Computers (ASILOMAR, 2012, Conference Record of the Forty Sixth Asilomar Conference on*, pages 8484–852. IEEE, 2012.

[22] Jun Liu, Hongbin Li, and Braham Himed. On the performance of the cross-correlation detector for passive radar applications. *Signal Processing*, 113:32–37, 2015.

[23] Alon Amar and Anthony J. Weiss. Fundamental limitations of the number of resolvable emitters using a geolocation system. *IEEE Transactions on Signal Processing*, 55(5), 2007.

[24] Anthony J. Weiss and Alon Amar. Direct geolocation of stationary wideband radio signal based on time delays and doppler shifts. In *IEEE 15th Workshop on Statistical Signal Processing*, 2009.

[25] Tom Tirer and Anthony J. Weiss. High resolution direct position determination of radio freuency sources. *IEEE Signal Processing Letters*, 23(2), 2016.

[26] Anthony J. Weiss and Tom Tirer. Performance analysis of a high-resolution direct position determination method. *IEEE Transactions on Signal Processing*, 65(3), 2017.

[27] Charles V. Jakowatz Jr., Daniel E. Wahl, Paul H. Eichel, Dennis C. Ghiglia, and Paul A. Thompson. *Spotlight-Mode Synthetic Aperture Radar: A Signal Processing Approach*. Springer Science & Business Media, 2012.

[28] Mark A Richards, James A Scheer, William A Holm, and William L Melvin. *Principles of modern radar basic principles*. SciTech Pub., 2010.

[29] Kaitlyn Voccola. *Statistical and analytical techniques in synthetic aperture radar imaging*. PhD thesis, Rensselaer Polytechnic Institute, 2011.

[30] Clifford Nolan and Margaret Cheney. Synthetic aperture inversion. *Inverse Problems*, 18(1):221, 2002.

[31] Can Evren Yarman, Birsen Yazici, and Margaret Cheney. Bistatic synthetic aperture radar imaging for arbitrary flight trajectories. *Image Processing, IEEE Transactions on*, 17(1):84–93, 2008.

[32] Nicholas J Willis. *Bistatic radar*. SciTech Publishing, 2005.

[33] Can Evren Yarman, Birsen Yazici, and Margaret Cheney. Synthetic aperture hitchhiker imaging using non-cooperative sources of opportunity. In *Defense and Security Symposium*, pages 656806–656806. International Society for Optics and Photonics, 2007.

[34] Can Evren Yarman and Birsen Yazici. Synthetic aperture hitchhiker imaging. *Image Processing, IEEE Transactions on*, 17(11):2156–2173, 2008.

[35] Nicholas J Willis and Hugh D Griffiths. *Advances in bistatic radar*. Scitech Publishing INC, 2007.

[36] Alan V. Oppenheim and Ronald W. Schafer. *Discrete-Time Signal Processing*. Pearson, 2014.

[37] The airsar project, 2008 Referenced October 2016. http://airsar.jpl.nasa.gov.

[38] Federal Communications Commission. How to apply for a radio or television broadcast station. https://fcc.gov/media/radio/how-to-apply, December 2015.

[39] Conversations With Dr. James Given of NRL.

[40] G Arfken. *Mathematical Methods for Physicists 2nd edn (New York: Academic)*. Academic Press, 1970.

[41] A.F. Bermant. *A Course Of Mathematical Analysis Part II*, volume 30 of *International Series of Monographs in Pure and Applied Mathematics*. Perfamon Press Limited, 1963.

[42] V.G. Boltyanskii. *Envelopes*, volume 12 of *Popular Lectures in Mathematics*. The Macmillan Company, 1961.

[43] Worlfram mathworld. http://mathworld.wolfram.com, July 2017.

[44] George B Thomas Jr., Maurice D. Weir, and Joel Hass. *Thomas' Calculus*. Pearson, 12th edition, 2010.

[45] Simon Haykin. *Communication Systems*. John Wiley & Sons Inc., 1983.

[46] Eric W. Weisstein. Wiener-Khinchin thoerem, Referenced May 2016. http://mathworld.wolfram.com/Wiener-KhinchinTheorem.html.

[47] Norman Bleistein and Richard A. Handelsman. *Asymptotic Expansions of Integrals*. Dover Publications Inc., 1986.

[48] Hyperbola. https://en.ekipedia.org/wiki/Hyperbola, January 2018.

Appendix A

THE CROSS CORRELATION FUNCTION

The cross-correlation of two signals provides a measure of the similarity between one signal and a time delayed version of a second signal. For a single signal recorded at two receivers, the cross-correlation is a function of the time delay and experiences a peak at the Time Difference of Arrival (TDOA) of the two recorded signal copies. [12,45]

The cross correlation of two functions h and g is defined as,

$$h(t) \star g(t) \equiv \bar{f}(-t) * g(t) \tag{A.1}$$

where $^{-}$ denotes complex conjugation. This may be written in integral forms as

$$h(t) \star g(t) = \int \bar{f}(\tau) g(t+\tau) d\tau. \tag{A.2}$$

If $h = g$, that is, if one cross correlates a function with itself, then the cross correlation is known as the autocorrelation. The autocorrelation thus provides a measure of the similarity between a signal and time delayed replica of itself. The *Wiener-Khinchin* theorem provides a useful formula for the autocorrelation in terms of the Fourier transform

$$h(t) \star h(t) = \mathcal{F}^{-1}\left\{|H(f)|^2\right\} \tag{A.3}$$

where $\mathcal{F}^{-1}$ denotes the inverse Fourier transform and H is the frequency domain version of h so that H is defined by $H(f) = \mathcal{F}\{h(t)\}$.

So, the autocorrelation of a function amounts to simply taking the inverse Fourier transform of the absolute square of the frequency domain version of the function. Put another way, the autocorrelation of a signal is equal to the Fourier transform of that signal's spectral density. [46] [45]

A more general result known as the Cross Correlation Theorem applies to the cross correlation of functions which are not identical.

Theorem: Let $H(f) = \mathcal{F}\{h(t)\}$ and $G(f) = \mathcal{F}\{g(t)\}$ be the Fourier transforms of h and g respectively. Then

$$\begin{aligned}
h(t) \star g(t) &= \int \bar{h}(\tau) g(t+\tau) d\tau = \int\int \bar{H}(f_1) e^{i2\pi f_1 \tau} df_1 \int G(f_2) e^{-i2\pi f_2 (t+\tau)} df_2 d\tau && \text{(A.4)} \\
&= \int\int\int \bar{H}(f_1) G(f_2) e^{-i2\pi f_2 t} e^{-i2\pi\tau(f_1 - f_2)} df_1 df_2 d\tau && \text{(A.5)} \\
&= \int\int \bar{H}(f_1) G(f_2) e^{-i2\pi f_2 t} \left[\int e^{-i2\pi\tau(f_1 - f_2)} d\tau \right] df_1 df_2 && \text{(A.6)} \\
&= \int\int \bar{H}(f_1) G(f_2) e^{-i2\pi f_2 t} \delta(f_1 - f_2) df_1 df_2 && \text{(A.7)} \\
&= \int \bar{H}(f_1) G(f_1) e^{-i2\pi f_1 t} df_1 && \text{(A.8)} \\
&= \mathcal{F}^{-1}\left\{ \bar{H}(f) G(f) \right\} && \text{(A.9)}
\end{aligned}$$

Appendix B

THE METHOD OF STATIONARY PHASE

This asymptotic method applies to integrals of the form

$$I(\lambda) = \int_a^b e^{i\lambda\phi(t)} f(t)dt. \tag{B.1}$$

The goal of the stationary phase calculation is to determine the leading order contributions to I. This is done by finding the critical points which contribute the bulk of the total value of I over the interval $[a, b]$. We will see that these points are precisely those for which $\phi' = 0$. [47]

First suppose that $\phi'(c) \neq 0$ for some value c. Then there exists a neighborhood of c denoted N_c such that $\phi(t)$ varies in N_c. If the value of λ is large then $\lambda\phi(t)$ is rapidly varying in N_c. Thus, $e^{i\lambda\phi(t)}$ is a rapidly oscillating function in N_c.

Now we consider the integral of $e^{i\lambda\phi(t)}$ over the neighborhood N_c.

$$I_c(\lambda) = \int_{N_c} e^{i\lambda\phi(t)} f(t)dt \tag{B.2}$$

Since N_c is assumed to be a small neighborhood we may take $f(t)$ to be roughly constant. That is, we simplify (B.2) by taking $f(t) \approx f(c)$ to achieve

$$I_c(\lambda) = \int_{N_c} e^{i\lambda\phi(t)} f(c)dt = f(c) \int_{N_c} e^{i\lambda\phi(t)} dt. \tag{B.3}$$

Thus I_c is the integral over a rapidly oscillating function so that it tends to cancel out over the interval and we expect the value of I_c to be near zero. The rate of cancellation is increased for increasing λ, thus the requirement for a large λ mentioned above.

In contrast let us assume that $\phi'(c) = 0$ for some c. Then there exists a neighborhood of c such that $\phi(t)$ is not rapidly varying regardless of the value of λ by which it is multiplied. Thus, the integral over such a neighborhood N_c would not be canceled out by rapidly varying oscillations as it is for the case where $\phi'(c) \neq 0$.

Here we note that the length of the interval $N_c(\lambda)$ for which $\lambda\phi(t)$ is not rapidly varying is dependent on the value of λ and decreases for increasing λ. Thus $N_c(\lambda) \to 0$ as $\lambda \to \infty$ and so the contribution to the integral $I(\lambda)$ for any such point c (referred to as a stationary point) goes to 0 as λ goes to infinity. The leading-order contribution to the integral from these stationary points behaves like $\frac{1}{\sqrt{\lambda}}$.

Furthermore, it can be shown that the contribution to $I(\lambda)$ from such stationary points dominates the contribution to the integral from the end points a and b. Thus, it is the coefficient of the leading order term which dominates any other contributions and is most important for approximating the integral value. [47]

For our case it is necessary to state the more complicated multidimensional approximation. Here we have that:

$$\int e^{i2\pi\omega\phi(x)} f(x) d^n x = \sum_{x_0 : D\phi(x_0)=0} \left(\frac{1}{\omega}\right)^{n/2} a(x_0) \frac{\exp[i2\pi\omega\phi(x_0)] \exp[i(\pi/4) sgn D^2\phi(x_0)]}{\sqrt{|det D^2\phi(x_0)|}} \tag{B.4}$$

Where D denotes the gradient, D^2 denotes the Hessian, and sgn denotes the signature of the matrix.

In practice, for our purposes, we use the method of stationary phase, not to approximate the integral directly, but to determine the critical points of the phase in order to ensure desirable behavior of the Point Spread Function in a neighborhood of those points. [31]

Appendix C

DERIVATION OF THE STOLT CHANGE OF VARIABLES

Let $f(\lambda)$ be any real valued function. Then from the Fundemental Theorem of Calculus we have

$$\int_z^x f'(\lambda)d\lambda = f(x) - f(z). \tag{C.1}$$

We may make a change of variables $\lambda = z + \mu(x - z)$ in the integrand above so that

$$\int_z^x f'(\lambda)d\lambda = \int_0^1 f'(z + \mu(x - z))(x - z)d\mu = f(x) - f(z) \tag{C.2}$$

where the $(x - z)$ factor arising from the Jacobian may be pulled outside the integral, yielding the expression

$$f(x) - f(z) = (x - z)\int_0^1 f'(z + \mu(x - z))d\mu. \tag{C.3}$$

This process can be extended for use in higher dimensions by application of the Gradient Theorem for Line Integrals. This theorem states that,

$$\int_C \nabla\mathbf{f} \cdot ds = \mathbf{f}(\mathbf{b}) - \mathbf{f}(\mathbf{a}) \tag{C.4}$$

where C is any curve in the plane and $\mathbf{b}$ and $\mathbf{a}$ are its end points. Considering then $\mathbf{x}, \mathbf{z}$ as the end points of such a curve we can write

$$\int_{\mathbf{z}}^{\mathbf{x}} \nabla f(s) \cdot ds = f(\mathbf{x}) - f(\mathbf{z}) \tag{C.5}$$

for any such curve.

Via the change of variables $s = \mathbf{z} - \mu(\mathbf{x} - \mathbf{z})$ with corresponding Jacobian $(\mathbf{x} - \mathbf{z})$ we have that, for an arbitrary function of three variables

$$f(\mathbf{x}) - f(\mathbf{z}) = (\mathbf{x} - \mathbf{z}) \cdot \int_0^1 \nabla f(\mathbf{z} + \mu(\mathbf{x} - \mathbf{z}))d\mu \tag{C.6}$$

as in the single variate case above.

For our particular case we simply let $f(\mathbf{x}) = r(s, \mathbf{x})$ which results in:

$$r(s, \mathbf{x}) - r(s, \mathbf{z}) = (\mathbf{x} - \mathbf{z}) \cdot \int_0^1 \nabla r(s, \mathbf{z} + \mu(\mathbf{x} - \mathbf{z}))d\mu. \tag{C.7}$$

We then define

$$\Xi(s, \mathbf{x}, \mathbf{z}) = \int_0^1 \nabla r(s, \mathbf{z} + \mu(\mathbf{x} - \mathbf{z}))d\mu \tag{C.8}$$

so that

$$(\mathbf{x} - \mathbf{z}) \cdot \Xi(s, \mathbf{x}, \mathbf{z}) = r(s, \mathbf{x}) - r(s, \mathbf{z}). \tag{C.9}$$

Fixing $\mathbf{x}$ and $\mathbf{z}$ allows us to define the Stolt change of variables in equation (4.43) as

$$(f, s) \to \xi = \frac{f}{c_0}\Xi(s, \mathbf{x}, \mathbf{z}). \tag{C.10}$$

Appendix D

THE BEYLKIN DETERMINANT

D.1 Analytic Derivation

First recall that we have defined:

$$r(s,\mathbf{x}) = |\gamma_1(s) - \mathbf{x}| - |\gamma_2(s) - \mathbf{x}| \tag{D.1}$$

and

$$\Xi(s,\mathbf{x},\mathbf{z}) = \int_0^1 \nabla r(s, \mathbf{z} + \mu(\mathbf{x} - \mathbf{z}))d\mu \tag{D.2}$$

where the differentiation takes place over the variable y for $r(s, y)$. Thus we may consider the case for $\mathbf{x}, \mathbf{z}$ fixed and for which $\mathbf{x} = \mathbf{z}$, which we have already seen is the point which contributes the bulk of the value of the backprojected image. We thus have

$$\Xi(s,\mathbf{z},\mathbf{z}) = \int_0^1 \nabla r(s,\mathbf{z})d\mu. \tag{D.3}$$

Here we may write

$$\nabla r(s,\mathbf{z}) = \frac{d}{dz_x dz_y}\left(|\gamma_1(s) - \mathbf{z}| - |\gamma_2(s) - \mathbf{z}|\right) = (-1)\left(\frac{(\gamma_1(s) - \mathbf{z}) \cdot D_{\mathbf{z}}}{|\gamma_1(s) - \mathbf{z}|} - \frac{(\gamma_2(s) - \mathbf{z}) \cdot D_{\mathbf{z}}}{|\gamma_2(s) - \mathbf{z}|}\right). \tag{D.4}$$

Recalling that $\mathbf{z} = [z_x, z_y, \psi(z_x, z_y)]$ we have

$$D_{\mathbf{z}} = \begin{bmatrix} 1 & 0 \\ 0 & 1 \\ \dot{\psi}(z_1,z_2)|_{z_1} & \dot{\psi}(z_1,z_2)|_{z_2} \end{bmatrix}. \tag{D.5}$$

Thus carrying out the integration above in μ we have:

$$\Xi(s,\mathbf{z},\mathbf{z}) = \begin{bmatrix} 1 & 0 & \partial\psi/\partial z_1 \\ 0 & 1 & \partial\psi/\partial z_2 \end{bmatrix} \left(\frac{(\gamma_2(s)-\mathbf{z})}{|\gamma_2(s)-\mathbf{z}|} - \frac{(\gamma_1(s)-\mathbf{z})}{|\gamma_1(s)-\mathbf{z}|} \right). \tag{D.6}$$

We note here that the two terms on the right hand side of (D.6) are unit vectors pointing from the location of the receivers to the point $\mathbf{z}$ in the scene. For a flat earth we have

$$\Xi(s,\mathbf{z},\mathbf{z}) = \begin{bmatrix} 1 & 0 & 0 \\ 0 & 1 & 0 \end{bmatrix} \left(\frac{(\gamma_2(s)-\mathbf{z})}{|\gamma_2(s)-\mathbf{z}|} - \frac{(\gamma_1(s)-\mathbf{z})}{|\gamma_1(s)-\mathbf{z}|} \right) \tag{D.7}$$

and in the case of a purely two dimensional test system we have:

$$\Xi(s,\mathbf{z},\mathbf{z}) = \begin{bmatrix} 1 & 0 \\ 0 & 1 \end{bmatrix} \left(\frac{(\gamma_2(s)-\mathbf{z})}{|\gamma_2(s)-\mathbf{z}|} - \frac{(\gamma_1(s)-\mathbf{z})}{|\gamma_1(s)-\mathbf{z}|} \right). \tag{D.8}$$

In any of these cases it should be clear that we have a 2×3 system multiplied against a 3×1 system or a 2×2 system multiplied against a 2×1 system so that the result will be a 2×1 vector. We may thus write

$$\Xi(s,\mathbf{z},\mathbf{z}) = (\Xi_1, \Xi_2). \tag{D.9}$$

This further justifies the previous change of variables $(s,f) \to \xi = \frac{f}{c_0}\Xi(s,x,z)$.

Explicitly for the case of a two dimensional system we have

$$\begin{bmatrix} \Xi_1 \\ \Xi_2 \end{bmatrix} = \begin{bmatrix} (\gamma_{2x}(s)-z_x)/m_2 - (\gamma_{1x}(s)-z_x)/m_1 \\ (\gamma_{2y}(s)-z_y)/m_2 - (\gamma_{1y}(s)-z_y)/m_1 \end{bmatrix} \tag{D.10}$$

where $m_1 = |\gamma_1(s)-\mathbf{z}|$ and $m_2 = |\gamma_2(s)-\mathbf{z}|$ and $\gamma_{ij}(s)$ denotes the jth component of the position of the ith receiver. For example $\gamma_{2x}(s)$ is the x-axis component of the position of the $2nd$ receiver at time s.

Recalling that we have defined $\xi = \frac{f}{c_0}\Xi(s,\mathbf{x},\mathbf{z})$ we may write the Beylkin determinant as

$$\left|\frac{d\xi}{d(s,f)}\right| = \begin{vmatrix} \frac{d\xi_1}{ds} & \frac{d\xi_2}{ds} \\ \frac{d\xi_1}{df} & \frac{d\xi_s}{df} \end{vmatrix} = \left|\frac{f}{c_0^2}\right| \left|\dot{\Xi}_1\Xi_2 - \Xi_1\dot{\Xi}_2\right| \tag{D.11}$$

where the dot notation denotes differentiation by s.

We then must derive $\dot{\Xi}_1$ and $\dot{\Xi}_2$. We therefore compute

$$\dot{\Xi}_1 = \frac{d}{ds}\left(\frac{\gamma_{1x}(s) - z_1}{|\gamma_1(s) - \mathbf{z}|} - \frac{\gamma_{2x}(s) - z_1}{|\gamma_2(s) - \mathbf{z}|}\right) \tag{D.12}$$

$$\begin{aligned} &= \frac{\dot{\gamma}_{1x}(s)|\gamma_1(s) - \mathbf{z}| - (\gamma_{1x}(s) - z_x)\frac{\gamma_1(s)-\mathbf{z}}{|\gamma_1(s)-\mathbf{z}|}\cdot\dot{\gamma}_1(s)}{|\gamma_1(s) - \mathbf{z}|^2} \\ &- \frac{\dot{\gamma}_{2x}(s)|\gamma_2(s) - \mathbf{z}| - (\gamma_{2x}(s) - z_x)\frac{\gamma_2(s)-\mathbf{z}}{|\gamma_2(s)-\mathbf{z}|}\cdot\dot{\gamma}_2(s)}{|\gamma_2(s) - \mathbf{z}|^2} \end{aligned} \tag{D.13}$$

where $\gamma_{1,x}(s)$ denotes the component of $\gamma_1(s)$ along the x axis.

Simplifying and expanding this expression yields

$$\dot{\Xi}_1 = \frac{\dot{\gamma}_{1x}(s)}{|\gamma_1(s) - \mathbf{z}|} - \frac{\dot{\gamma}_{2x}(s)}{|\gamma_2(s) - \mathbf{z}|} \tag{D.14}$$

$$- \frac{(\gamma_{1x} - z_x)\Big((\gamma_{1x}(s) - z_x)\dot{\gamma_{1x}}(s) + (\gamma_{1y}(s) - z_y)\dot{\gamma}_{1y}(s)\Big)}{|\gamma_1(s) - \mathbf{z}|^3} \tag{D.15}$$

$$+ \frac{(\gamma_{2x} - z_x)\Big((\gamma_{2x}(s) - z_x)\dot{\gamma_{2x}}(s) + (\gamma_{2y}(s) - z_y)\dot{\gamma}_{2y}(s)\Big)}{|\gamma_2(s) - \mathbf{z}|^3}. \tag{D.16}$$

Similarly,

$$\dot{\Xi}_2 = \frac{d}{ds}\left(\frac{\gamma_{1x}(s) - z_2}{|\gamma_1(s) - \mathbf{z}|} - \frac{\gamma_{2y}(s) - z_2}{|\gamma_2(s) - \mathbf{z}|}\right) \tag{D.17}$$

$$\begin{aligned} &= \frac{\dot{\gamma}_{1y}(s)|\gamma_1(s) - \mathbf{z}| - (\gamma_{1y}(s) - z_y)\frac{\gamma_1(s)-\mathbf{z}}{|\gamma_1(s)-\mathbf{z}|}\cdot\dot{\gamma}_1(s)}{|\gamma_1(s) - \mathbf{z}|^2} \\ &- \frac{\dot{\gamma}_{2y}(s)|\gamma_2(s) - \mathbf{z}| - (\gamma_{2y}(s) - z_2)\frac{\gamma_2(s)-\mathbf{z}}{|\gamma_2(s)-\mathbf{z}|}\cdot\dot{\gamma}_2(s)}{|\gamma_2(s) - \mathbf{z}|^2} \end{aligned} \tag{D.18}$$

which simplified and expanded is

$$\dot{\Xi}_2 = \frac{\dot{\gamma}_{1y}(s)}{|\gamma_1(s) - \mathbf{z}|} - \frac{\dot{\gamma}_{2y}(s)}{|\gamma_2(s) - \mathbf{z}|} \tag{D.19}$$

$$- \frac{(\gamma_{1y} - z_y)\Big((\gamma_{1,x}(s) - z_x)\dot{\gamma_{1x}}(s) + (\gamma_{1y}(s) - z_y)\dot{\gamma}_{1y}(s)\Big)}{|\gamma_1(s) - \mathbf{z}|^3} \tag{D.20}$$

$$+ \frac{(\gamma_{2y} - z_y)\Big((\gamma_{2x}(s) - z_x)\dot{\gamma_{2x}}(s) + (\gamma_{2y}(s) - z_y)\dot{\gamma}_{2y}(s)\Big)}{|\gamma_2(s) - \mathbf{z}|^3}. \tag{D.21}$$

D.2 The Beylkin Determinant for One Stationary Receiver

In Appendix D.1 we derived an explicit expression for the Beylkin determinant. For certain geometries however, this expression can be significantly simplified. We turn now to the form of the determinant appropriate to the case of a stationary receiver in the plane with a second receiver flying a straight line flightpath along the x-axis.

We can eliminate some of the terms in Equations (D.13) and (D.18) by noting that, in our case, we have one receiver stationary. We have chosen γ_1 to correspond to the stationary receiver so that $\dot{\gamma}_1(s) = [0, 0]$ and $\dot{\gamma}_{1x}(s) = \dot{\gamma}_{1y}(s) = 0$. Furthermore, if the flight path of the second receiver is confined to the x-axis then $\gamma_{1y}(s) \equiv 0$ for all points s.

In this case then, the entire first term of $\dot{\Xi}_1$ vanishes. Then in $\dot{\Xi}_2$ the entire first term vanishes because $\gamma_1(s)$ is stationary, and so its derivatives are 0 and the second term reduces significantly because $\gamma_{22}(s) \equiv 0$ and so $\dot{\gamma}_{22}(s) = 0$. Thus we have

$$\dot{\Xi}_1 = -\frac{\dot{\gamma}_{2x}(s)|\gamma_2(s) - \mathbf{z}| - (\gamma_{2x}(s) - z_1)\frac{\gamma_2(s) - \mathbf{z}}{|\gamma_2(s) - \mathbf{z}|} \cdot \dot{\gamma}_2(s)}{|\gamma_2(s) - \mathbf{z}|^2} \tag{D.22}$$

and

$$\dot{\Xi}_2 = -\frac{z_y \frac{\gamma_2(s) - \mathbf{z}}{|\gamma_2(s) - \mathbf{z}|} \cdot \dot{\gamma}_2(s)}{|\gamma_2(s) - \mathbf{z}|^2}. \tag{D.23}$$

However, we can also note that $\dot{\gamma}_2(s) = [\dot{\gamma}_{2x}(s), 0]$ so that the expressions above reduce to:

$$\dot{\Xi}_1 = -\frac{\dot{\gamma}_{2x}(s)}{|\gamma_2(s) - \mathbf{z}|} + \frac{\dot{\gamma}_{2x}(s)(\gamma_{2x}(s) - z_1)^2}{|\gamma_2(s) - \mathbf{z}|^3} \tag{D.24}$$

and

$$\dot{\Xi}_2 = -\frac{z_2(\gamma_{2x}(s) - z_1)\dot{\gamma}_{2x}(s)}{|\gamma_2(s) - \mathbf{z}|^3}. \tag{D.25}$$

This greatly simplifies the backprojection calculation for our early example simulations. Once we move into the examination of more general geometries however, the more complex expression derived in D.1 will become necessary.

Appendix E

CHARACTERIZING FAMILIES OF BACKPROJECTIONS IN 3D

In chapter 8 we demonstrated that a receiver which is stationary in a three dimensional data collection produces a focus for the the family of backprojections which moves in the ground plane dimensions during the data collection. In this appendix we further investigate the nature of this apparent motion. The idea behind this effort is that anything which better helps us to understand the family of backprojections which build up the SASL image will, in the future, have potential benefit for designing flight paths to optimize the resulting image.

As an example of this effect, two platforms flying (or in the case of a stationary receiver: hovering) at a height of 1km, as the moving receiver traverses a flight path of 20km will result in the virtual position of the stationary receiver moving approximately 20m. Thus, the effect of the height component is that the stationary receiver appears to move in the plane roughly 0.1% of the distance that the moving receiver does. This is illustrated in figure E.1.

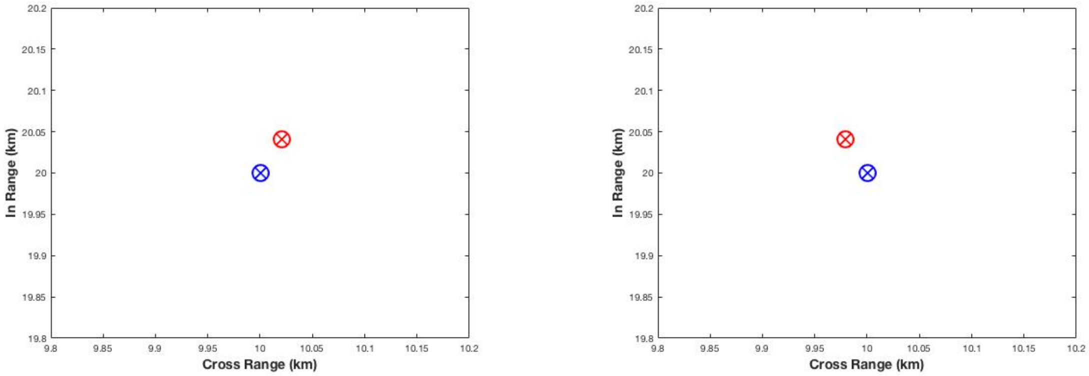

(a) A close up of Γ_1 and the projection of γ_1 for $\gamma_2(s) = (0km, 0km, 1km)$.

(b) A close up of Γ_1 and the projection of γ_1 for $\gamma_2(s) = (20km, 0km, 1km)$.

Figure E.1: The position of a virtual 'stationary' receiver changes due to the motion of the moving receiver at a height of $1km$. The blue X is the projection of the receiver position onto the ground plane. The red X is its virtual position.

Note that these images are zoomed in so that the separation of the two points is clearly visible. The moving receiver's flight path is 20km from that of the stationary receiver and thus very far below (with respect to the in range coordinate as plotted here) the patch of the plane plotted in the following figures.

As the height component of the receiver position is increased the virtual motion of the stationary emitter is correspondingly increased. At a height of 5km the movement of the virtual receiver occurs over roughly 1km. Thus at a height of 5km the scene point corresponding to the stationary receiver travels a virtual flight path roughly 5$\%$ as long as that traveled by the moving receiver, see figure E.2 and note that the scaling is different than in figure E.1.

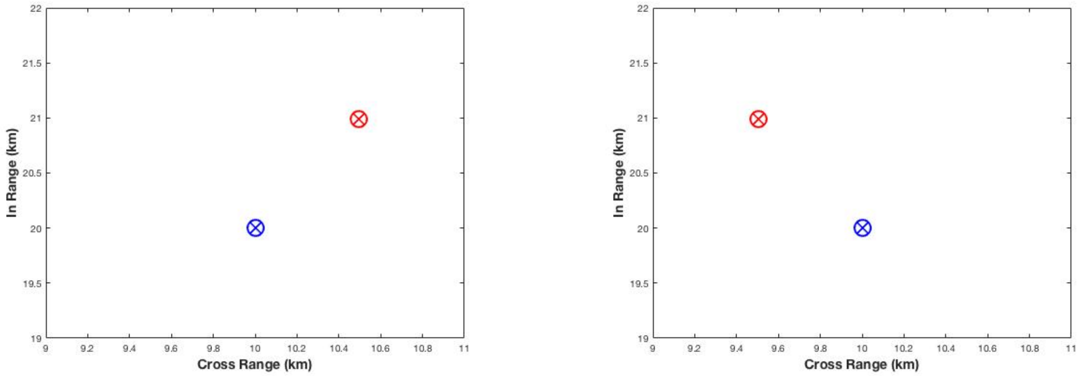

(a) A close up of Γ_1 and the projection of γ_1 for $\gamma_2(s) = (0km, 0km, 5km)$.

(b) A close up of Γ_1 and the projection of γ_1 for $\gamma_2(s) = (0km, 0km, 5km)$.

Figure E.2: The position of a virtual 'stationary' receiver changes due to the motion of the moving receiver at a height of $5km$. The blue X is the projection of the receiver position onto the ground plane. The red X is its virtual position. Note that the scale is different than that of figure E.1

To further illustrate the magnitude of the effect that receiver height plays in the virtual motion of a stationary receiver we plot the two previous examples on the same scale in figure E.3. Here we can see that at a 1km $\times$ 1km scale the effect of having our receiver at a height of 1km has relatively little effect on its virtual position, especially when compared to the effect of a 5km height.

It therefore seems reasonable to conclude that, when the two receivers are flying a trajectory which is close to the ground plane, the two dimensional simulations of the image formation under the assumption of a stationary receiver should be accurate to reality in at least an approximate

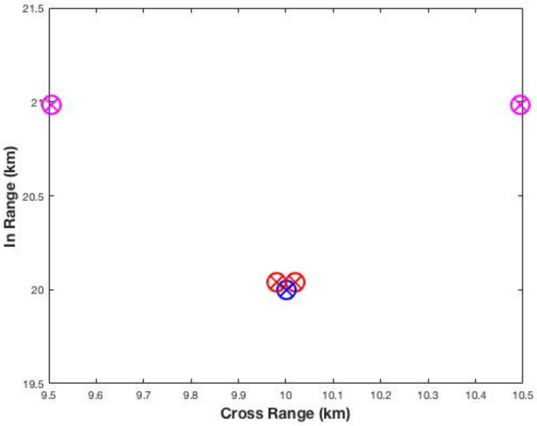

Figure E.3: The two previous examples on the same scale. The blue X is the projection of the receiver position onto the ground plane. The red X's are its virtual positions at the start and end of the flight path at a height of 1km. The magenta X's are its virtual positions at the start and end of the flight path at a height of 5km.

manner. However, when the receivers are flying well above the ground plane under surveillance a hovering receiver cannot be assumed to behave like a stationary receiver in the plane. In such a case, the family of the backprojection hyperbolas will not share a common foci as was the case for our two dimensional work.

It remains to be determined whether this apparent motion in the foci of the backprojection family will aid or detract from the ability to form an image of the target emitters. It is possible that the movement of the foci in the ground plane will allow for a slightly broader diversity of angles which would improve image quality. However, it is also possible that this motion may negatively impact the image due to unforeseen effects on the cross term phantoms present.

It is important to note that, regardless of the effects of this apparent motion, the three dimensional case of a stationary receiver which gives rise to two moving foci is not fundamentally different from the case of a single stationary receiver and a moving one in two dimensions. The backprojection techniques previously derived and simulated hold equally well in both cases and indeed are equally valid for two moving receivers. It was also proven in chapter 8 that these three dimensional flight paths do not produce additional phantom points when compared to the two dimensional case.

Furthermore, when we speak of two receivers flying low enough to the ground plane that a hovering receiver can be considered to produce an essentially stationary focus, we are not assuming in the backprojection process that the focus location is stationary and treating the motion as a form of error. Rather, we are are merely remarking that the various cases and results we have simulated throughout this dissertation regarding the effect of various emitter geometries on the final image will be very near reality for such cases.

In chapter 8 we derived an expression for the location of the foci when the two receivers are at all times located at the same height above the ground plane. We now derive a similar expression for a receiver pair in which the moving receiver is located at a fixed height above the ground and the stationary receiver is located in the ground plane. This ground based receiver could perhaps be a radar located on a fixed tower for example.

We are interested here in determining what can be said regarding the locations of the two foci of the backprojection hyperbolas in the ground plane for such a data collection. Namely, whether the stationary ground receiver can be viewed as a stationary focus for the family of backprojections or if, as was the case above, the foci of the backprojection family move as was the case in the example above.

We have seen that the backprojections for the case of a moving airborne receiver and a stationary ground based receiver can be put into the form

$$A_{xx}x^2 + A_{yy}y^2 - 2B_x x + C = 0 \tag{E.1}$$

where

$$A_{xx} = \frac{4d^2b^2 - a^2h^2}{4a^2d^2b^2} \tag{E.2}$$

$$A_{yy} = -\frac{1}{b} \tag{E.3}$$

$$B_x = -\frac{h^2}{4db^2} \tag{E.4}$$

$$C = -1 - \frac{h^2}{2b^2}. \tag{E.5}$$

From this expression we can derive the major and minor semiaxes α and β according to

$$\alpha^2 = \frac{\Delta}{\lambda_1 \mathcal{D}} = \frac{\Delta}{\lambda_1^2 \lambda_2} \tag{E.6}$$

$$\beta^2 = \frac{\Delta}{\lambda_2 \mathcal{D}} = \frac{\Delta}{\lambda_1 \lambda_2^2} \tag{E.7}$$

where Δ, λ_1, and λ_2 are defined below. [43, 44]

We define Δ as

$$\Delta = \begin{vmatrix} A_{xx} & A_{xy} & B_x \\ A_{xy} & A_{yy} & B_y \\ B_x & B_y & C \end{vmatrix} \tag{E.8}$$

this quantity is also sometimes referred to as the discriminant of the conic section. [48]

We substitute and simplify in equation (E.8) to obtain

$$\Delta = A_{yy} \begin{vmatrix} A_{xx} & B_x \\ B_x & C \end{vmatrix} = \frac{1}{b^2}\left(\left(1 + \frac{h^2}{2b^2}\right)\frac{4d^2b^2 - a^2h^2}{4a^2d^2b^2} + \frac{b^4}{16b^2d^4}\right). \tag{E.9}$$

The quantities λ_1 and λ_2 used in (E.6) and (E.7) are the roots of the quadratic

$$\lambda^2 - (A_{xx} + A_{yy})\lambda + \mathcal{D} = 0. \tag{E.10}$$

Using the quadratic formula $\frac{-b \pm \sqrt{b^2 - 4ac}}{2a}$ we find that

$$\lambda = \frac{1}{2}\left(A_{xx} + A_{yy} \pm A_{xx} \mp A_{yy}\right) \tag{E.11}$$

so that

$$\lambda_1 = A_{xx} \text{ and } \lambda_2 = A_{yy}. \tag{E.12}$$

Thus we find that

$$\alpha^2 = \left(1 + \frac{h^2}{2b^2}\right)\frac{4a^2d^2b}{4d^2b^2 - a^2h^2} + \frac{a^4b^5}{(4d^2b^2 - a^2h^2)^2} \tag{E.13}$$

$$\beta^2 = 1 + \frac{h^2}{2b^2} + \frac{a^2b^2}{16d^2b^2 - 4a^2h^2}. \tag{E.14}$$

The distance $\tilde{d}$ between the two foci of the backprojection hyperbola is given by

$$\tilde{d}^2 = \alpha^2 + \beta^2. \tag{E.15}$$

The center of the intersection hyperbola can be determined by

$$x_c = -\frac{1}{D}\begin{vmatrix} B_x & A_{xy} \\ B_y & A_{yy} \end{vmatrix} \tag{E.16}$$

and

$$y_c = -\frac{1}{D}\begin{vmatrix} A_{xx} & B_x \\ A_{xy} & B_y \end{vmatrix}. \tag{E.17}$$

[48]

For our data collection this yields a center of

$$(x_c, y_c) = \left(\frac{-a^2dbh^2}{4d^2b^2 - a^2h^2}, 0\right). \tag{E.18}$$

Thus, all other things being equal, as the height of the receiver in motion increases, the center of the backprojection hyperbola moves farther from the stationary receiver in the ground plane. As we demonstrated in 8, when this is taken to the extreme the intersection of the hyperboloid of TDOA and the ground plane becomes an ellipse rather than a hyperbola.

As the center of the backprojection hyperbola moves the foci will move as well. Thus, the family of backprojections in this case is also somewhat more complicated than that of the two dimensional case we first investigated. With future work it is hoped that these analytic expressions for the families of the backprojections will yield insights that allow for the optimization of flight paths in producing SASL images.